Science

AAAS

SPECIAL ISSUE

MUTATION
AND HUMAN DISEASE
Revealing pathology with genome sequencing

CONTENTS

25 SEPTEMBER 2015 • VOLUME 349 • ISSUE 6255

1450, 1510, & 1514
Edge states in a quantum gas

NEWS

PHOTO: © PHIL NOBLE/REUTERS

Published by AAAS

CONTENTS

1504
Kinetics and dynamics of protein folding

1459

RESEARCH

Science

Research and Insights

News

Published by AAAS

EDITORIAL

Preimplantation genetic screens

Although our knowledge of genetic abnormalities that cause health disorders is expanding, the pace of discovering cures for genetic diseases is not nearly as fast. However, technologies applicable to preventing heritable genetic diseases have been developing, among them so-called "next-generation sequencing." This efficient and inexpensive means to sequence DNA has revolutionized the study of genomics and could play a major role in future preimplantation genetic screening approaches. It may even improve screening during early pregnancy.

For 25 years, preimplantation genetic diagnosis has been used in circumstances where there is a high risk of a specific genetic defect in an embryo created by in vitro fertilization (IVF). If one or both genetic parents have a known genetic defect, testing can be performed on a single cell from an IVF embryo to determine whether it would be affected with a serious disorder. For many people undergoing IVF, new diagnostics are welcome, less risky alternatives to common prenatal testing for genetic disease (amniocentesis or chorionic villus sampling), which, if the diagnosis is unfavorable, can result in difficult decisions about whether to continue the pregnancy. In 2011, next-generation sequencing was used to simultaneously analyze carriers for more than 400 target genes associated with severe childhood recessive diseases,* helping to spur the availability of expanded carrier testing for disease-associated genetic defects. Earlier this year, several genetic and medical organizations issued a clarification to the genetic and clinical communities on the current state of the art of such carrier testing.† Another more recent approach called preimplantation genetic screening was introduced to detect aneuploidy (abnormal chromosome number) in IVF embryos derived from genetically normal parents. Both preimplantation genetic diagnosis and screening advanced through techniques that now allow longer in vitro cultivation of embryos (thereby providing more cells for analysis) and that detect gene copy number across all chromosomes using advanced molecular cytogenetics (comparative genomic hybridization on a DNA chip).

> *"...it should be possible to prevent the occurrence of...single-gene disorders in children..."*

What about the possibility of detecting de novo mutations in preimplantation IVF embryos? An estimated 500 genes may undergo de novo mutations in every human embryo, leading to severe conditions in up to 0.5% of all pregnancies.‡ But these mutations arise in the fetus, so expanded carrier testing will not identify couples at risk. However, screening IVF embryos for de novo mutations across the genome at high resolution is now theoretically possible with next-generation sequencing. For example, this technique could be applied to DNA from one to a few cultivated IVF embryonic cells, similar to the prenatal analysis of fetal DNA in the mother's plasma to detect aneuploidy. This deep sequencing requires unbiased whole-genome amplification starting with one or a few embryonic cells, and multiple efforts are being made to achieve this.

Through a combination of expanded carrier testing and preimplantation genetic diagnosis for inherited mutations, and preimplantation genetic screening with next-generation sequencing of most or all of the genome, it should be possible to prevent the occurrence of a great majority of both inherited and de novo single-gene disorders in children conceived through IVF. Furthermore, if new technologies allow the recovery of a few fetal cells from the mother's circulation during the first trimester of pregnancy, these diagnostics could theoretically detect severe deleterious genetic variations and mutations for all pregnancies and allow parents to consider the termination of pregnancy. As these sophisticated diagnostics evolve, raising difficult choices for some parents, society is likely to debate their use, interpretation of results, and costs. It is critical that the biomedical and scientific communities continue to engage with each other and with the public to ensure that the future vision of using next-generation sequencing in diagnostics remains clear.

– **Arthur L. Beaudet**

Arthur L. Beaudet is a professor in the Department of Molecular and Human Genetics at Baylor College of Medicine, Houston, TX. He is also Chief Medical Officer at Baylor Miraca Genetic Laboratories, a for-profit joint venture partially owned by Baylor College of Medicine that offers commercial genetic laboratory testing. E-mail: abeaudet@ bcm.edu

*C. J. Bell *et al.*, *Sci. Transl. Med.* **3**, 65ra4 (2011). †J. G. Edwards *et al.*, *Obstet. Gynecol.* **125**, 653 (2015). ‡J. de Ligt *et al.*, *Curr. Opin. Genet. Dev.* **23**, 257 (2013).

NEWS

$43,000,000,000,000

Projected economic damages due just to greenhouse gas emissions from thawing permafrost through the year 2100. That's on top of estimated global damages of $326 trillion because of other greenhouse gas emissions (*Nature Climate Change*).

DOI says a land conservation effort has reduced threats to sage grouse.

Sage grouse not 'endangered'

In a controversial move, the U.S. government has decided against declaring the greater sage grouse (*Centrocercus urophasianus*) an endangered species. The 22 September decision capped a lengthy debate over how best to protect North America's largest grouse, which has seen its numbers plummet by 90% over the past century (*Science*, 19 June p. 1304). Some conservation advocates wanted the grouse to get the greatest legal protection available under the federal Endangered Species Act (ESA). But others feared a listing would cause massive economic harm in the 11 western states where the bird lives, and would fuel political efforts to gut the law. To avoid that outcome, federal officials are trying what some call "a 21st-century approach to conservation." It essentially offers state governments and private landowners incentives to preserve and restore sage grouse habitat in exchange for avoiding restrictive regulation. The "historic effort … demonstrates that the [ESA] is an effective and flexible tool," Secretary of Interior Sally Jewell said in a statement. Both industry and conservation groups, however, may sue to undo the deal. http://scim.ag/endangeredgrouse

A brave scientist's work on bee stings won an Ig Nobel.

AROUND THE WORLD

Fluorescence mission gets nod

KRAKOW, POLAND | The €290 million FLuorescence EXplorer, or FLEX, was endorsed as the European Space Agency's (ESA's) next Earth Explorer mission by the agency's Earth Science Advisory Committee on 18 September. The satellite would measure the faint fluorescent glow of plants; when light strikes their chlorophyll molecules, about 1% of the light is re-emitted as a faint red glow. FLEX, which could launch in 2022, would measure that fluorescence at 300-meter resolution as a way to understand how plants soak up carbon dioxide under different environmental conditions. Formal selection of either FLEX or a rival mission proposal, CarbonSat, will be made in November, but ESA has always followed the recommendations of the advisory committee. http://scim.ag/ESAFLEX

Stings and pee: the Ig Nobels

CAMBRIDGE, MASSACHUSETTS | The most painful places to be stung by a honey bee include the nostril, the lips, and the shaft of the penis, according to Michael Smith, a Ph.D. student in entomology at Cornell University. Smith learned this the hard way: by stinging himself three times in each of 25 locations. His findings, published last year in *PeerJ*, have now earned him a 2015 Ig Nobel Prize, awarded 17 September at Harvard University's Sanders Theater. The Ig Nobels each year pay recognition to scientific research "that makes people laugh, and then think." Other awards this year went to scientists who discovered that experiencing a sharp pain while driving over speed bumps is a sensitive predictor of appendicitis, and to a team that described the Golden Rule: that various mammals, from dogs to elephants, take about 21 seconds to pee, regardless of the volume of urine in their bladders. http://scim.ag/2015IgNobel

U.K. application to edit embryos

LONDON | A researcher has applied to the United Kingdom's Human Fertilisation and Embryology Authority (HFEA) for a license to edit the genes of human embryos. Some worry that such experiments could someday lead to genetically modified human babies. The application filed with HFEA would involve only embryos in the lab, however, not any intended to lead to a birth. The applicant, Kathy Niakan, a developmental biologist at the Francis Crick Institute in London, investigates the genes that are active at the earliest stages of human development, before an embryo implants in the womb. Niakan hopes to use genome editing to tweak some of the key genes thought to be involved and study the effects they have on development. http://scim.ag/UKembryoedit
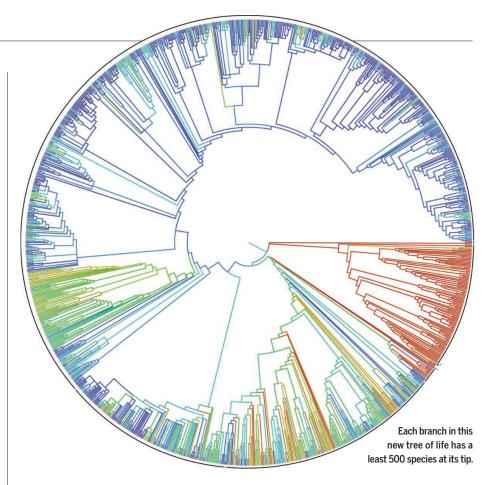
New research board proposed

WASHINGTON, D.C. | A U.S. National Academies' panel wants Congress to create a new entity to oversee federal policies that affect academic research. Its report, out this week, calls for a Research Policy Board that would be funded by universities and located within the White House Office of Science and Technology Policy. The quasi-governmental board would help federal officials develop new rules affecting the conduct of academic research and would also have the authority to police any institutions that violate those practices. Congress asked for the report in response to persistent complaints from U.S. universities that current rules are overly restrictive, redundant, burdensome, and dilute the nation's investment in academic research. http://scim.ag/researchboard

FINDINGS

New virus may be widespread

A dangerous tick-borne virus that first surfaced in humans in Missouri in 2009 appears to be common in wildlife across the central and eastern United States, according to a new study. Scientists believe the so-called Heartland virus is transmitted by the lone star tick, *Amblyomma americanum*. Last week, reporting in the journal *Emerging Infectious Diseases*, researchers at the Centers for Disease Control and Prevention in Fort Collins, Colorado, reported finding evidence of antibodies to the Heartland virus in blood samples from deer, raccoons, coyotes, and moose in 13 states from Maine to Texas. This, they suggest, means doctors should

Each branch in this new tree of life has a least 500 species at its tip.

If you build a tree, will they come?

Biologists have spent centuries trying to determine how life forms are related to one another. Now, with a few clicks, anyone can see what they have learned so far—well, almost. The Open Tree of Life (https://tree.opentreeoflife.org) knits together about 500 family trees published by previous authors to create a "supertree" of 2.3 million species. It's the first such comprehensive charting of all organisms—but still includes only a fraction of 6800 published trees, most of which could not be used because they lack digitized data. For example, bacteria (above, red), are well represented in public databases, but not larger organisms. Therefore, this draft tree, reported online on 18 September in the *Proceedings of the National Academy of Sciences,* "does not summarize what we know," says co-leader Karen Cranston, an evolutionary biologist at Duke University in Durham, North Carolina. But, Cranston says, the site was designed to make it easy for the community to fine-tune the supertree with feedback and additional data. "We hope the tree looks much different a year from now," Cranston adds.

be on the lookout for human patients who might go undetected. But other researchers are not convinced, noting that the lone star tick doesn't occur in northern New England, and that the antibodies found there may be directed against some other agent. http://scim.ag/heartlandvir

NEWSMAKERS

Obama nominates next FDA chief

President Barack Obama nominated veteran heart researcher **Robert Califf** to be the next head of the U.S. Food and Drug Administration (FDA). Califf, 63, was an administrator and clinical trial researcher at Duke University in Durham, North Carolina, for more than 30 years before coming to FDA earlier this year as deputy commissioner for medical products and tobacco. "Great news!" Francis Collins, director of the National Institutes of Health, tweeted in response to the 15 September White House announcement. *The Wall Street Journal* reported this week that Califf had received about $205,000 in consulting fees from pharmaceutical companies between 2009 and 2015. A spokesperson for Califf told the newspaper that the fees had been donated to nonprofit groups, and that Califf had ceased

The Gallery of Paleontology and Comparative Anatomy is more than a century old.

Famed museum plans overhaul

One of Paris's most celebrated science museums needs to undergo a massive renovation that will last several years and may cost as much as €100 million. The Gallery of Paleontology and Comparative Anatomy, home to an impressive collection of skeletons and fossils, is at risk of flooding and in need of repairs. Housed in a brick, steel, and glass building built for the 1900 Universal Exhibition, the gallery is best known for its main hall, which displays hundreds of animal skeletons all facing the same way as if in a gigantic parade. The renovation is "the next big operation" for France's National Museum of Natural History (MNHN), of which the gallery is part, says MNHN director Bruno David. Another iconic MNHN institution, the Museum of Man, will finally reopen on 17 October after a 6-year renovation.

work with drugmakers when he was hired by FDA. If confirmed by the Senate, Califf would succeed Margaret Hamburg, who stepped down this past March.

New head of Vatican Observatory

Pope Francis has selected Jesuit brother **Guy Consolmagno**, the first clergyman to win the American Astronomical Society's Carl Sagan Medal, to head the Vatican Observatory, where he will supervise a staff of 11 other Vatican astronomers. Consolmagno, 63, previously oversaw the Vatican's meteorite collection. He graduated from the Massachusetts University of Technology (MIT) in Cambridge in 1975 with bachelor's and master's degrees in planetary science, received his Ph.D. in planetary science from the University of Arizona in 1978, and was a postdoctoral fellow, first at the Harvard College Observatory and later at MIT, until 1983, when he joined the Peace Corps and

taught physics and astronomy in Kenya. He has co-authored five astronomy books, including *Would You Baptize an Extraterrestrial?* Consolmagno is the second American to lead the Vatican Observatory, located in the town of Castel Gondolfo outside of Rome.

Australia's new science minister

As part of a reshuffle by new Prime Minister Malcolm Turnbull, lawyer and veteran politician **Christopher Pyne** was sworn in as Australia's science minister this week. Pyne had been serving as the conservative government's education minister. Many Australian researchers say they hope Pyne's appointment will mark a turn in policy under Turnbull, who ousted Tony Abbott on 15 September after an internal party uprising. "After the weirdness of Abbott and the obtuse ideology of the hard right, we all hope for a better day," says Peter Doherty, an immunologist at the University of Melbourne and Nobel laureate who criticized the last government. As the newly minted minister for industry, innovation, and science, Pyne takes over from former industry and science minister Ian Macfarlane, who has been bumped entirely from Turnbull's ministerial team. http://scim.ag/AustSMPyne

Three Q's

Twenty artists have contributed sculptures to an auction organized by Cancer Research UK in an effort to raise money to complete the construction of the Francis Crick Institute, a biomedical research center in London. Cancer Research UK gave each artist a "blank slate"—a sculpture in the shape of a double helix—and asked them to use it to craft an answer to the question, "What's in your DNA?" Among the sculptures to be auctioned on 30 September at Christie's is one by artist **Kindra Crick**, the granddaughter of Francis Crick, entitled *What Mad Pursuit*. http://scim.ag/crickart

Q: How did you build your sculpture?
A: I was influenced by my grandparents, Francis and Odile Crick. My grandfather worked on elucidating the structure of DNA, and my grandmother drew the first image of DNA, used in the 1953 paper written with James Watson. In my art I try to express the wonder and the process of scientific inquiry, drawing on my backgrounds in molecular biology and in art.

Q: What themes do you explore?
A: In my sculpture, the DNA strand that is rising is this black, dusty, chalkboard with quickly scribbled notations. On the complementary strand, I have this vibrant blue, with a golden helix. I have these growing, abstracted forms that spread and mutate up and down the sculpture. It's an abstraction of cellular life … or infectious ideas, which metaphorically grow and mutate.

Q: What else would you like to add?
A: There's going to be another item at the auction. My father, Michael Crick, worked with Dr. J. Craig Venter at Human Longevity Inc. to create *The Crick Genome Portrait*, an atlas of my grandfather's genome. It's a linear map of the 23 chromosomes and also includes his mitochondrial DNA. It's a single edition piece of artwork, signed by Venter.

PHOTOS: (TOP TO BOTTOM) © DANIEL SANTOS MEGINA/ALAMY STOCK PHOTO; ALEX CRICK

STEM CELLS

Sleuthing sheds light on STAP cell fiasco

Researchers describe artifacts that could have misled authors and prompted sensational reprogramming claims

By **Gretchen Vogel**

Stressed out cells sometimes glow under fluorescent light. That phenomenon, a common problem for researchers using fluorescent microscopy, may be at the root of last year's sensational claims surrounding stimulus-triggered acquisition of pluripotency (STAP) cells, the supposedly powerful stem cells derived using a remarkably simple recipe.

The STAP claims have been shown to be false, and the two *Nature* papers describing the cells in January 2014 have both been retracted. Now, researchers from seven labs have described what they saw when they tried to replicate the experiments in the weeks and months following the original publications. All report observations that may have misled the researchers who made the original claims, they write in *Nature* this week—including cells that glow, faintly, under fluorescent light.

Their findings don't exculpate the team that reported the STAP claim, however. More cautious researchers would have realized they were on the wrong track, says Rudolf Jaenisch, a stem cell researcher at the Massachusetts Institute of Technology in Cambridge whose lab spent 2 months trying to make STAP cells and contributed data to the new paper. "If you know what you're doing, it's not that difficult," he says. And other investigations have found evidence suggesting deliberate wrongdoing.

In the STAP papers, researchers in the United States and Japan claimed that treating cells from newborn mice with acid or forcing them through thin pipettes somehow transformed them into pluripotent stem cells, which occur in early embryos and can develop into all of the body's cell types. The papers generated lots of excitement, not just because the technique was fast and easy, but also because the authors said STAP cells could form placental tissue, which pluripotent cells can't do. That suggested that the STAP cells were even more versatile than embryonic stem cells.

But the claims quickly fell apart when researchers around the world could not reproduce the experiments. Instead of deriving from newborn mouse tissue, the supposed STAP cells were genetically identical to embryonic stem cell lines present in one author's lab, according to an investigative committee at RIKEN, the Japanese research organization where lead author Haruko Obokata worked. (A RIKEN team published some of these data in another paper in this week's issue of *Nature*.) RIKEN also found evidence of misconduct by Obokata, who resigned in December 2014. Obokata's supervisor and co-author Yoshiki Sasai committed suicide in August 2014.

Obokata did her first STAP experiments in the lab of anesthesiologist Charles Vacanti of Brigham and Women's Hospital and Harvard Medical School in Boston. He has continued to stand by the claims and has posted several updated protocols for producing the cells on his lab's website, the

This mouse embryo grew from embryonic stem cells, not STAP cells, as researchers claimed.
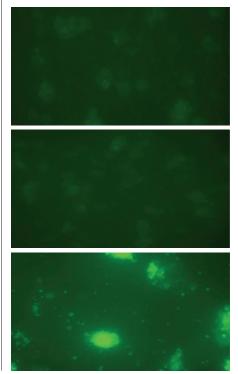
most recent from September 2014. But clues from Vacanti's lab suggested how he and other authors might have been misled when they tried to create STAP cells.

Around the time the STAP papers were published, stem cell researcher George Daley of Harvard Medical School and his colleagues had developed a method for analyzing the genes active in single stem cells. Daley contacted Vacanti to suggest that the method might help explain what was happening in STAP cells. Vacanti "was completely receptive," Daley says. "He invited participation in his lab." A student from Daley's group, Alejandro De Los Angeles, visited Vacanti's lab to learn how to make STAP cells. He soon discovered that the team had fallen for an artifact, Daley says.

The STAP team had used mice carrying a so-called reporter gene that would make the animals glow green under fluorescent light if they expressed *Oct4*, a key gene active in pluripotent stem cells. The acid-exposed cells formed spheres that glowed green, they reported, providing evidence that *Oct4* was turned on. When De Los Angeles and others repeated the experiments, they also saw

Mistaken identity

Cells treated with the STAP protocol fluoresce, whether they contain a reporter gene (top) or not (middle). Embryonic stem cells with a reporter gene (bottom) are much brighter.

the green spheres but noted that the signal was faint.

As they report this week, the signal was much fainter than the fluorescence from a bona fide embryonic stem cell containing a reporter gene. Instead it was consistent with autofluorescence, the low level of fluorescence produced by many cell types, especially those that are unhealthy or dying. "I think it is difficult to mistake autofluorescence for a genuine [Oct4] signal if you pay attention," says Hongkui Deng of Peking University in Beijing, a co-author on the replication paper. But inexperienced researchers can be easily misled, Deng says.

The STAP cell team also claimed that their cells could form teratomas, the jumbled tumors of multiple tissue types that pluripotent cells produce when injected under the skin of mice with faulty immune systems. (Teratoma formation is a classical test of pluripotency.) But Vacanti, Obokata, and their colleagues used a slightly altered technique, first seeding the cells into a polymer gel and then inserting that under the skin of mice. When Daley and his colleagues redid that test, the lumps that formed were not teratomas but scar tissue, he says. Vacanti declined to comment on the new papers.

In the months following the STAP papers, several labs made similar observations, Daley says, and scientists began comparing notes. "All of us had detected the artifacts," he says. "We decided that we should pool our data and go back with a response to *Nature*."

The paper also includes a reanalysis of the sequencing data published with the STAP papers. It confirms a finding by the RIKEN panel that the STAP cells reported in the paper were male, although the donor cells were from a female mouse. The authors also found that some supposed STAP cells carried genetic signatures that matched both a line of trophoblast stem cells—the type that produces placenta—as well as an embryonic stem cell line. Those results are unlikely to arise from an accidental mixing of cell lines, Daley says, since these two cell types need different culture conditions to grow in the lab.

To avoid a repeat of the STAP fiasco, Daley, Jaenisch, and others lay out criteria in *Nature* for future claims of "landmark reprogramming advances." They suggest a range of tests that should help protect against both misleading assays and cell line contamination; before they publish, researchers should also demonstrate that the technique can be replicated in independent laboratories. "Science is ultimately a self-correcting process," the authors write, "where the scientific community plays a crucial and collective role." ∎

With reporting by Dennis Normile.

EVOLUTION

How teeth got tough: enamel's evolutionary journey

Fossils show that ancient fish scales sported enamel long before this hard substance coated teeth

By **Sid Perkins**

The hardest bit of your body is the enamel coating your teeth. But new analyses of fish fossils, as well as genetic analyses of a living fish species, suggest that this specialized material once served a very different function: to toughen some bones and scales of ancient fish. The findings bolster earlier suggestions that ancient fish had enamel-armored scales, and they point to a new scenario for exactly how the substance ended up on teeth.

Enamel—an almost pure layer of a mineral called hydroxyapatite—coats the teeth of almost all tetrapods (four-limbed creatures) and lobe-finned fish such as coelacanths. Most living fish do not produce it, but Per Ahlberg, a paleontologist at Uppsala University in Sweden, found an ancient exception. Well-preserved fossils of an ancient fish called *Psarolepis romeri* reveal that this 20-centimeter-long minipredator, which prowled the seas between 410 million and 415 million years ago, had enamel in its scales and its skull—but not its teeth, according to a paper by Ahlberg and colleagues in the 24 September issue of *Nature*.

Other teams had found partial fossils of fish with enamel on their scales. But those fragments might not have belonged to the same individual, Ahlberg says, so researchers couldn't be sure just how the enameled bits were distributed across the body, or if they came from individuals at different ages or developmental stages.
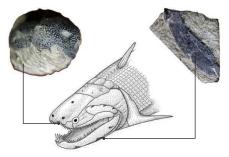
Ahlberg's team instead looked at a single specimen of *Psarolepis*, slicing through the jawbone, skull bones, and scales to get a microscopic peek at their internal structure and so identify what they were made of. The teeth were naked dentine, the same material that underlies the enamel in your teeth and those of most modern tetrapods. But the scales and skull bones of this ancient fish included some enamel.

Researchers had suggested that over millions of years of evolution, hardened structures such as external scales gradually migrated into the mouth and changed shape to become teeth. But the patchy distribution of enamel in *Psarolepis* may suggest a different scenario, in which the pattern of enamel production, rather than the of shape and location of already enameled structures, shifted over time.

Tooth enamel's fishy roots

Fossils show that the ancient fish *Psarolepis romeri* had enamel in its jawbone (right) and the roof of its skull (left). Enamel did not spread to teeth until millions of years later.

The team also analyzed the genome of the spotted gar (*Lepisosteus oculatus*), a modern-day species that produces a hard enamel-like material called ganoine that covers its scales. The genome shows that gar can produce two of the three proteins needed to make enamel, and suggests that ganoine is essentially a scale-coating version of enamel. Thus, it offers genetic support for the fossil evidence.

These findings "are very interesting," says Zerina Johanson, a paleobiologist at the Natural History Museum in London. In contrast to previous ideas, the work suggests that hardened structures such as scales may not have physically moved from one place in the body to another as species evolved. Instead, evolution may have shifted the activity of enamelmaking proteins to new body parts.

"This may provide a better understanding of what was going on inside primitive vertebrates," she says. ∎

An astronaut is stranded on the red planet in *The Martian*.

Q&A

The Martian's *ode to science*

The director, author, and a NASA expert on how they balanced realism and movie magic

By **Meghna Sachdev**

I f you're planning to watch *The Martian*, Ridley Scott's newest sci-fi extravaganza, get ready for a love story. No, we don't mean any romance involving Mark Watney (Matt Damon), the intrepid astronaut hero who gets stranded on Mars after a NASA mission goes awry. The story's real heartthrob is, well, science. *Science* spoke with director Ridley Scott; Andy Weir, whose debut novel provided the tale; and Jim Green, NASA's director of planetary science and an adviser on the film, to find out how this surprisingly plausible love song to science was composed. These interviews have been edited for clarity and consistency.

Q: Was it important to you to get the science in *The Martian* right?
Andy Weir: I'm one of those guys that will nitpick the science in a story. It really takes me out of a story when there's some blatant error, and I didn't want that to happen to my readers … And if you actually pay attention to all the science and all the detail, it ends up providing you with plot points, and that's really cool.
Ridley Scott: For the most part, it's all as accurate as we can possibly get it … That was refreshing; I loved it. I like to be restricted by the actual science of it. How do I illustrate what it means when someone says, "We'll do a slingshot around Earth and we'll never slow down, and by doing that we will conserve fuel?" Those kinds of questions I thought were really interesting.

Q: A lot of the story incorporates technology we haven't built yet. Where did all this information come from?
A.W.: I didn't know anyone in aerospace at all at the time that I wrote the book. I do now! My primary source was Google … I read tons and tons of research. Also, originally *The Martian* was a serial that I had posted on my website chapter-by-chapter. If there were errors in the physics or chemistry problems or whatever, [my readers] would email me. I got sort of crowd-sourced fact checking.
R.S.: Almost immediately [after] I decided to do it, we started to have conversations with NASA about process, the habitats, the Mars Ascent Vehicle (MAV), the suits and everything. And they sent us pictures, almost like photographs, of what they hoped it would all be.
Jim Green: We took [Ridley] to Johnson Space Center. We gave him the opportunity to see what the Habs (space habitats) are like … where do you make food, what do the vehicles look like, how do they function?

Q: Jim, Andy, how heavily were you both involved in making the movie?
J.G.: I quickly realized the difference between helping to write the script and adding to the visual stimulus and how things are created to complement the story. And that latter part was what I was involved in.
A.W.: Most of my job was to cash the check! But they chose to involve me, so when Drew Goddard was writing the screenplay, we talked on the phone a lot, almost every day.

Then, while they were filming, I would get questions filtered down to me from Ridley. And the level of detail in those technical questions made me realize [that] they're really putting effort in the scientific accuracy. [Ridley] said like, "Hey, can we show Mark [Watney] out on the surface of Mars, with the EVA [extra-vehicular activity] suit on, pouring hydrazine from one container to another?" I said, "No, I don't think so, because hydrazine is really volatile and in Mars's atmospheric pressure it would just boil off." They're like, "Okay, then we won't do it."

Q: Is there anything in the story that is just not at all plausible—total movie magic?
J.G.: There are a number of things in it, and not a large number, that are close but are not exactly correct. The starting dust storm—dust storms on Mars are not as hazardous as portrayed in the movie. Because of Mars's thin atmosphere it really doesn't produce the effects of blowing anything over. And the radioisotope power system is very hot. It has plutonium in it, and we'd never bury it. But there's an undercurrent of realism that is really quite refreshing and just delightful for us in the business.
A.W.: I deliberately sacrificed reality for drama with the [Mars] dust storm … In a man-versus-nature story, I decided I wanted nature to get the first punch in. The other deliberate thing I did was to basically hand-wave around radiation issues. That's actually one of the biggest challenges to sending a manned mission to Mars. I just said that in the intervening time they'd invented some kind of material that takes care of it.
R.S.: I never shoot for movie magic. I think that's the important thing even if you're doing a science fiction movie like *Alien*: If I hadn't got that beast right, you wouldn't have had a movie … But there's a bit of cheating here and there. Eventually they all say, "Well, you're making movies, so we'll forgive you!" ∎

BIOMEDICINE

NIH opens precision medicine study to nation

Panel's plan would allow anyone living in the United States to join million-strong effort

By **Jocelyn Kaiser**

Uncle Sam wants you—or at least your DNA and medical records. Next year, assuming Congress approves an initial budget request of $130 million, the National Institutes of Health (NIH) expects to begin recruiting at least 1 million people for what may become the world's largest study of how genes influence disease risks and drug responses. Plans for the study came into focus last week with the release of a blueprint from a panel of human geneticists, medical researchers, and other experts. It urges that NIH recruit participants not only through academic medical centers and health care organizations, but also by issuing an open invitation to anyone living in the United States.
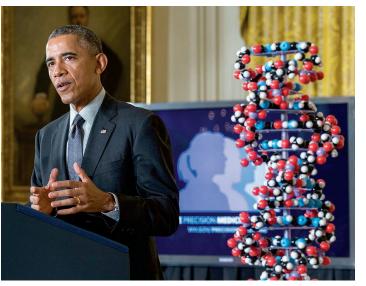
For NIH Director Francis Collins, the project, known as the Precision Medicine Initiative (PMI) Cohort Program, brings to fruition an idea he first proposed 11 years ago. "I am so excited to see this dream come to life," Collins said in a statement released after he accepted the recommendations. Outside researchers also approve. "I think the working group really came through with this concept that every American could volunteer," says pharmacogenomics researcher Dan Roden of Vanderbilt University in Nashville, Tennessee. But whether NIH can design and effectively manage such a massive endeavor remains an open question—it recently scuttled a long-planned, costly study of 100,000 children after much debate (*Science*, 19 December 2014, p. 1441).

President Obama gave Collins's idea a boost in January when he called for a large national research study as part of a broader effort to tailor medical care to individuals. Several other countries have already launched similar efforts to collect DNA and health information from large groups of people, or cohorts. But designing such a massive research effort in the United States, which lacks a centralized health care system, has been difficult until recently, when electronic health records made it more feasible.

Indeed, the working group had "unanimous enthusiasm" that the time has come for a large U.S. cohort study, says co-chair Richard Lifton of Yale University. Initially the working group considered knitting together existing cohort studies, such as the long-running Framingham Heart Study in Massachusetts and a Kaiser Permanente biobank that has already recruited 245,000 of the health care organization's members. But such studies often limit data access to the sponsor's own researchers and collect patient samples and data in disparate ways, the panel found. Instead, to build a consistent and nationally accessible dataset, it recom-

NIH now has a plan for carrying out the study of more than a million Americans that President Obama called for in January as part of his Precision Medicine Initiative.

mends recruiting new participants through health care providers. The study will also set aside slots for anyone in the United States who wants to participate. The two recruitment methods, which will seek volunteers of all ages including children, could bring the total enrollment to a million or more within 4 years, the panel said.

Each participant must give a blood sample so their DNA can be analyzed, undergo a clinical exam, and share their electronic health record. The study will also use mobile devices to record sleep and physical activity. Researchers might later request additional material, such as fecal samples that reveal the makeup of a person's microbiome. The panel urges that participants be allowed to see much of their genetic and other health data, at least from tests done by certified labs that have met regulatory standards for reliability.

Although understanding the interplay between health and a person's DNA is one of the study's main objectives, the advisers found that sequencing the full genome of every participant would be too expensive. Instead, the project will start by testing participants' DNA for single nucleotide polymorphisms, common mutations scattered along the genome that can point to disease risk genes. That can now be done for less than $50 per sample, whereas sequencing a whole genome still costs at least $1000.

One challenge is to assemble a cohort that represents the diversity within the United States. NIH Deputy Director for Science, Outreach, and Policy Kathy Hudson, who co-chaired the working group, says the project hopes to recruit some participants through federally funded health clinics that serve low income minority populations. But the open call for volunteers could still skew the sample, she notes. "We will need to figure out ... how to make sure that we're not filling up all of the available slots with a certain demographic," Hudson said during an advisory board teleconference last week.

Hudson acknowledges concerns that the project might suffer the same fate as the recently canceled National Children's Study, which foundered because of budget and management concerns. She says strong scientific leadership—NIH plans to recruit a prominent researcher to take charge and various committees will offer input—and a plan to be "flexible" and "nimble" about the data being collected should help.

One working group member who initially worried that the study would become too complex is happy with how the blueprint came out. The recruitment plan is "relatively straightforward," says heart disease genetics researcher Sekar Kathiresan of Massachusetts General Hospital in Boston and the Broad Institute in Cambridge, Massachusetts. "I think if the recommendations are implemented wisely, it will be a tremendous resource for this country." ∎

PHOTO: PETE SOUZA

ENVIRONMENT

China's island building is destroying reefs

Land creation and dredging in the South China Sea come at the expense of corals and fisheries

By **Christina Larson**, in Beijing

The geopolitical maneuvering in the South China Sea (SCS) is taking a heavy toll on the marine environment, scientists believe.

The Spratly, or Nansha, Islands, a cluster of coral reefs and atolls, has become the focus of a territorial dispute between China and its neighbors. To the dismay of other countries bordering the SCS—Vietnam, Malaysia, the Philippines, and Brunei—China claims most of the sea, and it is bolstering its claims with a massive landfilling effort to transform some of the atolls into full-fledged islands. The scale and speed of the effort emerged earlier this month, when the Center for Strategic and International Studies (CSIS) in Washington, D.C., released high-resolution satellite photos showing that over the past 2 to 3 years, China has created 13 square kilometers of island area—about a quarter the size of Manhattan.

That is not just a challenge to its neighbors, which also claim some parts of the sea. By piling sand, gravel, and dead coral onto reef flats to create new land and dredging shipping channels nearby, China has destroyed large areas of biodiverse reef that served as nurseries for fisheries throughout much of the SCS. "This is the most rapid permanent loss of coral reef in human history," says John McManus, a marine biologist at the University of Miami in Florida. "It's a terrible, terrible thing to do this."
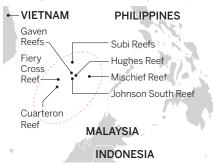
The waters around the Spratly archipelago are home to "some of the most beautiful and biodiverse coral in the world," McManus adds. Roughly equidistant between Vietnam and the Philippines, they are "like an oasis in the desert," says Ed Gomez, a marine biologist at the University of the Philippines, Manila.

The reefs are economically important, too, as McManus realized roughly 2 decades ago when he faced a puzzle. Overfishing had depleted fish stocks in the SCS; some fish species had apparently disappeared entirely from the coastal regions his team studied. Then, after several years, unexpectedly, the fish all reappeared. By analyzing ocean currents, McManus discovered that larvae from coral reefs in the Spratlys and the nearby Scarborough reefs were likely replenishing the sea. The reefs "serve as nursing grounds for a lot of species," Gomez says. "They are important sources of larvae for of all kinds of marine life."

Now, China "has deployed one of the world's largest dredging fleets," says Andrew

Terraforming at sea

To secure its claim on the Spratly Islands, China has developed reefs like Fiery Cross, where satellite images reveal new features including a 3000-meter runway and a port.

VIETNAM — PHILIPPINES
Gaven Reefs
Fiery Cross Reef
Cuarteron Reef
Subi Reefs
Hughes Reef
Mischief Reef
Johnson South Reef
MALAYSIA
INDONESIA

March 2006

September 2015

Erickson, an associate professor at the U.S. Naval War College's China Maritime Studies Institute in Newport, Rhode Island. The area of newly built land—where buildings, concrete plants, and three airstrips have been built or are under construction, according to CSIS—is more than 10 times the total area that other SCS nations cumulatively have built up, Erickson notes. "Whether in scale or sophistication, there are simply no grounds for comparison."

Perhaps the most extensive ecological damage comes from dredging. In creating shipping lanes near the islands, the Chinese cut through reefs. As the lanes will most likely be dredged frequently to remain navigable, "that's near permanent damage," McManus says. And at Fiery Cross Reef in the Spratlys, they've dug a huge harbor, Gomez says. "We don't know how much area has been destroyed underwater by deep dredging," he says. But digging a deep harbor, he notes, destroys corals, seaweeds, and seagrasses. "No productive ecosystem can survive."

The dredging takes a toll on nearby ecosystems as well. "Plumes of sediment that flow from the construction work will have an impact on whatever life relies on photosynthesis to survive," says Youna Lyons, a marine scientist and expert in marine law at the National University of Singapore. "If you don't have sunlight, nothing can grow. This impacts all the bottom of the food chain, including coral and algae."

The island building was expected to be on the agenda last week when Chinese President Xi Jinping visited Washington, D.C., given the U.S. government's concern about a military buildup in the SCS as well as its interest in ensuring freedom of navigation through one of the world's busiest shipping channels. Yet convincing China to reverse course will not be simple. "The Nansha Islands have been China's territory since ancient times," Xi told *The Wall Street Journal*. "China's development and maintenance of facilities on some of our garrisoned islands and reefs in the Nansha Islands does not impact on or target any other country."

Scientists have little hope that environmental concerns will make a difference. "China keeps saying it cares about the environment," Lyons notes, but it has not published an environmental impact assessment for any of its island building activities in the SCS.

In spite of Xi's reassurance, other countries will feel the consequences. "For centuries, many of the countries surrounding the SCS have been dependent on fishery resources from these chains of reefs and islands," Gomez says. Now, he says, key reefs are "forever gone" beneath the landfill and concrete. ∎

Kay (left) and Schultz aim to boost the number of basic discoveries at Scripps that make it to medicines.

BIOMEDICAL RESEARCH

Scripps hooks prominent pair to lead it to health

Steve Kay and Peter Schultz aim to focus basic science powerhouse on translational medicine

By **Robert F. Service**

Steve Kay and Peter Schultz are old deep-sea fishing buddies. Now, their skills will be tested as they navigate the choppy waters surrounding the Scripps Research Institute in San Diego, California, one of the world's largest basic biomedical research institutes. Last week, Scripps announced that Kay, formerly the dean of the college of arts and sciences at the University of Southern California (USC) in Los Angeles, will become the institute's president. Schultz, currently a Scripps chemist and director of the California Institute for Biomedical Research (Calibr) in San Diego, will become CEO.

The appointments portend a move that could strengthen Scripps's tight finances: extending the institute's historical strength in basic science into translational research, which aims to transform discoveries into novel treatments. "It's a very exciting move," says Peter Kim, formerly the head of the Merck Research Laboratories and now a biochemist at Stanford University in Palo Alto, California. He adds Scripps is "very fortunate" to have landed Schultz and Kay to share the top duties.

Although Kay will run day-to-day operations and Schultz will oversee Scripps's long-term strategic plan, both have long track records in translational research—and in raising money. In addition to running Calibr, Schultz previously led the Genomics Institute for the Novartis Research Foundation (GNF), and has been a founder of eight startups that used robotics and other high throughput technologies to advance biomedicine and materials science. Before joining USC, Kay also worked with Schultz at Scripps and GNF, and helped launch several biotech companies himself. Together the pair has raised well over $1 billion in backing from pharma companies, foundations, and private donations in their recent positions.

The announcement likely ends a contentious chapter at Scripps, which has an annual budget of $310 million, 2730 staffers, and campuses in San Diego and Jupiter, Florida. Just over a year ago, Scripps faculty led a revolt against the institute's former leadership amid a financial slump and discussions of a merger with USC (*Science*, 27 June 2014, p. 1435). But when Kay and Schultz met with Scripps faculty to lay out their vision last week, "The reaction was one of overwhelming enthusiasm from all of us," says Reza Ghadiri, a chemist at Scripps in San Diego.

The centerpiece of their approach will be a long-term push into translational research, Kay and Schultz say. Like most academic institutions, today Scripps sticks mainly to basic research, discovering the molecular underpinnings of health and disease. In contrast, pharmaceutical companies tend to focus their efforts at the other end of the drug development pipeline, moving potential drug compounds through human clinical trials into the market. In between is translational research, which aims to bridge the space between basic science and drug approval. It's come to be known as the "valley of death," because many promising findings never make it to market. To traverse the valley, translational researchers focus on refining promising early-stage compounds; they try to minimize their toxicity, for instance, and improve how long they circulate in the bloodstream and find their targets.

Today, a large chunk of translational research falls to biotech companies that license promising early-stage compounds and try to shepherd them into human clinical trials. But few biotech firms have the wide array of needed expertise, causing many compounds to fall by the wayside, says Patrick Griffin, who runs a translational research center at Scripps Florida. "If you can move a [would-be drug] along in a nonprofit, you can nurture it so it has a better opportunity to advance."

To make this easier for Scripps faculty to do in house, Kay and Schultz say they plan to form alliances with Calibr and other institutes. The collaborations should mean more compounds make it into human trials, they say. And that outcome could earn the institute new licensing royalties, they add. "If we are successful, not only are we making new medicines that can help people, we are potentially creating additional financial resources [for Scripps]," Schultz says.
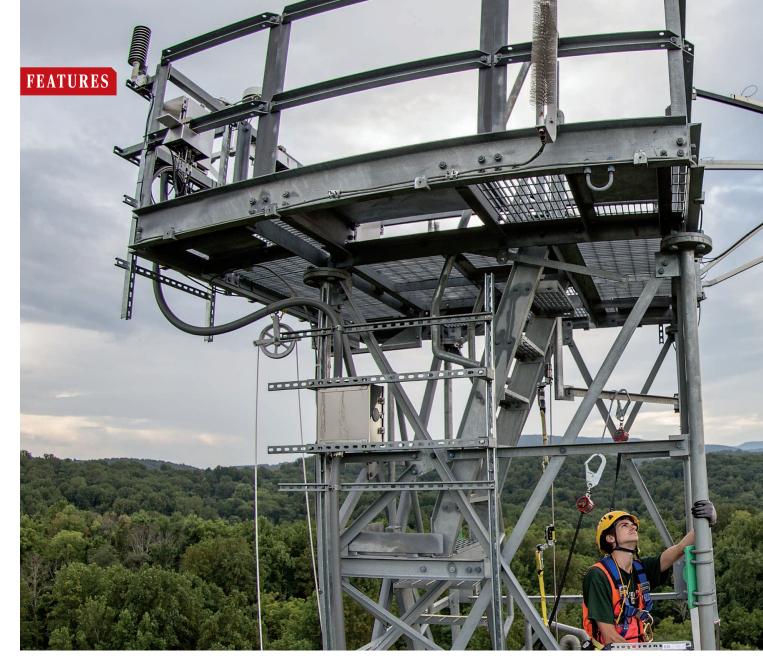
The duo also plans to take more immediate action to shore up Scripps's finances, which have suffered from a decline in revenue from National Instixues of Health grants and other funding streams. The institute's finances are currently "stable," according to a July report by Fitch, a bond rating agency. But Scripps has operated in the red for years, and has covered deficits by drawing down its endowment, which shrunk from $430 million in fiscal year 2012 to $397 million in fiscal year 2014.

One move that could save $12 million annually would be to unload nearly 37,000 square meters of leased lab space. "That would have a big impact pretty quick," Griffin says, although Scripps would have to raise more than $100 million to build two new lab buildings of its own. But ultimately, he says, Scripps's stability will depend on how effective Schultz and Kay are in hooking together formerly disparate parts of the drug development pipeline, and how many keeper drugs the fishing buddies manage to snare in their net. ∎

Ecology's tough climb

NSF's ambitious network of observatories runs into harsh budget and management realities   *By* **Jeffrey Mervis**

More than a decade ago, ecologist Scott Ollinger helped launch U.S. ecology's flagship foray into big science. He and other researchers worked to transform the National Science Foundation's (NSF's) dream of a continental-scale observatory that would monitor environmental change into a concrete plan. What emerged was the National Ecological Observatory Network (NEON), a unique string of more than 100 data collection stations spread from Alaska to Puerto Rico.

So Ollinger was thrilled when, in 2013, NEON offered him the chance to oversee the network's expected trove of data on long-term changes in climate, land use, bio-diversity, and invasive species. He arranged for a 3-year leave of absence from his post at the University of New Hampshire in Durham. Then he hit the road to NEON's headquarters in Boulder, Colorado.

En route, however, Ollinger learned that NSF, which is paying for NEON, had put a hold on an initial $111 million grant to begin operating some of the newly built stations.

A tower studded with sensors keeps watch at a NEON core terrestrial site near Front Royal, Virginia.

That meant "I was almost fired the day I arrived," he says.

The disturbing news was a harbinger of worse to come. Despite his impressive title of observatory director, Ollinger discovered that he had little influence over how NEON was being built, or the day-to-day activities of its growing scientific staff. Soon, "the number of decisions I tried to make that were overruled reached a point where I felt there was no way I could succeed," he recalls. Frustrated and feeling powerless, Ollinger returned home after less than a year.

Ollinger's experience reflects management problems that have dogged NEON since its birth and the project's tense relationship with the community of scientists who will ultimately use its data. This summer those problems came home to roost.

On 3 August, NSF abruptly announced it was scaling back the project in an attempt to prevent an 18-month slip in its schedule and a projected cost overrun of more than $80 million on its $434 million construction budget (*Science*, 7 August, p. 574). On 8 September, NEON Inc., the nonprofit that manages the project, fired CEO Russ Lea, a former forestry professor and university administrator, after the head of NSF's biology directorate, James Olds, ordered the corporation to correct "deficiencies in leadership." And last week Olds told a congressional committee investigating what has gone wrong that NSF would consider replacing NEON Inc. if it doesn't shape up.

NSF officials say NEON's "descoping" was prompted by ongoing difficulties in obtaining needed site permits and technical challenges in building NEON's sensors, some of which take novel approaches to collecting data. NEON's supporters note that other large, complex science projects that NSF has built have undergone periodic changes in scope and leadership, particularly as they transition from construction to operations. And NEON has been especially challenging because of its complexity and uniqueness, Olds says.

But scientists both inside and outside of NEON say the project's woes run much deeper. They point to a chronic disharmony among NSF, NEON Inc., and the research community. Ollinger, for instance, is one of five researchers who has held—and then left—NEON's top scientific post since 2007. This past spring, members of NEON's chief scientific advisory body even considered a mass resignation.

Now, as NEON regroups, the scientists with whom it has had a love/hate relationship say NSF and NEON Inc. need to turn things around, and fast. "I wish them luck," says Scott Collins, a plant biologist at the

University of New Mexico, Albuquerque, who helped get NEON off the ground as an NSF program manager in the early 2000s. "They need to wake up and change the way NEON operates and get the research community behind the project," he says. "NSF has invested a ton of money in the infrastructure," he adds, "and if NEON fails, ecology won't get another chance."

WHEN THEN-NSF DIRECTOR Rita Colwell proposed what became NEON in 2000, she hoped that it would generate questions researchers had never been able to ask—or answer. Although the agency had been funding Long-Term Ecological Research sites across the United States since 1980, those projects tended to focus on hypothesis-driven research by an individual investigator. They weren't designed to collect and share highly standardized, continental-scale data over many decades.

The move into Big Data is an intoxicating vision to many. "The idea of a community of ecologists coming together to put up a piece of infrastructure as significant as a telescope, atom smasher, or an icebreaker sucked me in," Lea said last month, explaining why he took the CEO job in early 2012.

It took NEON's planners a decade and several tries, however, to draw a blueprint acceptable to NSF's oversight body and Congress. The final plan called for dividing the United States into 20 ecological domains (see map, p. 1439). Each domain would host two "core" observing stations chock-full of standardized sensors and sampling sites (see graphic, below). One core site would focus on a terrestrial ecosystem such as a forest or grassland, the other on an aquatic environment such as a stream or lake. In addition, the domains would support a total of 56 "relocatable" stations that researchers could move a few times during the 30-plus years that NEON is expected to oper-
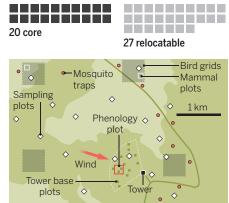
PODCAST

For a NEON interactive go to http://scim.ag/1KvdqJe

ate. The original plan also included a long-term experiment, called STREON (STReam Experimental Observatory Network), which would simulate abrupt environmental change in aquatic ecosystems by adding nutrients—phosphates and nitrogen—and removing some organisms at 10 sites.

Since 2011, project managers have completed construction on 48 sites—fewer than half of what was in the original plan—and spent approximately two-thirds of NEON's construction budget. The descoping preserves the 40 core sites, but eliminates 15 of the 56 relocatable sites—including seven dedicated to studying urban ecosystems. NEON also pulled the plug on two terrestrial instruments: sensors to measure fluxes of nitrogen oxides and methane, and fiber optic cables for collecting video of underground root growth. And it dropped the STREON experiment (although NSF officials emphasized that they would welcome

Outfitting a site

NEON will use a standardized suite of autonomous instruments and data collection protocols at dozens of terrestrial and aquatic sites to monitor long-term, continental trends in climate, land use, biodiversity, and invasive species. Core sites are expected to operate for 30+ years; relocatable sites would move every 8 to 10 years. Sites vary in size, the largest being a 500-sq-km swath of the Greater Yellowstone Ecosystem.

These graphics do not depict actual sites.

Terrestrial sites

20 core

27 relocatable

Study plots scattered across sites averaging 20 sq km will enable statistically valid sampling of flora and fauna including mosquitoes, beetles, birds, ticks, and small mammals.

Stackable modular segment

Sensors

Towers
Towers as tall as 60 meters will provide a platform for sensors, operating at different wavelengths, which will measure sunlight, carbon flux, and a host of atmospheric and meteorological parameters at distances up to 1500 m. A camera at the apex will record seasonal changes and snow depth every 15 minutes.

Soil sampling
A string of sensors up to 200 m long and buried in the soil will monitor changes in temperature, nutrient movements, and carbon dioxide.

Utility hut
A 6-by-2.5-meter utility hut, 3 meters high, stores scientific equipment and houses computer and communications gear with fiber optic, cellular, or satellite connections. Also contains battery back-up in case power grid fails.

new STREON-like proposals to another NSF funding program).

The loss of STREON was the latest defeat for aquatic scientists, who had long been unhappy with what they regarded as NEON's inattention to its river and lake sites. In June, several prominent scientists petitioned NEON to invest more in completing the aquatic observatories. Sensing that STREON was in danger, they also asked to be consulted on any decision to drop STREON.

NEON managers rebuffed both requests, saying that "we cannot make one component of the observatory a higher priority than others." But the descoping does exactly that, argues ecologist Walter Dodds of Kansas State University, Manhattan, who organized the petition and who has championed STREON. "It's terrible news for aquatic scientists."

IT'S NOT UNUSUAL for a federal agency to adjust its plans for a major scientific facility, such as a telescope or spacecraft, after construction is underway. But those changes are usually the product of discussions between scientists and project managers. On a typical NASA mission, for instance, "the job of the chief scientist is to understand the high-level science requirements of the mission and to engage in respectful conflict with the project manager to make sure that the best outcome occurs," says David Schimel, NEON's first CEO and later its first chief scientist. "They succeed or fail together."
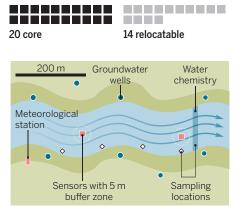
That give-and-take has not been the norm at NEON, Schimel and others say. In late 2007, for example, geophysicist Michael Keller left his job as a project scientist for a NASA-funded program in the Amazon, bought a house in Boulder, and moved his family in preparation for what he expected to be the crowning achievement of his career: chief of science at NEON. "We had a golden dream that was going to make this incredibly difficult thing happen," he recalls. "That idealism was our calling card."

Keller's first task was to reach a consensus on the scientific requirements for the observatory. "Then we converted those questions into what we were going to measure and how we would report them as products" that scientists could use, he says. The result, he says, was "a very respectable final design."

That's when things headed south. "We fully expected to have to adapt what we were doing on a site-by-site basis," Keller recalls. But that's not how NSF saw things. "NSF's model is that you do the science up front," he says. "And once you come up with the final design, it's up to the project manager to execute it." The message from NSF was clear, he says: "Once we had designed it, [scientists] were somewhat obsolete."

Ollinger says that approach may work well when building a single large facility with a clear and compelling scientific objective—he calls it a "north star". But NEON lacks that north star, he says. Instead, its fundamental objective is to generate high-

Aquatic sites

20 core   14 relocatable

Aquatic sites will be located at 27 streams and seven lakes. Some will be adjacent to terrestrial sites. Data will be collected at both inflows and outflows.

A vast domain

NEON will collect data from sites within 20 distinct ecological domains across the United States.

● Core aquatic
● Core terrestrial

Alaska   Puerto Rico   Hawaii

On the water
A suite of instruments, including a buoy in the middle of lakes, will periodically measure various chemical and physical attributes. Other sampling protocols will track changes in populations of microbes, algae, invertebrates, and fish.

On shore
Sensors will record the movement of ground water and collect various meteorological and hydrological data.

Tragic end for Puerto Rico site

By **Jeffrey Mervis**

For many of the National Ecological Observatory Network's (NEON's) 80-plus monitoring sites, getting the necessary permits to begin construction was the biggest hurdle. But one site in Puerto Rico was undone by tragedy.

This past spring, two security guards were gunned down at what was to have been a "relocatable," or movable, site in a village near Ponce. In June, NEON took down the nearly complete installation after deciding that the site, known as Mameyes, was too dangerous.

"The community said they wanted us to stay, but they couldn't guarantee our safety," says Russ Lea, who this month stepped down as NEON's CEO. "They haven't captured those responsible for the murders … so … the decision was clear."

The local contractor had hired armed guards after construction material started disappearing from Mameyes, making it NEON's only guarded site. In the predawn hours of 30 April, the guards were shot dead. Local authorities have declined to discuss the status of the investigation.

Although it pales next to the human tragedy, Lea says shuttering Mameyes meant abandoning a site that had required incredible resourcefulness by NEON managers. After a landslide in 1985 killed 130 people and destroyed the barrio, the remaining houses were bulldozed, and a dry forest grew up through the rubble. That history posed a special challenge to those installing the tower and monitoring equipment.

"The engineering skill needed to put that urban site into a rubble field, and not disturb the key environmental components, is a testament to what NEON is capable of achieving," Lea says. "And then having to pull it all out—it breaks me up just to think about it." There's also a loss to science, as Mameyes represents a unique ecosystem within an urban setting. ■

quality data that scientists will use to answer a wide array of questions.

After about 3 years at NEON, Keller "decided it was probably time for me to move on." In late 2010 he returned to Brazil to manage a sustainable development project funded by the United States and Brazilian governments.

Keller was succeeded by the man who had hired him: Schimel. A biogeochemist who has been a tireless advocate for NEON, Schimel initially tried to recruit people who understood both ecology and what it takes to build a large scientific facility—before realizing that those two cultures rarely overlap. "It was difficult to find ecologists with experience in large projects," Schimel says. "It was equally hard to find engineers and project managers with experience in ecology. And by difficult I mean impossible—they didn't exist."

Even so, Schimel says he's proud of the team he assembled during his 5 years at NEON. But eventually he was also pushed aside. "My science role was being increasingly marginalized," he recalls. "I was losing the authority and access to the systems engineering staff and other expertise I needed to do my job." Schimel left NEON in 2012 to join NASA's Jet Propulsion Laboratory in Pasadena, California, where he's analyzing global carbon data.

Next up was Ollinger, whose year at NEON was equally disheartening. Ollinger found out that he didn't have the promised authority to make sure that sensors passed muster before they went live at a site. Nor was he allowed to create career paths for NEON's growing staff of scientists, who could never get a straight answer from project managers about whether they would continue to have jobs once NEON was running (see sidebar, p. 1441). A third role that Ollinger relished—figuring out how outside scientists would access NEON's data—was impossible to fulfill, he says, because "the data weren't flowing."

Ollinger's successor as observatory director, C. J. Loria, lasted just 4 months. A former Navy test pilot hired for his business acumen, Loria was ousted this past winter at the same time that NEON Inc. eliminated the position of observatory director.

The churn has deepened the rift between scientists and the project by creating a "lack of a scientific presence" at the Boulder headquarters, Lea admitted before his departure. "The community wants a mano-a-mano relationship with a strong scientific leader at NEON on a daily basis," he said. "Scientists want to talk to their peers."

Lea's interim replacement as CEO is Eugene Kelly, a soil scientist at Colorado State University, Fort Collins, who only

this summer was hired to be NEON's visiting chief scientist. Kelly agrees that the research community "feels it has been kept in the dark about NEON for many years." The low point in NEON's relationship with the ecology community may have come this past winter, when members of its principal advisory panel, the Science, Technology and Educational Advisory Committee (STEAC), seriously considered disbanding the group.

STEAC "made several explicit recommendations over the years, and those recommendations were either ignored or opposed," explains the panel's chair, integrative biologist Todd Dawson of the University of California, Berkeley. "People were saying, 'There's no point having an advisory committee if [NEON] is not going to use it.'"

James Collins, chair of NEON's board of directors, agrees that top management has historically shown a disregard for what scientists can bring to the project, and says that attitude must change. A biology professor at Arizona State University, Tempe, who helped get NEON off the ground as head of NSF's biology directorate in the late 2000s, Collins says the board expects the next CEO to take a different approach. "The CEO has to set a tone in which people feel they are being treated well and their contributions are valued," he says.

Relations between NEON Inc. and NSF also need to improve, say scientists both within and outside the project. The funding delay that sabotaged Ollinger, for example, was the result of a festering disagreement over when a site is ready to be commissioned.

It's not a minor issue. NEON managers argue that a site should be considered operational once all the equipment works and the instruments start to generate data. Any delay in commissioning, they note, forces NEON to use construction dollars for operating costs, such as power and maintenance. That leaves less money to complete new sites.

NSF's position, however, is that a site cannot be commissioned until its data are available online, says Elizabeth Blood, the agency's longtime project manager for NEON. That process could add months to the commissioning process, she concedes, adding that NSF has no intention of changing its criteria.

NSF has the authority to decide the issue. But NEON's position got a strong endorsement this past July from a high-powered panel of scientists from both inside and outside the project, which reviewed NEON's future shortly before NSF announced the descoping. Some of NEON's cost overruns were due to "delayed transition to operations," the panel concluded. Its recommendation was unequivocal: "The cost of carrying field operations on the construction

NEON jobs plentiful but problematic

By **Jeffrey Mervis**

Getting a job in ecology can be tough, but the National Ecological Observatory Network (NEON) arguably has been hiring more ecologists than anyplace else; its workforce topped some 400 permanent and 100 summer employees earlier this year. But NEON's disarray has led to high turnover and taken a toll on promising careers.

Elizabeth Webb was hired in 2014 to manage field sampling protocols and sensors at a NEON site just outside Gainesville, Florida. Webb had worked with similar instruments in Alaska while earning her master's degree in biology, and thought her new job "would be a great opportunity to learn new things with a different setup."

Instead, Webb says, her bosses discouraged her from showing any initiative or using her knowledge to help the fledgling project. "Someone without a college education could have done my job," she says. For example, Webb says it took a month and several sign-offs to get approval to remove a wasp's nest hanging from the site's flux tower. In contrast, Webb says that she could have solved the problem with bug spray from Home Depot.

Webb quit after 5 months and now works as an outreach and facilities coordinator at the National High Magnetic Field Laboratory in Gainesville. "I really like the idea of NEON, but it's not working," she says. Webb "was one of my best students," says ecologist Edward Schuur, a one-time NEON adviser who recently moved to Northern Arizona University, Flagstaff. "If NEON can't retain people of her caliber, then something is seriously wrong with the organization."

Todd Dawson, chair of NEON's top scientific advisory panel, goes further. "I wouldn't encourage a young person to apply for a NEON job now," says the University of California, Berkeley, academic. "It's a sad commentary. But I want to know their plans for righting the ship, and then see some real progress in achieving them, before I would advise anyone to work there." ∎

project is unjustified," and NSF needed to start paying the operating costs.

Even NEON's critics are willing to cut NSF some slack, however, because they recognize that the foundation has little political margin for error. The Republican-led science committee in the U.S. House of Representatives has repeatedly questioned whether NSF has been a proper steward of taxpayer dollars, and NEON's missteps have provided some ammunition for those attacks. In recent months the committee has held hearings to berate NSF officials for allowing NEON Inc. to use $150,000 of its management fees on what the agency later admitted were inappropriate activities, including a Christmas party.

Last week, the panel grilled the agency on its oversight of the entire project, and Olds made it clear that the corporation is on shaky ground. "By December 1 NSF will have enough information to make a determination as to whether NEON Inc. has made sufficient improvement to successfully complete construction," Olds told the panel. Pressed by one legislator whether that could mean replacing the current contractor, Olds hemmed and hawed before concluding, "Yes, that is an option."

NSF has already shortened the leash. Olds said NSF is taking a closer look at the project's financial books, and an advisory committee to the biology directorate is examining whether the descoping will affect NEON's scientific goals. The National Science Board, NSF's oversight body, has formed a NEON task force. Olds was also critical of NSF's performance to date. "We could have done a better job," he admitted.

DESPITE ITS MANY PROBLEMS, NEON has made considerable progress. Managers said last month that 33 sites in 15 domains are now ready for operations. By September 2016, Lea predicts it will have "upward of 60% of final capability" at the 81 sites cur-

NEON will be trapping beetles at many sites.

rently planned. The final goal, he says, is "100% of capability by the end of 2017."

Getting to 100%, however, will require NEON to fully resolve longstanding permitting problems. NEON doesn't own any of its sites, so before it can do any work it must obtain the permission of the landowner—whether a federal or state agency, an environmental nonprofit, a university, or private individuals. Construction also has to go through numerous environmental reviews. It all has taken much longer than anyone anticipated. "We've needed probably five to 10 times more permits than was originally

thought," Lea says. "It's become a huge drain on time and resources."

STREON posed an especially high permitting hurdle that NEON never cleared. "Dropping pollutants into a reach of streams for 30 years was a hard thing for most people to swallow," Lea says.

NEON officials also have had to deal with everything from protests by local residents to a pair of murders that ultimately doomed an urban site in Puerto Rico (see sidebar, p. 1440). In Hawaii and Alaska, the permitting process has been so problematic that this past summer NSF officials proposed dropping those two states, plus Puerto Rico, from NEON. Scientists reacted with horror, pointing out that Hawaii alone provides 25% of the climate variability across NEON sites and that, together, the three locales double the amount of biodiversity being monitored. The idea, which NSF's Blood says was simply a trial balloon, was eventually abandoned.
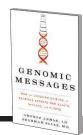
The descoping offers outside scientists a golden opportunity to reconnect with the project, Kelly says. Last month the Ecological Society of America issued a supportive letter from 16 present and past presidents. "We remain excited about the potential new science that could emerge" from NEON, they wrote, asking NSF and NEON Inc. "to re-engage with the ecological community."

But NEON board chair Collins acknowledges that the project's checkered history means it has a lot of ground to make up. "It still needs to prove itself to the community," he says. ∎

PERSPECTIVES

CLIMATE CHANGE

Extreme weather, made by us?

Individual climate events cannot be attributed to anthropogenic climate change

By **Andrew R. Solow**

Anthropogenic climate change is expected to increase the frequency of heat waves and other extreme weather events (*1*). When such an event occurs, it is natural to ask whether it can be attributed to human activities.

Conventional wisdom has long held that although it is possible to attribute an increase in the frequency of extreme events to human activities, the same is not true of individual events. Recent studies that appear to identify the role of anthropogenic climate change in, among other events, the 2010 Russian heat wave (*2*), the 2013 Australian heat wave (*3*), and the ongoing drought in California (see the photo) (*4*) suggest that this conventional wisdom has been overturned. But has it?

These and other examples of single-event attribution are based on the concept—borrowed from epidemiology—of attributable risk (*5*). Consider the case of lung cancer, which can be caused by smoking but also occurs in nonsmokers. When lung cancer is found in a particular smoker, it may be of interest—for example, in litigation—to know the probability that it can be attributed to smoking. If the frequency of lung cancer is, say, 100 times greater for smokers than for nonsmokers, then this probability is given by $1 - (1/100) = 0.99$. By the same reasoning, if the frequency of a specified type of extreme

weather event is β times greater after anthropogenic climate change than before, then the probability that a particular such event can be attributed to anthropogenic climate change is 1 − (1/β). Note that this calculation only makes sense if anthropogenic climate change does not decrease the frequency of the events in question so that β ≥ 1. If β < 1, then the problem is to determine whether an event that occurred prior to anthropogenic climate change can be attributed to its absence.
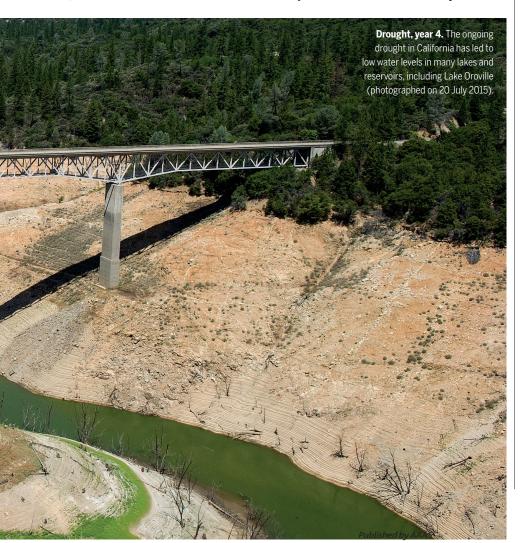
It is possible in principle to assess β by comparing the observed frequencies of events in historical periods with and without anthropogenic climate change. However, this can be challenging in practice. First, the historical record can be short in relation to the frequencies of events and, particularly in the pre–climate change period, unreliable. For example, it has been suggested that climate change will increase the frequency of intense hurricanes (6). It has been difficult to verify this from the observational record of category 5 hurricanes in the Atlantic, which dates back only to 1924 and contains only 33

Woods Hole Oceanographic Institution, Woods Hole, MA 02543, USA. E-mail: asolow@whoi.edu

Drought, year 4. The ongoing drought in California has led to low water levels in many lakes and reservoirs, including Lake Oroville (photographed on 20 July 2015).

events. Moreover, the ability to characterize hurricane intensity in the presatellite era has been questioned (7). Second, single-event attribution is commonly motivated specifically by an event that is observed to be historically rare; further historical analysis merely confirms this.

In part to avoid these problems, recent single-event attribution studies get at β through experiments with climate models. In broad terms, this involves simulating climate in the absence of human influence (i.e., without enhanced greenhouse forcing) and under current conditions and comparing the frequencies at which the simulated events of interest occur. Sometimes statistical methods are used to extend model results—for example, by fitting an extreme value distribution to the magnitudes of the simulated events—but this does not change the basic idea. More generally, there are well-developed statistical methods for inference about β based on either observed or simulated records of events (8).

Because attributable risk is a function of the event frequencies with and without anthropogenic climate change, single-event attribution based on attributable risk is actually a statement about these frequencies. In

this sense, the conventional wisdom about single-event attribution remains intact. Although this may seem like a matter of semantics, it is worth keeping the distinction straight. For example, even if it is certain that anthropogenic climate change has caused the frequency of European heat waves to double, as estimated in (9), the odds that this summer's European heat wave was caused by anthropogenic climate change are only even.

There is another subtler issue about attributing a single event to anthropogenic climate change (8). Underlying single-event attribution is the notion that the effect of anthropogenic climate change is to add events to a list of those that would occur anyway. This notion makes sense in the case of smoking and lung cancer because the effect of smoking is confined to the smoker (and possibly those around him or her). In contrast, the effect of anthropogenic climate change on atmospheric processes is pervasive, and the notion that some events (and nonevents) are free from its influence may be untenable. Although it is still meaningful to ask the conventional question—has the presence of anthropogenic climate change increased the frequency of events?—it may simply not make sense to ask whether a particular event would have occurred in its absence.

If the conventional wisdom about single-event attribution remains intact, one thing has changed. Up to now, efforts to connect single events to anthropogenic climate change have been confined to the scientific literature, including special issues of the *Bulletin of the American Meteorological Society* [e.g., (10)]. However, the market expanded this year with a widely cited report by the private organization Climate Central attributing this summer's European heat wave to anthropogenic climate change (9). As with any expanding market, it is important that consumers have a clear understanding of what they are getting. ∎

REFERENCES

1. C. Field *et al.*, Eds., *Managing the Risks of Extreme Events and Disasters to Advance Climate Change Adaptation* (Cambridge Univ. Press, Cambridge, 2012).
2. F. Otto, N. Massey, G. van Oldenborgh, R. Jones, M. Allen, *Geophys. Res. Lett.* **39**, L04702 (2012).
3. S. Lewis, D. Karoly, *Geophys. Res. Lett.* **40**, 3705 (2013).
4. A. Williams *et al.*, *Geophys. Res. Lett.* 10.1002/2015GL064924 (2015).
5. M. Allen, *Nature* **421**, 891 (2003).
6. K. Emanuel, *Nature* **436**, 686 (2005).
7. C. W. Landsea, B. A. Harper, K. Hoarau, J. A. Knaff, *Science* **313**, 452 (2006).
8. G. Hansen, M. Auffhammer, A. Solow, *J. Clim.* **27**, 8297 (2014).
9. www.climatecentral.org/europe-2015-heatwave-climate-change
10. S. Herring, M. Hoerling, T. Peterson, P. Stott, Eds., *Explaining Extreme Events of 2013 from a Climate Perspective* (*Bull. Am. Meteorol. Soc.* **95**, special supplement) (2014).

BEHAVIOR

Female genital cutting is not a social coordination norm

New data from Sudan question an influential approach to reducing female genital cutting

By **Charles Efferson,**[1][†] **Sonja Vogt,**[1][†]
Amy Elhadi,[2] **Hilal El Fadil Ahmed,**[2]
Ernst Fehr[1][†]

The World Health Organization defines female genital cutting as any procedure that removes or injures any part of a female's external genitalia for nonmedical reasons (*1*). Cutting brings no documented health benefits and leads to serious health problems. Across six African countries, for example, a cohort of 15-year-old girls is expected to lose nearly 130,000 years of life because of cutting (*2*). We report data that question an influential approach to promoting abandonment of the practice.

A prominent view of female genital cutting is that it is a social norm that evolved culturally within the context of a coordination game, which is a type of social interaction in which all parties face incentives to match strategies (*3–6*). An especially influential application of this idea has been to interpret cutting as a coordinated practice that families use to prepare their daughters for future marriage (*4–9*). Under this interpretation, marriage brings prestige from successful reproductive pairings in natal-

POLICY

ist societies, and it provides the increased social influence and spreading of risk that result when families use marriage to strengthen alliances.

According to this theory, a critical threshold exists such that, if the share of families who cut and demand cut daughters for their sons is above the threshold, all families have an incentive to cut. If the share of families is below the threshold, however, the probability of finding husbands without cutting one's daughters is

---

"[C]utting rates show no trace of the discontinuity they should exhibit if families were coordinating..."

---

sufficiently high for families to reap the benefits of marriage without the health costs of cutting. The strong policy implication is that development workers must assemble a critical mass of families in a short period of time to move the share of cutting families from above to below the threshold (*4–6*). After publicly crossing the critical

threshold, cutting should then disappear on its own, quite apart from the activities of the development agency. This idea has been attractive because it suggests how a limited intervention can lead to long-term improvements in well-being.

Development agencies spend considerable resources for programs based on this approach (*6, 9–11*). Along with other activities, development workers gradually try to convince families in a community to abandon cutting and to declare publicly that they have done so. Once the development workers estimate they have enough families to cross the critical threshold, they have a public declaration (*6–8*), typically a large festival where many families declare they will no longer cut their daughters. The hope is that this public declaration will lead the remaining families who cut to realize that abandoning the practice is now in their own interests.

It is surprising given the considerable development funds at stake (*6, 9–11*), no one has provided data clearly showing that female genital cutting exhibits the characteristics of a social norm based on coordination. In particular, if coordination is an appropriate theoretical framework, two related predictions hold (see the chart). First, communities should have either very low or very high cutting rates, with attitudes reflecting either a noncutting norm or a cutting norm, respectively. Second, if cutting practices and attitudes vary, a pronounced discontinuity should separate noncutting from cutting communities.

To see if such a pattern can be detected, we developed empirical methods that do not rely on interviews with parents. This enabled us to collect data in the state of Gezira, Sudan, that were not compromised
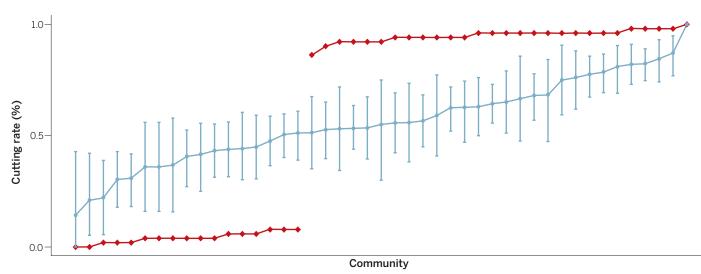
Cutting rates in Gezira communities. Red diamonds show ordered cutting rates as predicted by the coordination game model (*12*). Green dots show actual cutting rates across the 45 communities with 95% boot-strapped confidence intervals.

by the potential social desirability biases associated with asking parents about cutting [for details, see (12)]. Nine teams of professional photographers and medical doctors visited 45 schools in Gezira, one school in each of the 45 communities in our study (12). Girls in Gezira are typically cut during the summer vacation just before entering primary school or earlier (12). Henna is almost always applied to a girl's feet when she is cut, and this is the only time in a young girl's life when henna is applied. As residual henna remains on toenails for several weeks, our team photographed the feet of nearly all girls in the 45 schools within the first few days of the girls first entering primary school (12).

We also added one question to the medical exams normally sponsored by the Gezira government. The doctors asked each girl if she had been "purified," which is a literal translation of the Arabic word used in the local area to describe being cut. If either the photo or the girl's response indicated cutting, we coded the girl as cut (12).

Communities varied substantially in terms of their estimated cutting rates, but they did not vary in any way that reveals the signature of social norms that evolved within the context of a coordination game (see the chart). Apart from a single community with an estimated cutting rate of 100%, cutting rates were neither extremely high nor extremely low. Moreover, when ordered, cutting rates show no trace of the discontinuity they should exhibit if families were coordinating on cutting practices at the community level.

A formal modeling analysis supports this conclusion (12). The data were best explained, by far, with a heterogeneous model that assumes a different cutting rate for each community. Other models, including a coordination game model that assumes communities had coordinated on either a cutting norm or a noncutting norm, were much worse.

If families were coordinating in marriage pools that were not the same as communities, the observed intermediate cutting rates could conceivably be consistent with the coordination model. However, a representative survey with roughly 2500 adults revealed a very high degree of community endogamy (12). Within each community, a substantial number of participants told us that their families would not refuse marriage with other families in the community

because of cutting practices. These results show that marriage pools did not typically divide or fragment communities based on cutting practices. Moreover, an extended theoretical analysis of the coordination game model shows that, even if one allows for multiple marriage pools within communities, coordination cannot support stable intermediate cutting rates of the sort observed in our data (12).

Finally, if multiple marriage pools with different cutting norms exist within communities, a discontinuity in normative attitudes about cutting should also exist within communities. We developed an implicit association test to measure attitudes in an unobtrusive way (12), and we implemented the test with adults from 2260 randomly selected households in the 45 communities. We found that communities with high cutting rates had significantly more negative attitudes toward uncut girls (Spearman's rank correlation, $\rho = -0.493$, $P < 0.001$). At the individual level, however,

---

"Public declarations indicate neither widespread abandonment nor that a program has co-opted coordination incentives..."

---

the distribution of attitudes showed no evidence of a discontinuity that should have been present if two norms, one in favor of cutting and the other against, co-existed. This conclusion holds whether we look at attitudes over all participants from all communities or at the 45 communities separately (12). Cutting rates and attitudes varied substantially and covaried across communities. Neither measure, however, indicated that cutting was a social norm based on coordination.

The enormous heterogeneity we observed in cutting practices within and across communities points toward other potent forces sustaining cutting. Families may value cutting because they see it as a religious obligation (13), or they see cutting as the only way to produce feminine women in a society where gender must be clearly marked (13). Alternatively, perhaps cutting families believe that some men wield considerable power in the mating market and providing these men with costly signals of sexual fidelity brings a net benefit (13). Finally, families who cut may underestimate the risks of cutting because they do not link cutting to later health problems (14).

Heterogeneity means that a single criti-

cal threshold is unlikely to exist. Each family will have its own threshold. Thus, the claim that a public declaration will reduce cutting lacks empirical foundation. A public declaration of abandonment runs the risk of merely assembling families who already place a low intrinsic value on cutting, while the families who give it high intrinsic value will remain unconvinced. Public declarations indicate neither widespread abandonment nor that a program has co-opted coordination incentives in a way that will lead to reductions in cutting (12).

Other policies may contribute more effectively to the reduction of cutting. Identifying the benefits families attribute to cutting is crucial to promoting sustainable changes in values, preferences, and the harmful practices that sometimes follow. This may lead to different kinds of policy interventions such as communications-based programs or increasing the benefits of abandonment with conditional transfers. ∎

REFERENCES AND NOTES

1. World Health Organization, Female Genital Mutilation (2014); www.who.int/topics/female_genital_mutilation/.
2. D. Bishai et al., *Bull. World Health Organ.* **88**, 281 (2010).
3. G. Mackie, *Am. Sociol. Rev.* **61**, 999 (1996).
4. G. Mackie, J. LeJeune, "Social dynamics of abandonment of harmful practices: A new look at the theory" (Innocenti Working Paper 2009-06, UNICEF Innocenti Research Centre, Florence, Italy, 2009).
5. N. Diop et al., *The TOSTAN Program: Evaluation of a Community Based Education Program in Senegal* (Population Council, Washington, DC, 2004).
6. UN Population Fund (UNFPA)–UN Children's Fund, (UNICEF), Joint Evaluation of the UNFPA-UNICEF Joint Programme on Female Genital Mutilation/Cutting (FGM/C): Accelerating Change (2013); http://bit.ly/FGM-CProgrammeEval.
7. TOSTAN, Community Empowerment Program (2013); http://bit.ly/TostanCEP.
8. B. Shell-Duncan, K. Wander, Y. Hernlund, A. Moreau, *Soc. Sci. Med.* **73**, 1275 (2011).
9. UK Department for International Development, Towards Ending Female Genital Mutilation/Cutting in Africa and Beyond (DFID, London, 2013); http://devtracker.dfid.gov.uk/projects/GB-1-203024/.
10. L. Featherstone, The UK announces…measures to end female genital mutilation/cutting [news story] (DFID, London, 2014); http://bit.ly/measuresFGM-C.
11. TOSTAN, Annual Reports and Financials (2013); www.tostan.org/annual-reports-financials.
12. Materials and methods are available as supporting material on *Science* Online.
13. E. Gruenbaum, *The Female Circumcision Controversy: An Anthropological Perspective* (Univ. of Pennsylvania Press, Philadelphia, 2001).
14. K. Hoff, "Behavioral economics and social exclusion: can interventions overcome prejudice?" (Policy Research Working Paper 7198, World Bank, Washington, DC, 2015).

¹Department of Economics, University of Zurich, 8006 Zurich, Switzerland. ²Khartoum, Sudan. *These authors contributed equally to this research. †Corresponding author.
E-mail: charles.efferson@econ.uzh.ch; sonja.vogt@econ.uzh.ch; ernst.fehr@econ.uzh.ch

10.1126/science.aaa7978

CELL BIOLOGY

GATA get a hold on senescence

A transcription factor's abundance connects autophagy to cellular senescence and a secretory phenotype

By **Liam D. Cassidy** and **Masashi Narita**

Cellular senescence is a state of "permanent" arrest of the cell division cycle. It is associated with hyperactivated secretion of proinflammatory factors and with a range of pathophysiological processes such as wound healing, aging, and cancer (1). The processes that control the senescence-associated secretory phenotype (SASP) are not well defined. One candidate effector mechanism is macroautophagy (herein referred to as autophagy), a major intracellular degradation system, but whether it promotes or inhibits senescence is disputed (2). On page 1503 of this issue, Kang et al. begin to unravel this paradox and provide new insights into the mechanisms by which the SASP is controlled (3).

Autophagy was initially described as a nonspecific lysosomal degradation system, with critical roles in energy homeostasis and the quality control of macromolecules and intracellular organelles. However, it is increasingly becoming associated with the degradation of specific targets that are selected for destruction through an association with adapter proteins. This "selective" autophagy is thus an integral mediator of cellular phenotypes (4). Kang et al. identified the transcription factor GATA4 as a substrate of selective autophagy (it is targeted to the autophagy pathway by the

University of Cambridge, Cancer Research UK Cambridge Institute, Robinson Way, Cambridge CB2 0RE, UK. E-mail: masashi.narita@cruk.cam.ac.uk

adapter protein p62). The authors demonstrate that stabilization of GATA4 is both sufficient and partially necessary for the induction of senescence and the SASP in cultured human cells. Because "global" autophagy is activated during senescence in various contexts (2), the finding raises an interesting question: What is the net contribution of autophagy to senescence?

Kang et al. addressed this question using inducible RNA interference to block the expression of autophagy related 5 (ATG5) and 7 (ATG7), proteins that are essential for autophagosome formation. Inhibiting autophagy stabilized GATA4 and triggered
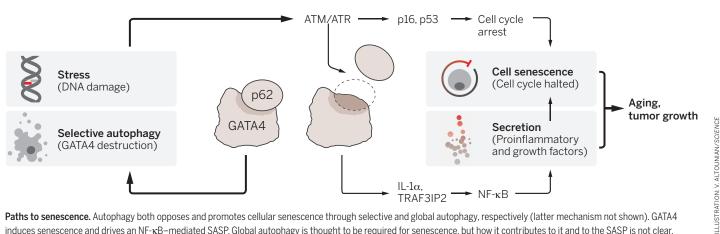
> **"The processes that control the senescence-associated secretory phenotype (SASP) are not well defined."**

senescence, an effect that was greatest in response to transient inhibition of autophagy. Long-term autophagy inhibition actually led to a failure to induce senescence. These data correspond to a model wherein selective autophagy and global autophagy have opposing effects on the SASP. Depletion of p62, which is required for GATA4 degradation but not global autophagy, consistently induced senescence more efficiently than did ATG5/7 depletion. Therefore, differences in the relative contribution of selective and global autophagy may in part

explain the apparent discrepancies regarding the role of autophagy in senescence.

In contrast to the downstream functionality of the SASP, its upstream control is a relatively unexplored area, and only a few such effectors have been described. One of these is the DNA damage response, including the regulators ataxia telangiectasia mutated (ATM) and ataxia telangiectasia and Rad3-related (ATR). The other effector is p38 mitogen-activated protein kinase (MAPK). Both ATM/ATR and p38 converge on nuclear factor κB (NF-κB), a transcription factor that works cooperatively with CCAAT/enhancer-binding protein β (C/EBPβ) to drive the expression of major SASP components (5). Kang et al. show that ATM/ATR signaling, but not the transcription factor p53, is required for GATA4 liberation from p62-directed autophagy during senescence. Once stabilized, GATA4 activates NF-κB by increasing the expression of at least two factors, tumor necrosis factor receptor–associated factor interacting protein 2 (TRAF3IP2) and interleukin-1α (IL-1α). The former is likely to be a direct target gene of GATA4, and the latter is a unique SASP component that can act upstream of NF-κB. TRAF3IP2 is best described as an NF-κB–activating protein in a signaling cascade initiated by the cytokine IL-17, but it can also activate p38 MAPK and C/EBPβ (6). Thus, GATA4 might activate the SASP through multiple mechanisms during senescence (see the figure).

The findings of Kang et al. also underscore the importance of p62 in NF-κB regulation. Accumulated p62 can act as a signaling hub, driving NF-κB activation by promoting oligomerization of TRAF-associated factor 6 (TRAF6) (7). Kang et al. now provide an additional mechanism: Degradation of p62 also leads to NF-κB activation. Do these two mechanisms cooperate? Considering that GATA4 appears to control senescence in both a SASP-dependent and a SASP-independent

Paths to senescence. Autophagy both opposes and promotes cellular senescence through selective and global autophagy, respectively (latter mechanism not shown). GATA4 induces senescence and drives an NF-κB–mediated SASP. Global autophagy is thought to be required for senescence, but how it contributes to it and to the SASP is not clear.

manner (3), it would be helpful to know whether the senescence phenotype induced by p62 depletion is accompanied by the NF-κB–SASP program.
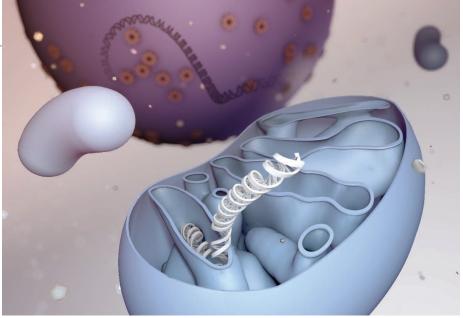
Kang *et al.* also provide evidence of in vivo relevance. They observed that cells expressing the senescence marker p16 also have increased expression of GATA4 in aged mouse livers and human brains. During aging, the expression of some genes involved in autophagy, including the gene encoding p62, declines in several organs, including the mouse liver (8, 9). This supports a model in which the reduction of basal autophagy—selective autophagy in particular—may contribute to the age-related accumulation of senescent cells through derepression of GATA4 activity. Indeed, mice lacking p62 exhibit an accelerated aging phenotype (8), but whether a GATA4-mediated senescence program is active in these mice remains an open question.

Kang *et al.* provide a molecular basis for the relationship between autophagy and the SASP (10, 11) and reinforce the role of p62 as a major regulator of NF-κB. The nutrient sensor mechanistic target of rapamycin (mTOR) controls autophagy and translation of messenger RNA. Although the translation arm of mTOR activity is required for the SASP (12), the importance of the mTOR-autophagy arm within the context of the findings of Kang *et al.* remains to be elucidated. This raises a potential link between nutrient sensing and the SASP wherein nutrient states may well affect the sensitivity of cells to senescence-inducing triggers, in part mediated through GATA4 abundance. A complex picture has emerged in which the major upstream regulators of senescence and the SASP have been described in isolation. Each is associated with a multitude of diverse effects, downstream signaling, and complex feedback loops, perhaps providing a dynamic fine-tuning mechanism for the SASP regulatory network. ■

REFERENCES

1. J.-P. Coppé, P.-Y. Desprez, A. Krtolica, J. Campisi, *Annu. Rev. Pathol.* **5**, 99 (2010).
2. P. A. Pérez-Mancera, A. R. J. Young, M. Narita, *Nat. Rev. Cancer* **14**, 547 (2014).
3. C. Kang *et al.*, *Science* **349**, aaa5612 (2015).
4. V. Rogov, V. Dötsch, T. Johansen, V. Kirkin, *Mol. Cell* **53**, 167 (2014).
5. A. Freund, C. K. Patil, J. Campisi, *EMBO J.* **30**, 1536 (2011).
6. N. Shembade, E. W. Harhaj, *Cell. Mol. Immunol.* **8**, 447 (2011).
7. J. Moscat, M. T. Diaz-Meco, *Trends Biochem. Sci.* **37**, 230 (2012).
8. J. Kwon *et al.*, *EMBO Rep.* **13**, 150 (2012).
9. D. C. Rubinsztein, G. Mariño, G. Kroemer, *Cell* **146**, 682 (2011).
10. A. R. J. Young *et al.*, *Genes Dev.* **23**, 798 (2009).
11. M. Narita *et al.*, *Science* **332**, 966 (2011).
12. R.-M. Laberge *et al.*, *Nat. Cell Biol.* **17**, 1049 (2015).

10.1126/science.aad2501

Mitochondrial-nuclear DNA combinations. Processes such as pronuclear transfer that mismatch mtDNA and nuclear DNA could affect bioenergetics and mitochondrial-nuclear signaling pathways and elicit immunogenic responses.

GENETICS

Mitochondrial-nuclear DNA mismatch matters

Could different nuclear DNA–mitochondrial DNA combinations affect disease severity?

By **Kimberly J. Dunham-Snary**[1] *and* **Scott W. Ballinger**[2,3]

Diseases caused by pathogenic mutations in mitochondrial DNA (mtDNA) often lead to severe, multisystem complications and death during childhood or adolescence, and in some cases, adult onset can lead to premature death. Researchers have proposed techniques to prevent the transmission of mtDNA disease through mtDNA replacement therapies that involve combining healthy nuclear and mtDNA from three individuals. This past February, the United Kingdom became the first country to legalize mtDNA replacement (the United States continues to consider the ethical and social implications). Although mitochondrial and nuclear genomes are physically separate in the cell, they work together functionally to control various metabolic and developmental processes, including energy production, cell growth, programmed cell death, and thermogenesis. This intergenomic

relationship raises questions about possible effects of different mtDNAs (those that are not the original mtDNAs in a given cell) on cellular bioenergetics and disease susceptibility (see the figure). Recent studies in mice that have examined this issue suggest that different mtDNA and nuclear DNA combinations could plausibly have differential effects on gene expression and cell function.

In animal cells, mitochondria are the only organelles that contain their own genomes. A cell can have up to several thousand mitochondria, and each can contain 2 to 10 copies of mtDNA (there can be 100 to 10,000 separate copies of mtDNA per cell). Moreover, nearly all organisms have low levels of mtDNA variants, conferring some degree of heteroplasmy within and between tissues or organ systems of an individual. The onset and severity of mtDNA diseases are influenced by the type of pathogenic mtDNA mutation (missense, transfer RNA, ribosomal RNA, or deletions of multiple genes). Additional factors such as aging, exposure to toxic environmental substances, and gender can also play roles in disease progression.

The development of mitochondrial genetic therapies could drastically reduce or eliminate some forms of rare mitochondrial genetic disorders (*1–9*). Mitochondria are

[1]Department of Medicine, Queen's University, Kingston, ON K7L 3N6, Canada. [2]Department of Pathology, Division of Molecular and Cellular Pathology, University of Alabama at Birmingham, Birmingham, AL 35294, USA. [3]Center for Free Radical Biology, University of Alabama at Birmingham, Birmingham, AL 35294, USA. E-mail: sballing@uab.edu

ILLUSTRATION: V. ALTOUNIAN/*SCIENCE*

inherited solely from a mother through her eggs. A technique called pronuclear transfer (6) involves transferring the nuclear genome from the pronuclear-stage zygote (fertilized egg) of the affected woman (carrying pathogenic mtDNA) to an enucleated, healthy, recipient zygote, resulting in a fertile, reconstituted zygote containing the "normal" mtDNA of the recipient zygote and the transferred nuclear genome from the donor zygote (representing the nuclear genomes of the father and the mother with the pathogenic mtDNA). Another method called maternal spindle transfer can be performed with an unfertilized oocyte to generate an oocyte containing the nucleus from the female carrying the pathogenic mtDNA mutation and the "normal" mtDNA from the host oocyte, which can subsequently be fertilized in vitro (10). In either case, these techniques result in a so-called "three-parent embryo" containing nuclear genes from the male and affected female, and mtDNA from an unaffected female donor.

Ethical concerns surrounding these techniques (6, 11) certainly warrant discussion. At the same time, the biological effects of combining nuclear DNA with different mtDNA should be investigated. In mice, an approach quite similar to pronuclear transfer has been used to examine the effects of different mtDNAs on cellular bioenergetics and disease susceptibility. Mitochondrial-nuclear exchange (MNX) in mice is an approach still in early stages of examination (12, 13). It involves the transfer of the nuclear genome from one mouse strain into an enucleated, recipient zygote of a different mouse strain. MNX mice that were generated by two strains with distinct susceptibilities to atherosclerosis and insulin resistance, for example, show that mtDNA genetic background affects oxygen utilization and responses to cardiac tissue injury. The MNX mice appear healthy and fertile, yet also have different levels of oxidative stress, resistance to a surgically induced model of heart failure, and altered lipid concentrations relative to control counterparts, depending upon the mtDNA–nuclear DNA combination (12, 13).

Another recent study in mice has examined the immunogenicity of "mismatched mitochondria" using an approach involving mouse embryonic stem cells (ESCs) that have been derived through somatic cell nuclear transfer (14). There have been conflicting results on the few studies that have examined transplantation of mitochondrial mismatched cells or tissues. In the recent study, the nucleus of a somatic cell is transferred into an enucleated oocyte. Nuclear-transfer-derived embryonic stem cells (NT-ESCs) can then be generated from such an oocyte. NT-ESCs thus acquire "healthy" mitochondria

from the oocyte donor. The study found that NT-ESCs harboring the nuclear DNA of one mouse strain and the mtDNA from another mouse strain remained pluripotent. However, when transplanted into the thighs of mice, those NT-ESCs with "mismatched mitochondria" to the recipient animal possessed alloantigenicity and were subject to immune rejection (14). Whether the characteristics reported in the MNX mice or with NT-ESCs would be found with the maternal spindle transfer approach is not known.

Because mitochondrial-nuclear communication and interaction are part of normal cell function, and because normal biological reproduction allows for the coevolution of nuclear and mitochondria genomes (e.g., Mendelian and mitochondrial genetic selection occur simultaneously during meiosis), processes such as pronuclear transfer have the potential to alter this form of evolutionary selection and adaptation and therefore may have unintended effects on cellular bioenergetics and mitochondrial–nuclear signaling pathways. The introduction of "new" mtDNA to a nucleus after Mendelian selection, whereby allelic selection and gene expression were calibrated by a different mtDNA, bypasses aspects of Mendelian-mitochondrial evolution, or "mito-Mendelian" genetics. It therefore seems prudent to consider matching mtDNA haplogroup (minus the pathogenic mutation) of donor and recipient cells to minimize the possibility of altered interactions between the nucleus and the mitochondrion that may influence susceptibility to diseases of metabolism. In this respect, mtDNA haplogroup can influence penetrance of mtDNA mutations that cause Leber hereditary optic neuropathy (15).

Therapies based on mtDNA replacement represent important medical advances. However, evaluating the characteristics of the donor mitochondrial genomes seems reasonable as it could provide valuable insights for optimizing such therapies. ∎

REFERENCES

1. P. Amato, M. Tachibana, M. Sparman, S. Mitalipov, *Fertil. Steril.* **101**, 31 (2014).
2. A. L. Bredenoord, G. Pennings, G. de Wert, *Hum. Reprod. Update* **14**, 669 (2008).
3. M. R. Chiaratti, F. V. Meirelles, D. Wells, J. Poulton, *Mitochondrion* **11**, 820 (2011).
4. J. Poulton, P. Oakeshott, *BMJ* **345**, e6651 (2012).
5. K. Reinhardt, D. K. Dowling, E. H. Morrow, *Science* **341**, 1345 (2013).
6. D. S. Rubenstein *et al.*, *Camb. Q. Healthc. Ethics* **4**, 316 (1995).
7. M. Tachibana *et al.*, *Nature* **461**, 367 (2009).
8. A. Tavare, *BMJ* **344**, e540 (2012).
9. L. Craven *et al.*, *Nature* **465**, 82 (2010).
10. M. Tachibana *et al.*, *Nature* **493**, 627 (2013).
11. F. Baylis, *Reprod. Biomed. Online* **26**, 531 (2013).
12. A. M. Betancourt *et al.*, *Biochem. J.* **461**, 223 (2014).
13. J. L. Fetterman *et al.*, *Biochem. J.* **455**, 157 (2013).
14. T. Deuse *et al.*, *Cell Stem Cell* **16**, 33 (2015).
15. A. Torroni *et al.*, *Am. J. Hum. Genet.* **60**, 1107 (1997).

10.1126/science.aac5271

PHYSICS

Probing the edge with cold atoms

Trapped atoms can mimic the nature of edge currents in quantum Hall systems

By **Alessio Celi** *and* **Leticia Tarruell**

The quantum Hall effect is a hallmark of topological physics. It is the first example in which the topology of the system determines a macroscopic phenomenon, the quantization of Hall conductance. In a seminal paper, Halperin related it to the existence of skipping orbits for the electrons at the edge of the sample (1). Although the Hall conductivity is nowadays routinely measured with high precision and used to define the SI unit of

> *"...visualizing the electrons' trajectories is more challenging. The task is much easier using instead synthetic solids made of ultracold atoms in optical lattices."*

electrical resistance, observation of the underlying skipping orbits has been elusive. On pages 1514 and 1510 of this issue, Stuhl *et al.* (2) and Mancini *et al.* (3) report a striking visualization of these trajectories using ultracold atoms trapped in a synthetic lattice.

What is the quantum Hall effect? Classically, a strong magnetic field accelerates a charged particle perpendicularly to its velocity, such that it describes a circular cyclotron orbit. Quantum mechanics provides the essential ingredient that the energy of the orbit is quantized. This picture explains the confinement of motion of bulk electrons in two-dimensional materials subjected to strong magnetic fields and their insulating behavior. However, close to the edge of the
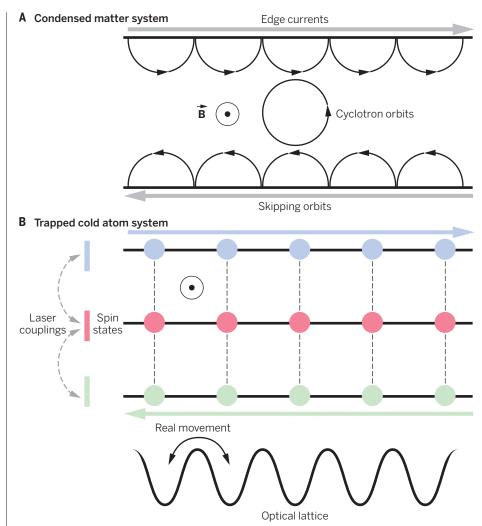
ICFO-Institut de Ciencies Fotoniques, Barcelona Institute of Science and Technology, 08860 Castelldefels, Barcelona, Spain. E-mail: alessio.celi@icfo.es; leticia.tarruell@icfo.es

sample, an electron will not have sufficient space to complete the orbit; it bounces off the edge and starts a new one. As this process continues, the electron moves along the edge, always in the same direction, which leads to chiral edge currents with a direction imposed by the magnetic field (see the figure, panel A). Because the orbits are quantized, the edge currents are also quantized and are extremely robust against small perturbations. These properties lead to the universal quantum of conductance at the heart of the integer quantum Hall effect.

These effects are clearly observed in solid-state systems, which are ideal for measuring transport properties. However, visualizing the electrons' trajectories is more challenging. The task is much easier using instead synthetic solids made of ultracold atoms in optical lattices (4). Because these systems are extremely dilute, with lattice spacing thousands of times larger than in conventional materials, they are excellent candidates for the direct imaging of the particle trajectories. However, observation of the skipping orbits presents several challenges: Atoms are neutral and so do not couple to magnetic fields as electrons do, but their effect on the atom motion can be mimicked using laser beams (5); to observe the edge states, a system with sharp boundaries is desirable, but ultracold atoms are usually confined in soft traps; and single-site resolved imaging is required to visualize the atomic trajectories at the boundaries. The last two challenges have been overcome by using an elegant experimental trick—the use of a synthetic dimension (6).

What is a synthetic dimension? Or rather, what is a dimension? In lattice systems like the ones used in these experiments, "dimension" relates to the connectivity—the number of independent directions, or states, the atoms can move in. Thus, in addition to real dimensions where motion corresponds to a displacement in space, one can consider a synthetic dimension where motion corresponds to a change of spin states (see the figure, panel B). This simple but innovative concept has key experimental advantages: Changes of spin states can be induced using the same laser beams that generate the appropriate synthetic magnetic field; the system has intrinsically sharp boundaries because the number of spin states is finite; and single-site detection in the synthetic dimension is obtained through spin-dependent measurements, which gives excellent access to the particle trajectories along the edges (7).

The two papers consider complementary situations: Stuhl et al. use a rubidium Bose-Einstein condensate; Mancini et al. use an ultracold Fermi gas of ytterbium atoms. Both

A Condensed matter system

Edge currents

$\vec{B}$ ⊙ — Cyclotron orbits

Skipping orbits

B Trapped cold atom system

Laser couplings — Spin states

Real movement

Optical lattice

Visualizing synthetic edges. (**A**) Closed and skipping orbits in a quantum Hall ribbon subjected to a strong magnetic field B (indicated as B with arrow). (**B**) Experimental semisynthetic ribbon: The atoms move in a real dimension along an optical lattice and in a synthetic dimension formed by spin states (green, red, and blue) coupled by lasers. The laser beams also induce a synthetic magnetic field. The chiral edge currents (arrows) are the result of the skipping orbits and are experimentally detected by measuring the spin-state motion.

exploit the synthetic dimension trick to create narrow ribbons made of three synthetic sites and subjected to a synthetic magnetic field. By preparing the atoms on the system edges, and suddenly allowing them to move, they directly observe the edge currents and can reconstruct the skipping orbits.

This synthetic dimension approach opens up a wealth of new possibilities for future experiments. One of the most intriguing is the realization of interacting systems displaying exotic fractional quantum Hall physics, in which effective particles with fractional charge emerge (8). Their fingerprint in solids is the existence of fractional Hall conductance. In cold atom experiments, it may be possible to observe these particles directly and even make use of their braiding to perform quantum computations. In addition, by wrapping the synthetic dimension in a circle, the system acquires a cylin-

drical shape and becomes periodic. In such conditions, the elusive Hofstadter fractal energy spectrum, a manifestation of topology complementary to edge states, could be directly observed. A number of exotic lattice topologies could be implemented, including, for instance, Möbius strips. Finally, by considering the three spatial dimensions, synthetic lattices offer the opportunity to simulate four-dimensional phenomena. ■

REFERENCES

1. B. I. Halperin, *Phys. Rev. B* **25**, 2185 (1982).
2. B. K. Stuhl et al., *Science* **349**, 1514 (2015).
3. M. Mancini et al., *Science* **349**, 1510 (2015).
4. M. Greiner, S. Fölling, *Nature* **453**, 736 (2008).
5. Y. J. Lin, R. L. Compton, K. Jiménez-García, J. V. Porto, I. B. Spielman, *Nature* **462**, 628 (2009).
6. O. Boada, A. Celi, J. I. Latorre, M. Lewenstein, *Phys. Rev. Lett.* **108**, 133001 (2012).
7. A. Celi et al., *Phys. Rev. Lett.* **112**, 043001 (2014).
8. R. B. Laughlin, *Phys. Rev. Lett.* **50**, 1395 (1983).

BATTERIES

Expanding the chemical space for redox flow batteries
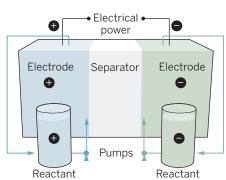
Flow batteries offer low-cost electricity storage for grid-scale renewable power sources

By **Mike L. Perry**

Redox flow batteries (RFBs) have many advantages for grid-level energy storage, a key requirement for implementing intermittent renewable sources. Like other rechargeable batteries, a flow battery uses reversible electrochemical couples on two electrodes to store chemical energy (*1*). However, instead of storing the active materials within the electrodes, the reactants are dissolved in two electrolyte solutions and stored in external tanks (see the figure). This configuration allows their cost to scale better as size increases compared to conventional batteries. To date, the redox-active species have often been transition-metal ions, which can have limited electrochemical potential range. On page 1529 of this issue, Lin *et al.* (*2*) report on the use of transition-metal complexes and organic molecules as redox species that are both low in cost and relatively nontoxic.

Flow batteries were originally developed in the 1970s by NASA and others (*1*). The first generation of RFB chemistries were primarily based on single-element active materials dissolved in aqueous electrolytes. Transition metals, such as iron, chromium, and vanadium, were often used because the transitions between their oxidation states occurred at a desirable standard electrochemical reduction potential (SERP). Other single-element reactants have also been used, such as hydrogen and some halogens. However, this single-element approach enables only a small set of RFB chemistries because of a limited number of reactants with the desired SERPs.

The next generation of RFB chemistries are likely to be engineered molecules or complexes that allow the SERP to be shifted to a more desirable potential. One approach is ligand-modified transition metals, which can be dissolved in aqueous or nonaqueous electrolytes. Another is the use of relatively complex organic molecules. For example, the SERP of known redox couples (e.g., quinones) can be shifted by tailoring organic molecules to include one or more of these redox cou-

United Technologies Research Center, East Hartford, CT 06108, USA. E-mail: perryml@utrc.utc.com

Liquid flows for current flows. A simplified schematic of a redox flow battery (RFB) system. Each RFB cell contains two electrodes where faradaic reactions occur as the positive and negative reactants flow through the electrodes and an ionic-conducting separator to facilitate the transport of charge carriers (e.g., protons) between the two electrodes. The flow direction is the same while charging or discharging, but the ionic charge carriers and electrons change direction.

ples. Functionalization—for example, with hydroxyl or sulfonate groups—can alter both the SERP and solubility. The RFB chemistry developed by Lin *et al.* includes examples of both approaches. Operating under highly basic conditions, the negative electrode uses an organic-based reactant and the positive reactant is a ligand-modified iron compound. Recent reviews provide more comprehensive lists of various types of RFB chemistries (*1, 3*).

Historically, the level of investment and research devoted to RFB technology has been relatively small compared to the amount invested in conventional batteries because RFBs are not well suited for portable or transportation applications, given their system complexity and relatively poor energy density. However, there is a growing interest in electrical-energy storage (EES) for a broad range of applications in the electricity-generation and -transmission industry. For example, grid-scale EES can mitigate electrical-transmission bottlenecks and provide various ancillary services, in addition to supplying stable and continuous power when coupled to inherently variable renewable-energy sources (*4*).

The primary barrier to greater adoption of EES systems on the grid has been capital cost (*5*). RFBs are well suited for large-scale applications because they scale up in a more cost-effective manner than other batteries. Because the energy and power capacities of a RFB system are independent variables, the required capacities for any application can be met by using correctly sized energy and power modules.

Another compelling attribute of RFBs for stationary EES applications, especially long discharge-duration applications, is a high ratio of energy stored or delivered to the discharge rate (power output)—this ratio can exceed 4 hours. Also, the RFB architecture enables long operational lifetimes because the electrodes are not inherently required to undergo physicochemical or structural changes during charge-discharge cycles. Thus, RFBs offer a promising pathway to cost-effective large-scale EES, especially on a cycle-life basis. Prototype RFB systems deployed in real-world EES applications have demonstrated their technical viability (*3, 5*).

The combination of the relative immaturity of RFB technology and the growing interest and investment in grid-scale EES has already resulted in substantial technology improvements (*1*). For example, dramatic improvements in the power density of RFB cells enable reductions in the cost of the inactive materials; and further improvements in cell performance can be expected. However, the most critical factor in any battery is the chemical composition of the active materials, and the inherent costs of these materials (on a dollar per kilowatt-hour basis).

Other key properties of the electrolyte solutions will dictate the performance (and cost) of the cells and the rest of the system, including solvent cost, the ionic conductivity of the solutions and the separator, and the open-circuit voltage. A detailed techno-economic analysis concluded that advanced RFB chemistries with the right combination of these key attributes could achieve <$150 per kilowatt-hour at relatively modest production volumes (10 gigawatt-hours per year) (*6*). Thus, new RFB chemistries are critically important means to further improving the commercial viability of RFBs. The study by Lin *et al.* is an excellent example of an especially promising pathway because entire families of new RFB chemistries are theoretically feasible by using organic and organometallic coordination complexes. ∎

REFERENCES

1. B. R. Chalamala *et al.*, *IEEE Proc.* **102**, 976 (2014).
2. K. Lin *et al.*, *Science* **349**, 1529 (2015).
3. G. L. Soloveichik, *Annu. Rev. Chem. Biomol. Eng.* **2**, 503 (2011).
4. S. Chu, A. Majumdar, *Nature* **488**, 294 (2012).
5. U.S. Department of Energy, *Grid Energy Storage* (U.S. DOE, Washington, DC, 2013).
6. R. Darling, K. Gallagher, J. Kowlaski, S. Ha, F. Brushett *Energy, Environ. Sci.* **7**, 3459 (2014).

10.1126/science.aad0698

ILLUSTRATION: P. HUEY/SCIENCE

BOOKS *et al.*

NEUROSCIENCE

Thinking differently

The history of autism and what it means for the future

By **Francesca Happé**

Steve Silberman's new book, *Neuro-Tribes*, blows many common beliefs about autism out of the water. Along the way, it tells the real stories of children and adults with autism, their families, and the clinicians and researchers trying to understand their very different minds. *NeuroTribes* is part history, part investigative reporting, part biography, and all poetry.

Autism was first recognized and named entirely independently by Leo Kanner in Baltimore in 1943 and Hans Asperger in Vienna in 1944. Or so we have always thought. In *NeuroTribes*, Silberman has meticulously unpacked this story, tracing the entangled lives and work of Asperger and Kanner. We learn that in response to the rise of Nazism in Vienna, Asperger's colleagues Georg Frankl and Anni Weiss fled to the United States, where they began working closely with Kanner in 1938. Kanner has long been hailed as the first to discover and name "autism," but Silberman's detective work places Asperger and his colleagues at the very start of the autism story.

Why did Kanner get the credit for discovering autism while Asperger's work went largely unnoticed? For Silberman, much of the answer lies in personality and narrative. While Asperger was reportedly shy, Kanner was a socially adroit clinician who wrote a smash-hit textbook. But for Silberman, it was Kanner's ability to bring the experiences of children with autism to life on the page that sealed his place as the founding father of autism.

Like Kanner, Silberman has a gift for case histories. In addition to Kanner and Asperger, Silberman profiles more recent pioneers in autism research, including Bernard Rimland, the autism parent and researcher who waged war on the 1960s notion that "refrigerator" (emotionally cold) parenting

caused autism, and Lorna Wing, another parent/researcher, who established the notion of an autism spectrum and introduced the term "Asperger syndrome" in the 1980s. Other cases highlight highly eccentric figures who made important contributions to science and culture, including the 18th-century scientist Henry Cavendish, who discovered hydrogen, and John McCarthy, who taught the first undergraduate computer programming course at MIT in the 1950s and later launched the Stanford Artificial Intelligence Laboratory in what would become Silicon Valley. Contemporary portraits of people such as Shannon and Craig Rosa and their

Diagnosed with autism at the age of 2, Temple Grandin is one of the world's leaders in the design of livestock-handling facilities.

autistic son Leo ("the boy who loves green straws") or Ari Ne'eman, the brilliant and indefatigable autism self-advocate, convey the reality of living with autism.

These are portraits beautifully penned and as affectionate as they are insightful. Early in the book, and in Silberman's own journey into understanding autism, he describes interviewing 11-year-old Nick: "The music of his speech was pitched high, alternately poetic and pedantic, as if the soul of an Oxford don had been awkwardly reincarnated in the body of a boy…. I liked him immediately."

Silberman hasn't simply rewritten the history of autism; he has also written autism into historical context. He charts autism's rise from a supposedly rare syndrome (by 1957, Kanner claimed to have seen just 150 "true cases") through the expansion of diag-

nostic criteria in the 1980s to include bright and highly verbal people with Asperger syndrome and the consequent rise in diagnosis. He traces the resultant fears about vaccines and possible environmental causes and explores the current "neurodiversity" movement in which self-advocates argue against the need for a "cure" for their different way of processing the world.

The tension between changing individuals with autism to fit the "neurotypical" world and changing the world to be more autism-friendly is explored against a wide historical backdrop. From the Nazi eradication of the disabled and mentally ill to the eugenics movement in 1920s America, Silberman shows how propaganda highlighted the financial costs of people who were not able to work or care for themselves. It is ironic that autism charities today find themselves having to appeal to economic arguments, showing how the costs to society can be cut with better services and research. At the same time, parents are bombarded with expensive "cures" with little or no scientific basis.

During the height of the persecution of the disabled and mentally ill, Asperger sought to mitigate the stigma of autism, writing in 1938 that "The good and bad in a person, their potential for success or failure, their aptitudes and deficits—they are mutually conditional, arising from the same source." Indeed, recent research suggests genetic overlap between the tendency for talent and the eye for detail that makes tolerating change so hard for those with autism (1).

NeuroTribes can be seen, in part, as a tribute to the contributions that eccentric and socially awkward outsiders have made to technology, culture, and 21st-century society. It is a beautifully written and thoughtfully crafted book, a historical tour of autism, richly populated with fascinating and engaging characters, and a rallying call to respect difference.

REFERENCES

1. F. Happé, P. Vital, *Philos. Trans. R. Soc. London Ser. B Biol. Sci.* **364**, 1369 (2009).

The reviewer is at the Institute of Psychiatry, Psychology, and Neuroscience, King's College London, London SE5 8AF, UK. E-mail: francesca.happe@kcl.ac.uk

10.1126/science.aac4990

As the amount of personal genetic information we have access to grows, so, too, do the legal and ethical implications.

GENOMICS

The future of health care

Making informed decisions in the age of genomic medicine

By **Henry T. Greely**

George Annas and Sherman Elias, two longtime experts on the medical and social implications of genetics, wrote *Genomic Messages* for nonexperts, to "help you make your own decisions about whether and how to use the evolving genomics in your own life." Annas, a law professor and bioethicist, and Elias, an obstetrician/gynecologist and medical geneticist, largely succeed in this aim.
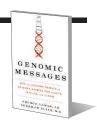
Genomic Messages consists of a series of chapters on how genomic information might apply to individual health, including personalized medicine; the nature/nurture knot; pharmacogenomics; assisted reproduction (a digression that has little to do with genetics); prenatal, neonatal, and childhood testing; and cancer. Each chapter ends with a box with several summarizing thoughts for readers to consider: "It is unlikely that you or your physician will use genomics to determine your drug or dose in the near future," for example, or "There is no perfect genome and no genetically perfect fetus."

Useful real and hypothetical cases stemming from Elias's practice as a medical geneticist pepper these chapters, and the information is presented at a level interested general readers can understand. The advice tends to be conservative, expressed specifically in the context of human behavioral genomics. "We are easily seduced by genomics and need to keep our common

The reviewer is at the Center for Law and the Biosciences, Stanford University, Stanford, CA 94305, USA. E-mail: hgreely@stanford.edu

sense fully engaged," they maintain. Some will consider the book too skeptical about what genomics can tell people today, although I think it generally hits a reasonable balance.

The biggest problem for the book is inherent in its subject. Genomics is just too many things: It is omnipotent and irrelevant; unchangeable or acutely responsive to its environment. It is about health and disease, as well as human enhancement. It can be used as a tool for tracing ancestry, from our ethnic forebears to more recent family, and it has become key to criminal identification.

The most common consumer genetic tests are undoubtedly those that purport to provide information about one's ancestry. The book says nothing about the strengths, weaknesses, benefits, and risks of such kits. Similarly, the implications of genomics for common diseases are a world apart from the lives of people trying to cope with rare genomic conditions. *Genomic Messages* does not, and cannot, provide the depth needed to inform those families. [Readers interested in a more in-depth treatment of the latter topic should consider the gripping new book *Orphan*, by Philip Reilly (*1*).]

The last two chapters shift the book's focus. In Chapter 9, the authors look at privacy issues, databases, and gene patents. Here, the book moves from what people may want to do to what policies they want in place, touching perhaps too quickly on many complicated issues. The authors sum up the chapter by saying "your DNA is yours—it's your property, and it contains information that is most important to you."

But at other points they seem to hold a different opinion, urging regulation to define what genomic information should be conveyed and what information should be withheld from people. They also concede that families share DNA, making total control over one's own genome problematic. These issues are complicated, and the discussion does not go deep enough to produce well-informed readers.

The final chapter juxtaposes themes from dystopian science fiction with speculation based on cutting-edge research fields, discussing de-extinction, human cloning, transhumanism, immortality, and other futuristic scenarios. In these brief considerations, the book sometimes falls to pronouncements rather than analysis—for example, when the authors state, "Replication of a human by cloning could radically alter the very definition of a human being…." Is that true in a nontautological way? And is it reasonable to say that reviving extinct species is "simply unscientific and a waste of time and resources," without offering some relevant facts or arguments? Although these issues add drama, they detract from the stated mission of the book.

This book is strongest when it sticks to helping people figure out how they should use genomic technologies for their health and the health of their families. It does that well, although I am sure the authors would agree that their book should be a first step in an education that may need to include genetic counselors, medical geneticists, expert physicians, and others.

Sadly, this book comes at the close of a partnership between Annas and Elias that began in 1983. Elias died unexpectedly in July 2014, just after the book was completed. Through their 30 years of joint writing, Annas and Elias learned much about the intersections of genetics, society, and individual people. This book is a fitting culmination of that partnership, conveying that knowledge and wisdom to people seeking to understand their own "genomic messages."

REFERENCES

1. P. R. Reilly, *Orphan: The Quest to Save Children with Rare Genetic Disorders* (Cold Spring Harbor Press, Cold Spring Harbor, NY, 2015).

10.1126/science.aac9664
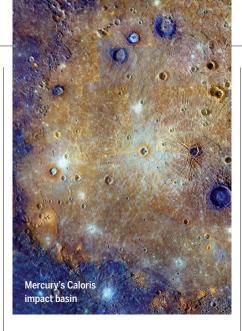
Edited by **Jennifer Sills**

Mercury and the Moon

IN THEIR REPORT "Low-altitude magnetic field measurements by MESSENGER reveal Mercury's ancient crustal field" (22 May, p. 892, published online 7 May), C. L. Johnson *et al.* provide convincing evidence for detection of ancient crustal magnetization on a fourth body in the solar system (after Earth, the Moon, and Mars). However, Johnson *et al.* suggest that Mercury's crustal field sources originated from purely internal processes, such as the crystallization of minerals that preserve a record of an ancient magnetic field. Their hypothesis ignores much of what was learned about lunar crustal magnetism from the Apollo landings and subsequent investigations. Mercury is very similar to the Moon, so this is an important omission.

An important finding of the MESSENGER study is that the strongest magnetic fields on Mercury's surface are found near smooth plains. Johnson *et al.*'s main example was Suisei Planitia, which they interpreted as material deposited by a volcano almost 4 billion years ago. However, a careful reading of the primary reference for this interpretation (*1*) shows that another explanation cannot be ruled out: The plains may have been formed after impact from an asteroid. In this case, material from the basin created upon impact may have been converted to liquid, ejected, and deposited nearby (*2*). Suisei Planitia, which is one of a number of smooth plains concentrated around the enormous Caloris impact basin, may have been formed this way.

The lunar results are relevant because the strongest surface magnetic fields were measured at the Apollo 16 landing site in an area dominated by a smooth plains unit known as the Cayley Formation. Before Apollo, the Cayley was believed to be volcanic in origin (*3*), but it was found upon landing to instead be composed of impact-produced materials. It is now believed to have been formed by material ejected after an impact (*4*). The Cayley formation is the single geologic unit that correlates best with the magnetic field observed from orbit (*5*). These two results led to the leading (but not fully accepted) hypothesis that basin ejecta are the main sources of unexpected magnetic variations in the lunar crust (*6*–*8*). The discovery of the Mercurian anomalies and their association with smooth plains may therefore add weight to arguments that the smooth plains near the Caloris basin

have an impact-related origin and that the sources of the strongest orbital anomalies on both the Moon and Mercury consist of basin ejecta materials.

Lon L. Hood

Lunar and Planetary Laboratory, University of Arizona, Tucson, AZ 85721, USA. E-mail: lon@lpl.arizona.edu

REFERENCES
1. B. W. Denevi *et al.*, *J. Geophys. Res. Planets* **118**, 891 (2013).
2. D. E. Wilhelms, *Icarus* **28**, 551 (1976).
3. D. J. Milton, U.S. Geol. Surv. Map I-748 (1972).
4. D. E. Wilhelms, U.S. Geol. Surv. Prof. Paper 1348 (Washington, DC, 1987), p. 216.
5. J. S. Halekas *et al.*, *J. Geophys. Res.* **106**, 27841 (2001).
6. D. W. Strangway *et al.*, *Nature* **246**, 112 (1973).
7. L. L. Hood *et al.*, *J. Geophys. Res.* **106**, 27825 (2001).
8. L. L. Hood *et al.*, *J. Geophys. Res. Planets* **118**, 1 (2013).

Emissions reduction is not enough

IN THEIR REVIEW "Contrasting futures for ocean and society from different anthropogenic CO_2 emissions scenarios" (Reviews, 3 July, p. 45), J.-P. Gattuso *et al.* write that anthropogenic greenhouse gas (GHG) emissions must be drastically reduced to avoid "massive and effectively irreversible impacts on ocean ecosystems." They call for policies that would limit emissions to those restricting global warming to 2°C. However, it is now very unlikely that we can stay within 2°C warming by emissions reduction alone.

Reaching the needed atmospheric CO_2 level requires not only rapid reduction in emissions, but also post-emissions drawdown of atmospheric CO_2 through natural CO_2 sinks and by thus far little-researched and unproven "negative emissions" technologies (*1*, *2*). The quantity of post-emissions CO_2 that must be removed from the atmosphere ranges from 180 Gt to

more than 5000 Gt (*3*, *4*). Furthermore, inadequate control of atmospheric GHG and resulting warming could lead to large releases of GHG from current natural reservoirs (such as permafrost) and reductions in natural CO_2 sinks (*1*), defeating emissions reduction efforts.

Given the preceding, the marine science and policy communities must not only advocate emissions reduction, but also call for an expanded search for additional methods of managing atmospheric GHG, as well as exploration of new marine conservation strategies in case current strategies fail. However, Gattuso *et al.* only once mention removal of CO_2 from the atmosphere, citing it as an "engineering-intensive" management technique and ignoring methods that simply enhance natural CO_2 sinks (*1*, *2*, *5*, *6*). The authors correctly dismiss conventional marine conservation techniques as offering "only limited protection" in the context of GHG impacts, a shortcoming that will continue without an expanded search for new and better approaches (*7*, *8*). To conclude, it is risky to pin the fate of the ocean and the planet solely on our ability to reduce GHG emissions without also actively fostering and objectively evaluating additional actions.

Greg H. Rau¹* and Charles H. Greene²

¹Institute of Marine Sciences, University of California, Santa Cruz, CA 95064, USA. ²Ocean Resources and Ecosystems Program, Cornell University, Ithaca, NY 14853, USA.

*Corresponding author. E-mail: ghrau@sbcglobal.net

REFERENCES
1. P. Ciais *et al.*, in *Climate Change 2013: The Physical Science Basis. Contribution of Working Group I to the Fifth Assessment Report of the Intergovernmental Panel on Climate Change*, T. F. Stocker *et al.*, Eds. (Cambridge Univ. Press, Cambridge, 2013), ch. 6.
2. M. K. McNutt *et al.*, *Climate Intervention: Carbon Dioxide Removal and Reliable Sequestration* (National Academies Press, Washington, DC, 2015).
3. United Nations Environment Programme (UNEP), *The Emissions Gap Report 2014* (UNEP, Nairobi, 2014).
4. T. Gasser *et al.*, *Nat. Commun.* **6**, 7958 (2015).
5. G. H. Rau, in *Global Environmental Change Handbook of Global Environmental Pollution, Vol. 1*, B. Freedman, Ed. (Springer, Dordrecht, Netherlands, 2014), pp. 817–824.
6. C. H. Greene, B. C. Monger, M. E. Huntley, *Solutions* **1**, 57 (2010).
7. G. H. Rau, E. L. McLeod, O. Hoegh-Guldberg, *Nat. Clim. Change* **2**, 720 (2012).
8. The Paul G. Allen Ocean Challenge: Mitigating Acidification Impacts (www.pgafamilyfoundation.org/oceanchallenge/).

Research fraud as tort

IN THEIR POLICY FORUM "Self-correction in science at work" (26 June, p. 1420), B. Alberts *et al.* propose that "incentives should be changed so that scholars are rewarded for publishing well rather than often." They recommend, for example, replacing the word "retraction" with

Mercury's Caloris impact basin

alternate phrasing, such as "voluntary withdrawal" and "withdrawal for cause," depending on the absence or presence of fraud or other research misconduct.

In addition to reforming the reward structure of scientific publishing—a worthy goal—we would also draw attention to the possibility of legal liability for research fraud. Beyond the possibility of a mere retraction (or as Alberts *et al.* propose, a "withdrawal for cause"), scientific researchers should be held to the same legal standards as any individual or business. By way of example, we propose extending the well-established tort of fraudulent misrepresentation to fraudulent research published in journals based in the United States.

Proving fraudulent misrepresentation is not easy. In the context of research fraud, the duped journal would have to prove that the fraudulent researcher intended to deceive the journal, that his or her misrepresentations were material—i.e., essential for being accepted for publication—and that the journal was justified in relying on the researcher's misrepresentations in making the decision to publish (*1*). By making scientific researchers who publish in U.S. journals liable in tort for their acts of fraud,

we would expect to deter the incidence of fraud before it occurs. If we wish to promote integrity in science, let's not forget to use sticks as well as carrots.

Enrique Guerra-Pujol

Dixon School of Accounting, University of Central Florida, Orlando, FL 32816, USA.
E-mail: Enrique.Guerra-Pujol@ucf.edu

REFERENCE

1. Legal Information Institute, Fraudulent Misrepresentation (www.law.cornell.edu/wex/fraudulent_misrepresentation).

TECHNICAL COMMENT ABSTRACTS

Comment on "Whole-genome analyses resolve early branches in the tree of life of modern birds"

Kieren J. Mitchell, Alan Cooper, Matthew J. Phillips

Jarvis *et al.* (Research Articles, 12 December 2014, p. 1320) presented molecular clock analyses that suggested that most modern bird orders diverged just after the mass extinction event at the Cretaceous-Paleogene boundary (about 66 million years ago). We demonstrate that this conclusion results from the use of a single inappropriate maximum bound, which effectively precludes the Cretaceous diversification overwhelmingly supported by previous molecular studies.

Full text at http://dx.doi.org/10.1126/science.aab1062

Response to Comment on "Whole-genome analyses resolve early branches in the tree of life of modern birds"

Joel Cracraft, Peter Houde, Simon Y. W. Ho, David P. Mindell, Jon Fjeldsa, Bent Lindow, Scott V. Edwards, Carsten Rahbek, Siavash Mirarab, Tandy Warnow, M. Thomas P. Gilbert, Guojie Zhang, Edward L. Braun, Erich D. Jarvis

Mitchell *et al.* argue that divergence-time estimates for our avian phylogeny were too young because of an "inappropriate" maximum age constraint for the most recent common ancestor of modern birds and that, as a result, most modern bird orders diverged before the Cretaceous-Paleogene mass extinction event 66 million years ago instead of after. However, their interpretations of the fossil record and timetrees are incorrect.

Full text at http://dx.doi.org/10.1126/science.aab1578

TECHNICAL COMMENT

AVIAN GENOMICS

Comment on "Whole-genome analyses resolve early branches in the tree of life of modern birds"

Kieren J. Mitchell,[1]* Alan Cooper,[1] Matthew J. Phillips[2]

Jarvis *et al.* (Research Articles, 12 December 2014, p. 1320) presented molecular clock analyses that suggested that most modern bird orders diverged just after the mass extinction event at the Cretaceous-Paleogene boundary (about 66 million years ago). We demonstrate that this conclusion results from the use of a single inappropriate maximum bound, which effectively precludes the Cretaceous diversification overwhelmingly supported by previous molecular studies.

Substantial discrepancies exist between the first appearance in the fossil record of many avian lineages and their age as estimated by molecular clock analyses (*1*). A particularly contentious topic is the time scale for the divergences between modern bird orders (*2*). The oldest fossil generally agreed to fall within Neornithes—the clade comprising all living birds (Fig. 1A)—is *Vegavis* (*3*), from the end-Cretaceous ~67 million years ago (Ma). However, most molecular dating studies have suggested that Neornithes began diversifying more than 110 Ma (*4–6*). Conversely, Jarvis *et al.* (*7*) presented genome-based molecular clock results that supported predominantly post-Cretaceous dates for the diversification of modern birds.

Although Jarvis *et al.*'s genomic data set and phylogeny are impressive leaps forward for the field, the influence of their calibrations requires closer investigation. Their phylogeny was calibrated by applying minimum and maximum bounds to key nodes. Best-practice approaches for defining minimum bounds are well established (*8, 9*): The origin of a clade necessarily predates the appearance of its first unequivocal fossil representative. However, maximum bounds (the earliest plausible age of a clade) are a more difficult proposition, yet just as important for estimating dates (*10, 11*).

Jarvis *et al.*'s only maximum age constraint among birds (the root of Neornithes) was weakly justified. They implemented a strong prior against the diversification of Neornithes occurring before the Late Cretaceous (99.6 Ma). This decision effectively precluded results consistent with many previous molecular clock studies, which have generally recovered ages for Neornithes between 110 and 140 Ma (*4–6*). Their first justification for the 99.6-Ma bound, that it is 30 million years

older than their age estimate for Neoaves (two nodes shallower), is immaterial. Their second justification, that the bound "far exceeds the age of paleontological evidence for the existence of Neornithes" [supplementary materials for (*7*)] [e.g., the putative neornithine, *Austinornis* at ~85 Ma (*12*)], is only relevant if it covers relatively well-sampled fossil assemblages in potential geographic areas of origin that contain no putative clade members but do preserve ancestral forms or ecological equivalents (*10, 13*). However, the few fossils attributable to Euornithes (neornithines and their close relatives) (see Fig. 1A) during this period (from ~85 Ma to Jarvis *et al.*'s maximum at 99.6 Ma) are taphonomically biased, including only a handful of seabirds (*14*). Because early neornithines may well have been terrestrial (Fig. 1A), assigning a maximum constraint based on this Late Cretaceous record is clearly inappropriate.

We reanalyzed Jarvis *et al.*'s molecular dating data set (722,202 nucleotides from 51 diapsid species, including 48 birds) using the authors' total evidence nucleotide tree (TENT) topology, while varying the maximum bound for Neornithes. Our analyses were otherwise performed according to the methods described in the original study.

Recent studies have used the absence of neornithines from some Early Cretaceous deposits, where the avian fossil record is far superior, to set a 97.5% prior maximum bound of 117.5 Ma (*5*). When we reanalyzed Jarvis *et al.*'s genomic data with this more appropriate maximum bound, the number of sampled neornithines with pre–Cretaceous-Paleogene (K-Pg) mean divergence estimates increased from 15 to 22 out of 47 [nodes with 95% highest posterior densities (HPDs) entirely pre–K-Pg increased from 10 to 13], and the posterior mean for the origin of modern birds fell close to the maximum, at 117.2 Ma (Fig. 1B).

However, even this older maximum constraint remains inappropriate if modern birds were ini-

tially restricted to Gondwana, as is presently the case for most basal neornithine clades, including ratites, megapodes, cracids, and screamers. Within Late Cretaceous Gondwana, the oldest bird fossil is a putative neornithine (*15*), and the known Early Cretaceous Gondwanan fossil record is largely uninformative, containing only the non-euornithine *Nanantius* and taxonomically indeterminate fragments. When such potential geographic origins are considered, it becomes difficult to justify even a 117.5-Ma maximum. Removing the maximum bound on Neornithes altogether resulted in pre–K-Pg mean estimates for a full 37 of our 47 neornithine divergences (29 nodes with 95% HPDs entirely pre–K-Pg), and the posterior mean for the origin of modern birds increased to 162.5 Ma (Fig. 1B). This date is substantially older even than *Archaeopteryx*, suggesting that substitution or rate variation models are misspecified.

In summary, Jarvis *et al.* (*7*) employed a strong maximum constraint on the age of Neornithes that is poorly supported by the fossil record and that heavily influenced their inference of post-Cretaceous bird diversification. Without imposing this constraint, their genomic data and remaining calibrations favor deep Neornithes origins, with most interordinal divergences occurring in the Cretaceous, consistent with previous molecular dating studies. If indeed the major diversification of modern birds occurred after the K-Pg mass extinction event, which arguably better fits the fossil record, it could be explained by parallel rate decelerations across modern avian clades being nonidentifiable even to relaxed clock methods. However, support for such agreement with fossil records must come from improvements in either the model of molecular rate variation or better fossil sampling and not from the imposition of artificially strong maximum age constraints.

REFERENCES AND NOTES

1. D. T. Ksepka, J. L. Ware, K. S. Lamm, *Proc. Biol. Sci.* **281**, 20140677 (2014).
2. G. Mayr, *Palaeontology* **57**, 231–242 (2014).
3. J. A. Clarke, C. P. Tambussi, J. I. Noriega, G. M. Erickson, R. A. Ketcham, *Nature* **433**, 305–308 (2005).
4. O. Haddrath, A. J. Baker, *Proc. Biol. Sci.* **279**, 4617–4625 (2012).
5. W. Jetz, G. H. Thomas, J. B. Joy, K. Hartmann, A. O. Mooers, *Nature* **491**, 444–448 (2012).
6. J. W. Brown, J. S. Rest, J. García-Moreno, M. D. Sorenson, D. P. Mindell, *BMC Biol.* **6**, 6 (2008).
7. E. D. Jarvis *et al.*, *Science* **346**, 1320–1331 (2014).
8. R. R. Reisz, J. Müller, *Trends Genet.* **20**, 237–241 (2004).
9. J. F. Parham *et al.*, *Syst. Biol.* **61**, 346–359 (2012).
10. M. J. Phillips, *Palaeontol. Electronica* **2015**, 18.1.5FC (2015).
11. L. A. Hug, A. J. Roger, *Mol. Biol. Evol.* **24**, 1889–1897 (2007).
12. T. S. Myers, *J. Paleontol.* **84**, 1071–1081 (2010).
13. R. Barnett *et al.*, *Curr. Biol.* **15**, R589–R590 (2005).
14. The data were downloaded from the Paleobiology Database (https://paleobiodb.org) on 5 March 2015.
15. F. L. Agnolin, F. E. Novas, G. Lio, *Ameghiniana* **43**, 245–248 (2006).

[1]Australian Centre for Ancient DNA, School of Biological Sciences, University of Adelaide, Australia. [2]School of Earth, Environmental and Biological Sciences, Queensland University of Technology, Brisbane, Australia.
*Corresponding author. E-mail: kieren.mitchell@adelaide.edu.au
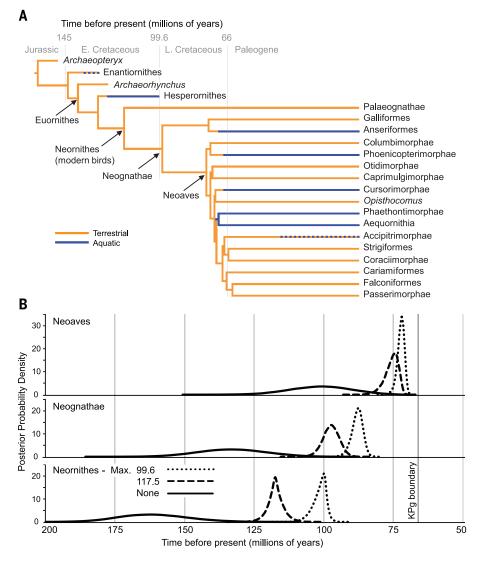
Fig. 1. Reanalysis of Jarvis *et al.*'s genomic data set. (**A**) Jarvis *et al.*'s TENT topology (partially collapsed for clarity) placed into temporal context with the earliest records for several older avian lineages. Divergence dates among living species are derived from analyses following Jarvis *et al.* (*7*) but employ a more appropriate 117.5-Ma maximum bound for the diversification of neornithines. In addition, ancestral habitat was reconstructed under maximum parsimony for terrestrial (orange) and aquatic (blue) lineages, with approximate transition times based on fossil records. Dotted lines indicate the existence of derived aquatic taxa within a clade for which terrestriality appears ancestral. (**B**) Posterior age distributions for several key nodes under three different maxima for Neornithes: 99.6 Ma (dotted line), 117.5 Ma (dashed line), and removal of this maximum constraint (solid line).

TECHNICAL RESPONSE

AVIAN GENOMICS

Response to Comment on "Whole-genome analyses resolve early branches in the tree of life of modern birds"

Joel Cracraft,[1]*† Peter Houde,[2]* Simon Y. W. Ho,[3]* David P. Mindell,[4] Jon Fjeldså,[5] Bent Lindow,[6] Scott V. Edwards,[7] Carsten Rahbek,[8,9] Siavash Mirarab,[10] Tandy Warnow,[10,11] M. Thomas P. Gilbert,[6,12] Guojie Zhang,[13,14] Edward L. Braun,[15]† Erich D. Jarvis[16,17]†

Mitchell *et al.* argue that divergence-time estimates for our avian phylogeny were too young because of an "inappropriate" maximum age constraint for the most recent common ancestor of modern birds and that, as a result, most modern bird orders diverged before the Cretaceous-Paleogene mass extinction event 66 million years ago instead of after. However, their interpretations of the fossil record and timetrees are incorrect.

I t is well known that changing the prior maximum age constraint in a Bayesian relaxed clock analysis can change estimates of species divergence times (*1*). Jarvis *et al.* (*2*) estimated the rapid diversification of Neoaves to be near the Cretaceous-Paleogene (K-Pg) boundary based on data-rich analyses, including first and second codon positions of 1156 clocklike nuclear genes, 19 internal fossil calibrations, and a maximum age constraint of 99.6 million years ago (Ma) on the most recent common ancestor (MRCA) of Neornithes (modern birds) based on the Early-Late Cretaceous boundary. Mitchell *et al.* (*3*) claim that our 99.6-Ma constraint was "inappropriate." Their contention is, instead, that a maximum constraint at 117.5 Ma—well into the Early Cretaceous (~145 to 99.6 Ma)—is "more appropriate," and upon applying it, they unsurprisingly found that many divergences moved deeper in time, thus implying a major radiation of Neoaves in the Late Cretaceous (~99.6 to 66 Ma) before the 66-Ma K-Pg mass extinction event. Evaluating Mitchell *et al.*'s arguments requires answers to two questions: (i) is the maximum age constraint they used more appropriate than that used by Jarvis *et al.* (*2*) and (ii) does the use of different constraints for the MRCA of Neornithes substantially alter conclusions regarding timing of the neoavian radiation?

Addressing question (i), although Mitchell *et al.* claim that their 117.5-Ma prior is more appropriate, in fact it is a calibration product of the Early Cretaceous (110 Ma) fossil *Gansus yumenensis* (*4*) and a prior probability density chosen by Jetz *et al.* (*5*), rather than direct fossil evidence. Further, *Gansus* is an ornithurine (*4*) lying far outside other Mesozoic fossils more closely related to Neornithes (*6, 7*) and thus is an inappropriately old constraint for dating modern birds. Consequently, the empirical basis for their calibration is not well justified.

Mitchell *et al.* criticize our use of the empirical fossil record on the grounds that the record is taphonomically biased across space and time due to poor preservation of Southern Hemisphere Late Cretaceous terrestrial avian fossils, which they infer represent the most basal neornithines. Although the Northern Hemisphere is better sampled than the Southern Hemisphere (*8*), small terrestrial non-neornithine birds ecologically equivalent to terrestrial neornithines are conspicuous in the Late Cretaceous avifaunas from Argentina (*9*) and Madagascar (*10*), whereas neornithines are conspicuously absent. Moreover, based on their survey of the avian fossil record, Fountaine *et al.* (*11*) conclude that "it is unlikely that the modern clades would have remained independently cryptic throughout [the Late Cretaceous]."

Mitchell *et al.* also largely dismiss the Early Cretaceous fossil record as uninformative with respect to the origin of neornithines, but then call attention to several fossils from the beginning of the Late Cretaceous to bolster their argument for an Early Cretaceous origin. We believe, however, that their interpretations of these fossils are faulty. Mitchell *et al.* refer to *Austinornis* at 85 Ma and cite Myers (*12*). However, Myers (*12*) does not mention *Austinornis* or an 85-Ma age for it. Clarke (*13*), on the other hand, while noting that *Austinornis lentus* has one character that suggests it might be a stem-galliform, stresses that this fossil should not be used in dating analyses (it lacked 99% of the characters in her matrix). Mitchell *et al.* raise the issue of a putative neornithine fossil from Patagonia ~83 to 94 Ma (*14*). However, the neornithine relationships of this fragmentary fossil are uncertain (*15*), and even if it were a neornithine, there would be no inconsistency with our results. Our results are consistent with the most convincing pre–K-Pg Neornithes fossil to date, *Vegavis*, a very Late Cretaceous (66 to 68 Ma) (*16*) inferred stem-anseriform (*2*). In contrast, the diverse and well-preserved Jehol Biota of China, which provides a window into a ~130 to 120 Ma Early Cretaceous period (*17*), has never yielded a neornithine fossil. The issue is not whether fossils assignable to the avian crown group (Neornithes) will be found in the Early to Late Cretaceous but that, with the exception of *Vegavis,* they have not been documented. The fossil record does not support the presence of a diverse Neornithine avifauna in the Early or Late Cretaceous, and especially not of Neoaves, the focus of Jarvis *et al.* (*2*).

To address question (ii), we examined the sensitivity of our relaxed clock analyses to different maximum age constraints for Neornithes in more detail. We note that even younger age constraints have been proposed (*18*), which Jarvis *et al.* (*2*) examined. Comparing results from all three proposed maximum constraints of 86.5 (*18*), 99.6 (*2*), and 117.5 Ma (*3*), among the 37 divergences of major ordinal lineages in Neoaves, only 1 to 4 out of 37 (3 to 11%), 5 to 9 out of 37 (14 to 24%) and 10 to 15 out of 37 (31 to 41%), respectively, predate the K-Pg boundary (Fig. 1, A to C) (mean dates). The exact numbers of divergences pre–K-Pg vary slightly depending on parameters and stochasticity of software dating methods (see figure legend) and the exact date used for the K-Pg, since so many divergences are near it. Importantly, the 95% credibility intervals (CI) showed that few divergences were exclusively pre–K-Pg boundary (0, 8, and 14%) under all three constraints, whereas the vast majority of CIs overlapped with the

[1]Department of Ornithology, American Museum of Natural History, New York, NY 10024, USA. [2]Department of Biology, New Mexico State University, Las Cruces, NM 88003, USA. [3]School of Biological Sciences, University of Sydney, Sydney, New South Wales 2006, Australia. [4]Department of Biochemistry and Biophysics, University of California, San Francisco, CA 94158, USA. [5]Center for Macroecology, Evolution and Climate, Natural History Museum of Denmark, University of Copenhagen, Universitetsparken 15, DK-2100 Copenhagen Ø, Denmark. [6]Centre for GeoGenetics, Natural History Museum of Denmark, University of Copenhagen, Øster Voldgade 5-7, 1350 Copenhagen, Denmark. [7]Department of Organismic and Evolutionary Biology and Museum of Comparative Zoology, Harvard University, Cambridge, MA 02138, USA. [8]Center for Macroecology, Evolution and Climate, Natural History Museum of Denmark, University of Copenhagen, Universitetsparken 15, DK-2100 Copenhagen Ø, Denmark. [9]Department of Life Sciences, Imperial College London, Silwood Park Campus, Ascot SL5 7PY, UK. [10]Department of Computer Science, The University of Texas at Austin, Austin, TX 78712, USA. [11]Departments of Bioengineering and Computer Science, University of Illinois at Urbana-Champaign, Urbana, IL 61801, USA. [12]Trace and Environmental DNA Laboratory Department of Environment and Agriculture, Curtin University, Perth, Western Australia 6102, Australia. [13]China National GeneBank, BGI-Shenzhen, Shenzhen 518083, China. [14]Centre for Social Evolution, Department of Biology, Universitetsparken 15, University of Copenhagen, DK-2100 Copenhagen, Denmark. [15]Department of Biology and Genetics Institute, University of Florida, Gainesville, FL 32611, USA. [16]Department of Neurobiology, Duke University Medical Center, Durham, NC 27710, USA. [17]Howard Hughes Medical Institute, Chevy Chase, MD 20815, USA.
*These authors contributed equally to this work. †Corresponding author. E-mail: jlc@amnh.org (J.C.); ebraun68@ufl.edu (E.L.B.); jarvis@neuro.duke.edu (E.D.J.)

Fig. 1 Genome-scale avian timetrees with 95% CIs and different maximum age constraints for Neornithes. (**A** to **C**) Timetrees using the 86.5, 99.6, and 117.5 Ma maximum constraints, respectively, on exons of 1156 clocklike genes and the most recent version of the MCMCTREE program (*20*). The 95% CIs (blue bars) in (A) and (B) are slightly narrower and some divergences moved backward or forward in time by approximately one million years compared with those in Jarvis *et al.* (*2*), as a result of stochastic MCMC sampling effects and using an updated version of the software. However, the overall results are similar and all lie within the previously defined 95% CIs. Branches with multiple species in the same suborder have been collapsed, and the reptilian outgroups (lizard, turtle, and alligator) are not shown. We do not show the four extinct lineages included in the Mitchell *et al.* (*3*) tree because they are not directly used in the Bayesian dating analysis. Order/suborder names are color coded according to large monophyletic groups. (**D**) Comparison of dates and 95% CIs for key avian divergences using the different maximum constraints. There are no dramatic shifts in dates beyond the Neornithes, Palaeognathae, and Neognathae splits, unless one eliminates the maximum age constraint for Neornithes altogether. MYA, million years ago.

K-Pg (24, 32, and 57%) or were exclusively post–K-Pg (76, 60, and 30%) (Fig. 1, A to D). Thus, most divergences are very near the K-Pg boundary, not many millions of years before. Removing the maximum age constraint altogether results in much earlier divergence-time estimates (Fig. 1D). However, such removal is difficult to justify given the absence of Early Cretaceous neornithine fossils. Inappropriately, Mitchell *et al.* try to contradict our conclusions using divergence dates for all Neornithes in the tree, when our claim was only about Neoaves (*2*). Moreover, they collapsed the branches of nearly all post–K-Pg ordinal divergences into deeper ones, making it appear that most divergences were pre–K-Pg.

In summary, our previous conclusion that Neoaves underwent a rapid radiation near the K-Pg boundary is well founded. Although the estimated dates of the origins of Neornithes and Neognathae do vary with the choice of maximum age constraints, the divergence times for Neoaves are much less sensitive. Improvements to relaxed clock methods may further reduce error due to model fit, but the interpretation of the fossil record will remain the most important component of relaxed clock analyses (*19*). The extremely short branch lengths at the base of Neoaves, along with the evidence for discordance among gene trees due to incomplete lineage sorting [figure 3 in Jarvis *et al.* (*2*)], support what many previous analyses have found, that Neoaves underwent a very rapid radiation near the K-Pg boundary. Such rapid radiations are often associated with ecological drivers. The K-Pg Chicxulub asteroid impact with global ecological changes and mass extinctions around 66 Ma is consistent with its being one potential driver.

REFERENCES AND NOTES
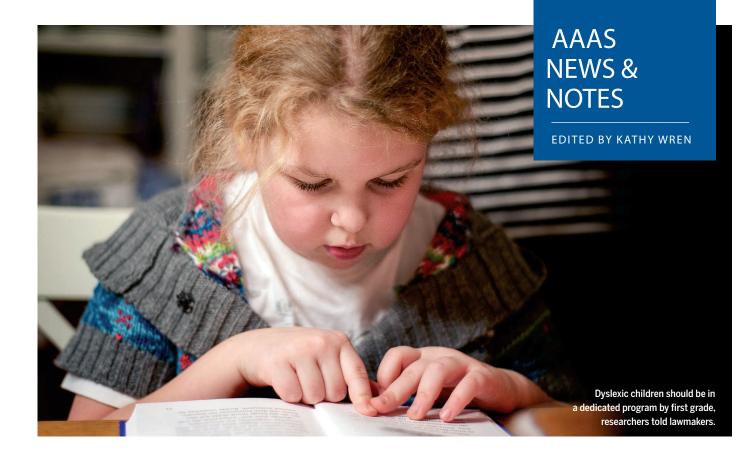
1. R. C. M. Warnock, Z. Yang, P. C. J. Donoghue, *Biol. Lett.* **8**, 156–159 (2012).
2. E. D. Jarvis *et al.*, *Science* **346**, 1320–1331 (2014).
3. K. J. Mitchell, A. Cooper, M. J. Phillips, *Science* **349**, 1460 (2015).
4. H. L. You *et al.*, *Science* **312**, 1640–1643 (2006).
5. W. Jetz, G. H. Thomas, J. B. Joy, K. Hartmann, A. O. Mooers, *Nature* **491**, 444–448 (2012).
6. J. K. O'Connor, Z. Zhou, *J. Syst. Palaeontology* **11**, 889–906 (2013).
7. M. S. Y. Lee, A. Cau, D. Naish, G. J. Dyke, *Syst. Biol.* **63**, 442–449 (2014).
8. L. M. Chiappe, L. M. Witmer, *Mesozoic Birds: Above the Heads of Dinosaurs* (University of California Press, Berkeley, 2002).
9. C. A. Walker, G. J. Dyke, *Isr. J. Earth Sci.* **27**, 15–62 (2009).
10. P. M. O'Connor, C. A. Forster, *J. Vertebr. Paleontol.* **30**, 1178–1201 (2010).
11. T. M. R. Fountaine, M. J. Benton, G. J. Dyke, R. L. Nudds, *Proc. Biol. Sci.* **272**, 289–294 (2005).
12. T. S. Myers, *J. Paleontol.* **84**, 1071–1081 (2010).
13. J. A. Clarke, *Bull. Am. Mus. Nat. Hist.* **286**, 1–179 (2004).
14. F. L. Agnolin, F. E. Novas, *Paläont. Zeit* **86**, 85–89 (2012).
15. G. Mayr, *Paleogene Fossil Birds* (Springer, Berlin, Heidelberg, 2009).
16. J. A. Clarke, C. P. Tambussi, J. I. Noriega, G. M. Erickson, R. A. Ketcham, *Nature* **433**, 305–308 (2005).
17. M. Wang *et al.*, *Nat. Commun.* **6**, 6987 (2015).
18. M. J. Benton, P. C. J. Donoghue, R. J. Asher, in *The Timetree of Life*, S. B. Hedges, S. Kumar, Eds. (Oxford Univ. Press, New York, 2009), pp. 35–86.
19. S. Y. W. Ho, *Trends Ecol. Evol.* **29**, 496–503 (2014).
20. M. Dos Reis, T. Zhu, Z. Yang, *Syst. Biol.* **63**, 555–565 (2014).

Dyslexic children should be in a dedicated program by first grade, researchers told lawmakers.

For kids with special learning needs, roadblocks remain

Neuroscience has shed light on the struggle, but early intervention and cost remain challenges

By **Gavin Stern**

Despite decades of neuroscience advancement, new diagnostic technologies, and a focus on studying children with disabilities, many children with special needs like attention deficit hyperactivity disorder (ADHD) and dyslexia are still being left behind at school.

"We have all this stuff—new brain imaging technologies, big data samples, etc.—why are we not making really fast progress?" said Damien Fair, associate professor in behavioral neuroscience and psychiatry at the Oregon Health & Science University.

Fair spoke at a 9 September briefing on Capitol Hill, as one of three scientists presenting the latest research on why these children tend to fare poorly in school and what can be done about it. The briefings, organized by AAAS with support from the Dana Foundation, provide scientific evidence to lawmakers with the hope that it will help them find solutions to society's problems, said Erin Heath, associate director of the AAAS Office of Government Relations.

"Education is a topic that comes up again and again, because it touches nearly every aspect of our society," Heath said.

Early identification is the first roadblock that separates special needs children from an effective education. For children with ADHD, that is due in part to the "heterogeneity problem," in which children diagnosed with the same condition have different underlying issues in their brain, said Fair. Doctors may check the same boxes to diagnose two children with ADHD, but the cause may not be the same, making it difficult to identify the appropriate therapies. Studies of the brain have found that normal control populations are also heterogeneous in brain physiology and behavior, further complicating efforts to study people with ADHD.

Figuring out how to characterize this variation is likely to be a major research area going forward, Fair said, and may lead to more individualized therapies.

Even when special needs children are identified, many children are deprived of intervention because their parents can't afford the best programs.

In the case of dyslexia, specialized schools may charge tuition that rivals an expensive university, said Sally E. Shaywitz, co-director of the Yale Center for Dyslexia and Creativity and a professor in learning development at Yale University.

"Many of the people hardest hit by dyslexia are minority students and those from low-income families," Shaywitz said, even though the condition affects all population segments and languages.

Roughly 8 to 10% of children in the United States have a learning disability, and about 1 in 5 people suffer from dyslexia. Across the general population, there is a link between strong reading skills and high IQ. That's not the case for people with dyslexia, which means that even very bright children can have a reading deficit.

In the wrong setting, even a smart kid can think herself a failure because of dyslexia.

"Allowing children to fail, to think they're 'dumb,' is no longer acceptable," Shaywitz said.

Dyslexic children are best identified and placed in a special program by the first grade, according to research by Shaywitz scheduled for publication in October. That is two grades earlier than most previous estimates.

The best model, she said, is a specialized charter school that doesn't charge tuition. "We need early identification, and it can be done. And we need early intervention. If you wait until third grade, kids give up," Shaywitz said. "We now know it's first grade, and we need to act on it."

For children with ADHD, learning difficulties tend to appear later on in development, said Martha Denckla, a neurology professor at the Johns Hopkins University School of Medicine and director of developmental cognitive neurology at the Kennedy Krieger Institute.

"In my clinic, we find that for grades K-1 to 3, children with ADHD didn't show up with academic lags. But later on, the deficits emerged," she said. "Yes, we should do early identification, but we can't drop our vigilance."

Around third grade, a student with ADHD begins to academically "fall apart." The child may seem to be doing well while they're learning. But wait a few minutes after the lesson, and they have trouble remembering what they've learned.

"Something seems to be interfering with these children's new learning," Denckla said.

Children with ADHD tend to react slower when tested for motor ability, eye movements, comprehension, and processing speed, according to Denckla.

These students need to be taught in a way that reduces competing demands on attention, allows them more freedom of movement while learning, and encourages repetition of skills, she said. Focusing on sitting still or positioning a pen on paper takes up too many cognitive resources.

"Anything you ask children with ADHD to respond to with consistent speed, they do not do as well as others," Denckla said. "Sometimes children who are hyperactive are slow." ∎

Symposium briefs religion writers on science topics

By **Gavin Stern**

The discovery of several thousand exoplanets over the last three decades has had profound implications for scientists and non-scientists alike, potentially rattling our understanding of humanity's place in the universe, according to Jennifer Wiseman, director of the AAAS Dialogue on Science, Ethics, and Religion (DoSER) program.

"What does that mean for our sense of human identity that there are hundreds of billions of galaxies, each filled with billions of stars and potentially billions of planets?" Wiseman asked an audience of religion writers at a 27 August symposium at the 66th Religion Newswriters Association conference in Philadelphia.

Crash courses in astrobiology, artificial intelligence, and gene editing were on the program at the DoSER-organized event, which was part of an initiative to strengthen communication between scientists and religious communities.

"We wanted to create a safe space where [religion reporters] can hear about some of the more interesting developments in science and feel free to ask questions, so they'll feel more confident in writing about science for their audiences," said Wiseman. The symposium was the first step of DoSER's new Science for Religion Reporters awards program, which will send up to 12 religion reporters to the 2016 AAAS Annual Meeting in Washington, DC.

The symposium exposed religion writers to several cutting-edge science topics that raise modern ethical and philosophical questions about human identity, technological enhancements, and manipulations of life. The writers also learned how the scientific enterprise operates today, including the processes of funding, peer review, and publication.

While Wiseman introduced the writers to the state-of-the-art methods astronomers use to find and study planets outside of the solar system, Robert T. Pennock, a professor at Michigan State University, presented on artificial intelligence and robotics. Each new technological advancement developed by science, from advanced prosthetic limbs to the drones of modern warfare, makes people consider what it means for them to be human, he said.

"We can really shape ourselves," Pennock said. "I think we're going to have to make choices not just about whether to use things as weapons, but what kind of people we will be."

Ethical and moral choices also abound in genetic engineering, another forefront science topic at the symposium. Gene-editing technology has the potential to stop many diseases at their source code before a person is born. But does it go too far if parents get to pick their children's eye color—or enhance their intellect? What happens if some people can afford those enhancements while others cannot?

Due in part to these ethical questions, said MIT Professor Doug Lauffenburger, the National Institutes of Health does not currently fund gene-editing techniques on human embryos.

"Technology always moves faster than one guesses," said Lauffenburger, who provided an overview on genetic engineering technologies like CRISPR/Cas9. "This is not something that the scientific community is trying to sweep under the rug." ∎

AAAS annual election: Preliminary announcement

The 2015 AAAS election of general and section officers is scheduled to begin in October. All members will receive a ballot for election of the President-Elect, members of the Board of Directors, and members of the Committee on Nominations. Additionally, members registered in sections (up to three) will receive ballots for the specified section elections. Biographical information for the candidates will be provided along with ballots. The general election slate of candidates is listed below. The full list, including section candidates, can be viewed at www.aaas.org/annual-election.

General Election

President-Elect: John L. Anderson, Illinois Institute of Technology; Susan Hockfield, Massachusetts Institute of Technology

Board of Directors: Cynthia M. Beall, Case Western Reserve Univ.; May R. Berenbaum, Univ. of Illinois at Urbana-Champaign; Marie Lynn Miranda, Rice Univ.; Donald T. Stuss, Ontario Brain Institute (Canada)

Committee on Nominations: Rick E. Borchelt, U.S. Department of Energy; Alice M. Clark, Univ. of Mississippi; Sharon Dunwoody, Univ. of Wisconsin-Madison; Joseph S. Francisco, Univ. of Nebraska-Lincoln/Purdue Univ.; Susan L. Graham, Univ. of California, Berkeley; Barbara Herr Harthorn, Univ. of California, Santa Barbara; William H. Press, Univ. of Texas at Austin; Peter H. Raven, Missouri Botanical Garden

HUNTING MUTATIONS,
TARGETING DISEASE

By **Laura M. Zahn** *and* **John Travis**

A s sequencing technology races toward ever cheaper, faster, and more accurate ways to read an individual's entire genome, understanding the health implications of variations in the genetic code becomes more crucial. This genetic variation can be as small as a single nucleotide base-pair change, insertion, or deletion, or as large as the gain or loss of multiple chromosomes.

Genetic mutations can cause suffering and early death. It is thus vital to understand their origins and how they affect biological function. Some deleterious mutations may arise and be maintained over generations within populations. These may only come to light when an individual carries two copies, as for a recessive Mendelian trait. Others may be exposed as soon as they arise within an individual. Such mutations can cause developmental defects if they occur very early in life, or contribute to aging and disease, notably cancer, in later life.

Recent technological advances have made it easier to detect human mutations and link them to pathology. Our ability to identify and target cancer-specific mutations has opened up a new and promising line of research. The rise of new genetic editing tools and a deeper understanding of the genetic architecture of traits, combined with reproductive technologies, offer the possibility to eliminate or mitigate the deleterious impact of mutations. While some mutations are easier to target than others, which can cause frustration at the pace of translating genetic information into medical help, enormous progress has arguably been made in the decade since the first human genome was decoded—and there's the promise of even more clinical applications in the future.

PHOTO: GENOME RESEARCH LIMITED
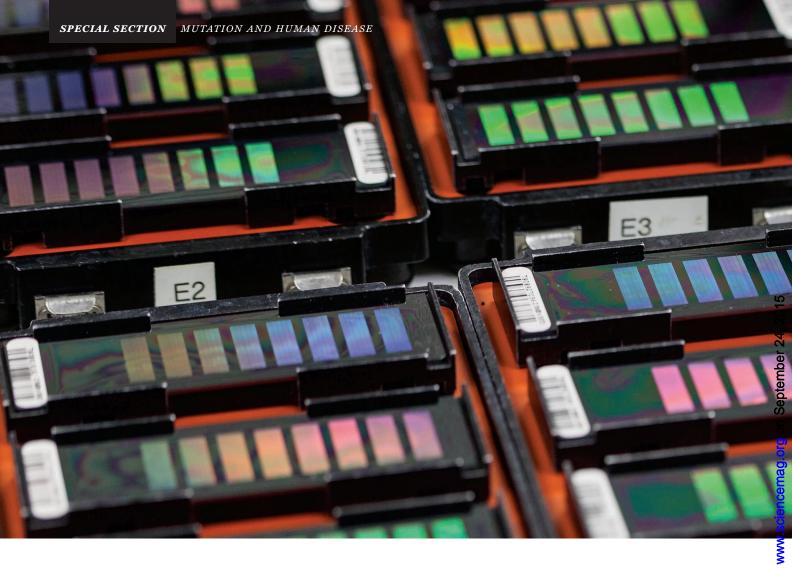
Genomic data centers that help connect human mutations to illness continue to expand. This one at the Sanger Institute in Hinxton, U.K., currently has 16 petabytes of DNA sequence information on file.

Can 23andMe have it all?

The consumer genetics company has amassed DNA from more than a million people. Now, it wants to find drugs to treat them

By **Kelly Servick**, *in Mountain View, California*

How much do your eyes water when cutting onions? Does fresh cilantro taste like soap to you? Do you have stretch marks on your hips, thighs, or the backs of your arms? Have you ever been diagnosed with brain cancer?

Mail off your spit for a $99 genetic analysis from 23andMe, and you will get information about your ancestry, served up on a web account. You will also encounter a list of optional survey questions. A *lot* of survey questions. Some are quirky que-

ries about your tastes and habits. Others are intimate probes into your experiences with disease and medicine.

For the team of more than 30 geneticists and statisticians behind one of the world's largest genetic biobanks, the surveys are bread and butter, allowing them to pin down links between DNA markers and people's health, appearance, and bodily idiosyncrasies. New medical and physiological connections have been incorporated into the $99 analysis, adding value for customers. The formula has en-

abled the Silicon Valley firm to outlast most of its competitors and become a poster child for the fledgling field of direct-to-consumer genetic testing.

23andMe suffered a major setback in 2013 when the U.S. Food and Drug Administration (FDA) warned the firm it was illegally returning health information using tests that the agency hadn't vetted. But even though the growth of its customer base slowed after the company pulled the health data from its personal genome service for new customers, 23andMe's research team

pushed ahead. Today, the company has collected DNA from more than a million people. (That amounts to more than 2000 liters of saliva.) And its self-curious customers seem almost addicted to participating in research; they collectively answer about 2 million new survey questions every week as the company searches for new health-related DNA sequences.

Gradually, a research group that started out analyzing the genetics of freckles and the sneeze reflex has moved into deeper scientific waters: the hunt for disease-related genes that could make good drug targets. "It's really been an evolution from, 'Tell us whether you're a morning person or not,' to 'Let's solve disease,'" says Joyce Tung, 23andMe's director of research.

The company says it has made roughly 30 deals with pharmaceutical and biotech companies seeking access to its database—14 of them last year, most of them undisclosed. "There's no other group that has as many samples," Tim Behrens, Genentech's senior director of human genetics in San Francisco, says of 23andMe's database of Parkinson's disease patients, which Genentech paid an initial $10 mil-

lion to explore, with the promise of up to $50 million more.

23andMe went even further in March, when it announced that it would hire a therapeutics team and begin drug discovery efforts of its own. That's a move even some of its champions see as audacious. "Their main contribution, to me, has been democratization of genomics," says Eric Topol, a physician and geneticist at the Scripps Research Institute in San Diego, California, who studies digital health technologies. "This is a very different look, and a pivot. Maybe they'll accomplish it, but there are a lot of entities out there that are trying to develop drugs."

23ANDME SITS ALONG THE CALTRAIN tracks in downtown Mountain View, in a four-story glass cube that doesn't quite feel lived in yet. The company logo, a whimsical doodle of pink and green crisscrossed chromosomes, is still taped above the entrance, printed across four sheets of letter-sized white paper. On this summer morning, Anne Wojcicki is breezing around the deserted staff cafeteria in flip flops, preparing a hard-boiled egg. A row of treadmills

23andMe analyzes its customers' DNA with a customized "SNP chip," which uses fluorescent tags to identify 650,000 potential genetic variants.

outfitted with standing desks sits idle on the other side of the room.

This is a building that Wojcicki, 23andMe's co-founder and CEO, intends to grow into. In May, the company abandoned its previous nest on the campus of Google, Mountain View's most famous corporate resident. Google was both an early investor in 23andMe and an influence on Wojcicki's vision. A biologist and health care investment analyst, she launched the company in 2006 with biologist Linda Avey and financial executive Paul Cusenza based on what she calls a social mission to "integrate genetic information into the world," and on the theory that collecting DNA and health information from every person could turn disease research into "a data problem."

Tung, lured away from academia after a postdoc at Stanford University in Palo Alto, in which she studied the genetics of pigmentation in mice and people, was among the company's first recruits. At the time, skepticism abounded about the firm's vision of

gleaning valuable data from a relatively cheap genetic test and an online survey. "My postdoc adviser was like 'Well, it's nice that you guys want to do research, but you're never going to find anything real—like medical, or anything like that,'" she recalls.

In a glass-walled meeting room upstairs from the cafeteria, Tung's thunderous laugh rings out at unpredictable moments. When asked what makes the database valuable for researchers now, she stretches her arms dramatically and exclaims: "It's big!"

23andMe has extracted genetic information from its growing stockpile of samples

other variants that are likely to be inherited alongside those tested directly.

For its customers, 23andMe uses the SNPs to predict ancestry and other traits. The analysis can say what percentage of a customer's DNA originates from a population in Northern Europe, for example. And until 2013, it could warn about potentially elevated risk of conditions including Parkinson's disease, breast cancer, and cardiomyopathy. (One of the company's initial analyses famously informed Sergey Brin, Google's co-founder and Wojcicki's ex-husband, that he has a gene that substantially increases

smaller projects have targeted sarcoma, myeloproliferative neoplasms—a group of rare bone marrow diseases—inflammatory bowel disease, and lupus.

All of the survey responses and genotypes are stripped of identifying information to protect privacy. And the participants readily volunteer more data. When the team sends out a new survey question, Tung says, it's not unusual to get millions of fresh data points within 24 hours. That responsiveness sets the 23andMe cohort apart from the average subjects recruited into a research study, who are often "ready to quit at the

23andMe's scientific leadership (left to right): research director Joyce Tung, principal scientist David Hinds, senior research director Joanna Mountain, Chief Executive Officer Anne Wojcicki, platform architect Arnab Chowdry, and head of therapeutics Richard Scheller.

by testing them for single nucleotide polymorphisms (SNPs, pronounced "snips"), relatively common variations in a single DNA base pair. DNA from each customer's saliva is broken into fragments and washed over a "SNP chip"—a credit card–sized plate of microscopic silica beads covered in DNA probes. Each single-stranded probe grabs the DNA fragment with a complementary sequence, leaving exposed the DNA letter at a location of interest. Then, free-floating nucleotides with fluorescent tags bind to and reveal the identity of that SNP.
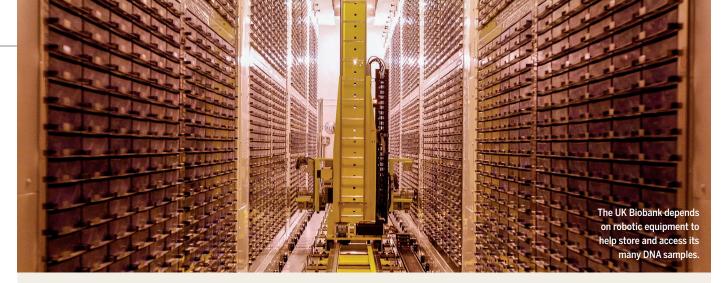
Biophysicist Arnab Chowdry, responsible for 23andMe's technology platforms, is always trying to squeeze more information from the limited chip real estate. The current model detects 650,000 SNPs, but using publicly available reference genomes, the team can also predict more than 14 million

his risk of Parkinson's; Brin, who publicly disclosed that finding, has since become a major funder of research into the disease.)

Using survey responses from more than 800,000 customers who have agreed to take part in the research, 23andMe's scientists look for new links between SNPs and physical traits, or phenotypes. Their stock-in-trade is the genomewide association study (GWAS): They group customers who share a phenotype—haters of cilantro, or those with type 2 diabetes—and identify SNPs that occur more frequently in that group than a control.

Since 2009, 23andMe has also provided its personal genome service for free to certain patient populations in exchange for their participation in more focused, disease-specific surveys. Its Parkinson's disease "community" now includes 12,000 people;

drop of a hat," says George Church, a geneticist at Harvard University and a member of 23andMe's scientific advisory board. "The 23andMe cohort—for whatever reason, they're highly engaged."

23andMe has cultivated this community carefully. Its researchers devote part of their time to studies that will pique customer interest, but that are unlikely to win grants from the National Institutes of Health. They've found four SNPs associated with a tendency to develop stretch marks, for example, and observed that a variant nestled among olfactory receptor genes turns cilantro soapy for certain tasters.

Yet the online surveys that have helped 23andMe's database flourish have also made it a questionable source of information in the eyes of some disease researchers. "It was met with incredible skepti-

The UK Biobank depends on robotic equipment to help store and access its many DNA samples.

Who has your DNA—or wants it

By **Jocelyn Kaiser**

More and more groups are amassing computer server–busting amounts of human DNA. *Science*'s informal survey found at least 17 biobanks that hold—or plan to hold—genomic data on 75,000 or more people. The data range from scans of common mutations known as single nucleotide polymorphisms (SNPs) to the protein-coding portions of the genome (exomes) to whole genomes.

23andME
SIZE: >1 million **GENETIC DATA:** SNPs
This popular personal genomics company now hopes to apply its data to drug discovery (see main story, p. 1472).

ANCESTRY.COM
SIZE: >1 million **GENETIC DATA:** SNPs
This genealogy firm now has a collaboration with the Google-funded biotech Calico to look for longevity genes.

HUMAN LONGEVITY, INC.
SIZE: 1 million planned
GENETIC DATA: whole genomes
Founded by genome pioneer Craig Venter, this company plans to sequence 100,000 people a year to look for aging-related genes.

100K WELLNESS PROJECT
SIZE: 107 (100,000 planned)
GENETIC DATA: whole genomes
Led by another sequencing leader, Leroy Hood, this project is taking a systems approach to genetics and health.

MILLION VETERAN PROGRAM
SIZE: 390,000 (1 million planned)
GENETIC DATA: SNPs, exomes, whole genomes
This U.S. Department of Defense–funded effort is probing the genetics of kidney and heart disease and substance abuse.

U.S. NATIONAL RESEARCH COHORT
SIZE: 1 million planned
GENETIC DATA: to be determined
Part of President Obama's Precision Medicine Initiative, this project will use genetics to tailor health care to individuals.

UK BIOBANK
SIZE: 500,000 **GENETIC DATA:** SNPs
Study of middle-aged British is probing links between lifestyle, genes, and common diseases.

100,000 GENOMES PROJECT
SIZE: 5500 (75,000 normal + 25,000 tumor genes planned)
GENETIC DATA: whole genomes
This U.K.-funded project focusing on cancer and rare diseases aims to integrate whole genomes into clinical care.

deCODE GENETICS
SIZE: 140,000
GENETIC DATA: SNPs, whole genomes
Now owned by Amgen, this pioneering Icelandic company hunted for disease-related genes in the island country.

KAISER-PERMANENTE BIOBANK
SIZE: 200,000 (500,000 planned)
GENETIC DATA: SNPs
This health maintenance organization has published on telomeres and disease risks.

GEISINGER MYCODE
SIZE: 60,000 (250,000 planned)
GENETIC DATA: exomes
Geisinger, a Pennsylvania health care provider, works with Regeneron Pharmaceuticals to study DNA links to disease.

VANDERBILT'S BIOVU
SIZE: 192,000 **GENETIC DATA:** SNPs
Focused on genes that affect common diseases and drug response, BioVU data have been permanently deidentified.

BIOBANK JAPAN
SIZE: 200,000 **GENETIC DATA:** SNPs
This study collected DNA from volunteers between 2003 and 2007 and is now looking at genetics of common diseases.

CHINA KADOORIE BIOBANK
SIZE: 510,000 **GENETIC DATA:** SNPs
This study is probing links between genetics, lifestyle and common diseases.

EAST LONDON GENES & HEALTH
SIZE: 100,000 planned
GENETIC DATA: exomes
One aim is to find healthy "human knockouts"—people who lack a specific gene—in a population in which marrying relatives is common.

SAUDI HUMAN GENOME PROGRAM
SIZE: 100,000 planned
GENETIC DATA: exomes
One aim of this national project is to find genes underlying rare inherited conditions.
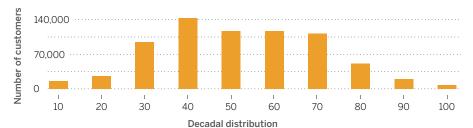
CHILDREN'S HOSPITAL OF PHILADELPHIA
SIZE: 100,000
GENETIC DATA: SNPs, exomes
The world's largest pediatric biorepository connects DNA to the hospital's health records for studies of childhood diseases.

A cohort of customers

More than a million people have had the DNA from their saliva analyzed by 23andMe, most paying $99 for the service, and more than 800,000 have allowed that DNA to be used in research.
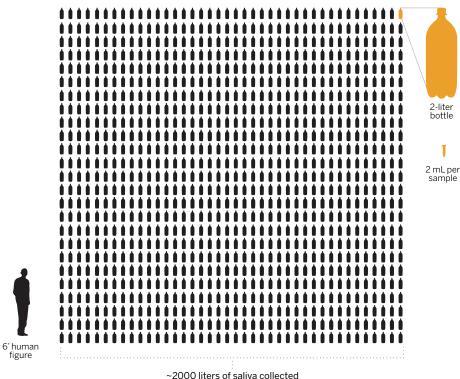
Customer age

Customer ancestry

A saliva stockpile

~2000 liters of saliva collected

cism," says Mark Cookson, a cell biologist studying Parkinson's disease at the National Institute on Aging's laboratory of neurogenetics in Bethesda, Maryland. Casual questionnaires seemed to many to be a poor substitute for a medical exam or a patient's health records. "The clinical guys were saying, 'Well hang on, if you don't know that someone has Parkinson's, how will you get clean data sets?'"

Cookson says that skepticism has faded somewhat. For one thing, the search for statistically significant associations between a trait and a DNA sequence "is a numbers game," he says, and with enough responses, concerns about reliability "melt a little bit." And 23andMe has shown in several studies that the associations its researchers turn up match results from other groups.

By 2012, 23andMe had more than 180,000 customers, and had contributed to studies identifying new genetic associations for freckles, curly hair, alopecia, Parkinson's disease, and hypothyroidism. At that year's annual gathering of the American Society of Human Genetics (ASHG), 23andMe's principal scientist, statistical geneticist David Hinds, noticed that his status had changed. "Between one ASHG meeting and the next, it went from largely disinterest in what we were doing—thinking it was not very relevant—to being approached by lots of people who were interested in collaborating with us, getting access to our data." As of this summer, the 23andMe team had put out more than 30 papers, many of them in collaboration with academic labs.

The 23andMe team has also demonstrated—retrospectively—that its database can help guide drug discovery. At the 2014 ASHG meeting, they presented an analysis of 2751 candidate drugs showing that 23andMe data could predict which ones succeeded in clinical trials. They observed a nearly twofold increase in the odds that a drug would ultimately be approved by FDA if the 23andMe database revealed an association between the disease trait and a SNP somewhere on or around the gene whose product the drug targeted, compared with a drug without a genetic association.

But association studies alone are feeble drug discovery tools. The SNPs linked to a disease are often just markers for a nearby region of the genome where the real disease-influencing mutation lies. Association studies also fail to lay out how illness might arise from a mutation, or how targeting a gene product might affect the body. Until recently, a completed GWAS was "sort of the end of the road" for the 23andMe team, Hinds says. "We were pretty limited, because we could find associations, but we're not set up to do biology."

INDEED, THE COMPANY'S WIDE-OPEN office space is more suggestive of a generic Silicon Valley internet startup than a biotech lab. Headset-clad customer service representatives field calls at their standing desks. "Welcome to our gene pool" balloons flag the workstations of new hires.

But Richard Scheller, the most conspicuous new hire, is here to do biology. Last December, on the same day the 61-year-old drug discovery veteran announced his retirement from a 15-year career at Genentech, he got an email from Wojcicki. "I knew he had not retired," she says. "I grew up on Stanford's campus. I know his phenotype. That man is never going to stop." Wojcicki says she had long been debating whether the company should do its own drug discovery, and Scheller's enthusiasm for the idea pushed her over the edge.

At 23andMe, Scheller is on foreign ground. The informatics experts on Tung's team are not his scientific ilk. "They use algorithms with famous statisticians' names behind them, and I have absolutely no idea what they're talking about," he says.

Drug discovery is new territory for 23andMe's core research team, too. The group has long aspired to influence how drugs are developed, says Chowdry, but "I don't think most of us really imagined that we would ever bring it in-house." Still, he quickly got on board. "If we actually believe that there's value in the database—which all of us do—having it in-house means that we get a bigger chunk of the value."

As head of the new therapeutics group, Scheller plans to hire about 25 scientists by sometime next year, and to double the team again in another year. He is checking out potential lab space in South San Francisco and talking to contract labs. Slowly, 23andMe may start to look more like a typical biotech firm, doing the dicey work of drug development: finding candidate genes, screening compounds that might interact with them or their proteins, testing the compounds in animals and then in people.

The company has revealed almost nothing about what its new group will pursue. The only area definitively ruled out is neuropsychiatric disease—because of its "particular complexities," says Scheller, who headed a Stanford neuroscience lab before joining Genentech. He also says that 23andMe's first drug candidates will likely be antibodies that target disease-related molecules, because they are easier to make than small molecule drugs.

Running a drug discovery program will mean going beyond 23andMe's old standby, the SNP chip, to partial- or full-genome sequencing. SNP chips are generally geared toward flagging common mutations—occurring in roughly 3% to 5% of the population—and these have so far failed to explain a large percentage of a person's genetic risk for common diseases. 23andMe's chip has been tweaked to include many rarer SNPs, but it can't physically accommodate hundreds of uncommon variants for every given gene. And it can only probe for known mutations—not reveal new ones.

Newer efforts to scan huge collections of DNA for disease-causing mutations—including geneticist J. Craig Venter's San Diego–based Human Longevity, Inc. and the 1-million-person cohort launched in January as part of President Obama's precision medicine initiative—are betting on large-scale genome sequencing instead (see sidebar, p. 1475). As DNA sequencing gets cheaper, "a whole realm of genetic variation that we've just not had access to is possible,"

> ## "It's really been an evolution from, 'Tell us whether you're a morning person or not,' to 'Let's solve disease.'"
>
> **Joyce Tung,**
> 23andMe's director of research

says Genentech's Behrens, who is heading an effort to sequence the genomes of 3000 Parkinson's patients in the 23andMe database. He says the company decided to ramp up its sequencing projects when the cost dipped to about $1600 last year.

23andMe has preserved many other saliva samples, with the customers' permission, and they are ripe for fuller sequencing. But $1600 is still astronomical in the context of 23andMe's model of $99 genotyping for the masses. "Some people ask me, 'Wouldn't it be much better if you just did sequences?'" Scheller says. "That would be $2 billion, and most of that sequence would be completely uninteresting to us." Instead, he intends to use SNPs to identify interesting regions of the genome, and then use sequencing to zoom in on those regions in certain patients. (Wojcicki says the company will eventually integrate sequencing into the personal analysis it provides to consumers.)

The bigger hurdle facing 23andMe is the one confronting any group with ambitions of genome-based drug development, Cookson says: the challenge of moving from a DNA region suspected of having a disease connection to a druggable target. "Can they get smart enough to really make contributions to the next stage? … I don't know," he says, "But not that many people have really done that, so it would be churlish of me to say, 'Oh, those guys will never do it.' I haven't done it either."

FOR ALL THE BUZZ around 23andMe's new foray into therapeutics, much of Wojcicki's energy is focused on a more immediate business goal: relaunching its consumer health service. That service was shut down after FDA warned that the company hadn't demonstrated that its health-related tests were properly validated, or responsibly communicated to customers, who might be confused or alarmed by the estimates of disease risk.

Wojcicki says the run-in with the agency arose from a poor understanding of government regulation and what was expected. 23andMe is now working with FDA to bring its health reports for customers back by the end of the year. In February, the agency approved 23andMe's test for whether a person carries a recessive mutation that could give offspring Bloom syndrome, a rare disease that affects the stability of DNA structure and elevates the risk of cancer. FDA also exempted other such carrier tests from its premarket review process, meaning the company won't have to seek approval before providing those results to customers. But it's not clear whether or when 23andMe will resume providing other kinds of health information, such as drug responses and disease risks. "There's going to be a path forward," Wojcicki says, but "we might have to make certain kinds of compromises."

Meanwhile, the company is quick to dismiss the idea that it's shifting focus away from spit kits—and the customers whose willingness to expound on their experiences with cilantro and cancer built the drug discovery platform in the first place. "We make a consumer product," Tung says. Part of her responsibility, she says, is to figure out "what is the next coolest thing that we can provide back to our customers?"

In that light, there's a certain "inevitable logic" in a consumer genetics company turning to drug discovery, says Michael Eisen, a biologist at the University of California, Berkeley, and a member of 23andMe's scientific advisory board. "If there's really a long-term future in this, if it's anything more than just a curiosity for people, we've got to be able to use people's genetic information to provide them with actual treatment." ∎

REVIEW

The origins, determinants, and consequences of human mutations

Jay Shendure and Joshua M. Akey

Germline mutations are the principal cause of heritable disease and the ultimate source of evolutionary change. Similarly, somatic mutations are the primary cause of cancer and may contribute to the burden of human disease more broadly than previously appreciated. Here, we review recent insights into the rates, spectrum, and determinants of genomic mutations and how these parameters inform our understanding of both Mendelian and complex human diseases. We also consider models for conceptualizing mutational consequences and outline several key areas for future research, including the development of new technologies to access and quantify the full spectrum of mutations, as well as to better interpret the consequences of mutations with respect to molecular functionality, evolutionary fitness, and disease pathogenicity.

D espite the exquisite molecular mechanisms that have evolved to replicate and repair DNA with high fidelity, mutations happen. Each human is estimated to carry on average ~60 de novo point mutations (with considerable variability among individuals) that arose in the germline of their parents (*1–4*). Consequently, across all seven billion humans, about 10^{11} germline mutations—well in excess of the number of nucleotides in the human genome—occurred in just the last generation (*5*). Furthermore, the number of somatic mutations that arise during development and throughout the lifetime of each individual human is potentially staggering, with proliferative tissues such as the intestinal epithelium expected to harbor a mutation at nearly every genomic site in at least one cell by the time an individual reaches the age of 60 (*6*).

Advances in DNA sequencing (*7*) have enabled the identification of human germline and somatic mutations at a genome-wide scale. These studies have confirmed, refined, and extended our understanding on the origins, mechanistic basis, and empirical characteristics of human mutations, including both replicative and nonreplicative errors (*8*), heterogeneity in the rates and spectrum of mutations within and between the genomes of individuals (*1–3, 9–11*), the influence of sex and parental age on mutation rates (*2, 4, 12*), and the similarities and differences between patterns and characteristics of germline and somatic mutations (*13–15*). Yet, gaps in interpreting the functional, phenotypic, and fitness effects of mutations remain. These gaps must be filled if we are to effectively identify de novo disease-causing mutations (*16*), distinguish between causal and noncausal mutations in cancer (*13*), and interpret the genetic architecture of human diseases (*17*).

The germline human mutation rate
A number of distinct approaches have been used to estimate the germline mutation rate of base

substitutions (Fig. 1), which we focus on here unless otherwise noted. Historically (*18*), and even more recently (*6*), estimates of mutation rates have been derived from the incidence of highly penetrant Mendelian diseases. The largest such study aggregated data across ~60 loci, estimating an average germline mutation rate of 1.28×10^{-8} per base pair (bp) per generation (*6*). However, disease-based estimates make a number of assumptions, and because inferences are confined to a small number of loci, they may not be representative of mutation rates at large. Phylogenetic methods have also been used to estimate mutation rates at putatively neutral loci on the basis of the amount of sequence divergence between humans and nonhuman primates, yielding a higher genome-wide average germline mutation rate of 2.2×10^{-8} per bp per generation (*19*). Phylogenetic methods also make assumptions such as the time to most recent common ancestor between humans and nonhuman primates, generation time, and that the loci studied do not have fitness consequences. In addition, phylogenetic estimates may be influenced by evolutionary processes other than mutation and selection, such as biased gene conversion, which influences substitution rates in mammals (*20*).

New sequencing technologies have enabled more direct estimates of mutation rates by identifying de novo mutations in pedigrees (i.e., those observed in a child but not their parents). Whole-genome sequencing studies (*1–3, 9–11*) of pedigrees estimate the germline mutation rate to be ~1.0 × 10^{-8} per bp per generation [extensively reviewed in (*8*)], which is less than half that of phylogenetic methods but in better agreement with disease-based estimates. An important caveat to pedigree-based sequencing is that heavy data filtering is necessary and analysis choices may influence both false-positive and false-negative rates (*8*). Nonetheless, complementary approaches for estimating mutation rates on the basis of the number of "missing mutations" that would be expected to have occurred in the time between when an archaic hominin individual (such as Neanderthal) died and the present (*21*) and the accumulation of

heterozygous variants within autozygous regions of founder populations (*1*) are broadly consistent with pedigree-based approaches (~1.1 and 1.2 × 10^{-8} per bp per generation, respectively).

Although a twofold range for the estimated germline mutation rate might appear inconsequential, it has important implications for our understanding of human evolution and disease (e.g., influencing estimates of effective population sizes as well as the inferred timing of when modern humans separated from other archaic hominin groups, when modern humans dispersed out of Africa, and the time of divergence between modern human populations more generally) (*22*). Moreover, there is accumulating evidence that de novo mutations and rare variants in coding sequences contribute not only to rare Mendelian diseases (*16*) but also to common but genetically heterogeneous diseases such as neurodevelopmental disorders (*23*) and early-onset breast cancer (*24*). The observation that de novo mutations and rare variants play a major role in some common diseases suggests that these phenotypes have a large mutational target size (*16*), such that mutations of large effect that occur in any one of many distinct genes can influence disease risk (*25*). Thus, an accurate estimate of the germline mutation rate is also critical for interpreting the patterns, prevalence, and architecture of human disease (*26*).

The estimates discussed above are specifically for the germline mutation rate of single-nucleotide substitutions. There have also been some attempts to estimate the de novo mutation rate for small insertions and deletions (indels) as well as copy number variants (CNVs). For example, whole-genome sequencing in families estimated a rate of 2.94 small indels (1 to 20 bp) and 0.16 structural variants (>20 bp) per generation (*27*). Of note, structural mutations affect many more nucleotides of the genome, on average, than substitutions. It is important to recognize that whole-genome sequencing with short reads has likely underascertained structural events, particularly insertions or deletions of modest size (*28*). More refined estimates of the germline mutation rate for structural variants will likely emerge as sequencing technologies continue to improve. De novo structural events can lead both to well-defined Mendelian syndromes (*29*) and to the same neurodevelopmental diseases that de novo point mutations contribute to [reviewed in (*16*)]. Indeed, family-based discovery of such de novo CNVs helped to motivate investigations of the role of de novo point mutations in these diseases (*30*).

Germline mutations exhibit remarkable heterogeneity in rates and patterns across the genome at both fine and broad scales (*31*), with sequence composition (*32*) and functional context influencing local mutation rates. The largest effect occurs at CpG dinucleotides, where the mutation rate of cytosine is higher by a factor of ~10 than other dinucleotides, consequent to spontaneous deamination of methylated cytosine to thymine. The higher CpG content of coding sequences, along with other differences in sequence composition, may contribute to the higher germline mutation

Department of Genome Sciences, University of Washington, Seattle, WA 98195, USA.
E-mail: shendure@uw.edu (J.S.); akeyj@uw.edu (J.M.A.)

Fig. 1. Approaches to infer the human germline mutation rate. (**Top**) Methods based on the prevalence of individuals with highly penetrant Mendelian disease (denoted as filled circles and squares), identification of de novo mutations in pedigrees (mutations found in offspring but not their parents), and by finding mutations that arise in autozygous regions in pedigrees from founder populations (mutations that appear as heterozygous sites in regions of long stretches of homozygosity). (**Bottom**) Comparative genomics approaches include phylogenetic estimates (based on the number of mutations that have occurred between human and nonhuman primates) and by inferring how many mutations are missing in an archaic hominin sequence (how many mutations would have accumulated if the archaic group did not go extinct). In all panels, red lines indicate mutations.

rate observed in the exome than the genome in pedigree-based studies (~1.5 × 10^{-8} versus ~1.0 × 10^{-8} per bp per generation) (8). Heterogeneity in rates and patterns can also result from non-uniform repair—e.g., transcription-coupled repair of genes expressed in the germline (33). Fluctuations in mutation rates at larger scales, reflected in patterns of single-nucleotide polymorphism density and human-chimpanzee nucleotide divergence, likely relate in part to factors such as chromatin structure (14) and replication timing (2, 15).

Sex and parental age effects

Consequent to sex-specific differences in germ cell biology (34), the majority of germline mutations resulting from errors in DNA replication are inherited from fathers. Furthermore, pedigree-based sequencing has recently yielded quantitative insights into the relationship between paternal age and the rate of de novo point mutations. Specifically, paternal age is estimated to explain 95% of the variation in the number of de novo mutations among offspring; following puberty, an additional ~1 to 2 mutations are observed per paternal year (4); the proportion of de novo mutations in genic regions increases by 0.26% per paternal year, such that offspring born to 40-year-old fathers carry

twice as many genic mutations compared with children of 20-year-old fathers (~19.1 versus ~9.6, respectively) (2). These results are qualitatively similar to exome sequencing studies of sporadic autism cases, which found that de novo point mutations showed a 4:1 parental bias (12). Maternal age effects are generally not seen for point mutations but instead are well documented for chromosomal nondisjunction errors (35). Beyond point mutations, rates of nonrecurrent de novo CNVs also show a strong paternal bias and age effect (36), implicating replication-based mechanisms of CNV formation such as fork stalling and template switching (37). More broadly, differences in mutational rates, spectrum, and age effects in males and females reflect the underlying mechanisms by which various classes of mutations originate.

Somatic mutations and disease

From zygote to adult, a human undergoes trillions of cell divisions, with somatic mutations accumulating at each division. Tissues such as epithelial cells divide throughout life, and even terminally differentiated tissues continue to acquire somatic mutations through nonreplicative processes. It has been estimated that mutation rates in somatic cells are 4 to 25 times as high as in germline cells (6), and the acquisition of somatic mutations is in-

timately related to cancer. Because mutations need only be compatible with the life of a cell, rather than that of the full organism, the spectrum of mutations observed in cancer is much more diverse than typically observed in germline mutations (e.g., aneuploidy, chromothripsis, etc.). Furthermore, each individual cancer exhibits a characteristic burden and spectrum of mutation, although commonalities are present within cancer types (13, 38).

Variation in fine-scale somatic mutation patterns reflect the contributions of environmental mutagens and/or intrinsic dysfunction in DNA replication or repair (39). At broader scales, variation in mutation rates across cancer types correlate with histone marks defining repressive versus open chromatin, replication timing, and transcription-coupled repair (13, 14). It remains unclear whether mutational spectra inherently contribute to specific types of cancer, but understanding these patterns has nonetheless been key for the identification of genes that are significantly mutated over cancer-specific background levels (13).
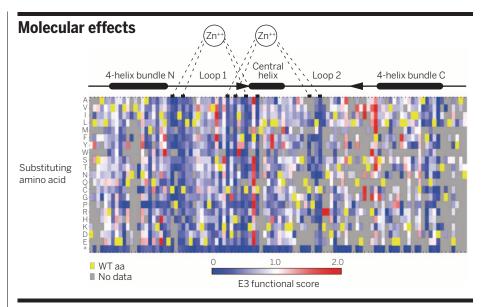
It is increasingly recognized that somatic mutations underlie a much broader spectrum of human disease beyond cancer. For example, somatic mutations occurring early in development underlie a surprising fraction (6 to 20%) of studied

Mendelian disorders (*40*). Some single-gene disorders are exclusively caused by somatic mutations (*41*), presumably because germline mutations are lethal during embryonic development. Somatic mutations affecting gonadal tissues in an unaffected parent can result in multiple children with the same de novo mutation (germline mosaicism). Finally, somatic mutations also may result in reversion of constitutional disease in subsets of cells (*42*). Overall, it is likely that the role of somatic mutation in diseases other than cancer is greater than documented (*43*).

Conceptual models of mutational effects

Although the rates of germline and somatic mutations are coming into focus, interpreting their consequences remains challenging. A straightforward way to conceptualize the consequences of mutations is as having a distribution of effects. For example, in population genetics, the distribution of fitness effects (DFE) of new mutations is a well-established concept. Although estimating or measuring the DFE is challenging (discussed below), it is clear that the DFE is a complex distribution that differs between organisms as well as across genomes (*44*). Deleterious mutations have a distribution-of-fitness effects that is likely multimodal and varies by functional class, e.g., protein coding versus noncoding (*44, 45*). Evolutionarily advantageous mutations are rare, and the distribution of their fitness effect sizes remains largely unexplored.

In considering the consequences of new mutations, we can distinguish between the concepts of fitness, pathogenicity, and molecular function (Fig. 2). All of these relate to "function" but in different ways. Fitness is a continuous property that can be defined in terms of the reproductive success of genotypes carrying the mutant allele relative to genotypes carrying the wild-type allele. Fitness effects and their distribution (i.e., the DFE) are relevant over a wide range of time scales. For example, new mutations with extremely large deleterious fitness effects may fail to transmit for even a single generation, whereas weakly deleterious mutations will exhibit allele frequency trajectories that vary over many generations as a function of population history and chance.

Pathogenicity refers to the propensity of a mutation to cause clinically manifest disease within a single individual. Historically, pathogenic mutations have been defined for Mendelian diseases, in discrete terms wherein a given mutation is classified as either disease-causing or not. However, it may be more useful to think of pathogenicity as a continuous property by which mutations or variants confer risk for a particular disease or diseases, perhaps quantified by an odds ratio. Analogous to the DFE, we can conceptualize a distribution of pathogenic effects for new mutations, in relation to a specific disease or to disease in the broader sense [referred to below as a distribution of pathogenic effects (DPE)]. At one extreme are Mendelian disease-causing variants with extremely high odds ratios (although it is worth noting that
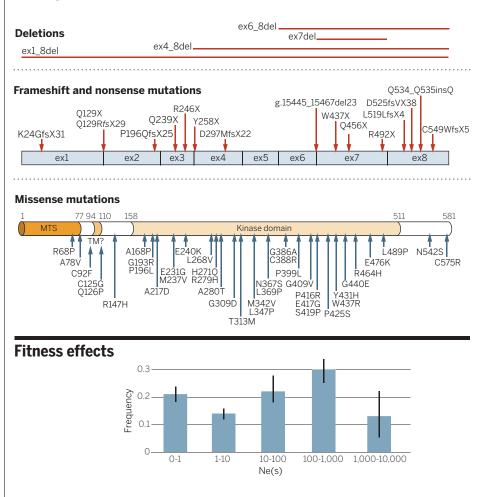
Fig. 2. Conceptual models for mutational effects. (**Top**) Molecular effects of mutation on protein structure and function, illustrated by deep mutational scanning of the RING domain of BRCA1. Figure reproduced from (*51*) with permission. (**Middle**) Pathogenic effects, illustrated by a recessive form of Parkinson's disease caused by mutations in the Parkin protein. Figure reproduced from (*60*) with permission. (**Bottom**) Fitness effects, illustrated by a histogram of inferred values for $N_e * s$, the product of effective population size (N_e), and the strength of selection (s). [Figure reproduced from (*44*) with permission]

because Mendelian disease-causing mutations typically are only ascertained in diseased individuals, we often lack formal measurements of their penetrance). In contrast, the vast majority of variants or haplotypes implicated by genome-wide association studies (GWAS) have very small odds ratios and may be neither necessary nor sufficient to cause disease.

Finally, mutations have evolutionary (e.g., fitness) or organismal (e.g., pathogenic) consequences by virtue of disruptive effects that they have at the molecular level. The molecular consequences of a given mutation—whether in a protein-coding or regulatory sequence—are of course highly dependent on the function of the sequence in which it resides and, moreover, likely to be highly context dependent (i.e., relevant in only certain cell types and developmental stages). Nonetheless, all of these contingencies can be conceptualized within a distribution of molecular effects (DME) for mutations in particular sequences or across the genome.

The DFE, DPE, and DME for a given sequence are undoubtedly correlated. For instance, variants with large molecular effects are more likely to be deleterious and/or pathogenic, and pathogenicity can be predicted on the basis of deleteriousness (46). However, the relationship between these distributions is not straightforward. For example, a variant might have no measurable contribution to disease status but might nonetheless affect reproductive fitness over short or long time scales. A highly penetrant mutation for disease that affects later life may not affect reproductive fitness. A variant might have a large molecular effect, but this might have only environmentally dependent consequences. At present, there is no single measure of mutational effects that is useful in all circumstances, and the choice of what type of mutational effect makes the most sense to measure or predict depends heavily on one's goals.

The DFE has been estimated experimentally by mutation accumulation or mutagenesis, followed by fitness measurements. These approaches are limited to model organisms, often rely on mutagens, and generally only identify mutations with large fitness effects. An alternative approach is to compare genomes for patterns of fixed or standing variation (47). The DFE clearly differs for coding and regulatory sequences in the human genome, and although a higher proportion of coding mutations have large known fitness effects, the absolute amount of noncoding sequence under purifying selection is greater than that of coding sequence [although precisely how much greater is debated (48)].

In principle, the DPE can be measured by examining the odds ratios for individual mutations in a gene associated with a particular disease. However, in practice, this is challenging. First, mutations are usually ascertained on the basis of phenotype, such that we lack quantification of how often pathogenic mutations occur in disease-free individuals. Second, although in principle every mutation that is compatible with life occurs in several hundred present-day humans (5), we lack whole genomes for billions of humans such that most mutations are—and will, for the near future, remain—unobserved. Finally, we can only quantify odds ratios for those variants in GWAS that have risen to high allele frequencies. For rare alleles or new mutations, even sequencing every human on the planet might be insufficient to detect low or modest effect sizes.

In contrast to the DFE and DPE, distributions of molecular effects for particular sequences of interest are amenable to empirical measurement. For example, saturation mutagenesis studies characterized the distribution of effects on transcriptional activation (for cis-regulatory elements) or on enzymatic or signaling activities (for protein-coding sequences) for a diversity of sequences. The modern equivalents of these methods, termed massively parallel reporter assays and deep mutational scans, enable multiplex mutagenesis and functional characterization of thousands of mutations (e.g., all possible point mutations or amino acid swaps in a sequence of interest) (49, 50). Of course, how the DME informs the DFE and DPE for any given sequence of interest will remain unknown. However, provided that the experimental assay used to test the sequence of interest is appropriate for the physiologically relevant function of a sequence, it may be reasonable to infer the DFE or DPE from the DME. For example, one could define subsets of mutations in a gene of interest with similar molecular effects and treat these as a group for estimating the odds ratio with which such mutations confer disease risk (51).

The interplay of mutation rates, mutation effects, and human disease

Any given disease has its own set of potential mutations that contribute to risk, with a particular distribution with respect to both the odds of occurring as well as odds of causing disease. For most Mendelian diseases, the mutational target consists primarily of protein-altering mutations in a specific gene. For genetically heterogeneous disorders, there may be as many as hundreds of target genes. However, this picture is even more complex if one considers that there likely exists a broader range of mutations that much more modestly affect expressivity and severity. However, such modifiers remain largely undiscoverable at present because we lack the sample sizes to robustly identify them.

Mendelian diseases are typically early onset and severe, such that the consequences of mutations underlying them with respect to pathogenicity and deleteriousness are tightly linked. Genetically complex, common disorders with more variable and often much later onset, such as type 2 diabetes and cardiovascular disease, may have substantially different genetic architectures, perhaps reflected in the fact that de novo mutations and rare variants of large effect have not, at least to date, been shown to be major contributors to the burden of these diseases. Instead, although enriched within coding sequences, the majority of the GWAS signal appears to lie within regulatory sequences defined by deoxyribonuclease I hypersensitivity (52). However, variants implicated in common disease tend to have very modest effects with respect to pathogenicity. Moreover, many variants underlying GWAS are unlikely to have been strongly deleterious, allowing allele frequencies to rise within the population and be detected through association studies.

To illustrate the diversity of relationships between patterns of mutation and disease, we consider three examples. First, the mutational spectrum of disease caused by nonsynonymous mutations is highly heterogeneous, with changes at arginine and glycine residues accounting for ~30% of such mutations (Fig. 3A) (26, 53). This is largely due to the higher mutation rates at arginine and glycine codons, most of which begin with a CpG dinucleotide. CpG mutations at arginine codons result in amino acid changes that may be particularly disrupting to protein structure. Thus, the intrinsic mutability of particular codons combined with their biochemical effects can shape the mutational spectrum of disease-causing nonsynonymous mutations.

Second, as discussed above, there is a substantial increase in mutation rate as a function of paternal age. Whole-genome sequencing of ~250 parent-child trios identifying >11,000 de novo mutations showed that replication timing bias in de novo mutations was present in younger, but not older, fathers (2) (Fig. 3B). Because early replicating regions of the genome are associated with higher levels of gene density and transcriptional activity, this bias reduces the proportion of de novo mutations in coding regions. In older fathers, in addition to the overall increased rate of mutations, the mitigation or absence of this bias results in an increased proportion of mutations in genic regions (Fig. 3B).

Finally, it has been noted that certain somatic mutations in cancer appear more likely to occur on specific germline haplotypes. Replication timing quantitative trait loci (rtQTLs) have been identified that influence variation in replication timing between individuals. One such rtQTL influences replication timing of JAK2 (Fig. 3C), a gene in which haplotype-dependent variation in mutation likelihood had previously been noted (54, 55). Thus, this germline variant locally influences replication timing, which in turn may affect the rate of somatic mutations in a gene that underlies specific types of cancer.

Future challenges

The recent progress in cataloging and characterizing human mutations has raised myriad new questions, challenges, and opportunities. Studies of de novo mutations highlight the large gaps in knowledge that remain about the basic biological mechanisms that shape the mutational spectrum. Empirical patterns of mutations requiring more study include clustering of mutations (2), context-dependent effects (32), and recurrent mutation (56), among others. The drive to understand the underlying mechanisms and selective forces behind these phenomena should stimulate
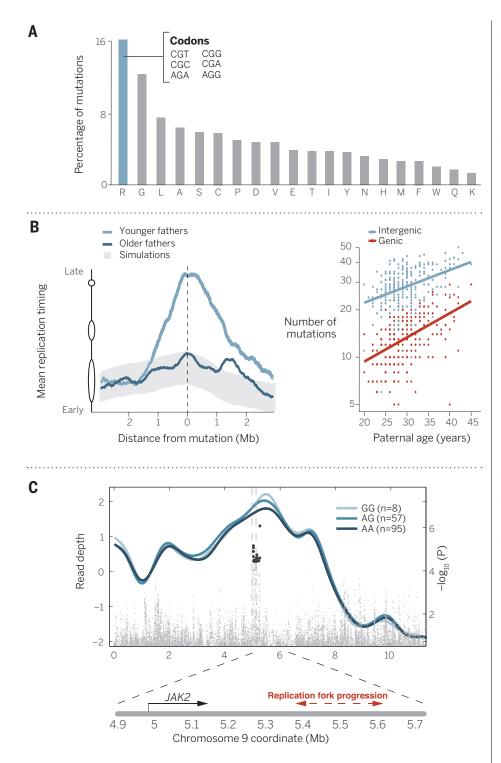
Fig. 3. Relationship between patterns of mutation and disease. (**A**) The frequency of mutations that occur at each amino acid among a panel of ~4000 putative disease-causing nonsynonymous mutations [data from (*53*)]. The high percentage of mutations at arginine (R) residues is due, in part, to its CpG-rich codons. (**B**) Mean replication timing as a function of distance from de novo mutations shows that mutations in children of younger fathers (<28 years old) are biased toward late-replicating DNA sequences (left). No significant replication timing bias is observed in the children of older fathers. The replication timing bias difference results in the accumulation of mutations in protein-coding regions at a higher rate in older compared with younger fathers (right). Figure reproduced with permission from (*2*). (**C**) Identification of a replication timing QTL (higher read depth is correlated with earlier replicating sequences) in the *JAK2* gene, which may influence rates of somatic mutation. Note the significant difference in mean replication timing as a function of genotype as measured in 160 individuals. [Figure reproduced with permission from (*54*)]

experimental studies providing a more comprehensive understanding into how and how often mutations occur.

We are also on the precipice of major opportunities, driven in large part by ongoing advances with respect to the quality and cost of DNA sequencing. We anticipate that the number of de novo germline mutations ascertained by whole-genome sequencing will exponentially grow in the next few years, identifying hundreds of thousands or millions of de novo mutations of all types across studies. Additionally, the ability to accurately sequence whole genomes from single cells, directly or expanded ex vivo (*57*), will further our understanding of rates and patterns of somatic mutation. The increasing depth of mutational catalogs—which we predict may approach saturation of the ~10^{10} possible substitution mutations to the human genome, will further our understanding not only of mutational processes but also of their consequences with respect to molecular function, deleteriousness, and pathogenicity.

It is also of considerable interest to better delimit the extent of heritable variation in germline and somatic mutation rates among individuals and how such heritable variation contributes to disease burden, and to integrate individualized mutation rate estimates into inferences of lifetime risk for particular diseases. Heritable variation of mutation rates seems plausible given the fact that genetic variation occurs in genes encoding components of DNA repair pathways, influences susceptibility to cancers (*58*), and is apparent from studies of de novo mutations (*10*). For example, there is evidence that European populations have a 50% higher germline mutation rate of TCC → TTC transitions (*59*), the most common somatic mutation found in melanoma cancers. Although it is not clear if this observation is related to ultraviolet exposure, the results are striking and suggest that mutation rates may evolve over much shorter time scales than previously thought, influencing individual and population-specific disease risks.

Last, we anticipate that massively parallel experimental approaches, including some based on genome editing, will facilitate measurements of the DME and DFE for diverse sequences, both protein-coding and regulatory. Although of great interest in their own right, such dense empirical catalogs will also inform the DPE for the same sequences, ideally enabling a solution to the long-standing challenge of variants of uncertain significance in clinical genetics.

The study of human mutations has entered an exciting new era. Although considerable technological, computational, and conceptual challenges remain, the ensuing discoveries will have profound implications for interpreting human evolutionary history, patterns and prevalence of human disease, and the mechanisms underlying one of life's most fundamental biological processes.

REFERENCES AND NOTES

1. C. D. Campbell *et al.*, *Nat. Genet.* **44**, 1277–1281 (2012).
2. L. C. Francioli *et al.*, *Nat. Genet.* **47**, 822–826 (2015).
3. J. C. Roach *et al.*, *Science* **328**, 636–639 (2010).

4. A. Kong *et al.*, *Nature* **488**, 471–475 (2012).
5. W. Fu, J. M. Akey, *Annu. Rev. Genomics Hum. Genet.* **14**, 467–489 (2013).
6. M. Lynch, *Proc. Natl. Acad. Sci. U.S.A.* **107**, 961–968 (2010).
7. J. Shendure, H. Ji, *Nat. Biotechnol.* **26**, 1135–1145 (2008).
8. L. Ségurel, M. J. Wyman, M. Przeworski, *Annu. Rev. Genomics Hum. Genet.* **15**, 47–70 (2014).
9. Y. H. Jiang *et al.*, *Am. J. Hum. Genet.* **93**, 249–263 (2013).
10. D. F. Conrad *et al.*, *Nat. Genet.* **43**, 712–714 (2011).
11. J. J. Michaelson *et al.*, *Cell* **151**, 1431–1442 (2012).
12. B. J. O'Roak *et al.*, *Nature* **485**, 246–250 (2012).
13. M. S. Lawrence *et al.*, *Nature* **499**, 214–218 (2013).
14. B. Schuster-Böckler, B. Lehner, *Nature* **488**, 504–507 (2012).
15. J. A. Stamatoyannopoulos *et al.*, *Nat. Genet.* **41**, 393–395 (2009).
16. J. A. Veltman, H. G. Brunner, *Nat. Rev. Genet.* **13**, 565–575 (2012).
17. J. K. Pritchard, N. J. Cox, *Hum. Mol. Genet.* **11**, 2417–2423 (2002).
18. J. B. Haldane, *J. Genet.* **83**, 235–244 (2004).
19. Chimpanzee Sequencing and Analysis Consortium, *Nature* **437**, 69–87 (2005).
20. L. Duret, P. F. Arndt, *PLOS Genet.* **4**, e1000071 (2008).
21. Q. Fu *et al.*, *Nature* **514**, 445–449 (2014).
22. A. Scally, R. Durbin, *Nat. Rev. Genet.* **13**, 745–753 (2012).
23. D. H. Geschwind, J. Flint, *Science* **349**, 1489–1494 (2015).
24. T. Walsh *et al.*, *Proc. Natl. Acad. Sci. U.S.A.* **107**, 12629–12633 (2010).
25. J. McClellan, M. C. King, *Cell* **141**, 210–217 (2010).
26. D. N. Cooper, M. Krawczak, *Hum. Genet.* **85**, 55–74 (1990).
27. W. P. Kloosterman *et al.*, *Genome Res.* **25**, 792–801 (2015).
28. M. J. Chaisson *et al.*, *Nature* **517**, 608–611 (2015).
29. J. R. Lupski, *Nat. Genet.* **39** (suppl.), S43–S47 (2007).
30. J. Sebat *et al.*, *Science* **316**, 445–449 (2007).
31. A. Hodgkinson, A. Eyre-Walker, *Nat. Rev. Genet.* **12**, 756–766 (2011).
32. D. G. Hwang, P. Green, *Proc. Natl. Acad. Sci. U.S.A.* **101**, 13994–14001 (2004).
33. P. Green, B. Ewing, W. Miller, P. J. Thomas, E. D. Green, *Nat. Genet.* **33**, 514–517 (2003).
34. J. F. Crow, *Nat. Rev. Genet.* **1**, 40–47 (2000).
35. S. L. Sherman *et al.*, *Hum. Mol. Genet.* **3**, 1529–1535 (1994).
36. J. Y. Hehir-Kwa *et al.*, *J. Med. Genet.* **48**, 776–778 (2011).
37. J. A. Lee, C. M. Carvalho, J. R. Lupski, *Cell* **131**, 1235–1247 (2007).
38. L. B. Alexandrov *et al.*, *Nature* **500**, 415–421 (2013).
39. I. Martincorena, P. J. Campbell, *Science* **349**, 1483–1489 (2015).
40. R. P. Erickson, *Mutat. Res.* **705**, 96–106 (2010).
41. M. J. Lindhurst *et al.*, *N. Engl. J. Med.* **365**, 611–619 (2011).
42. R. Hirschhorn, *J. Med. Genet.* **40**, 721–728 (2003).
43. A. Poduri, G. D. Evrony, X. Cai, C. A. Walsh, *Science* **341**, 1237758 (2013).
44. A. Eyre-Walker, P. D. Keightley, *Nat. Rev. Genet.* **8**, 610–618 (2007).
45. M. Soskine, D. S. Tawfik, *Nat. Rev. Genet.* **11**, 572–582 (2010).
46. M. Kircher *et al.*, *Nat. Genet.* **46**, 310–315 (2014).
47. F. Racimo, J. G. Schraiber, *PLOS Genet.* **10**, e1004697 (2014).
48. P. Green, B. Ewing, *Science* **340**, 682 (2013).
49. D. M. Fowler, S. Fields, *Nat. Methods* **11**, 801–807 (2014).
50. R. P. Patwardhan *et al.*, *Nat. Biotechnol.* **27**, 1173–1175 (2009).
51. L. M. Starita *et al.*, *Genetics* **200**, 413–422 (2015).
52. A. Gusev *et al.*, *Am. J. Hum. Genet.* **95**, 535–552 (2014).
53. D. Vitkup, C. Sander, G. M. Church, *Genome Biol.* **4**, R72 (2003).
54. A. Koren *et al.*, *Cell* **159**, 1015–1026 (2014).
55. P. J. Campbell, *Nat. Genet.* **41**, 385–386 (2009).
56. A. Hodgkinson, E. Ladoukakis, A. Eyre-Walker, *PLOS Biol.* **7**, e1000027 (2009).
57. S. Behjati *et al.*, *Nature* **513**, 422–425 (2014).
58. F. Altieri, C. Grillo, M. Maceroni, S. Chichiarelli, *Antioxid. Redox Signal.* **10**, 891–938 (2008).
59. K. Harris, *Proc. Natl. Acad. Sci. U.S.A.* **112**, 3439–3444 (2015).
60. O. Corti, S. Lesage, A. Brice, *Physiol. Rev.* **91**, 1161–1218 (2011).

REVIEW

Somatic mutation in cancer and normal cells

Iñigo Martincorena[1] and Peter J. Campbell[1,2]*

Spontaneously occurring mutations accumulate in somatic cells throughout a person's lifetime. The majority of these mutations do not have a noticeable effect, but some can alter key cellular functions. Early somatic mutations can cause developmental disorders, whereas the progressive accumulation of mutations throughout life can lead to cancer and contribute to aging. Genome sequencing has revolutionized our understanding of somatic mutation in cancer, providing a detailed view of the mutational processes and genes that drive cancer. Yet, fundamental gaps remain in our knowledge of how normal cells evolve into cancer cells. We briefly summarize a number of the lessons learned over 5 years of cancer genome sequencing and discuss their implications for our understanding of cancer progression and aging.

Although most of the somatic mutations that steadily accumulate in our cells are harmless, occasionally a mutation affects a gene or regulatory element and leads to a phenotypic consequence. A fraction of these mutations can confer a selective advantage to the cell, leading to preferential growth or survival of a clone. We use the term "driver mutation" to denote mutations under positive selection within a population of cells, and we use "passenger mutation" for variants that have either no phenotypic consequences or biological effects that are not selectively advantageous to the clone (*1*). One end product of somatic cell evolution is cancer, a disease in which an autonomous clone of cells escapes from both the in-built programs of normal somatic cell behavior and the exogenous restraints on cell proliferation.

A very brief history of somatic mutation and cancer

Cancer results from the clonal expansion of a single abnormal cell. In 1914, the observation of chromosomal abnormalities in cancer cells was one of the first links between mutation and cancer (*1*). The causal role of somatic mutations in cancer was later supported by the discovery that many carcinogenic chemicals are also mutagenic (*2*). Conclusive evidence came from studies showing that the introduction of DNA fragments from cancer cells into normal cells led to malignant transformation and also from the identification of the responsible mutations in the transforming DNA (*1*). This work led to the discovery of the first oncogenes, whose mutation can bring about a gain of function that drives transformation into cancer. In parallel, studies on hereditary cancers led to the discovery of tumor suppressor genes (*3*), which are typically inactivated by mutations, either germline or somatic.

As the link between somatic mutation and cancer was established, cancer was described as an example of Darwinian evolution, in which cells acquire the hallmarks of cancer through somatic mutation and selection (*4, 5*). This remains a widely accepted framework for understanding the progression of cancer, but we still lack quantitative information about the role of different factors in the evolution of normal cells into cancer cells.

In the past decade, high-throughput DNA sequencing has enabled the systematic sequencing of more than 10,000 cancer exomes and 2500 whole cancer genomes. This has revolutionized our understanding of the genetics of cancer, leading to the discovery of previously unrecognized cancer genes, new mutational signatures, and fresh insights into cancer evolution.

Mutational processes in cancer

Mutations arise from replication errors or from DNA damage that is either repaired incorrectly or left unrepaired. DNA damage can be caused by exogenous factors, including chemicals, ultraviolet (UV) light, and ionizing radiation; by endogenous factors, such as reactive oxygen species, aldehydes, or mitotic errors; or by enzymes involved in DNA repair or genome editing, among others (*6*). Additionally, viruses and endogenous retrotransposons can cause insertions of DNA sequence.

The rates of different mutational processes vary among tumors and cancer types (Fig. 1A). Though numbers vary widely, most cancers carry 1000 to 20,000 somatic point mutations and a few to hundreds of insertions, deletions, and rearrangements (*7–10*). Pediatric brain tumors and leukemias typically have the lowest numbers of mutations, whereas tumors induced by exposure to mutagens, such as lung cancers (tobacco) or skin cancers (UV rays), present the highest rates (*8–10*). Although these are common figures, some cancers acquire dramatically increased mutation rates due to the loss of repair pathways or chromosome integrity checkpoints (*6, 8*). Depending on which process is affected, this can manifest as a very high rate of point mutations, microsatellite instability, or chromosome instability.

[1]Wellcome Trust Sanger Institute, Hinxton CB10 1SA, Cambridgeshire, UK. [2]Department of Haematology, University of Cambridge, Cambridge, UK.
*Corresponding author. E-mail: pc8@sanger.ac.uk
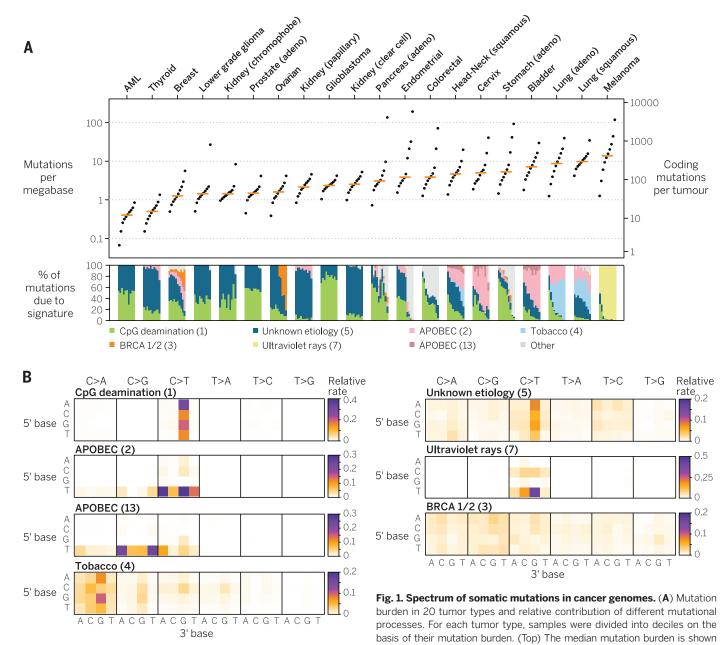
Thus, both exogenous and endogenous mutational processes contribute to different cancers to various extents. Although in some tissues the mutations and incidence of cancer are dominated by exposure to external mutagens (*8*), intrinsic factors—such as the number of cell divisions in a tissue—seemingly dominate other cancer types (*8*, *11*) (Fig. 1A).

Signatures of mutational processes in cancer genomes

Different mutational processes leave idiosyncratic patterns of mutations, termed "mutational signatures." These patterns allow us to identify known and novel mutational processes and quantify their action on a cancer genome (*8*). Features that can characterize the action of a given mutational process are: (i) the type of mutations observed, (ii) local sequence context, (iii) distribution across the genome, (iv) evidence of repair, and (v) timing during cancer evolution.

Often, a mutational process will cause only one type of somatic mutation; for example, the carcinogen aristolochic acid causes A>T base substitutions almost exclusively (*12*). In contrast, the loss of the homologous recombination genes *BRCA1* or *BRCA2* in breast, ovarian, and pancreatic cancers is associated with a distinctive pattern of base substitutions, medium-sized indels, and larger chromosomal duplications and deletions (*13*).

Mutations are often enriched in specific local sequence contexts. For example, UV light induces pyrimidine dimers, whose erroneous repair leads to C>T mutations at CpC or TpC dinucleotides (Fig. 1B). For mutations induced by enzymatic damage, the local sequence context derives from properties of the enzyme. One of the most widespread mutational signatures in human cancers is due to off-target modification of DNA by the APOBEC family of proteins (*8*, *13*), which

Fig. 1. Spectrum of somatic mutations in cancer genomes. (**A**) Mutation burden in 20 tumor types and relative contribution of different mutational processes. For each tumor type, samples were divided into deciles on the basis of their mutation burden. (Top) The median mutation burden is shown as a dot plot (substitutions and small indels); orange bars denote the median burden of all samples. AML, acute myeloid leukemia. (Bottom) The mean percentage contribution of different mutation signatures is depicted by stacked bars. Data are from The Cancer Genome Atlas (TCGA) (http://cancergenome.nih.gov/) (top) and L. B. Alexandrov [updated from (*8*)] (bottom) and are visualized as in (*8*, *9*). (**B**) Context-dependent mutation spectrum of several mutational signatures found in cancer genomes [COSMIC (Catalogue of Somatic Mutations in Cancer) database (*26*)]. Heat maps show relative rates per trinucleotide.

Fig. 2. Frequency of mutations in recurrently mutated cancer genes across tumor types. This reference table summarizes the percentage of patients carrying a nonsynonymous coding substitution or small indel in each gene. Data are from TCGA and are visualized as in (*60*). Different colors emphasize the frequency of mutations. The list of 198 cancer genes corresponds to all genes in the curated list of 174 mutated genes from the COSMIC database (version 73) (*26*) and any Cancer Gene Census database gene found recurrently mutated in (*59*).

predominantly causes C>T or C>G substitutions at sites preceded by a thymine nucleobase (Fig. 1B).

Some mutation processes show considerable variation in genomic distribution. Rates of point mutations vary along the genome and are typically higher in regions with low expression levels, repressed chromatin, and late replication times (*14, 15*). Such patterns are also observed in human evolution (*16*) and in somatic mutations in normal cells (*17, 18*). Some of this variation may be driven by reduced access of mismatch repair machinery to closed chromatin regions (*19*). In contrast, other mutational processes show enrichment in regions of open chromatin (*20, 21*).

We can occasionally infer the action of repair processes in the distribution of mutations. Transcription-coupled repair leads to a reduction in mutations on the transcribed strand compared with the nontranscribed strand (*14*) and is evident in some sources of exogenous DNA damage, such as UV light or tobacco exposure (*8*). The medium-sized indels associated with *BRCA1/2* deficiency show a signature of repair by microhomology-mediated end-joining, as this pathway repairs double-stranded DNA breaks in the absence of homologous recombination (*13*).

Finally, information about timing of mutational processes can sometimes be inferred from genomics data. Surprisingly, some mutational events occur as one-off catastrophes during cancer evolution. Chromothripsis is characterized by clusters of tens to hundreds of rearrangements that occur as a single event (*22*), which has now been experimentally recreated in vitro in a single cell division (*23*). Other clusters of simultaneous mutations include breakage-fusion-bridge cycles (*24*), chromoplexy (*25*), and clusters of point mutations (kataegis) (*13*). In contrast, other mutational processes seemingly show steady rates of accumulation over time.

By studying the patterns of mutations in cancer genomes, we are beginning to unravel the action of many known and novel mutational processes in cancer. This pursuit also helps us to identify preventable sources of mutations behind certain cancers, such as the role of particular herbal medicines in some bladder cancers in Asia (*12*).

Positive selection on somatic mutations

Of the many thousands of mutations that cancer genomes have, typically only a handful (the driver mutations) have been positively selected. The vast majority are effectively neutral or mildly deleterious mutations that occurred before or soon after a driver mutation and "hitchhiked" as the cell containing the driver clonally expanded (*1*). Across multiple patients, positive selection of driver mutations manifests as a higher rate of mutations in a gene or a region than that expected by neutral mutation accumulation. Since the discovery of the Philadelphia chromosome (*1*), mutation recurrence has proven to be a powerful tool for the identification of new cancer genes. As data sets have grown larger, it has be-
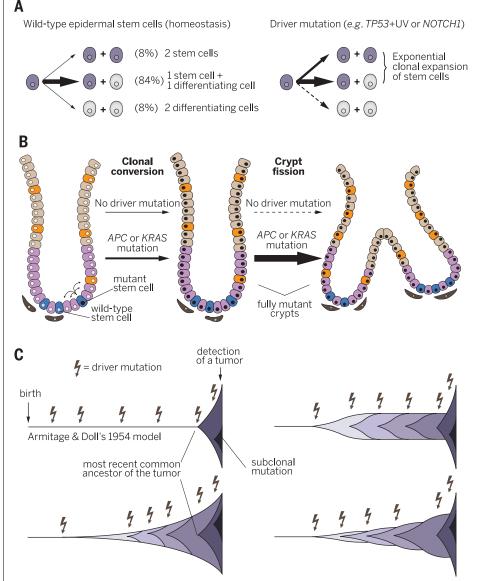
Fig. 3. Selection and clonal expansion of early driver mutations. (**A**) Cell fate model proposed for epithelial stem cells in skin, esophagus, and lung (*45–48*). Probabilities of the three possible outcomes shown here are representative of normal murine epidermis (*46*). (**B**) Schema of two steps in the clonal expansion of a mutation in intestinal epithelium. (**C**) Four different models of successive clonal expansions induced by driver mutations accumulated throughout life. The first example (top left) corresponds to Armitage and Doll's model (*54*), in which only the first five mutations are rate limiting. The dynamics of intermediate clonal expansions are unknown, but they are critical for the correct modeling of age-incidence statistics and for our understanding of cancer evolution.

come increasingly important to develop accurate models of the background mutation rate for discovering more rarely mutated cancer genes, because overly simplistic models yield large numbers of false positives (*9*).

The Cancer Gene Census, a database of genes recurrently mutated in cancer, presently contains 572 genes (*26*). Of these, ~90% are altered by somatic mutation and ~20% by germline mutations that predispose to cancer (familial cancers). Figure 2 summarizes the frequency of somatic mutations (substitutions and indels) in 198 cancer genes across 20 tissues. Only three genes are mutated in more than 10% of patients across the range of

tumor types shown here: *TP53* (36.1%), *PIK3CA* (14.3%), and *BRAF* (10%).

Most large sequencing studies have used exome sequencing, and thus most known driver mutations affect protein-coding regions of the genome. Though an increasing number of studies are employing whole genomes, the yield of driver mutations appears much less dramatic in noncoding regions (*27, 28*). Nonetheless, there are examples of driver mutations affecting regulatory regions, such as mutations in the promoter of the telomerase gene (*TERT*) in up to 71% of melanomas (*29*) and more than half of bladder cancers and glioblastomas (*30*). These mutations

create a new transcription factor–binding motif, leading to overexpression of the *TERT* gene. Structural variation in noncoding regions can also contribute to cancer development. For example, lymphomas frequently overexpress *BCL2* and *BCL6* by translocation of the genes adjacent to the immunoglobulin locus (*31*). More recently, overexpression of cancer genes by juxtaposing them with active enhancers has been described in some cancers (*32, 33*).

Progression of normal cells to cancer

The study of established cancers has provided many clues about the temporal evolution of cancers, but many gaps in our understanding remain. It seems that a clone must acquire a handful of driver mutations to transform into a cancer (*1*); yet, the mutation rate of normal cells is believed to be insufficient to generate enough driver mutations in one cell to explain the incidence of cancer. Two explanations, not mutually exclusive, have been proposed: cells can acquire hypermutation (the "mutator hypothesis") (*34*) and/or early driver mutations trigger clonal expansions, increasing the pool of cells at risk for further driver mutations (*35*). Studies of normal tissues will probably settle this debate by quantifying the mutation rate and the extent of clonal expansions across normal tissues.

Mutation rates and signatures in normal cells

Estimates of the somatic mutation rate in human B and T lymphocytes and in fibroblasts are on the order of 2 to 10 mutations per diploid genome per cell division. Similar rates have been estimated in the retina and the intestinal epithelium (*36*). Thus, the substitution rate per cell division in normal somatic cells may be an order of magnitude higher than in germ cells (*36*). Although estimates of the rate of stem cell divisions in adult tissues are controversial and vary widely (*11*), normal cells of different tissues are predicted to accumulate hundreds to a few thousands of substitutions, not too far from the num-

bers in cancers, without the need for acquired hypermutation. Nonetheless, there is marked heterogeneity in the rates of various mutational signatures across cancers. If these rates and signatures are not mirrored in normal cells, this finding will suggest that acquisition of an increased mutation rate is important in cancer development.

Systematic sequencing studies of normal tissues are needed to clarify this debate. Unfortunately, such studies are still technically challenging, as the error rate of single-cell sequencing remains too high for accurate detection of de novo mutations, and only clonally expanded mutations can be reliably detected with current technologies. Despite these limitations, sequencing studies of normal blood and skin have recently been conducted, revealing burdens and signatures of somatic mutations broadly similar to the cancers from those cell types (*18, 37–40*).

Beyond point mutations, little is known about the rate of rearrangements or large structural variations in normal tissues. Multiple studies have reported structural mutations—including indels (*18*), copy-number aberrations (*18, 41, 42*), retrotransposition (*43*), and even chromothripsis (*44*)—in normal cells from individuals without cancer. Nevertheless, it is often argued that acquired chromosomal instability is restricted to cancer cells (*10*).

Selection and clonal expansions in normal cells

Sequencing studies in normal blood and skin have revealed insights into patterns of clonal expansion associated with driver mutations. In blood, driver mutations can be found in ~10% of individuals older than 65 years of age, showing the typical patterns seen in leukemias (*37–39*). Occasionally, these mutations drive expansions such that most blood cells derive from the mutant clone but still provide the essential biological functions of blood. Individuals carrying these driver mutations have an elevated future risk of blood cancers (*37, 38*), suggesting that these are genuine precancerous clones.

By middle age, sun-exposed skin cells carry thousands of point mutations, and about 25 to 30% of these cells have already acquired at least one driver mutation (*18*). Positive selection is evident in most known driver genes of squamous skin cancer, but clone sizes are relatively limited and similar across individuals, suggesting that the growth of clones with driver mutations slows relatively early in their expansion. The mechanisms constraining the expansion of driver clones are not known but are likely to represent an essential protection against cancer.

Selection in different tissues can act in different ways. These include increasing the relative rate of cell proliferation over differentiation; eluding quiescence, senescence, or cell death; or colonizing nearby areas. Typically, driver mutations must occur in stem or proliferating cells to lead to clonal expansions. For example, stem cells in the epithelia of the skin (*45, 46*), esophagus (*47*), and lung (*48*) have three types of divisions: an asymmetric division into one stem cell and one differentiated cell, or symmetric divisions producing either two stem cells (proliferation) or two differentiated cells (differentiation) (Fig. 3A). Homeostasis is maintained by having identical rates of symmetrical divisions, whereas increasing the ratio of proliferation to differentiation leads to exponential clonal expansions. Driver mutations in *TP53* and *NOTCH1* can cause this imbalance (*45, 47*). Alternatively, in the intestinal epithelium, a stem cell can take over an intestinal crypt, even in the absence of selection, but expansion beyond a crypt is physically constrained. In this tissue, selection seems to manifest as an increase in the ability of stem cells to extend beyond a crypt (*49*). Mutations in the colorectal cancer genes *APC* and *KRAS* induce large increases in the rate of crypt fission, colonizing neighboring areas (*49, 50*) (Fig. 3B).

Precancerous conditions

The terms "precancer" or "precancerous lesion" are often used to refer to areas of a tissue that show certain histological changes associated with an
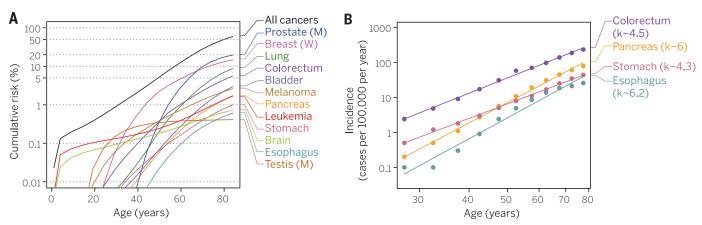
Fig. 4. Age incidence of cancer. (**A**) Cumulative risk of cancer versus age. This plot shows the risk of suffering a given cancer before a particular age. (**B**) Log-log representation of the incidence of different cancers (cases per year per 100,000 people) versus age. The regression lines highlight the approximately geometrical increase of cancer incidence with age, although the association is imperfect and only correlative for some cancer types (*54*). k denotes line slope. U.S. cancer-incidence data are from the SEER (Surveillance, Epidemiology, and End Results Program) Cancer Statistics Review (data are from 2008 to 2012 and include any race and both genders, unless otherwise specified; M, men; W, women).

increased risk of cancer (*51*). Examples of early histological changes known to precede some epithelial cancers are hyperplasia, dysplasia, and metaplasia. These early changes can evolve into carcinoma in situ, where cells present the morphological features of cancer but do not yet invade the underlying tissue. Some examples of precancerous lesions are adenomatous polyps of the colon, Barrett's esophagus, breast ductal carcinoma in situ (DCIS), and cervical intraepithelial neoplasia. The risk of these lesions evolving into cancer is variable.

Genomic studies of precancerous conditions can illuminate the dynamics of tumor progression. In the transition from Barrett's esophagus to esophageal adenocarcinoma, the majority of driver genes are mutated at similar frequency in the precursor lesion, with the exception of *TP53* and *SMAD4*, which are more frequently mutated in the invasive tumors (*52*). This suggests that Barrett's esophagus is, genetically speaking, an advanced precancerous lesion. Similar findings have been described for patients with DCIS and invasive breast cancer (*53*).

These observations seem consistent with the stepwise model of progression to cancer, in which a series of events, mutational or otherwise, drives successive clonal expansions with progressively more disordered phenotypes. However, the majority of cancers arise without a histologically discernible premalignant phase, and it may be that different modes of tumor evolution are operative here. If strong cooperation between driver mutations occurs, major histological changes may not take place until the full repertoire of variants is acquired (Fig. 3C). Furthermore, catastrophic mutational processes such as chromothripsis or telomere crises may fuel a rapid accumulation of driver mutations, resulting in a transformation from normal to malignant cells without easily detectable intermediate stages.

Cancer, aging, and the evolution of protection mechanisms

Cancer is virtually inevitable in complex, long-lived, multicellular organisms. Virtually every cell in an organism has the information and the potential to propagate rapidly, but the success of multicellularity relies on the evolution of mechanisms to suppress this ability. Yet, somatic mutations inevitably accumulate with time and, aided by selection at the tissue level, can erode these suppressive mechanisms.

Age-incidence statistics and the number of driver events per tumor

Time plays a major role in the occurrence of cancer. In fact, the risk of suffering any cancer before the age of 40 is ~2%, but by age 80 this risk increases to 50% (Fig. 4A). Moreover, the incidence of some common cancers rises roughly to the power of four to six as a function of age (Fig. 4B). As early as 1954, this observation was used to propose that cancer could be the result of four to six rate-limiting steps accumulating randomly at a constant rate throughout life (*54*). The exact numbers are disputed, because fits are imperfect and models with clonal expansions (Fig. 3C) can predict fewer rate-limiting steps, but this observation

remains very influential (*1, 10*). With the discovery of the role of somatic mutations in cancer, it is tempting to propose that at least some of these steps are driver mutations, as was exemplified by Knudson for retinoblastoma in 1971 (*3*).

Although driver mutations and rate-limiting steps from age-incidence curves are likely to be related, they are not equivalent. For example, when tumors are sufficiently large or acquire hypermutation, analogous or even identical mutations can occur frequently enough to appear independently in multiple subclones, which suggests that mutations may not be rate limiting in later stages of tumor development (*53*). Also, some rate-limiting steps are likely to be nonmutational, such as epigenetic changes and changes in the microenvironment of a tumor.

Despite 5 years of systematic sequencing of thousands of cancer genomes, we have not yet determined the number of driver mutations required to make a tumor. It is easier to identify regions with an overall excess recurrence of mutations than it is to attribute driver or passenger status to a given mutation in a given patient. This is especially true in tumors with high mutation rates and for noncoding mutations or complex structural changes, for which detection of driver events remains a major challenge.

Evolution of protection mechanisms against cancer

Over millions of years, species have evolved protective mechanisms to keep the incidence of cancer low. These include high-fidelity replication, DNA repair pathways, cellular senescence, stem cell hierarchies, tumor suppressor genes, immune surveillance, and microenvironmental control of cellular behavior.

Given the availability of protective mechanisms against cancer, why does cancer still exist? Some answers can be found in evolutionary theory, which predicts fundamental limits to how much evolution can reduce the incidence of cancer. Most importantly, selection is virtually powerless to fight causes of death after reproductive age, so mechanisms will mainly evolve to reduce cancer in the young. Yet, even these mechanisms will be limited by genetic drift, which makes cancer incidence in the young unlikely to be reduced below ~1/10,000 in humans (*16*). Finally, as argued to explain the evolution of aging in maximizing reproduction success, selection can favor traits that benefit the young at the cost of an added burden later in life (*55*).

Further, at least two additional factors can increase the incidence of cancer above the lower limit set by evolution. Exposure to unfamiliar mutagens (such as tobacco smoke) to which a species has not yet adapted can strongly increase the incidence of certain cancers. Also, recent rapid changes in human evolution might explain higher rates of certain cancers. For instance, the increase in brain size and changes in the development of long bones have been proposed to explain the relatively high frequency of childhood brain and bone cancers, respectively, in humans (*56*).

Together with the roughly geometric rise in cancer incidence predicted by the stepwise model

of cancer, these evolutionary considerations can help to explain why cancer incidence is low, but not zero, in the young, as well as why incidence rises rapidly later in life (Fig. 4).

Cancer as an example of aging

Owing to their association with age and contribution to morbidity and mortality late in life, many cancers can be considered a natural part of aging. In fact, cancer offers a particularly well-understood example of an aging process, exemplifying how a linear accumulation of errors (somatic mutations) can cause a rapid (geometric) rise in morbidity and mortality after reproductive age.

Multiple theories—including the progressive accumulation of DNA damage, somatic mutations, oxidation of mitochondrial DNA, progressive loss of epigenetic regulation, chromatin disorganization, and/or expression deregulation (*55, 57*)—have been proposed to explain the molecular basis of aging. All of these and other forms of progressive molecular degradation are believed to place a burden on the organism and may, together, explain the varied manifestations of aging (*55*).

Somatic mutations are thought to play an important role in aging, beyond causing cancer (*57, 58*). Interestingly, several premature aging disorders, such as Werner syndrome, are caused by DNA repair deficiency. Although the link between somatic mutation and aging is not fully understood, studies in which the rate of DNA damage is increased or reduced have shown acceleration or deceleration, respectively, of aging in cell and animal models (*57, 58*). In general, the accumulation of somatic mutations, occasionally amplified by clonal expansions, over time may lead to alterations in the ability of tissues to function normally. Mutations can alter key genes for the cell or tissue, affect DNA repair, activate cell senescence pathways, or alter gene regulation in the cells, all of which can contribute to the hallmarks of aging (*57, 58*). Sequencing studies of aging tissues should further clarify the extent and the role of somatic mutation in aging.

Conclusions

In just a few years, cancer genome sequencing has revolutionized our understanding of the genetics of cancer. The sequencing of larger numbers of tumors and poorly explored tumor types will continue to yield previously unidentified cancer genes and mutational signatures. Studies exploiting detailed clinical information will correlate these findings with treatment responses and clinical outcomes. The extent of driver mutations in noncoding elements and structural variation remains to be determined. Whole-genome sequencing and novel statistical methods, aided by large sequencing efforts, will help us answer these questions.

We believe that the next decade will see systematic analyses of somatic mutation in normal tissues and its role in cancer progression and aging. Direct studies of mutation burden, mutation signatures, clonal dynamics, and cellular phenotypes will provide a bridge from epidemiological findings to mechanistic insights into the earliest steps of cancer.

REFERENCES AND NOTES

1. M. R. Stratton, P. J. Campbell, P. A. Futreal, *Nature* **458**, 719–724 (2009).
2. L. A. Loeb, C. C. Harris, *Cancer Res.* **68**, 6863–6872 (2008).
3. A. G. Knudson Jr., *Proc. Natl. Acad. Sci. U.S.A.* **68**, 820–823 (1971).
4. J. Cairns, *Nature* **255**, 197–200 (1975).
5. P. C. Nowell, *Science* **194**, 23–28 (1976).
6. E. C. Friedberg *et al.*, *DNA Repair and Mutagenesis* (ASM Press, Washington, DC, ed. 2, 2005).
7. P. J. Stephens *et al.*, *Nature* **462**, 1005–1010 (2009).
8. L. B. Alexandrov *et al.*, *Nature* **500**, 415–421 (2013).
9. M. S. Lawrence *et al.*, *Nature* **499**, 214–218 (2013).
10. B. Vogelstein *et al.*, *Science* **339**, 1546–1558 (2013).
11. C. Tomasetti, B. Vogelstein, *Science* **347**, 78–81 (2015).
12. S. L. Poon *et al.*, *Genome Med.* **7**, 38 (2015).
13. S. Nik-Zainal *et al.*, *Cell* **149**, 979–993 (2012).
14. E. D. Pleasance *et al.*, *Nature* **463**, 191–196 (2010).
15. B. Schuster-Böckler, B. Lehner, *Nature* **488**, 504–507 (2012).
16. I. Martincorena, N. M. Luscombe, *BioEssays* **35**, 123–130 (2013).
17. S. Behjati *et al.*, *Nature* **513**, 422–425 (2014).
18. I. Martincorena *et al.*, *Science* **348**, 880–886 (2015).
19. F. Supek, B. Lehner, *Nature* **521**, 81–84 (2015).
20. Y. Drier *et al.*, *Genome Res.* **23**, 228–235 (2013).
21. E. Papaemmanuil *et al.*, *Nat. Genet.* **46**, 116–125 (2014).
22. P. J. Stephens *et al.*, *Cell* **144**, 27–40 (2011).
23. C. Z. Zhang *et al.*, *Nature* **522**, 179–184 (2015).
24. S. F. Bunting, A. Nussenzweig, *Nat. Rev. Cancer* **13**, 443–454 (2013).
25. S. C. Baca *et al.*, *Cell* **153**, 666–677 (2013).
26. S. A. Forbes *et al.*, *Nucleic Acids Res.* **43**, D805–D811 (2015).
27. N. J. Fredriksson, L. Ny, J. A. Nilsson, E. Larsson, *Nat. Genet.* **46**, 1258–1263 (2014).
28. N. Weinhold, A. Jacobsen, N. Schultz, C. Sander, W. Lee, *Nat. Genet.* **46**, 1160–1165 (2014).
29. F. W. Huang *et al.*, *Science* **339**, 957–959 (2013).
30. J. Vinagre *et al.*, *Nat. Commun.* **4**, 2185 (2013).
31. Y. Tsujimoto, L. R. Finger, J. Yunis, P. C. Nowell, C. M. Croce, *Science* **226**, 1097–1099 (1984).
32. K. H. Nord *et al.*, *Nat. Genet.* **46**, 474–477 (2014).
33. P. A. Northcott *et al.*, *Nature* **511**, 428–434 (2014).
34. L. A. Loeb, K. R. Loeb, J. P. Anderson, *Proc. Natl. Acad. Sci. U.S.A.* **100**, 776–781 (2003).
35. I. P. Tomlinson, M. R. Novelli, W. F. Bodmer, *Proc. Natl. Acad. Sci. U.S.A.* **93**, 14800–14803 (1996).
36. M. Lynch, *Proc. Natl. Acad. Sci. U.S.A.* **107**, 961–968 (2010).
37. G. Genovese *et al.*, *N. Engl. J. Med.* **371**, 2477–2487 (2014).
38. S. Jaiswal *et al.*, *N. Engl. J. Med.* **371**, 2488–2498 (2014).
39. T. McKerrell *et al.*, *Cell Reports* **10**, 1239–1245 (2015).
40. J. S. Welch *et al.*, *Cell* **150**, 264–278 (2012).
41. A. H. Yang *et al.*, *J. Neurosci.* **23**, 10454–10462 (2003).
42. P. S. Larson *et al.*, *J. Clin. Oncol.* **23**, 8613–8619 (2005).
43. J. K. Baillie *et al.*, *Nature* **479**, 534–537 (2011).
44. D. H. McDermott *et al.*, *Cell* **160**, 686–699 (2015).
45. A. M. Klein, D. E. Brash, P. H. Jones, B. D. Simons, *Proc. Natl. Acad. Sci. U.S.A.* **107**, 270–275 (2010).
46. E. Clayton *et al.*, *Nature* **446**, 185–189 (2007).
47. M. P. Alcolea *et al.*, *Nat. Cell Biol.* **16**, 615–622 (2014).
48. V. H. Teixeira *et al.*, *eLife* **2**, e00966 (2013).
49. S. L. Preston *et al.*, *Cancer Res.* **63**, 3819–3825 (2003).
50. H. J. Snippert, A. G. Schepers, J. H. van Es, B. D. Simons, H. Clevers, *EMBO Rep.* **15**, 62–69 (2014).
51. D. E. Brash, J. Pontén, *Cancer Surv.* **32**, 69–113 (1998).
52. J. M. Weaver *et al.*, *Nat. Genet.* **46**, 837–843 (2014).
53. L. R. Yates *et al.*, *Nat. Med.* **21**, 751–759 (2015).
54. P. Armitage, R. Doll, *Br. J. Cancer* **8**, 1–12 (1954).
55. T. B. Kirkwood, *Cell* **120**, 437–447 (2005).
56. A. M. Leroi, V. Koufopanou, A. Burt, *Nat. Rev. Cancer* **3**, 226–231 (2003).
57. C. López-Otín, M. A. Blasco, L. Partridge, M. Serrano, G. Kroemer, *Cell* **153**, 1194–1217 (2013).
58. T. Finkel, M. Serrano, M. A. Blasco, *Nature* **448**, 767–774 (2007).
59. M. S. Lawrence *et al.*, *Nature* **505**, 495–501 (2014).
60. C. Kandoth *et al.*, *Nature* **502**, 333–339 (2013).

REVIEW

Genetics and genomics of psychiatric disease

Daniel H. Geschwind[1]* and **Jonathan Flint[2]***

Large-scale genomic investigations have just begun to illuminate the molecular genetic contributions to major psychiatric illnesses, ranging from small-effect-size common variants to larger-effect-size rare mutations. The findings provide causal anchors from which to understand their neurobiological basis. Although these studies represent enormous success, they highlight major challenges reflected in the heterogeneity and polygenicity of all of these conditions and the difficulty of connecting multiple levels of molecular, cellular, and circuit functions to complex human behavior. Nevertheless, these advances place us on the threshold of a new frontier in the pathophysiological understanding, diagnosis, and treatment of psychiatric disease.

Genetic findings are set to illuminate the causes and to challenge the existing nosology of psychiatric conditions, some of which, until recently, were purported to have a non-biological etiology (*1*). After decades of false starts, we now have confirmed associations between genetic variants that increase the risk of schizophrenia (SCZ), autism spectrum disorder (ASD) (*2*), major depression, and bipolar disorder (BPD), and in some cases the underlying gene(s) have been identified (*3–8*). These achievements were not necessarily a forgone conclusion. Despite evidence for the relatively high heritability of some psychiatric disorders, claims of successful genetic mapping followed by replication failure (*9, 10*), along with doubts about the biological validity of the inherently syndromic categorical psychiatric diagnoses, suggested that behavioral disorders would prove to be less tractable to molecular genetic dissection.

The recent discoveries in psychiatric genetics follow technological advances in molecular biology and conceptual advances in the genetics of complex disorders (*11, 12*). By interrogating genetic variation at millions of single-nucleotide polymorphisms (SNPs) in the genome using microarrays, one can efficiently perform genome-wide association studies (GWASs) in thousands of individuals. Sufficiently large sample sizes have enabled the robust detection of association between disease status and common alleles ("common variants," population frequencies usually greater than 5%) (*13*). In the majority of cases, loci identified through GWASs lie in regulatory regions of the genome (*14*) and do not unequivocally implicate a specific gene. However, because many regulatory regions lie close to their cognate genes (*15*), investigators typically report the closest gene as responsible (in the absence of functional data, we follow that tradition here but recognize its limitations). Microarrays have also permitted

the detection of multiple rare structural chromosomal variants referred to as copy number variation (CNV; the gain or loss of DNA >1 kb in size) that contribute to a variety of psychiatric disorders, including ASD and SCZ (*16*). Last, advances in genome sequencing have made it possible to obtain the complete protein coding sequence [whole-exome sequencing (WES)] of tens of thousands of individuals (*17*), with whole-genome

> *"Genetic findings blur not only psychiatric disease boundaries but also the boundaries between disease state and normal variation....as risk genes are identified..."*

sequences at a similar scale on the horizon. The identification of rare mutations in protein-coding domains ("rare variants," frequency usually <0.1%) via WES has become a standard approach, exemplified by the findings that rare protein-disrupting variants contribute to the risk of ASD (*4*) and SCZ (*18, 19*). Although these advances do not yet deliver a complete picture of the genetic architecture (the number of loci and relative contribution from different forms of genetic variation) for any psychiatric disorder (Fig. 1), there is sufficient information to draw some general conclusions.

The polygenicity of psychiatric illness

In addition to finding specific genes, molecular genetics can provide information about the heritability of psychiatric disease, an approach that has led to some important insights about the genetic architecture of psychiatric illness. The degree of SNP sharing among disease cases estimates the common, inherited portion of a trait (*20*). Such SNP heritability estimates can be used to test hypotheses about the extent to

[1]Departments of Neurology, Psychiatry, and Human Genetics, David Geffen School of Medicine, University of California, Los Angeles, Los Angeles, CA 90095, USA. [2]Wellcome Trust Center for Human Genetics, University of Oxford, Oxford, UK.
*Corresponding author. E-mail: dhg@mednet.ucla (D.H.G.); jf@well.ox.ac.uk (J.F.)
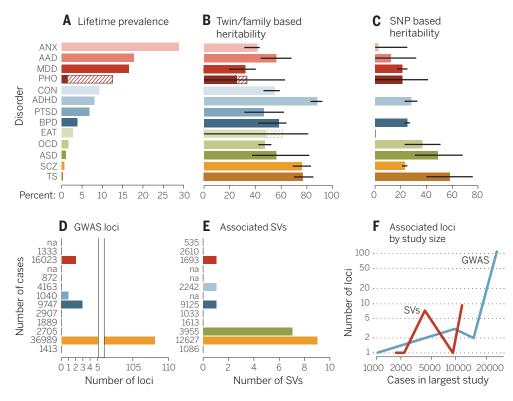
Fig. 1. Summary of genetic analyses performed on 13 psychiatric disorders. (**A**) Highest lifetime (point for ASD) prevalence in percentages. The discontinuous bar in phobias represents the range in different forms. (**B**) Heritability estimates; bars, standard error (SE). (**C**) SNP-based heritability estimates; bars, SE. (**D**) Number of genome-wide significant loci. The *x* axis is discontinuous because of the large difference of associated loci between disorders. (**E**) The number of associated structural variants (SVs) that either reach genome-wide significance or have been replicated with $P \leq 0.01$ in another study. (**F**) The *y* axis shows associated GWAS loci (blue) and SVs (green) by the number of cases (*x* axis) in the largest study for that disorder. The number of cases in the largest study for GWAS (D) and SV studies (E) is reported next to each disorder. Abbreviations are as follows: ANX, any anxiety disorder; AAD, alcohol abuse disorder; MDD, major depressive disorder; PHO, = any phobia; CON, conduct disorders; PTSD, post traumatic stress disorder; EAT, eating disorders; TS, Tourette syndrome. The order of disorders and their color coding are maintained throughout the bar plots. See table S1 for underlying data and references amalgamated from many sources.

which heritability arises from many loci of small effect ("polygenicity"). Using this approach, a large proportion of the genetic contribution to psychiatric disease is found to consist of common variants at a large number of loci, although each variant has only a small effect on disease risk, consistent with findings from other common, complex diseases (*21*). Thus, a major component of risk of psychiatric illness is polygenic. At the same time, the SNP heritability does not explain all of the estimated additive heritability, suggesting that other, as-of-yet–unmeasured factors such as rare variants, also contribute.

Polygenicity, the small effects of individual loci, and the rarity of large-effect loci mean that the most critical requirement for successful genetic dissection of a psychiatric disorder is the availability of sufficiently large clinical cohorts, emphasized by the recent discoveries of the Psychiatric Genomics Consortium (PGC), whose collaborative large-scale approach has had a major impact on the field (*3*). However, there is an in-

herent practical tradeoff between sample size and the depth of phenotyping. Disorders with large environmental risk factors, such as anxiety and depression, may benefit from more attention to clinical phenotyping. Rigorous attention to the phenotype and screening for known and putative risk factors may increase the power to detect genetic effects, as evidenced by the recent CONVERGE GWAS in depression (*22*).

Major-effect-size contributions

A common perception is that GWASs have returned few biological insights, and, consequently, that deeper insights will come from studying the effects of individual large-effect-size genes. Mutations that segregate in a Mendelian fashion are one example of being both necessary and sufficient to cause disease, but these are rare and hard to find in most psychiatric diseases. Analysis of CNV and WES provide another source of rare penetrant mutations.

Particularly convincing has been the recent discovery of the role of large-effect de novo (arising in

gametes) mutations in ASD, where the first genome-wide studies of de novo mutations in psychiatric disorders revealed a role for rare (<0.1%) de novo CNVs in ASD (*23, 24*). Studies indicate that large (>500 kb) rare de novo gene–containing CNVs occur in ~5 to 7% of people with nonsyndromic ASD, versus ~1% of unaffected siblings (*25*). Several of these rare CNVs are recurrent, some inherited from apparently unaffected parents (such as 15q11-13 or 16p11.2), and none individually account for more than 1% of cases of ASD. Studies of smaller gene-disrupting CNVs also suggest a role for inherited CNVs with lower penetrance (*26*).

Several major-effect loci due to de novo or inherited CNV also increase the risk for SCZ. These loci display variable expressivity and incomplete penetrance (*27, 28*), and several are associated with other disorders, including ASD, epilepsy, and intellectual disability (*29, 30*). The role of large rare CNVs (rare or de novo) in BPD, major depression, substance abuse, obsessive-compulsive disorder (OCD), attention deficit hyperactivity disorder (ADHD), or anxiety disorders is less clear and, with a few exceptions, have a smaller magnitude of contribution relative to ASD or SCZ. In ADHD, sample sizes have been relatively small, and the greatest signal resides in those with comorbid intellectual disability (*31*). Studies of parent-child trios in SCZ and BPD (*32*) have observed odds ratios (ORs) for carrying large rare de novo CNVs of about five for both, although if de novo CNVs <500 kb are considered, the OR is higher, albeit with wide confidence intervals. Similar to ASD, the contribution from de novo events comes mostly from sporadic rather than familial cases, where the rate of de novo CNVs is closer to that of controls.

Finding a rare causal mutation via WES is challenging, because variants changing protein-coding sequences are common (*33*); identifying sufficient recurrent mutations to confirm the candidacy of a specific gene requires resequencing of thousands of individuals (*34*) and parents if the goal is to define causal or contributory de novo mutations. Success varies by disorder. In ASD, WES in nearly 5000 probands across two large studies has demonstrated the contribution of rare de novo protein-disrupting mutations to disease risk, identifying 33 genes that are recurrently mutated and therefore highly likely to be pathogenic (*4, 35*). An additional several hundred mutant genes are observed only once in probands, each with an estimated 40% chance of being contributory, based on the frequency of similar events in controls (*4*). Overall, current estimates from families containing a single affected individual suggest that up to about 30% of cases harbor large-effect de novo coding mutations,
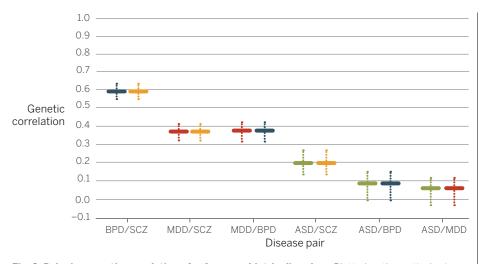
Fig. 2. Pairwise genetic correlations for four psychiatric disorders. Plotted on the vertical axis are BPD, SCZ, MDD, and ASD (*2*). The horizontal colored lines mark the mean of the genetic correlation based on SNP sharing for each pair of illnesses, and the dotted vertical colored lines are the SEs of the estimates. Data are from Maier *et al.* (*69*).

observing that the number of loss-of-function events in cases is almost three times higher than in control family trios (8.7% compared to 2.9%) (*39*). However, studies with larger sample sizes (*18, 19*) failed to confirm an overall enrichment of de novo mutations, and identification of individual susceptibility genes via WES has eluded researchers. Enrichment of mutations was found, but only when analysis was restricted to sets of hypothesis-driven candidate genes (*19*).

On the other end of the spectrum, relatively rare variants (SNPs with frequencies less than 5%) are predicted to account for 21% of the heritability in Tourette syndrome but none of the heritability of OCD (*40*). Still, for Tourette syndrome, only a single very rare dominant mutation has been identified in one family (*41*). For other disorders, ranging from major depression to substance abuse and anxiety disorders, for which there is strong evidence of heritable polygenic risk, we lack significant evidence of rare large-effect-size variant contributions, consistent with differences in genetic architecture across psychiatric diseases, although study design and small cohort sizes may also contribute.

Cross-disorder overlap: Genetics as a tool for nosology

SNP data can also be used to estimate the genetic correlation (tagged by common variation)

due to either single-nucleotide variants or structural variants (*4*), each of which is rare in the population. As is the case with CNV (*26, 36*), inherited rare single-nucleotide variants also play a role in ASD (*37*), although their contribution warrants further refinement.

Similar success evades genetic analysis of other psychiatric disorders, for which we have very few large-effect genes that have been independently replicated. Work on SCZ is closest to identifying mutations in specific genes. Initial studies identified increased rates of de novo mutations (*38*),

Fig. 3. Heterogeneous genetic risk factors converge in biological networks. Different study designs, such as trios, multiplex affected families, or case-control (shown at far left) identify different forms of genetic risk in cases (the arrow size indicates the relative effect size). By integrating these data with biological network data, one can assess in a genome-wide manner whether disease-associated risk variants are enriched in specific biological networks (*46*). Here, for illustration, we depict rare de novo variants associated with ASD, enriched in the yellow module. The function of this module of co-regulated genes can be further annotated using gene ontology, which implicates these large-effect ASD-associated variants in chromatin remodeling, transcriptional regulation, and neurogenesis. Networks can be subsequently mapped onto developmental time points, brain regions, circuits, or cells.

Clinical diagnosis

ADHD   ASD   SCZ   BPD   MDD   ADD

Population-level genetic characterization

GWAS, analysis of CNV and other structural chromosomal variation
(microarray and WGS), identification of rare genetic variants (via WES and WGS)

Define individual genetic risk

. . .

Refinement of clinical classification based on genetics and neurobiology
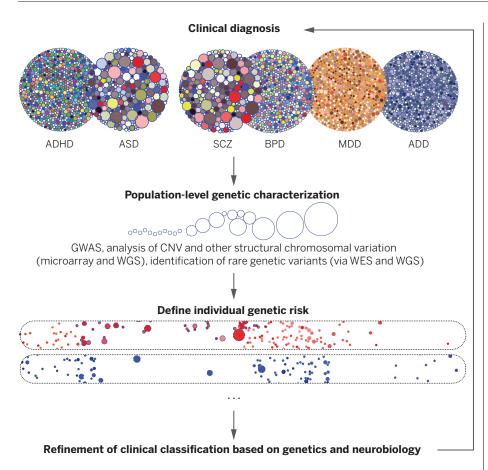
Fig. 4. Refining diagnoses based on genetic susceptibility. Clinical disorders (abbreviations are as in Fig. 1) and their overlap, represented by the big circles. The smaller dots within each circle represent contributing genetic or environmental risk factors. Once genetic risk is defined in population studies, it can be used to define factors underlying disease risk in individuals, identifying distinct (or overlapping) entities, two of which are represented by the elongated ovals at the bottom, grounded in causal mechanistic understanding. These subtypes should more clearly inform prognosis and treatment than do current categorical disease entities. The sizes of the dots within the circles represent the relative effect sizes of variants.

between disorders (*42*) (Fig. 2). Some disorders clearly share genetic risk: Between BPD and SCZ the correlation is 0.68; between BPD and major depressive disorder, the correlation is 0.47. Six genome-wide significant loci are associated with a combined BP+SCZ phenotype (*42*). However, SNPs for both BP and SCZ were genome-wide significant in *CACNA1C, ANK3* and *ITIH3-ITIH4*, but not in *MHC, ODZ4, TCF4* and other loci that were genome-wide significant for either disorder separately. Thus, both polygenic risk scores (*42*) and GWAS hits (*42*) discriminate between disorders, and both overlapping and disease-specific genetic risk factors can be identified (*43*).

A similar view of diagnostic overlap and specificity is provided by rare, penetrant mutations that are risk factors for multiple psychiatric disorders. Mutations in evolutionarily constrained, fetal-brain expressed genes, many of whose RNAs are bound by the Fragile X mental retardation protein (FMRP) (*4, 18, 44, 45*), are associated with ASD, SCZ, and intellectual disability (ID), as well as epilepsy. Similarly, few large CNVs are disease-specific, and the most common such mutation, the

22q11-13 deletion, predisposes to both ASD and SZ, as do others (*29, 30*). The observed variable expressivity is consistent with the hypothesis that large-effect mutations that disrupt highly evolutionarily constrained genes do not lead to a specific clinically defined disorder, but rather increase risk for a range of developmental disorders associated with ID via disruption of the highly canalized process of brain development (*46*). From this perspective, clinically defined disorders may represent either the limited repertoire or our limited measurements of behavioral responses to the insult. Moreover, the complexity of brain function and structure is not reflected in recognized in current psychiatric disease nosology. This view provides impetus to the Research Domain Criteria initiative (RDOC) (*47*) in which psychiatric classification would be replaced with assessment of neurobiological mechanisms, informed largely by genetic discoveries (Fig. 3) (*48*).

Phenotype definition

Genetic findings blur not only psychiatric disease boundaries but also the boundaries be-

tween disease state and normal variation. One recent study suggests that polygenic risk for BPD and SCZ contributes to creativity (*49*). Unaffected individuals within families harboring major psychiatric illness often harbor quantitative traits shared with affected individuals, but below the diagnostic threshold, so-called intermediate phenotypes or endophenotypes (*50*). Yet despite many attempts to break psychiatric diseases into simpler intermediate components, the use of quantitative or qualitative endophenotypes in genetic studies has had mixed success (*51–53*). Severity or age of onset may be useful for risk stratification in some cases (*22, 54*) but not in others. Additionally, many potential endophenotypes, ranging from cognitive, to behavioral, to anatomical, although highly heritable, appear nearly as genetically complex as the disorders with which they are associated, as is the case for structural neuroimaging phenotypes (*55*). Still, as risk genes are identified, studying genotype-intermediate phenotype relationships should greatly inform our understanding of disease mechanisms (*48*).

Neurobiological mechanisms via genetically guided disease modeling

A major reason for identifying the genetic basis of a psychiatric disorder is to develop platforms for understanding disease mechanisms at a cellular-molecular level and accelerate therapeutic development. Despite the potential limitations of studying psychiatric disease in model organisms, mouse models of large-effect-size or Mendelian risk genes for ASD appear promising (*56, 57*). Many show large behavioral or cognitive deficits relative to wild-type littermates, as well as cellular or physiological phenotypes that may underlie disease pathophysiology. In parallel, advances in stem cell biology now make it possible to generate and study human neurons and their development in vitro (*58*), providing a platform for drug discovery and phenotypic screening. However, significant challenges exist, including the potential for in vitro artifacts, rigorous definition of cell types, or matching to in vivo brain development. The few studies examining monogenic forms of psychiatric disease via induced pluripotent stem cell–derived neurons are very encouraging (*59–61*), but consist of relatively small sample sizes. Integrating in vivo modeling in model organisms with in vitro modeling based on tissues derived from human stem cells will help balance the limitations of each system alone.

Additionally, there is an inherent tension between the study of individual genes and the emerging genetic architecture of psychiatric illness, which implicates potentially thousands of genes in each disorder. If psychiatric disorders are a collection of rare conditions, then detailed individual investigation is the most direct route forward. The evidence supports this hypothesis at least in part for ASD and other childhood-onset disorders, in which we now know that the effects of different rare major–effect-size alleles account for some of the

phenotypic complexity. Yet there is remarkably little evidence that this is true for SCZ, BPD, major depression, substance abuse, and the anxiety disorders. The apparent specificity of drug action in some of these conditions might be interpreted to imply shared mechanisms among responders. Yet one would not assume shared etiologies among patients with infectious or rheumatologic diseases, whose fevers symptomatically respond to aspirin. The existence of only a few central switches that determine vulnerability to illness is challenged by the extreme polygenicity and apparent genetic heterogeneity in these disorders. We need to understand in an unbiased manner whether there is a convergence of these multiple complex genetic factors on a relatively constrained set of biochemical pathways (62).

Systems genetics approaches

The highly polygenic nature of psychiatric disease and the failure of genome-wide studies to support the role of candidate genes (with a few exceptions) suggest that generalizable mechanistic insight is unlikely to be obtained from analysis of a single dysfunctional molecule in isolation. Genes do not act in isolation, but most models only account for a few features at a time. A systems genetics approach that considers function at a network level permits us to methodically approach the daunting task of connecting heterogeneous genetic risk factors to brain mechanisms (46) (Fig. 4).

Several recent genome-wide network studies in ASD and SCZ do indeed suggest that the disorder risk converges on shared molecular pathways, where currently identified genetic variation is enriched (46). In ASD, these pathways involve the regulation of transcription and chromatin structure during neurogenesis, and subsequent processes of synaptic development and function during early fetal cortical development. Alternative approaches based on protein interactions alone, and the integration of protein, gene expression, or phenotype data, identify similar pathways or show the convergence of multiple ASD risk loci on similar biological processes or networks. A network study of genetic variation underlying SCZ implicates similar risk stages during the development of the prefrontal cortex (63), which is consistent with neuroanatomical and physiological studies.

Although there is evidence that both common and rare disease susceptibility loci are likely to converge on specific molecular and biological pathways in ASD and potentially SCZ (64), many issues remain. The pathways as currently defined are broad and should be refined at the level of protein function and cellular signaling to obtain more specific insight into disease pathogenesis. Furthermore, knowing how these pathways reflect genetic risk at the level of individuals is necessary to develop a mechanistic understanding of disease.

Moving forward

We now have a reasonable framework for understanding the basic genetic architecture underlying psychiatric disease, yet the number of susceptibility loci so far identified accounts for only a small percentage of the variance in liability to disease (65). With the exception of SCZ and ASD, so few replicated loci have been identified that the need to identify more is undeniable. Still, the field is at an appropriate juncture to consider when it would be reasonable to stop looking for genes and focus entirely on studying their function. Certainly, a more complete catalog of genes and mutations would provide a clearer indication of cross-disorder overlap and disease-specific biochemical and circuit convergence. One important justification for the creation of a more complete catalog is the need to address disease heterogeneity and to understand composite genetic risk in individuals. A measure of success would be the ability to genotype individuals at known risk loci and classify their disease based on a neurobiological framework (47); this is a feasible goal for the next decade (Fig. 3). Leveraging electronic medical records, remote data gathering, and electronic media, coupled with forthcoming population-level clinical whole-genome studies, should accelerate these efforts.

In the meantime, comparative studies are needed to understand the shared and distinct phenotypic effects of rare large-effect alleles in humans and model systems. To some extent, the phenotypes of psychiatric disease must represent the common outcome of multiple different pathways at the level of brain systems that underlie their shared behavioral and cognitive phenotypes (29, 62). Decades of research have identified ASD in multiple rare genetic syndromes with specific constellations of multi-organ phenotypes, including Timothy syndrome, tuberous sclerosis, Potocki-Lupski syndrome, cortical dysplasia focal epilepsy syndrome, and fragile X syndrome. New syndromes identified via WES are no different, suggesting that the phenotypic complexity of ASD may in part be explained by the effects of different rare major-effect-size alleles (66). Such inverse mapping or genotype-first approaches are at early stages in SCZ and BPD (48). Additionally, it is not known what genetic or environmental factors influence the diversity of clinical outcomes in people harboring most of the major-effect loci. Understanding the mechanisms of such variable expressivity will undoubtedly provide critical pathophysiological clues.

Rigorous attempts to define intermediate phenotypes that represent components of the underlying disease neurobiology are also necessary to develop a more therapeutically meaningful nosology, but this area has proven very challenging (67). One potential avenue is using more data-driven approaches in humans, such as genetic risk scores and Mendelian randomization based on the joint effects of multiple risk loci to refine causal relationships between disease and intermediate phenotypes (68). Moreover, specificity of action is a prerogative of neural development and neuronal circuits, not genes. Technologies that have brought activity in neuronal circuits under exogenous control repeatedly demonstrate the existence of circuits that are responsible for specific behaviors. Circuits and diseases that can be modeled in genetically tractable organisms permit hypothesis testing that draws on genetic results to propose genes for functional testing.

One key piece of basic biological information that is missing is knowledge of cell type diversity and its molecular basis in the brain. To fully interpret the mechanisms of genetic variants it is necessary to have a more complete molecular and cellular parts list of the developing and mature brain. Moreover, as most common variants lie in presumptive regulatory regions, we need to integrate emerging knowledge about cells and circuits with an unbiased understanding of mechanisms of gene regulation across neurodevelopmental stages. All of these goals will be hastened by organized efforts such as the Brain Initiative (braininitiative.nih.gov/), the Allen Institute (http://alleninstitute.org), psychEncode (http://psychencode.org), Genotype-Tissue Expression (www.gtexportal.org), and the PGC.

We conclude by emphasizing the transformational role that genetic insights can play when investigating conditions for which nothing is currently known about their underlying biology. The idea that psychiatric disease might be purely "functional" can no longer be entertained. With ASD, we are entering an era where genetic dissection informs phenotypic heterogeneity and where biological insights are starting to emerge. The next few years will undoubtedly see a radical transformation of our understanding of the biological origins of all neuropsychiatric disorders.

REFERENCES AND NOTES

1. B. Bettelheim, *The Empty Fortress: Infantile Autism and the Birth of the Self* (Free Press, New York, 1972).
2. H. Stefansson *et al.*, *Nature* **455**, 232–236 (2008).
3. S. Ripke *et al.*, *Nature* **511**, 421–427 (2014).
4. I. Iossifov *et al.*, *Nature* **515**, 216–221 (2014).
5. S. De Rubeis *et al.*, *Nature* **515**, 209–215 (2014).
6. M. E. Talkowski *et al.*, *Cell* **149**, 525–537 (2012).
7. Psychiatric GWAS Consortium Bipolar Disorder Working Group, *Nat. Genet.* **43**, 977–983 (2011).
8. Cross-Disorder Group of the Psychiatric Genomics Consortium, *Lancet* **381**, 1371–1379 (2013).
9. J. R. Kelsoe *et al.*, *Nature* **342**, 238–243 (1989).
10. D. F. Levinson *et al.*, *Science* **296**, 739–741 (2002).
11. L. Kruglyak, *Nat. Rev. Genet.* **9**, 314–318 (2008).
12. N. Risch, K. Merikangas, *Science* **273**, 1516–1517 (1996).
13. M. I. McCarthy *et al.*, *Nat. Rev. Genet.* **9**, 356–369 (2008).
14. M. T. Maurano *et al.*, *Science* **337**, 1190–1195 (2012).
15. ENCODE Project Consortium, *Nature* **489**, 57–74 (2012).
16. International Schizophrenia Consortium, *Nature* **455**, 237–241 (2008).
17. J. A. Tennessen *et al.*, *Science* **337**, 64–69 (2012).
18. S. M. Purcell *et al.*, *Nature* **506**, 185–190 (2014).
19. M. Fromer *et al.*, *Nature* **506**, 179–184 (2014).
20. J. Yang *et al.*, *Nat. Genet.* **43**, 519–525 (2011).
21. G. B. Ehret *et al.*, *Nature* **478**, 103–109 (2011).
22. CONVERGE Consortium, *Nature* (2015).
23. M. L. Jacquemont *et al.*, *J. Med. Genet.* **43**, 843–849 (2006).
24. J. Sebat *et al.*, *Science* **316**, 445–449 (2007).
25. S. J. Sanders *et al.*, *Neuron* **70**, 863–885 (2011).
26. M. Bucan *et al.*, *PLOS Genet.* **5**, e1000536 (2009).
27. D. F. Levinson *et al.*, *Am. J. Psychiatry* **168**, 302–316 (2011).

28. V. Vacic et al., Nature 471, 499–503 (2011).
29. D. H. Geschwind, Trends Cogn. Sci. 15, 409–416 (2011).
30. D. Moreno-De-Luca et al., Am. J. Hum. Genet. 87, 618–630 (2010).
31. N. M. Williams et al., Lancet 376, 1401–1408 (2010).
32. D. Malhotra et al., Neuron 72, 951–963 (2011).
33. D. G. MacArthur et al., Science 335, 823–828 (2012).
34. B. J. O'Roak et al., Science 338, 1619–1622 (2012).
35. D. H. Geschwind, M. W. State, Lancet Neurol. (2015).
36. D. Pinto et al., Nature 466, 368–372 (2010).
37. N. Krumm et al., Nat. Genet. 47, 582–588 (2015).
38. S. L. Girard et al., Nat. Genet. 43, 860–863 (2011).
39. B. Xu et al., Nat. Genet. 44, 1365–1369 (2012).
40. L. K. Davis et al., PLOS Genet. 9, e1003864 (2013).
41. A. G. Ercan-Sencicek et al., N. Engl. J. Med. 362, 1901–1908 (2010).
42. S. H. Lee et al., Nat. Genet. 45, 984–994 (2013).
43. D. M. Ruderfer et al., Mol. Psychiatry 19, 1017–1024 (2014).
44. J. C. Darnell et al., Cell 146, 247–261 (2011).
45. M. Irimia et al., Cell 159, 1511–1523 (2014).
46. N. N. Parikshak, M. J. Gandal, D. H. Geschwind, Nat. Rev. Genet. 16, 441–458 (2015).
47. T. Insel et al., Am. J. Psychiatry 167, 748–751 (2010).
48. H. Stefansson et al., Nature 505, 361–366 (2014).
49. R. A. Power et al., Nat. Neurosci. 18, 953–955 (2015).
50. I. I. Gottesman, T. D. Gould, Am. J. Psychiatry 160, 636–645 (2003).
51. T. A. Greenwood et al., Am. J. Psychiatry 170, 521–532 (2013).
52. J. K. Lowe, D. M. Werling, J. N. Constantino, R. M. Cantor, D. H. Geschwind, Am. J. Psychiatry 172, 266–275 (2015).
53. P. Chaste et al., Biol. Psychiatry 77, 775–784 (2015).
54. T. Walsh et al., Science 320, 539–543 (2008).
55. D. P. Hibar et al., Nature 520, 224–229 (2015).
56. E. J. Nestler, S. E. Hyman, Nat. Neurosci. 13, 1161–1169 (2010).
57. J. A. Chen, O. Peñagarikano, T. G. Belgard, V. Swarup, D. H. Geschwind, Annu. Rev. Pathol. 10, 111–144 (2015).
58. R. Dolmetsch, D. H. Geschwind, Cell 145, 831–834 (2011).
59. S. P. Paşca et al., Nat. Med. 17, 1657–1662 (2011).
60. A. Sugathan et al., Proc. Natl. Acad. Sci. U.S.A. 111, E4468–E4477 (2014).
61. A. Shcheglovitov et al., Nature 503, 267–271 (2013).
62. D. H. Geschwind, Cell 135, 391–395 (2008).
63. S. Gulsuner et al., Cell 154, 518–529 (2013).
64. Network and Pathway Analysis Subgroup of Psychiatric Genomics Consortium, Nat. Neurosci. 18, 199–209 (2015).
65. T. Gaugler et al., Nat. Genet. 46, 881–885 (2014).
66. S. S. Jeste, D. H. Geschwind, Neurology 10, 74–81 (2014).
67. C. E. Bearden, N. B. Freimer, Trends Genet. 22, 306–313 (2006).
68. D. M. Evans, G. Davey Smith, Annu. Rev. Genomics Hum. Genet. 16, 327–350 (2015).
69. R. Maier et al., Am. J. Hum. Genet. 96, 283–294 (2015).

REVIEW

Mutations causing mitochondrial disease: What is new and what challenges remain?

Robert N. Lightowlers, Robert W. Taylor, Doug M. Turnbull*

Mitochondrial diseases are among the most common and most complex of all inherited genetic diseases. The involvement of both the mitochondrial and nuclear genome presents unique challenges, but despite this there have been some remarkable advances in our knowledge of mitochondrial diseases over the past few years. A greater understanding of mitochondrial genetics has led to improved diagnosis as well as novel ways to prevent transmission of severe mitochondrial disease. These and other advances have had a major impact on patient care, but considerable challenges remain, particularly in the areas of therapies for those patients manifesting clinical symptoms associated with mitochondrial dysfunction and the tissue specificity seen in many mitochondrial disorders. This review highlights some important recent advances in mitochondrial disease but also stresses the areas where progress is essential.

Mitochondrial diseases are a common group of genetic human disorders, which we define here as those leading to a primary defect in mitochondrial oxidative phosphorylation (OXPHOS), the main source of cellular adenosine triphosphate (ATP). The mitochondrial electron transport chain, which is required for human life, is composed of four multisubunit complexes (CI to CIV) and two mobile electron carriers (ubiquinone and cytochrome c). This system produces a transmembrane proton gradient that is harnessed by the protein complex known as complex V (F_oF_1 ATP synthase) to synthesize ATP, a usable energy source for the cell. Freely moving respiratory complexes and mobile carriers coexist in the inner mitochondrial membrane with larger structures called respiratory supercomplexes (1).

OXPHOS proteins are uniquely under the dual genetic control of the mitochondrial and nuclear genomes. The circular mitochondrial genome (mtDNA) consists of only 16,569 base pairs (2) but is present in multiple copies in all cells. MtDNA encodes only 37 gene products, of which 13 are polypeptides that are structural OXPHOS subunits, plus 22 transfer RNAs (tRNAs) and two ribosomal RNAs (rRNAs) required for their synthesis. The remaining mitochondrial proteins including the majority of OXPHOS subunits, the assembly and ancillary factors of the OXPHOS complexes, and those involved in maintenance and expression of mtDNA, intraorganellar protein synthesis, and mitochondrial dynamics are nuclear-encoded, synthesized in the cytosol, and imported into mitochondria.

Clinical features and prevalence of mitochondrial disease

One of the great challenges of mitochondrial disease remains the marked variation in clinical

Wellcome Trust Centre for Mitochondrial Research, Institute for Cell and Molecular Biosciences and Institute of Neuroscience, Medical School, Newcastle University, Newcastle upon Tyne NE2 4HH, UK.
*Corresponding author. E-mail: doug.turnbull@ncl.ac.uk

features in patients, involving several different organs and leading to multisystem presentations. Mitochondrial diseases can arise throughout each decade of life. Patients presenting in childhood often have severe and progressive disease due to recessively inherited nuclear gene disorders (3). Clinical syndromes include Leigh syndrome and Alpers syndrome, with prominent involvement of the central nervous system; however, some patients may present with cardiac, skeletal muscle, or other organ involvement reflecting genetic heterogeneity. In adult-onset disease, mtDNA mutations predominate, although Mendelian disorders caused by autosomal dominant mutations of gene products, such as components of the mtDNA replication machinery [e.g., DNA polymerase gamma (POLG) and Twinkle helicase (PEO1)] that usually lead to severe autosomal recessive disease in children, may manifest later in life. As with pediatric presentations, there are commonly recognized clinical phenotypes in adult-onset mitochondrial disease including chronic progressive external ophthalmoplegia, subacute blindness associated with Leber hereditary optic neuropathy (LHON), MELAS (mitochondrial encephalopathy, lactic acidosis, and stroke-like episodes), and MERRF (myoclonic epilepsy and ragged red fibers). However, many patients do not fit clearly defined syndromes, and this is perhaps especially true for those with the common m.3243A>G mutation (4), present in almost one-third of adult patients with mitochondrial disease, often delaying patient diagnosis.

Another key goal in mitochondrial disease is to understand the tissue specificity associated with specific mitochondrial genotypes. A good example of this is the frequent isolated involvement of the optic nerve in patients with primary LHON mutations (5). It is presumed that the retinal ganglion cells are particularly susceptible to the effects of these complex I mutations, but it is of interest that the same mutation that causes LHON can also lead to a devastating severe

dystonia with no obvious eye involvement in other patients (6). This is also exemplified by the remarkable phenotypic differences observed in patients with mutations of mt-aminoacyl tRNA synthetases, particularly given these are ubiquitous enzymes (see below). Such selective vulnerability, however, is not unique to mitochondrial disease but is seen with many neurological disorders. Progress in this area is slow because of the difficulties in modeling human mitochondrial diseases. At present, modifying the mitochondrial genome in a specific way is difficult (see below), and many different animal models of nuclear genetic defects do not replicate the phenotype in humans (7, 8). Clearly, mtDNA heteroplasmy cannot explain the remarkable tissue variability in these disorders, but it is interesting to note that the mitochondrial transcriptome also harbors substantial heteroplasmy in unaffected individuals (9); little is currently known about what

may cause such RNA heteroplasmy, but it is another way in which the composition of OXPHOS components could vary within an individual, tissue, or cell.

Extensive clinical and genetic heterogeneity means that the exact prevalence of mitochondrial disease is difficult to establish. Published studies looking at the prevalence in children suggest a minimum birth prevalence of 6.2/100,000, although the frequency is much higher in some consanguineous communities because of the high incidence of autosomal recessive disease (10). Adult mitochondrial disease, which includes pathogenic mutations of both the mitochondrial and nuclear genomes, is estimated to be approximately 1 in 4300 of the population affected or at risk of developing mitochondrial disease, with mtDNA mutations identified in more than 75% of total clinically affected adults (11). Although classification of mitochondrial dis-

eases is complex, we present a simplified version in Table 1.

Mitochondrial DNA genetic disorders

A major advance for families with mtDNA mutations has been the increase in reproductive options available and a realistic possibility that the transmission of these diseases can be prevented. Such reproductive techniques to prevent the transmission of mitochondrial disease are important because of the lack of curative treatment and the progressive nature of such diseases. For nuclear mutations that cause mitochondrial disease, similar options are available as for other nuclear genetic conditions, including prenatal and preimplantation genetic diagnosis. For families with pathogenic mtDNA mutations, the challenges are greater, reflecting the different genetic mechanisms and unique maternal transmission of mtDNA (12). MtDNA mutations may be homoplasmic (with all mtDNA copies mutated), as observed in the majority of patients with LHON; more commonly they are heteroplasmic, with a mixture of mutated and wild-type mtDNA present within the individual and in cells. A cellular threshold level of mutated mtDNA is believed to be a requirement for a manifest biochemical defect (13) (almost certainly due to the absolute amount of wild-type mtDNA). The same is true for clinical defects, with the risk of developing severe disease correlated with the level of heteroplasmy.

Not all mtDNA mutations behave similarly in terms of the distribution of heteroplasmy, which is crucial for our understanding of disease pathogenesis, diagnosis, and inheritance. MtDNA is maternally inherited (12). For heteroplasmic mutations, this inheritance pattern is complicated by a genetic bottleneck due to relatively few mtDNA copies in individual cells of developing embryos and relaxed mtDNA replication (14, 15). For heteroplasmic mutations, such as m.8344A>G and m.3243A>G, the genetic bottleneck results in variable levels of mtDNA mutation in mature oocytes. However, single, sporadic large-scale mtDNA deletions can occur, although the risks of transmission to offspring are small.

It is estimated that the average number of births per year from women at risk of transmitting serious mtDNA disease is 152 in the United Kingdom and 778 in the United States (16). For these women, expert genetic counseling is important to inform them of the specific risks associated with their particular mtDNA mutation and to discuss their reproductive options (17). These include adoption or ovum donation, but there is a limitation of donor oocytes and many women want their own genetically related children. After counseling, some families prefer to conceive naturally, albeit with some risk of having an affected child. Some at-risk mothers may consider prenatal testing at the chorionic villus stage or amniocentesis to determine the level of mtDNA mutation in the developing fetus. Preimplantation genetic diagnosis, determined on the basis of analysis of either one or two blastomeres of a day-3 embryo, is increasingly used to reduce the risk of

Table 1. A simplified genetic classification of mitochondrial diseases. Shown are examples of mutations (mtDNA) or disease genes (nuclear disorders).

Mitochondrial DNA mutations	
mtDNA rearrangements	Sporadic, single large-scale mtDNA deletions
Protein synthesis gene	mt-tRNA gene mutations (e.g., m.3243A>G, m.8344A>G)
	mt-rRNA gene mutations (e.g., m.1555A>G)
Protein-encoding gene	mt-mRNA gene mutations (e.g., m.8993T>G/C; primary LHON mutations)
Mendelian mitochondrial disorders	
OXPHOS structural gene	Mutations of complex I-V protein subunits
OXPHOS assembly factor	Mutations in proteins required for complex assembly (e.g., SURF1, BCS1L, ACAD9, TMEM70)
mtDNA maintenance gene	Mutations in proteins involved in mtDNA replication (e.g., POLG, PEO1, MGME1, RNASEH1) or dNTP synthesis/salvage (e.g., DGUOK, TK2) leading to secondary mtDNA abnormalities (multiple mtDNA deletions or mtDNA copy number loss)
mt-translation disorders	Mutations in translation and release factors (e.g., TUFM, TSFM, C12orf65)
	Mutations in mt-tRNA modifying proteins (e.g., MTO1, GTPBP3, MTFMT, TRIT1)
	Mutations in mRNA processing enzymes (e.g., LRPPRC, ELAC2, PNPT1, MRPP2)
	Mutations in mt-aminoacyl tRNA synthetases (e.g., AARS2, DARS2, RARS2, EARS2, YARS2, FARS2)
	Mutations in mitoribosomal proteins (e.g., MRPS16, MRPS22, MRPL3, MRPL12, MRPL44)
Lipid metabolism	Mutations in AGK, TAZ
Phospholipid remodeling	Mutations in SERAC1
Disulfide relay system	Mutations in GFER
Mitochondrial homeostasis	Mutations in FBXL4, CLPB
Fe-S cluster assembly/homeostasis	Mutations in ISCU, BOLA3, NFU1, IBA57, LYRM4
Mitochondrial fission/fusion	Mutations in OPA1, MFN2, DLP1
Mitochondrial protein import	Mutations in TIMM8A, DNAJC19
Apoptosis	Mutations in AIF1, APOPT1, FASTKD2
Coenzyme Q10 biogenesis	Mutations in COQ2, COQ4, COQ9, PDSS1, PDSS2, CABC1, ADCK3
Mitochondrial chaperones	Mutations in SPG7, AFGL32
Mitochondrial metabolism	Mutations in ETHE1, HIBCH, ECHS1

Fig. 1. Mitochondrial donation. Mitochondrial donation involves the transfer of the nuclear chromosomal DNA from an oocyte or zygote from a woman with pathogenic mtDNA mutation (shown in pink) into an enucleated, recipient donor oocyte or zygote (blue). In these techniques the mitochondria (and mitochondrial DNA) are from the donor (shown in green). (**A**) Metaphase II spindle transfer involves removal of the spindle from the donor egg and transfer of the patient's spindle into the donor oocyte followed by fertilization and development. (**B**) Pronuclear transfer occurs after fertilization and the pronuclei are transferred from the patient zygote to the donor zygote.

transmitting some mtDNA mutations and has become an option for some women with specific mtDNA mutations (*18*, *19*). Furthermore, TALENS and other potential genetic editing techniques (see below) may be able to reduce the level of mtDNA mutation in individual oocytes (*20*). The latter is an attractive approach, but in cases with high levels of heteroplasmy, the total mtDNA copy number may be lowered to levels that prevent implantation, and these techniques would not be amenable for homoplasmic mtDNA mutations.

For women with high levels of heteroplasmic mutations or those with homoplasmic mutations, the present options are in reality limited to ovum donation or adoption, although mitochondrial donation may soon become a viable option. Mitochondrial donation is an in vitro fertilization (IVF) technique that involves the transfer of the nuclear genes from an oocyte or zygote at the metaphase II spindle, polar body, or pronuclear stage (*21–24*) into an enucleated donor oocyte or zygote (Fig. 1). These techniques use an established method (*25*) successfully applied both to animal models (*26*) and to human oocytes with minimal carryover of mtDNA (*22*, *24*, *27*). These techniques could prevent the transmission of mtDNA disease, but they raise ethical issues (*28*) and may not be univer-

sally available. In the United Kingdom, after extensive ethical deliberations, public consultation, and independent scientific scrutiny, new regulations to allow mitochondrial donation were debated and approved in both Houses of Parliament in February 2015 and became legal in March 2015, and are regulated by the Human Fertilisation and Embryology Authority.

Nuclear genetic mitochondrial disease

One area of mitochondrial disease research that has seen important recent advances has been the application of next-generation sequencing technologies to the identification of genes linked with Mendelian mitochondrial disorders, and the subsequent characterization of their associated proteins. Mitochondrial disorders are particularly amenable to such strategies, as they are characterized by a complex and expanding spectrum of clinical phenotypes associated with marked genetic heterogeneity difficult to resolve with candidate gene approaches.

The mitochondrial proteome is well characterized (*29*). Therefore, specific biochemical signatures of OXPHOS dysfunction identified as part of a multidisciplinary diagnostic work-up (e.g., an isolated or multiple OXPHOS deficiency)

and a mitochondrial localization can help prioritize and diagnose candidate gene variants when incorporated in the bioinformatic pipeline. Both exon capture/sequencing of all predicted mitochondrial genes (so-called "Mitoexome") (*30*, *31*) and whole-exome sequencing (WES) (*32*, *33*) have been applied to cohorts of patients with severe, early-onset presentations of mitochondrial disease. This assumes an autosomal recessive mode of inheritance, although in some patient cohorts, particularly the late-onset adult mitochondrial presentations, this filtering strategy may not be as applicable. Where large, predominantly pediatric, cohorts have been studied, diagnostic yields range from ~20% to 60% (*30–33*). In cases of small families and singleton cases, however, the availability of robust next-generation sequencing and variant filtering protocols can produce diagnoses (*34*), facilitating reliable prenatal screening and genetic counseling. More recently, WES has successfully been used to identify genetic defects in cohorts of adult patients (*35*).

In addition to molecular diagnostics, WES of patients with mitochondrial disease has provided important insight into mitochondrial pathophysiology and basic biochemical pathways. This has been particularly valuable in those

patients with multiple OXPHOS disorders due to a generalized disorder of mitochondrial protein synthesis implicating a number of processes in intraorganellar translation that have been studied in detail. These include processing of mt-mRNA transcripts, assembly and function of the mitoribosome and translation machinery, posttranscriptional modification of mt-tRNA, and function of mt-aminoacyl tRNA synthetases (mt-ARSs) (Fig. 2).

Rescue of the mitochondrial phenotype after lentiviral delivery of a wild-type copy of the candidate gene is the gold-standard practice to assign pathogenicity. Defects involving mt-ARS enzymes highlight many of the peculiarities of mitochondrial disease presentations, with mutation of different genes in a common pathway leading to a wide-ranging pathology with central nervous system and other organs involved. For some genes, however, there are clear genotype-phenotype correlations, particularly in relation to neuroradiological features, such as pontocerebellar hypoplasia type 6 for *RARS2* mutations (*36*) and leukoencephalopathy with thalamus and brainstem involvement for *EARS2* mutations (*37*).

One of the most fascinating groups of disorders relates to nuclear-encoded mt-tRNA–modifying enzymes, given that >30 different modified mt-tRNA positions have been identified as necessary to facilitate faithful protein translation (*38*). Human defects arising from mutations in these mt-tRNA–modifying enzymes also show organ specificity. For example, the related proteins MTO1 (*39*) and GTPBP3 (*40*) are almost always associated with cardiomyopathy when mutated. The application of mitoribosome profiling to these disorders (*41*) shows promise in unraveling the molecular mechanisms, which may lead to novel treatment strategies (*42*).

By applying WES to mitochondrial patients, proteins previously thought not to be involved in mitochondrial function, nor with clear evidence of mitochondrial localization, have been identified as potentially causative of disease. For example, The FBXL4 protein was previously thought to localize exclusively in the nucleus but has been implicated as a cause of early-onset mitochondrial encephalopathy associated with severe loss of mtDNA copy number (*43*, *44*).

Studies have also highlighted avenues for therapeutic intervention and the "repurposing" of some mitochondrial proteins relative to their function. *ACAD9* encodes an enzyme of mitochondrial β-oxidation that also functions as a key chaperone of complex I biogenesis (*45*); patients with mutations in this gene and complex I deficiency can partially respond to riboflavin therapy. Also, the neurodegenerative disease genes *SPG7* and *AFGL32* have been identified as causing late-onset disorders of mtDNA maintenance in patients with complex neurological presentations, characterized by progressive external ophthalmoplegia and cerebellar ataxia (*46*, *47*).

Although WES has been successful in identifying Mendelian mitochondrial disease, challenges remain. Late-onset, likely dominant mitochondrial disorders may prove difficult to solve by WES; a diagnostic application of whole-genome sequencing should facilitate the identification of copy number variations (CNVs) and deep intronic mutations missed by exome capture. However, debate is ongoing to determine when to undertake WES within a multidisciplinary diagnostic algorithm that incorporates functional testing (assessment of mitochondrial enzyme activities); in patient populations with high rates of parental consanguinity, WES should be a frontline

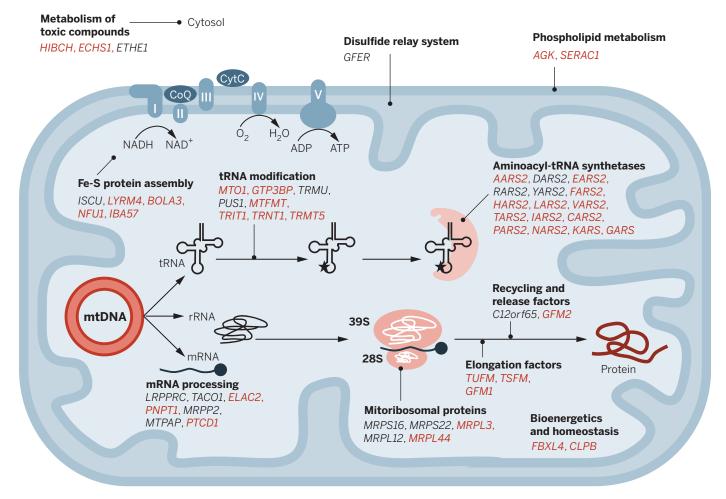**Fig. 2. Nuclear gene defects causing multiple mitochondrial OXPHOS abnormalities.** Schematic showing mitochondrial genes and pathways, many involved in key component steps of mitochondrial translation, in which human mitochondrial diseases associated with combined OXPHOS activity deficiencies have been identified. Those shown in red indicate disease genes identified by next-generation, largely whole-exome sequencing studies.

test prior to a muscle biopsy. Clearly, in some scenarios these tests assist the interpretation of the sequence data.

Treatment of mitochondrial disease

Treating patients with established mitochondrial disease remains a major challenge. For the vast majority of patients, therapy is limited to either preventing or treating the complications of mitochondrial diseases, such as diabetes, cardiac involvement, and epilepsy. These limitations explain the efforts being made by many groups to develop effective treatments and to prevent the transmission of mitochondrial disease.

As mentioned above, there are some rare genetic defects that may respond to specific therapies. Specifically, patients unable to synthesize ubiquinone may respond to dietary ubiquinone supplementation, or patients with ACAD9 deficiency may benefit from treatment with riboflavin. Many compounds or approaches have been touted as putative therapeutics, and there have been numerous reports of cocktails of assorted nutrients, vitamins, and antioxidants. However, the number of properly controlled clinical trials has been limited (48). This is due in major part to the difficulties in finding sufficient patients with similar clinical presentations and/or genotypes to conduct controlled, meaningful clinical trials. This problem is being addressed by the development of patient cohorts and registries (4). Below, we highlight examples with potential therapeutic applications (Fig. 3).

Relieving metabolic stress and increasing mitochondrial biogenesis

Many OXPHOS disorders exhibit decreased cellular NAD$^+$/NADH ratios (ratios of nicotinamide adenine dinucleotide to its reduced form), leading to a loss of important NAD$^+$-linked enzymatic activities. This is exemplified by the sirtuins SIRT1 and SIRT3, which activate key transcription factors that in turn promote expression of gene products that regulate mitochondrial biogenesis. Treatment of mice deficient in the replicative helicase Twinkle ("deletor" mice) with the NAD$^+$ precursor nicotinamide riboside (NR) led to increased NAD$^+$ in skeletal muscle and brown adipose tissue (49). Consistent with the importance of retaining NAD$^+$ levels under conditions of mitochondrial dysfunction, inhibition of the NAD$^+$-consuming enzyme poly(adenosine diphosphate) ribose phosphorylase (PARP1) has also been shown to be efficacious with models of mitochondrial dysfunction (50), although human trials have not been reported. Increasing mitochondrial mass alone may be sufficient to help resolve mitochondrial dysfunction, because an increase in partially functioning mitochondria may be sufficient to restore OXPHOS activity. In particular, a key question has been how to induce PGC1 isoforms, the master regulators of mitochondrial proliferation. Several mitochondrial proliferators have been championed, including the pan-PPAR (peroxisome proliferator–activated receptor) agonist bezafibrate, the polyphenols resveratrol and epicatechin, and the ribonucleo-

tide AICAR. The literature surrounding the efficacy of these putative proliferators in ameliorating mitochondrial dysfunction is complex and often contradictory (51), requiring further study. It should also be considered that mitochondrial biogenesis can be engineered by exercise programs and has been shown to be safe and beneficial for patients with mitochondrial disease (52).

Improving the efficiency of OXPHOS or the mitochondrial protein synthesis system

The majority of cytochrome c is loosely bound to the anionic lipid cardiolipin, which is found mostly in the outer leaflet of the inner mitochondrial membrane. A small proportion, however, binds through hydrophobic interaction, causing a conformational change that results in cytochrome c peroxidase activation and subsequent cardiolipin oxidation (53). This can result in a loss of membrane curvature and cristae formation, detachment of cytochrome c from the membrane, reduced electron transfer efficiency, and eventually apoptosis (54, 55). An unusual tetrapeptide derivative, SS-31 or Bendavia, has been shown to localize to mitochondria and bind selectively to cardiolipin in vitro, inhibiting this hydrophobic interaction and promoting an increase in OXPHOS efficiency in isolated organelles (56). This compound has also been shown

to protect against loss of mitochondrial structure in a rat model of ischemic reperfusion injury, which is suggested to explain the more rapid recovery of ATP production following injury (57).

Many disorders are due to mutations in genes encoding mt-tRNAs, leading to a deficiency in mitochondrial protein synthesis and subsequent OXPHOS abnormality. Often, the mutation causes instability of the mt-tRNA. Mitochondrial leucyl tRNA synthetase can bind and protect RNA in the mitochondrial matrix of *Saccharomyces cerevisiae*. Overexpression of just 69 C-terminal residues of the human ortholog was sufficient to promote stabilization of pathogenic mt-tRNA species in cultured human cells, leading to an increase in mitochondrial protein synthesis and partial restoration of oxidative phosphorylation (58, 59). We propose that small-molecule screening to identify compounds that can stabilize mt-tRNAs is worth investigating.

Restoring mtDNA homeostasis or shifting mtDNA heteroplasmy

Mitochondrial neurogastrointestinal encephalomyopathy (MNGIE) is caused by a defect in thymidine phosphorylase that catabolizes thymidine and deoxyuridine. The subsequent buildup of these compounds eventually causes a deoxynucleotide triphosphate (dNTP) imbalance evidenced by
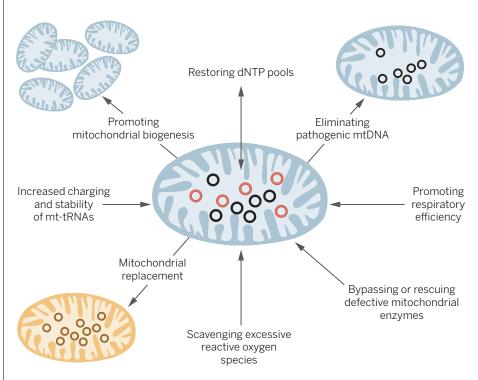
Fig. 3. Potential therapeutic interventions in patients with mitochondrial disease. A generic dysfunctional mitochondrion is shown (blue; middle). It can house heteroplasmic mtDNA (black, normal; red, mutated) or defective nuclear gene products. Therapeutic approaches include mitochondrial replacement (brown). Additional strategies include targeting alternative oxidases or single-subunit NADH dehydrogenases to mitochondria to bypass defective components of the oxidative phosphorylation machinery (67) and antioxidant ubiquinone derivatives (idebenone, EPI-473) (68, 69). Rescuing defects of mitochondrially encoded proteins by recoding for nuclear expression and mitochondrial targeting (allotopic expression) is controversial but undergoing trial (70).

increased matrix thymidine triphosphate (TTP) and decreased deoxycytidine triphosphate (dCTP) levels. By transducing the liver of an MNGIE mouse model with adeno-associated virus (AAV) expressing human thymidine phosphorylase, the levels of nucleoside pools in several, but not all tissues, were restored as nucleoside levels can equilibrate between cells and tissues (60). Although the MNGIE model has its limitations, these results are impressive and clinical trials have been suggested for those patients who may not be suitable for stem cell transplantation.

Another mitochondrial disorder associated with an imbalance in nucleotide metabolism is caused by a defect in the enzyme thymidine kinase 2 (TK2). This mitochondrial matrix protein phosphorylates deoxypyrimidine nucleosides to generate their respective monophosphates, thymidine monophosphate (TMP) and deoxycytidine monophosphate (dCMP). Patients with autosomal recessive mutations can present at any stage of life, but often present in early childhood with profound neuromuscular disease and mtDNA depletion. Encouraging results have been reported in a TK2-deficient mouse model, simply by orally administering the two deoxypyrimidine monophosphates early after birth (61). Partial restoration of mitochondrial TTP concentrations, mtDNA levels, and OXPHOS components was noted in various tissues, although this effect was markedly reduced in the brains of pups at a stage after the blood-brain barrier had been fully developed. Notably, an increase in life expectancy was measurable. The simplicity of this treatment is striking, and the potential for therapy in humans is clear.

In patients with heteroplasmic mtDNA mutations, the pathogenic mutation is normally recessive, with dysfunction only becoming apparent when >60% of mtDNA carried the mutation. Recent studies with cultured human cells have involved the design of TAL effector nucleases (TALENs) to specifically cleave mtDNA carrying defined pathogenic deletions and point mutations (62), or have used zinc finger nucleases to destroy the mtDNA molecules carrying either a single deletion or the pathogenic m.8993T>G point mutation (63). The natural next step for this approach would be to deliver AAV expressing such designer nucleases to heteroplasmic animal models with stable populations of the pathogenic mtDNA.

Could genome editing be used to target pathogenic mtDNA? There is a great deal of current interest in the CRISPR-Cas9–mediated genome editing process. Cas9 is an RNA-guided endonuclease and the RNA can be engineered to provide the sequence selectivity. Although numerous RNA species have been postulated to be imported into the human mitochondrial matrix, none of these species has a defined mitochondrial function. Irrespective of this, RNA vectors for mitochondrial import have been designed and published, along with details of a putative RNA import pathway (64, 65). Cas9-mediated cleavage of the mitochondrial genome could potentially be attained by targeting Cas9 protein

and a designed RNA chimera to the mitochondrion, with error-prone nonhomologous end joining effectively producing a gene knockout. Further complications would have to be resolved if Cas9-mediated knock-in mutations were ever likely, as homologous recombination of mammalian mtDNA appears to be rare (66).

Conclusion

The past 5 years have been an exciting time in mitochondrial disease research. Until recently, the complexity of the genetics and the clinical variability made mitochondrial disease a particularly challenging area of medicine. However, remarkable progress has been made, including the establishment of large patient cohorts; application of next-generation sequencing techniques to previously undiagnosed patients; the development of animal models of mitochondrial disease (not covered in this review); ethical, scientific, and legislative aspects of mitochondrial donation; and the development of potential therapeutic strategies. The next few years are likely to be equally exciting, with the major challenges of pinpointing the genetic defects in those cases not identified by WES, understanding the mechanisms involved in tissue specificity, and predicting disease progression. Finally, and most important, the development of effective treatments for all patients with mitochondrial disease must become a reality.

REFERENCES AND NOTES

1. E. Lapuente-Brun et al., Science 340, 1567–1570 (2013).
2. S. Anderson et al., Nature 290, 457–465 (1981).
3. W. J. Koopman, P. H. Willems, J. A. Smeitink, N. Engl. J. Med. 366, 1132–1141 (2012).
4. V. Nesbitt et al., J. Neurol. Neurosurg. Psychiatry 84, 936–938 (2013).
5. G. Singh, M. T. Lott, D. C. Wallace, N. Engl. J. Med. 320, 1300–1305 (1989).
6. R. McFarland et al., Neurology 69, 911–916 (2007).
7. Z. Zhu et al., Nat. Genet. 20, 337–343 (1998).
8. A. Agostino et al., Hum. Mol. Genet. 12, 399–413 (2003).
9. A. Hodgkinson et al., Science 344, 413–415 (2014).
10. D. Skladal, J. Halliday, D. R. Thorburn, Brain 126, 1905–1912 (2003).
11. G. S. Gorman et al., Ann. Neurol. 77, 753–759 (2015).
12. A. Pyle et al., PLOS Genet. 11, e1005040 (2015).
13. R. N. Lightowlers, P. F. Chinnery, D. M. Turnbull, N. Howell, Trends Genet. 13, 450–455 (1997).
14. L. M. Cree et al., Nat. Genet. 40, 249–254 (2008).
15. T. Wai, D. Teoli, E. A. Shoubridge, Nat. Genet. 40, 1484–1488 (2008).
16. G. S. Gorman et al., N. Engl. J. Med. 372, 885–887 (2015).
17. V. Nesbitt et al., Eur. J. Hum. Genet. 22, 1255–1259 (2014).
18. J. Steffann et al., J. Med. Genet. 44, 664–669 (2007).
19. S. Monnot et al., Hum. Mutat. 32, 116–125 (2011).
20. P. Reddy et al., Cell 161, 459–469 (2015).
21. M. Tachibana et al., Nature 461, 367–372 (2009).
22. L. Craven et al., Nature 465, 82–85 (2010).
23. T. Wang et al., Cell 157, 1591–1604 (2014).
24. D. Paull et al., Nature 493, 632–637 (2013).
25. J. McGrath, D. Solter, Science 220, 1300–1302 (1983).
26. A. Sato et al., Proc. Natl. Acad. Sci. U.S.A. 102, 16765–16770 (2005).
27. M. Tachibana et al., Nature 493, 627–631 (2013).
28. http://nuffieldbioethics.org/project/mitochondrial-dna-disorders/
29. D. J. Pagliarini et al., Cell 134, 112–123 (2008).

30. S. E. Calvo et al., Sci. Transl. Med. 4, 118ra10 (2012).
31. D. S. Lieber et al., Neurology 80, 1762–1770 (2013).
32. T. B. Haack et al., J. Med. Genet. 49, 277–283 (2012).
33. R. W. Taylor et al., JAMA 312, 68–77 (2014).
34. A. Götz et al., Am. J. Hum. Genet. 88, 635–642 (2011).
35. A. Reyes et al., Am. J. Hum. Genet. 97, 186–193 (2015).
36. S. Edvardson et al., Am. J. Hum. Genet. 81, 857–862 (2007).
37. M. E. Steenweg et al., Brain 135, 1387–1394 (2012).
38. T. Suzuki, T. Suzuki, Nucleic Acids Res. 42, 7346–7357 (2014).
39. D. Ghezzi et al., Am. J. Hum. Genet. 90, 1079–1087 (2012).
40. R. Kopajtich et al., Am. J. Hum. Genet. 95, 708–720 (2014).
41. K. Rooijers, F. Loayza-Puch, L. G. Nijtmans, R. Agami, Nat. Commun. 4, 2886 (2013).
42. C. Tischner et al., Hum. Mol. Genet. 24, 2247–2266 (2015).
43. P. E. Bonnen et al., Am. J. Hum. Genet. 93, 471–481 (2013).
44. X. Gai et al., Am. J. Hum. Genet. 93, 482–495 (2013).
45. J. Nouws, H. Te Brinke, L. G. Nijtmans, S. M. Houten, Hum. Mol. Genet. 23, 1311–1319 (2014).
46. G. Pfeffer et al., Brain 137, 1323–1336 (2014).
47. G. S. Gorman et al., JAMA Neurol. 72, 106–111 (2015).
48. G. Pfeffer, K. Majamaa, D. M. Turnbull, D. Thorburn, P. F. Chinnery, Cochrane Database Syst. Rev. 4, CD004426 (2012).
49. N. A. Khan et al., EMBO Mol. Med. 6, 721–731 (2014).
50. R. Cerutti et al., Cell Metab. 19, 1042–1049 (2014).
51. J. C. Komen, D. R. Thorburn, Br. J. Pharmacol. 171, 1818–1836 (2014).
52. T. Taivassalo et al., Brain 129, 3391–3401 (2006).
53. J. Hanske et al., Proc. Natl. Acad. Sci. U.S.A. 109, 125–130 (2012).
54. V. E. Kagan et al., Nat. Chem. Biol. 1, 223–232 (2005).
55. M. Schlame, M. Ren, Biochim. Biophys. Acta 1788, 2080–2083 (2009).
56. H. H. Szeto, Br. J. Pharmacol. 171, 2029–2050 (2014).
57. A. V. Birk et al., J. Am. Soc. Nephrol. 24, 1250–1261 (2013).
58. E. Perli et al., EMBO Mol. Med. 6, 169–182 (2014).
59. H. T. Hornig-Do et al., EMBO Mol. Med. 6, 183–193 (2014).
60. J. Torres-Torronteras et al., Mol. Ther. 22, 901–907 (2014).
61. C. Garone et al., EMBO Mol. Med. 6, 1016–1027 (2014).
62. S. R. Bacman, S. L. Williams, M. Pinto, S. Peralta, C. T. Moraes, Nat. Med. 19, 1111–1113 (2013).
63. P. A. Gammage, J. Rorbach, A. I. Vincent, E. J. Rebar, M. Minczuk, EMBO Mol. Med. 6, 458–466 (2014).
64. A. Smirnov et al., J. Biol. Chem. 285, 30792–30803 (2010).
65. A. Smirnov et al., RNA 14, 749–759 (2008).
66. E. Hagström, C. Freyer, B. J. Battersby, J. B. Stewart, N. G. Larsson, Nucleic Acids Res. 42, 1111–1116 (2014).
67. R. El-Khoury et al., PLOS Genet. 9, e1003182 (2013).
68. T. Klopstock et al., Brain 134, 2677–2686 (2011).
69. D. Martinelli et al., Mol. Genet. Metab. 107, 383–388 (2012).
70. B. L. Lam et al., JAMA Ophthalmol. 132, 428–436 (2014).

RESEARCH

Designing greener flow cell batteries
Lin *et al.*, p. 1529

IN *SCIENCE* JOURNALS
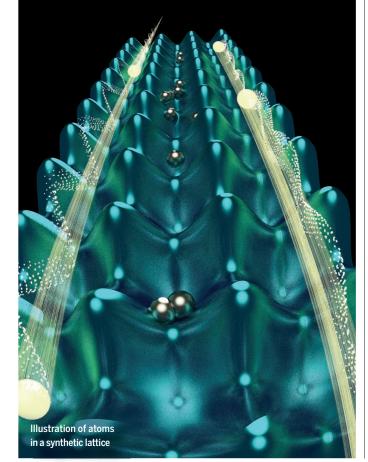
Edited by **Caroline Ash**

QUANTUM SIMULATION

Visualizing edge states in atomic systems

Simulating the solid state using ultracold atoms is an appealing research approach. In solids, however, the charged electrons are susceptible to an external magnetic field, which curves their trajectories and makes them skip along the edge of the sample. To observe this phenomenon with cold atoms requires an artificial magnetic field to have a similar effect on the neutral atoms (see the Perspective by Celi and Tarruell). Stuhl *et al.* obtained skipping orbits with bosonic atoms using a lattice that consisted of an array of atoms in one direction and three internal atomic spin states in the other. In a complementary experiment, Mancini *et al.* observed similar physics with fermionic atoms. — JS

Science, this issue pp. 1514 and 1510; see also p. 1450

Illustration of atoms in a synthetic lattice

MITOCHONDRIAL IMPORT

Dissecting the mitochondrial entry portal

Mitochondria, the powerhouses of the cell, are mainly composed of proteins made in the cytosol. These newly synthesized proteins need to be imported across the organelle's membrane through dedicated protein import machinery. Shiota *et al.* have worked out the architecture and mechanism of the mitochondrial protein import channel. — SMH

Science, this issue p. 1544

PROTEIN FOLDING

Interactions that slow protein folding

As proteins fold, they diffuse over an energy barrier that separates unfolded and folded states. The transition path defines how a single protein crosses the barrier and so contains key information on the mechanism of folding. Transition paths have not yet been experimentally observed, but Chung *et al.* have discovered which structural features of the protein affect the duration of the transition. As the protein folds, non-native salt bridges form and break, slowing diffusion along the transition path. — VV

Science, this issue p. 1504

NANOMATERIALS

Flat perovskite crystals

Bulk crystals and thick films of inorganic-organic perovskite materials such as $CH_3NH_3PbI_3$ have shown promise as active material for solar cells. Dou *et al.* show that thin films—a

single unit cell or a few unit cells thick—of a related composition, $(C_4H_9NH_3)_2PbBr_4$, form squares with edges several micrometers long. These materials exhibit strong and tunable blue photoluminescence. — PDS

Science, this issue p. 1518

ASTROPHYSICS

Placing bounds on gravity wave detection

Gravity waves are expected to be generated by the interaction of the massive bodies in black-hole binary systems. As gravity waves distort spacetime, it should be possible to verify their existence as they interfere with the pulses emitted by millisecond pulsars. However, after monitoring 24 pulsars with the Parkes radio telescope for 12 years, Shannon *et al.* found no detectable variation in pulsar records. This nondetection result indicates that a new detection strategy for gravity waves is needed. — ISO

Science, this issue p. 1522

TRANSPOSONS

Parasitic DNA targets a genomic home

Long-terminal-repeat (LTR) retrotransposons are a form of parasitic DNA that can jump around within the host's genome. To avoid damaging resident genes, they have been selected to integrate away from protein-coding sequences. For instance, the fission yeast LTR retrotransposon Tf1 inserts at nucleosome-free regions in gene promoters. Jacobs *et al.* show that Tf1 is directed to these

insertion sites by a specific DNA binding protein, Sap1, which forms DNA replication–fork barriers.

Science, this issue p. 1549

IMMUNOLOGY
Mitochondria signal 'eat me'

Cardiolipin becomes exposed if mitochondria become damaged. Under these circumstances it becomes an "eat me" signal. Cardiolipin is a phospholipid found in the inner mitochondrial membrane and in bacterial membranes. Balasubramanian *et al*. show that cardiolipin stimulates macrophages to phagocytose the damaged cells. But it also inhibits cytokine production from macrophages when they encounter bacterial lipopolysaccharide, which resembles cardiolipin in structure. — JFF

Sci. Signal. **8**, ra95 (2015).

EVOLUTIONARY ECOLOGY
Climate change decoupling mutualism

Many coevolved species have precisely matched traits. For example, long-tongued bumblebees are well adapted for obtaining nectar from flowers with long petal tubes. Working at high altitude in Colorado, Miller-Struttmann *et al*. found that long-tongued bumblebees have decreased in number significantly over the past 40

years. Short-tongued species, which are able to feed on many types of flowers, are replacing them. This shift seems to be a direct result of warming summers reducing flower availability, making generalist bumblebees more successful than specialists and resulting in the disruption of long-held mutualisms. — SNV
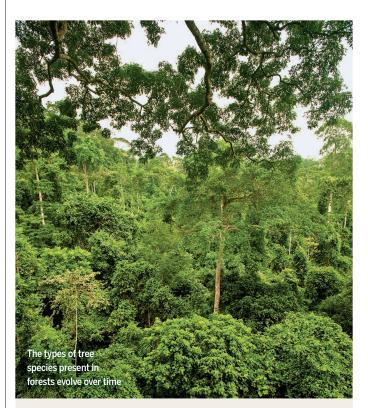
Science, this issue p. 1541

VIROLOGY
Therapeutic opportunity knocks

The urinary tract of most adults harbors JC polyomavirus (JCV) asymptomatically but persistently. In immunocompromised individuals, JCV can opportunistically infect the brain to cause the debilitating and frequently fatal disease progressive multifocal leukoencephalopathy (PML). No treatments are currently available for PML, but two papers have identified and exploited a gap in immune responses to JCV. Ray *et al*. report that JCV strains found in the cerebrospinal fluid of PML patients have mutations that prevent antibody neutralization and that these blind spots can be overcome by vaccination. Jelcic *et al*. suggest that broadly neutralizing antibodies derived from a patient who recovered from PML can also be used therapeutically. — ACC

Sci. Transl. Med. **7**, 306ra151, 306ra150 (2015).

Generalist bees replace specialists as climate warms

The types of tree species present in forests evolve over time

EVOLUTIONARY ECOLOGY
Successional specialism in forests

In forests, different tree species tend to occupy different stages of ecological succession, a process whereby the species structure of a particular habitat changes over time. However, scientists do not fully understand the evolutionary relationships behind these patterns. Letcher *et al*. studied this in tropical forest tree species across a gradient of precipitation. Specialism for particular stages of succession tended to be more conserved in related species in wet forest species than in dry forest species. More extreme environmental differences between early and late successional habitats in wet forest than in dry forest may cause this pattern, leading to successional niche similarity within species-rich rainforest tree lineages. — AMS

J. Ecol. **103**, 1276 (2015).

DEVELOPMENT
A wild hair day for mice

Petting your cat backward will probably elicit a not-so-friendly response. This is because a cat's fur grows from hair follicles that have a specific orientation. Proteins that make up the planar cell polarity (PCP) signaling pathway,

which regulate the polarization of groups of cells on a plane, help orient hair follicle growth in many vertebrates. Chang *et al*. now report on an intriguing mouse strain that has a ridge of hair across their backs where the hair follicles are oriented in the opposite direction. Mutations in the genes that encode Frizzled 6, a PCP protein, and Astrotactin2, known

ECOLOGY

Traffic noise effects on birds

Bird populations decline near roads, but teasing apart the reasons for these declines can be difficult. To identify how road noise affects migratory bird species, Ware *et al.* used traffic noise playbacks to create a "phantom road" in a road-free area in Idaho. Overall bird numbers were 31% lower at the phantom road site than at a quiet control site. Birds that stayed at the phantom road site had a lower body condition index, an indicator of fitness. One reason for the body condition changes is the need for increased vigilance in a noisy environment, reducing the time available for foraging. The noise levels used in the experiment are similar to those in suburban neighborhoods and in many protected areas. Noise reduction is thus of crucial importance for conservation. — JFU

Proc. Natl. Acad. Sci. U.S.A. 10.1073/pnas.1504710112 (2015).

Traffic noise repels and degrades the fitness of birds like the MacGilivray's warbler

for its role in guiding migrating neurons, are responsible for giving the mice such a wild hairdo. — BAP

PLOS Genet. 10.1371/journal.pgen.1005532 (2015).

ENERGY ECONOMICS

Uncovering site selection bias

Despite internal validity and massive replication, program evaluations may bias out-of-sample predictions and thus misinform policy discussions. Allcott analyzed 111 randomized controlled trials (RCTs) of the Opower energy efficiency intervention, involving 8.6 million U.S. households. Large-scale replication is intended to ensure external validity across RCT sites, populations, contexts, etc., but energy utilities were not all equally willing and able to participate. Utilities having more environmentalist customers were more inclined to partner earlier and to target their most high-consuming customers. Thus, earlier interventions, despite many replications, overestimated impacts relative to effects realized in later trials. — BW

Quart. J. Econ. 10.1093/qje/qjv015 (2015).

VIROLOGY

Giant virus varieties keep growing

A recent fascinating development in basic virology has been the discovery of "giant" viruses that are visible by light microscopy. Legendre *et al.* now report a fourth type of giant virus called *Mollivirus sibericum*. Like its cousin *Pithovirus sibericum*, it can still infect acanthamoeba (a common soil protozoan) after being found in 30,000-year-old Siberian permafrost. Its diameter spans 0.6 µm, with a 623-kb genome, but it differs from other giant viruses in how it replicates, how its genome is organized, and in the proteins it encodes. Nearly 65% of the proteins encoded by *Mollivirus* have no known homologs. — BJ
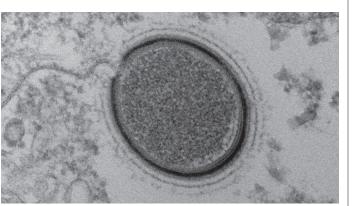
Proc. Natl. Acad. Sci. U.S.A. 10.1073/pnas.1510795112 (2015).

GEOPHYSICS

Broadening the source for hot spots

Certain volcanoes are fed by plumes of hot material originating at the very base of Earth's rocky mantle. Dynamic arguments suggest that the conduits feeding these hot-spot volcanoes should be narrow, because of the relatively small areas over which they erupt. French and Romanowicz use an improved whole-mantle seismic imaging technique to show that plumes are actually quite broad. Their surprising results imply that plumes are long-lived and may have a thermochemical origin. The vertical orientation of conduits suggests sluggish convection deep within the mantle. — BG

Nature 10.1038/nature14876 (2015).

LIVER CANCER

Suspicious behavior by a harmless virus

Every year doctors diagnose over 700,000 people worldwide with liver cancer. The most common risk factors are alcohol abuse and chronic infection with hepatitis B or hepatitis C viruses. A new study hints at a possible nefarious role of adeno-associated virus type 2 (AAV2), which infects about half of all adults with no obvious adverse effects. Nault *et al.* sequenced the genomes of 193 liver tumors and found that 11 harbored AAV2 sequences integrated near genes previously linked to cancer development. The viral sequences altered the expression of these genes, but whether the integration events contributed causally to tumorigenesis is unclear. Because modified versions of AAV2 are used as gene therapy vectors, answering this question is a priority. — PAK

Nat. Genet. 10.1038/ng.3389 (2015).

Transmission electron micrograph of a *Mollivirus* particle

ALSO IN *SCIENCE* JOURNALS

Edited by **Caroline Ash**

AGING
Transcriptional control of cell senescence

Senescent cells that have stopped proliferating secrete molecules that influence the cells around them. Prevention of this senescence-activated secretory phenotype seems to slow organismal aging. Kang *et al.* explored the regulatory process behind cell senescence and found that DNA damage led to stabilization of the transcription factor GATA4 (see the Perspective by Cassidy and Narita). Increased activity of GATA4 in senescent cells stimulated genes encoding secreted factors. GATA4 also accumulates in the brains of aging mice or humans. — LBR

Science, this issue p. 1503; see also p. 1448

BIOCATALYSIS
A clean and green approach to amines

Enzymes evolved to operate in water and to modify their substrates using comparatively nontoxic reagents. Thus, a major advantage of applying enzymes to synthetic chemistry is their compatibility with environmentally benign conditions. Mutti *et al.* report that two enzymes—alcohol and amine dehydrogenases—can operate in tandem to convert alcohols to amines. The reaction proceeds with ammonium as the only input and water as the only byproduct. The mechanism relies on consecutive oxidation and reduction steps, with hydrogen shuttled by a nicotinamide coenzyme. — JSY

Science, this issue p. 1525

BATTERIES
A solution for scalable-flow batteries

Flow batteries, in which the redox active components are held in tanks separate from the active part of the cell, offer a scalable route for storing large quantities of energy. A challenge for their large-scale development is to avoid formulations that depend on toxic transition metal ions. Lin *et al.* show that quinones can be dissolved in alkaline solutions and coupled with ferricyanides to make a flow cell battery (see the Perspective by Perry). This gives scope for developing flow cells with very low costs, high efficiencies at practical power densities, simplicity of operation, and inherent safety. — MSL

Science, this issue p. 1529; see also p. 1452

CATALYSIS
A trio helps activate C-H bonds in alcohols

Enzymes can accelerate chemical reactions by activating specific portions of a molecule through well-placed H bonds. Jeffrey *et al.* showcase the power of H-bonding in a synthetic context. Here, reactivity at the C centers of alcohols is selectively induced by using an H-bonding catalyst to bind the hydroxyl group of the alcohol. The adjacent C-H bonds now become susceptible to a reaction accelerated by another pair of catalysts. In combination, the trio of catalysts promotes C-C bond formation at the alcohol C within an array of competing sites. — JSY

Science, this issue p. 1532

CLIMATE
Extreme events under climate change

Extreme climate events, such as heatwaves and droughts, can have devastating consequences for human populations. Many of these events are likely to become more common under climate change. But is it correct to say that an individual climate event has been caused by climate change? In his Perspective, Solow argues that even if the event frequency (e.g., of drought conditions in Europe) increases, it is not possible to say whether an individual event would have happened without climate change. The effects of climate change have become so pervasive that it may not even make sense to ask the question. — JFU

Science, this issue p. 1444

PALEOCEANOGRAPHY
Flushing the deep ocean

Have changes in ocean circulation contributed to the sudden increases in the concentration of atmospheric carbon dioxide that occurred during the last deglaciation? Chen *et al.* provide a high-resolution radiocarbon record for that time, derived from deep sea corals. This record shows that two deep ocean "flushing" events were accompanied by abrupt rises in carbon dioxide and Northern Hemispheric warming. There is a clear connection between these ocean processes and the atmosphere during this interval. — HJS

Science, this issue p. 1537

RESEARCH ARTICLE

PROTEIN FOLDING

Structural origin of slow diffusion in protein folding

Hoi Sung Chung,[1]*† Stefano Piana-Agostinetti,[2]*†
David E. Shaw,[2,3]† William A. Eaton[1]†

Experimental, theoretical, and computational studies of small proteins suggest that interresidue contacts not present in the folded structure play little or no role in the self-assembly mechanism. Non-native contacts can, however, influence folding kinetics by introducing additional local minima that slow diffusion over the global free-energy barrier between folded and unfolded states. Here, we combine single-molecule fluorescence with all-atom molecular dynamics simulations to discover the structural origin for the slow diffusion that markedly decreases the folding rate for a designed α-helical protein. Our experimental determination of transition path times and our analysis of the simulations point to non-native salt bridges between helices as the source, which provides a quantitative glimpse of how specific intramolecular interactions influence protein folding rates by altering dynamics and not activation free energies.

O ne of the real surprises in studies of protein folding is that the rates for this complex self-assembly process can be adequately described by Kramers' theory for diffusion of a single Brownian particle over a barrier on a one-dimensional free-energy surface (1–6). The transition path, which corresponds to the barrier-crossing process, is the rare event in an equilibrium trajectory when the transition between folded and unfolded states actually takes place and contains all of the mechanistic information on how a protein folds and unfolds (Fig. 1). Thanks to recent advances in both experimental methods and computer simulations, we are beginning to gain a deeper understanding of transition paths and folding mechanisms. The average time to cross the barrier, the transition path time, can now be experimentally determined from a photon-by-photon analysis of single-molecule fluorescence experiments (7, 8). The transition path time is an important property because, unlike the folding time t_f (inverse of the folding rate coefficient k_f) (Eq. 1) (1), which depend exponentially on the free-energy barrier height, it is insensitive to the barrier height and gives direct information on the Kramers diffusion coefficient (Eq. 2) (7–11), i.e.,

$$\frac{1}{k_f} = t_f = \frac{2\pi}{\beta D^* \sqrt{\kappa^* \kappa_U}} \exp(\beta \Delta G^*) \quad (1)$$

[1]Laboratory of Chemical Physics, National Institute of Diabetes and Digestive and Kidney Diseases, National Institutes of Health, Bethesda, MD, 20892-0520, USA. [2]D. E. Shaw Research, New York, NY 10036, USA. [3]Department of Biochemistry and Molecular Biophysics, Columbia University, New York, NY 10032, USA.
*These authors contributed equally to this work. †Corresponding author. E-mail: chunghoi@niddk.nih.gov (H.S.C.); stefano.piana-agostinetti@DEShawResearch.com (S.P.-A.); david.shaw@DEShawResearch.com (D.E.S.); eaton@helix.nih.gov (W.A.E.)

$$t_{TP} = \frac{1}{\beta D^* \kappa^*} \ln(2e^\gamma \beta \Delta G^*) \quad (2)$$

where D^* is the diffusion coefficient for motion along the reaction coordinate at the barrier top and appears in the prefactor of both equations. ΔG^* corresponds to the barrier height, and κ_U and κ^* correspond to the stiffness (curvatures) of the unfolded well and barrier top. Subscripts f and TP are folding and transition path, respectively.

The experimentally measured times can now be compared with those obtained from long trajectories containing many folding or unfolding transitions in all-atom molecular dynamics (MD) simulations of the folding process (12). These simulations also provide a wealth of atomistic detail on many aspects of the apparent mechanism of self-assembly and offer a structural basis for interpreting the experimental results (13–16). Analysis of the transition paths in simulations shows that for small proteins, non-native contacts appear to play little or no role in the mechanism (17) of folding. Such contacts, however, can influence the rates of folding in several ways. In addition to increasing the free-energy barrier height, they can decrease folding rates by slowing diffusion over the barrier by introducing additional local minima and barriers in the underlying energy landscape, often called "roughness." The latter effect reduces the Kramers diffusion coefficient (D^*), which is a measure of the dynamics and appears in the prefactor for both the rates and the transition path times (Eqs. 1 and 2). Consequently, D^* is a key parameter in the theory of protein folding kinetics. It determines transition path times and sets the intrinsic time scale for folding rates. D^* and the curvatures of the free-

energy surface also provide an estimate of the maximum rate at which a protein can fold, the so-called protein folding "speed limit" (18, 19), analogous to the von Smoluchowski diffusion limited rate for a bimolecular chemical reaction.

In spite of the importance of understanding the determinants of D^*, there is as yet no information from experiments or simulations on the effect of specific types of interresidue interactions on D^*. The designed protein, α₃D (fig. S1) (20, 21), a three-helix bundle, provides us with an opportunity to investigate this question because of its readily measurable, long transition path time at neutral pH (Fig. 2) (8). Analysis of previous simulations at neutral pH for α₃D showed that many non-native contacts form during the transition paths (13, 17), which suggests that they are the structural origin for a lower D^* that produces the long transition path time (Fig. 2). Non-native contacts are theoretically predicted to be more important for the kinetics and dynamics of designed proteins than for naturally evolved protein (22). Previous kinetic studies of α₃D showed that the folding rates are markedly increased when the carboxylates are neutralized at low pH (23) in urea solution at room temperature, which suggests that non-native salt bridges may play an important role. To test this hypothesis, we report here measurements of the transition path time from single-molecule Förster resonance energy transfer (FRET) experiments, along with a comparison of interresidue interactions during transition paths from long-equilibrium molecular dynamics trajectories in the presence and absence of the salt bridges.

Experimental rates and transition path times
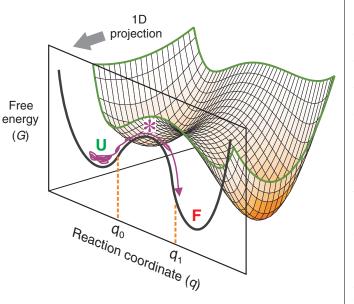
The FRET efficiency histograms in Fig. 3 and fig. S2 show a marked increase in the folding rate for α₃D as the pH is lowered (23), in spite of a small change in the stability (tables S1 and S2 and Fig. 3 and fig. S3). At neutral pH there are two clear peaks: one for the folded population at a high FRET efficiency and one for the unfolded population at a lower FRET efficiency. As the pH is lowered, the folded and unfolded peaks of the FRET efficiency histograms merge into a single peak at the average value for folded and unfolded molecules, because there is a continuous increase in the number of transitions between the states that occur within the 1-ms bin time (24). This phenomenon is similar to what is observed in nuclear magnetic resonance experiments where there are two peaks when structures exchange slowly compared with the difference in frequencies and a single peak when exchange is fast (24).

Using the maximum likelihood method of Gopich and Szabo (25), photon trajectories from which the histograms were constructed yield a relaxation rate ($k = k_f + k_u$, where k_f and k_u are folding and unfolding rate coefficients) that increases by 14-fold between pH 5.3 and 3.6 (Fig. 3B and table S2). The sharp increase near pH 4, the logarithmic acid dissociation constant (pK_a)

of glutamic acid and aspartic acid residues, immediately suggests that protonation of the carboxyl groups and, therefore, loss of salt bridges, is responsible for the rate increase, whereas the small change in the stability (table S2) suggests that rate change does not come from a change in the free-energy barrier height but from a change in D^* in the preexponential factor of Kramers' equation (Eq. 1).

We therefore studied the viscosity dependence of the folding relaxation rate at pH 3.6. Compared with neutral pH, where both the rate and transition path time exhibit a very weak viscosity dependence (8), much larger changes in rate were observed at pH 3.6. A relative viscosity change of 10-fold produces a 4.5-fold increase in the inverse relaxation rate without a substantial change in the stability, which suggests that the friction associated with the local barrier crossings does not come from the solvent but is dominated by internal friction (Fig. 3, D and E, and tables S1 and S3) (26, 27).

Even though the stability is unchanged when the pH is lowered, the rates could be increased by simply lowering the free-energy barrier. To more convincingly determine whether the effect of lowering pH on the rate results primarily from an increase in D^* rather than from a decrease in the free-energy barrier height requires measurements of the transition path time, because the transition path time is insensitive to the barrier height (Eq. 2). If the change of the free-energy surface is small, the transition path time would show the same pH and viscosity dependence as the inverse relaxation rate. The average transition path time for $\alpha_3 D$ in the absence of viscogen at pH 7.6 and room temperature was previously measured to be 12 ± 2 μs in GdmCl solution (8) and is 13 ± 2 μs in the current measurements in urea solution at pH 5.3 (Fig. 4). (The relaxation rates and stability are similar under both conditions.) If one assumes that all of the 14-fold increase in relaxation rate at pH 3.6, compared with pH 5.3, comes from a larger D^*, the data in tables S1 and S2 indicate that the transition path time is predicted to be only ~1 μs at pH 3.6. We therefore collected photon trajectories at the highest possible illumination intensity (an average of 600 to 900 photons/ms) that allowed observation of photon trajectories containing transitions before photobleaching of one of the dyes occurred. As before, the Gopich-Szabo maximum likelihood method—with a kinetic model consisting of folded, unfolded, and an additional virtual intermediate state to simulate the transition path (fig. S4)—was used for determining the average transition path times (7, 8).

Unlike the experiments at pH 5.3 where the transition path time was readily measurable from a peak in the difference log likelihood plot at 13 μs, only an upper bound of ~4 μs could be obtained at pH 3.6 (Fig. 4). To lengthen the transition path time and possibly make it experimentally resolvable, viscogens (glycerol or trehalose) were added to produce viscosities relative to the absence of viscogen of 3.3 and 15 (the highest viscosity at which solutions could be prepared at low pH in the presence of the high concentrations of urea necessary to attain 50% unfolding) (table S3). At the higher viscosities, where there is less bimolecular quenching of the dye triplet states that result in photochemistry,

Fig. 1. 1D free-energy surface description of kinetics and dynamics of protein folding. Protein folding dynamics are most often described by diffusion on a free-energy surface obtained from a 1D projection of a multidimensional free-energy landscape. The folding transition path of a single molecule in an equilibrium trajectory is one that crosses q_0 on the reaction coordinate and reaches q_1 on the other side of the free-energy barrier without recrossing q_0. The transition path appears as a jump in the experimental property being monitored in a single-molecule trajectory. The folding rate coefficient, k_f, is the inverse of the average waiting (residence) time spent exploring the configurations of the unfolded well from which numerous unsuccessful attempts are made at crossing the free-energy barrier.
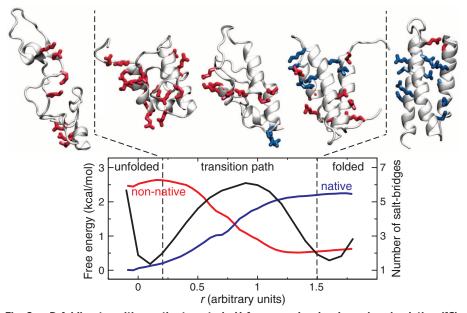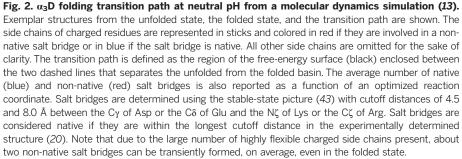
Fig. 2. $\alpha_3 D$ folding transition path at neutral pH from a molecular dynamics simulation (13). Exemplar structures from the unfolded state, the folded state, and the transition path are shown. The side chains of charged residues are represented in sticks and colored in red if they are involved in a non-native salt bridge or in blue if the salt bridge is native. All other side chains are omitted for the sake of clarity. The transition path is defined as the region of the free-energy surface (black) enclosed between the two dashed lines that separates the unfolded from the folded basin. The average number of native (blue) and non-native (red) salt bridges is also reported as a function of an optimized reaction coordinate. Salt bridges are determined using the stable-state picture (43) with cutoff distances of 4.5 and 8.0 Å between the Cγ of Asp or the Cδ of Glu and the Nζ of Lys or the Cζ of Arg. Salt bridges are considered native if they are within the longest cutoff distance in the experimentally determined structure (20). Note that due to the large number of highly flexible charged side chains present, about two non-native salt bridges can be transiently formed, on average, even in the folded state.

Fig. 3. pH and viscosity dependence of α₃D folding kinetics close to the chemical denaturant midpoint. (**A**) FRET efficiency histograms as a function of pH. The concentrations of urea are 5 M at pH 7.5 and 6 M at all other pHs (table S2). The FRET efficiency histograms were constructed from 1-ms bins in the trajectories with the mean photon count rate of >50 ms⁻¹. The near-identity of the measured histograms (wide bars) and the histograms constructed from recolored photon trajectories (red narrow bars), using the parameters obtained from the maximum likelihood method with the two-state model, indicate that this model is adequate (23, 25). (**B**) pH dependence of relaxation rate, k. (**C**) FRET efficiency histograms at different relative solvent viscosities. (**D** and **E**) Viscosity dependence of the inverse of the relaxation rate (D) at pH 7.6 (table S1) and (E) at pH 3.6 under conditions where the stability is only slightly altered (table S3). The data were fitted to the power-law function $A(\eta/\eta_0)^\alpha$ (orange) or a linear equation $A(\sigma + \eta/\eta_0)$ (green) (26), where A is an amplitude and σ is the internal viscosity, which reflects the internal friction. The blue dashed lines show the dependence expected when the folding times are proportional to the first power of the solvent viscosity.
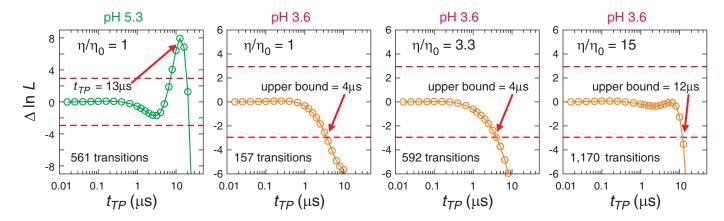
Fig. 4. Analysis of single-molecule photon trajectories. The difference of the log likelihood, $\Delta \ln L = \ln L(t_{TP}) - \ln L(0)$, is plotted as a function of the lifetime of the virtual intermediate state (= t_{TP}), for folding and unfolding transitions. $L(0)$ is the likelihood for a model with instantaneous folding and unfolding transitions. Therefore, $\Delta \ln L$ quantifies how much better or worse a model with a finite transition path time describes the data than a model with an instantaneous transition (fig. S4). The transition path time is determined from the maximum of the likelihood function above the upper 95% confidence limit ($\Delta \ln L = +3$, red dashed line), which is 13.3 (± 1.8) μs at pH 5.3. The error is the standard deviation obtained from the curvature at the maximum of the likelihood function. The upper bound of transition path time is determined by the time when the likelihood curve crosses the lower 95% confidence limit ($\Delta \ln L = -3$, red dashed line) (29).

it was necessary to include the interfering effect of fluorophore blinking in the analysis by adding nonfluorescent states to the kinetic scheme for determining the upper bound of the transition path time (figs. S5 and S6 and table S4) (28, 29). If the viscosity dependence is the same as found for the rate dependence at low pH (Fig. 3 and table S3), the predicted transition path times at these relative viscosities are ~2 and ~6 μs, below the current time resolution of these experiments, as judged by the analyses of simulated trajectories (fig. S7 and table S5). In keeping with this expectation, again no

peak is observed, and only upper bounds of 4 and 12 μs could be determined, even though the key parameters that determine the ability to observe a peak in the log likelihood plot are very similar to those at pH 5.3—the photon detection rate, the number of observed transitions, and the difference in average FRET efficiencies between the folded and unfolded molecules.

Additional information was obtained by simulating trajectories with an assumed transition path time using the experimental parameters (fig. S8) (29). The simulations, together with the

present experimental results, lead to our best estimate for the average transition path time of ~1 μs. Consequently, we conclude that most, if not all, of the 14-fold increase in the relaxation rate upon protonating the carboxyl groups can be accounted for by increasing D^* in the preexponential factor of Kramers' equation (Eq. 1).

Simulations of rates and transition path times

Molecular dynamics simulations were used to provide an atomic-level structural interpretation of the experimental observations (table S6). We performed equilibrium reversible-folding simulations of α_3D in water at both neutral pH (aspartate and glutamate ionized) and low pH (aspartate and glutamate protonated) (figs. S9 and S10). Two independent simulations were performed for each condition. During both the neutral- and low-pH simulations, α_3D reversibly folded several times to a structure less than 3 Å Cα root mean square deviation (RMSD) from the experimentally determined structure (Fig. 5, A and D). The calculated melting temperatures (~350 K at low pH and ~370 K at neutral pH) are consistent with the experimentally determined melting temperatures of 346 K at pH 2.2 and >363 K at neutral pH (21). Folding times were calculated using a dual cutoff at values of 0.20 and 1.50 of an optimized reaction coordinate (fig. S11 and Fig. 5B) (13). The calculated folding times at 370 K (10 ± 3 μs at low pH and 20 ± 4 μs at neutral pH) can be compared with the experimental values of 6 μs (21) and ~10 μs [obtained by extrapolation of the dena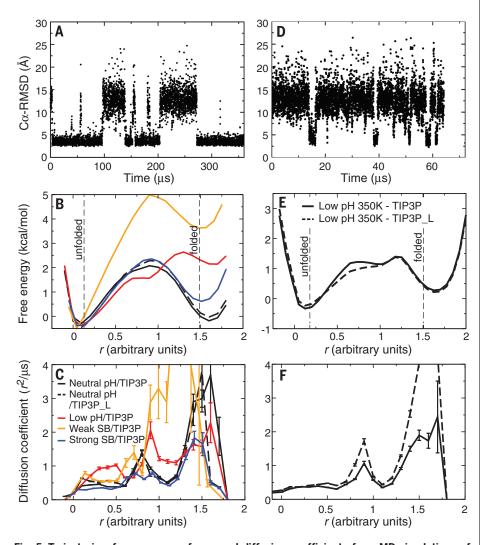turant dependence at 295 K (23), by assuming no temperature dependence; if the folding time increases with temperature, as observed at low pH and commonly observed in single-domain proteins, the folding time would be longer and the agreement between simulation and experiment would be even better]. This result indicates that, despite being less stable, α_3D folds considerably faster at low pH than at neutral pH.

This difference in folding rate cannot be readily explained by assuming a lower activation free energy, as the estimated folding free-energy barrier appears to be slightly higher in the low-pH simulations than in the neutral-pH simulations (Fig. 5B), a result that does not depend on the data used to optimize the reaction coordinate (fig. S12). The diffusion coefficient calculated in the region within 0.5 kcal mol^{-1} of the top of the barrier, however, is approximately a factor of 2 larger at low pH with respect to neutral pH (1.33 ± 0.02 $r^2\mu s^{-1}$ at low pH and 0.76 ± 0.02 $r^2\mu s^{-1}$ at neutral pH) (Fig. 5C). Accordingly, the calculated transition path time is shorter at low pH (0.24 ± 0.05 μs) than at neutral pH (0.43 ± 0.07 μs), by about a factor of 2. These results suggest that all of the decrease in both the folding time and transition path time at low pH is caused by a decrease in Kramers D^* and not by changes in curvatures of the one-dimensional (1D) free-energy surface (Eqs. 1 and 2), consistent with the interpretation of the experimental results.

Fig. 5. Trajectories, free-energy surfaces, and diffusion coefficients from MD simulations of reversible folding of α_3D. (**A**) Time series of the Cα RMSD from the experimental native structure for a 360-μs simulation of α_3D performed at 370 K and neutral pH. (**B**) 1D projection of the folding free-energy surface along an optimized reaction coordinate (29). The cutoffs used for determining rates and transition path times in the analysis to define the folded and unfolded states are indicated by two vertical lines. The different simulations are distinguished using the color scheme described in (C). (**C**) Diffusion coefficients along the optimized reaction coordinate for neutral-pH (black) and low-pH (red) simulations performed at 370 K. Results are also reported for simulations performed with weak (orange) or strong (blue) salt bridges and for a 370 K, neutral-pH simulation performed at low viscosity (black dashed line). (**D**) Time series of the Cα RMSD for a 65-μs simulation of α_3D performed at 370 K and low pH. (**E**) 1D projection of the folding free-energy surface for low-pH simulations performed at 350 K and either normal viscosity (black solid line) or low viscosity (black dashed line). (**F**) Diffusion coefficients (350 K) along the optimized reaction coordinate. The different simulations are distinguished using the same scheme used in (E).

To investigate the influence of viscosity on the folding rates in the different pH conditions, we performed low- and neutral-pH simulations near the melting temperature, using either a normal TIP3P water model or TIP3P_L, a water model with one-third of the total mass of TIP3P (*29*) that is characterized by a ~1.7 times lower viscosity (*30*). The use of TIP3P_L alters the dynamics, but not the thermodynamics, of the system. Indeed, we observed that essentially the same folding free-energy surface was obtained in normal- and low-viscosity simulations (Fig. 5, B and E).

In the simulations, as the viscosity was lowered by a factor of ~1.7, the folding time at low pH strongly decreased, whereas at neutral pH it remained essentially unchanged (Fig. 6A). A similar trend is observed for the average transition path time, which is very strongly dependent on viscosity at low pH but not at neutral pH. Similarly to what was observed when we lowered the pH, the decrease in both the folding time and the transition path time with the decrease in viscosity at low pH is at least partially reflected in the diffusion coefficient in the barrier top region, which increases from 0.55 ± 0.02 $r^2 \mu s^{-1}$ at normal viscosity to 0.72 ± 0.02 $r^2 \mu s^{-1}$ at low viscosity (Fig. 5F). These findings are again consistent with the experimental results, which show that the transition path time at neutral pH is weakly dependent on solvent viscosity and that the folding times are less dependent on solvent viscosity at neutral pH than they are at low pH (Fig. 3, D and E) (*8*). The smaller effects of pH observed in the simulations results from the high simulation temperature, where the apparent internal friction is much less (*8*), and therefore, there is a smaller change in D^*.

The comparison of the experiments and simulations is summarized in Figure 6A. The temperatures and solvent conditions are different between the experiment and simulation because the objectives used in single-molecule measurements cannot withstand the high temperatures of the simulations and because folding is much too slow in denaturant at room temperature to obtain a sufficient number of transitions in the molecular dynamics simulations to draw any meaningful conclusions. Despite the differences in temperatures and solvent conditions, the overall trends in the experiments and simulations for both the rates and the transition path times are very similar under conditions in which there are nearly equal populations of folded and unfolded molecules.

Analysis of transition paths from simulations

Analysis of the formation of secondary structure and hydrophobic contacts shows that the folding transition path involves an initial collapse to a molten globulelike structure containing native and non-native contacts, followed by a gradual reorganization of the structure (*17*) (Fig. 2). Salt bridges and hydrophobic contacts appear to be the two most common and persistent types of

side-chain interactions. We compared the average number and the average persistence time of these non-native contacts during the transition paths at the two different pH levels (Fig. 6B and table S7). The persistence time is expected to be determined primarily by the height of the local barriers and, together with the number of contacts that form and break, reflect the overall roughness of the landscape due to non-native interactions.

In the neutral-pH simulations, four to five non-native salt bridges are formed, on average, at any given time during the transition paths between the positively charged lysine and arginine residues and the negatively charged carboxyl groups of the aspartates and glutamates. These salt bridges have an average persistence time of a few nano-

seconds and occasionally may last for up to a few tens of nanoseconds. These interactions almost completely disappear at low pH—their population is reduced by an order of magnitude, and their persistence time is 50 to 75% of the time at neutral pH—because the addition of protons neutralizes the carboxylates and eliminates the Coulombic electrostatic attraction with the positively charged lysines and arginines (i.e., the salt bridges).

To analyze the relative importance of the total charge of the molecule, we performed simulations in which salt bridge interactions were either weakened or strengthened by slightly changing the nonbonded force field parameters while leaving the total charge of the system unchanged. When salt bridges are weakened, the native state is destabilized ($\Delta\Delta G_f$ of ~3.5 kcal mol^{-1}) (Fig. 5B),
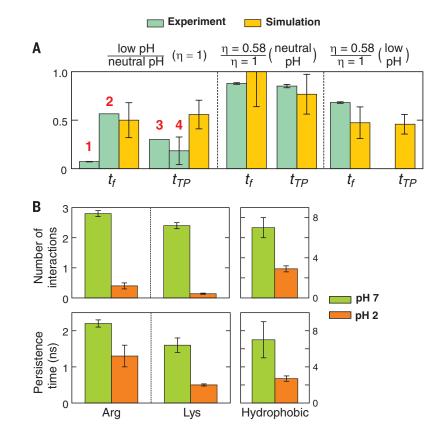
Fig. 6. Comparison of the effect of pH and viscosity on folding and transition path times from experiments and simulations and the average number and persistence time of non-native interactions during the transition path. (**A**) The ratio of the folding and transition path times in simulation (yellow bars) was calculated from the values in table S6. The experimental values (light blue bars) were calculated as follows. [1] The ratio of the relaxation times at pH 3.6 (low) and pH 5.3 (neutral) at 295 K; [2] the ratio of the folding time of 6 μs at pH 2 and 346 K (*21*) and the folding time of 10 μs at pH 7.5 obtained from the GdmCl dependence (*23*); [3] the transition path time at pH 3.6 is an upper bound; [4] the transition path time at pH 3.6 was assumed to be 1 μs at 295 K, and it was extrapolated to 370 K using the viscosity dependence of $t_{TP} \propto \eta^{0.7}$ obtained from the viscosity dependence of the kinetics (Fig. 3E). The transition path time at pH 7.5 and 370 K was calculated by extrapolation using the super-Arrhenius temperature dependence ($D \propto \exp[-\varepsilon^2 / (kT)^2]$) with the roughness ($\varepsilon^2$) of 2.3 kT (T = 295 K) and t_{TP} = 12.3 μs at 295 K (*8*). The experimental viscosity dependence was calculated using the power law dependence (η^{α}) with the powers (α) of 0.24 (t_f, neutral pH) (Fig. 3D); 0.30 (t_{TP}, neutral pH) (*8*); and 0.70 (t_f, low pH) (Fig. 3E). See table S6 for absolute times and additional details of the simulations. (**B**) Lowering pH substantially reduces the average number and persistence time of non-native salt bridges between positively charged side chains (Arg, Lys) and negatively charged side chains (Glu, Asp) and the non-native hydrophobic interactions during the transition path.
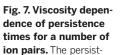
as was observed in the low-pH simulations. More important is that diffusion along the optimized reaction coordinate is greatly increased (Fig. 5), and the transition path time decreases (table S6). In contrast, when the strength of salt bridges is increased, there is very little change in protein stability, but diffusion along the reaction coordinate becomes slower (Fig. 5), and the folding time and transition path time increase (table S6). Taken together, these results support the idea that salt bridges directly influence the free-energy landscape roughness, whereas the total charge of the molecule plays a minor role, if any.

Another interaction that in simulation is relatively persistent and disappears at low pH occurs between Asp and Glu side chains and the protein backbone. To elucidate the relative contribution of this interaction to the roughness of the free-energy landscape, we performed simulations in which we selectively weakened this interaction (table S8). In these simulations, the stability of the folded state is unchanged, but the folding free-energy barrier increases slightly and diffusion on the free-energy surface is slightly faster (fig. S13). These results suggest that these non-native backbone–side chain interactions contribute to the stability of the transition state for folding, but also slightly increase the energy landscape roughness. This effect appears to be minor compared with that of salt bridge interactions.
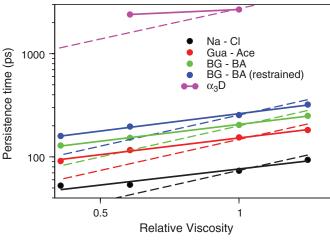
Having established that salt bridges provide an important contribution to the energy landscape roughness, we investigated the underlying reasons for the weak viscosity dependence of the folding rate of α_3D at neutral pH. To that end, we performed simulations of the viscosity dependence of the persistence times of ion-pair formation for systems of increasing complexity, ranging from the pairing of sodium chloride, to the pairing of Arg and Glu side chains, to the formation of Asp or Glu and Arg salt bridges in α_3D. In all of these systems, we observed a weak viscosity dependence that strongly deviates from

the simple power dependence with an exponent of 1.0 expected from Kramers' theory (Fig. 7). Ion-pair formation for the Arg and Glu side-chain analogs involves a first step, in which the ions diffuse through the solvent until they come into close proximity, followed by a reorganization step, in which the ions reorient themselves to achieve an optimal interaction (fig. S14). We find that the kinetics of the last step is affected very weakly by changes in solvent viscosity (fig. S14).

Discussion

By combining single-molecule experiments with extensive all-atom molecular dynamics simulations, we have gained quantitative insight into how a specific type of interresidue interaction influences the kinetics and dynamics in protein folding. The experiments show that the slower folding and longer transition path times for α_3D at neutral pH compared with low pH (Figs. 3 and 4)—where the carboxyl groups are neutral—are due to a smaller D^*, which appears in the preexponential factor for the folding time and the prelogarithmic factor for the transition path time (Eqs. 1 and 2). In the molecular dynamics simulations, similar differences are also observed (Fig. 6A) and explained by changes in D^* (Fig. 5, C and F), so we can use them to gain insight at an atomistic level into what interactions are responsible. Although salt bridge interactions are almost completely eliminated at low pH in the experiments, this does not demonstrate that they are solely responsible for the larger landscape roughness at neutral pH, as reflected in the smaller D^*. Indeed, at low pH the net charge of the protein increases from approximately −1 to +11, which leads to a slightly more expanded transition path ensemble, featuring a smaller number of non-native hydrophobic interactions compared with neutral pH (Fig. 6B and table S7). To disentangle the importance of these two contributions to the landscape roughness, we took advantage of the ability of simulations to selectively alter the strength of

specific interactions while leaving the rest of the system unperturbed. Decreasing the strength of the salt bridges at neutral pH markedly increases D^* and shortens the transition path time, whereas increasing the strength has the opposite effect (table S6). These results support the idea that salt bridges directly influence the landscape roughness, whereas the total charge of the molecule plays a minor role, if any.

Understanding the dependence of the folding and transition path times on solvent viscosity in detail is a more subtle and difficult problem. At low pH, in both experiments (Fig. 3, D and E) and simulations (Fig. 5) the folding time is more sensitive to solvent viscosity than at neutral pH, but the dependence is less than the first power expected from Kramers' theory if all of the friction ($\zeta^* = k_BT/D^*$) comes from the solvent and is linear in the solvent viscosity (Stokes law). Fractional power has been observed for isolated α helices and other α-helical proteins (31–36). Jas et al. (31) suggested that the fractional power dependence for α helices arises from a breakdown in Kramers' theory due to barrier-top crossing times for the dihedral angle rotations that are faster than the solvent relaxation. In fact, their exponent of 0.6 for the folding relaxation rate is remarkably close to the value of 0.7 observed for the all-α-helical α_3D at low pH (Fig. 3E). This interpretation has also been suggested on theoretical grounds by Portman et al. (37) and supported by simulations of Best, Papoian, and their co-workers. (38–40). The more challenging result to explain, however, is the much smaller fractional exponent of 0.2 to 0.3 for the folding and transition path times (8) at neutral pH (Fig. 3D). One possibility is that it is caused by internal friction due to collisions between atoms of the non-native salt bridges. However, in the simulations, the non-native salt bridges are almost completely exposed to the solvent molecules, so internal friction can provide only a partial explanation. The simulations suggest a more plausible additional non-Markovian effect. As shown in Fig. 7, the persistence time of ion pairs show reduced viscosity dependence ($\sim\eta^{0.5}$), a finding consistent with previous studies on the ion-pair association process of sodium chloride, where it has been shown that the reorganization step (in this case, involving only the solvent shell) cannot be modeled accurately by Kramers' theory (41, 42). The weak viscosity dependence observed for α_3D in the presence of non-native salt bridges may be the result of a combination of these two non-Markovian effects.

REFERENCES AND NOTES

1. H. A. Kramers, *Physica* **7**, 284–304 (1940).
2. N. D. Socci, J. N. Onuchic, P. G. Wolynes, *J. Chem. Phys.* **104**, 5860–5868 (1996).
3. J. D. Bryngelson, J. N. Onuchic, N. D. Socci, P. G. Wolynes, Funnels, pathways, and the energy landscape of protein folding: A synthesis. *Proteins* **21**, 167–195 (1995).
4. M. Oliveberg, P. G. Wolynes, *Q. Rev. Biophys.* **38**, 245–288 (2005).
5. J. Kubelka, E. R. Henry, T. Cellmer, J. Hofrichter, W. A. Eaton, *Proc. Natl. Acad. Sci. U.S.A.* **105**, 18655–18662 (2008).
6. D. K. Klimov, D. Thirumalai, *Phys. Rev. Lett.* **79**, 317–320 (1997).

Fig. 7. Viscosity dependence of persistence times for a number of ion pairs. The persistence time is reported on a logarithmic plot as a function of viscosity relative to TIP3P for the Na...Cl ion pair (black), the guanidinium...acetate ion pair (red), the butyl-guanidinium...butyric acid ion pair (green, representing the side chains of Arg and Glu), a butyl-guanidinium...butyric acid ion pair where the terminal carbon atoms have been restrained at a distance of 10 Å (blue), and the Arg...Glu/Asp salt bridges in the α_3D transition path (purple). A power-law fit with exponents ranging between 0.51 and 0.56 is reported in solid lines, whereas the exponent of 1.0 predicted by hydrodynamic Kramers' theory is shown as a dashed line.

7. H. S. Chung, K. McHale, J. M. Louis, W. A. Eaton, *Science* **335**, 981–984 (2012).
8. H. S. Chung, W. A. Eaton, *Nature* **502**, 685–688 (2013).
9. G. Hummer, *J. Chem. Phys.* **120**, 516–523 (2004).
10. H. S. Chung, J. M. Louis, W. A. Eaton, *Proc. Natl. Acad. Sci. U.S. A.* **106**, 11837–11844 (2009).
11. H. S. Chung, I. V. Gopich, *Phys. Chem. Chem. Phys.* **16**, 18644–18657 (2014).
12. D. E. Shaw *et al.*, in *SC'09, Proceedings of the Conference on High Performance Computing, Networking, Storage, and Analysis*, Portland, OR, 14 to 20 November 2009 (ACM Press, New York, 2009); http://dl.acm.org/citation.cfm?id=1654099.
13. K. Lindorff-Larsen, S. Piana, R. O. Dror, D. E. Shaw, *Science* **334**, 517–520 (2011).
14. S. Piana, K. Lindorff-Larsen, D. E. Shaw, *Biophys. J.* **100**, L47–L49 (2011).
15. S. Piana, K. Lindorff-Larsen, D. E. Shaw, *Proc. Natl. Acad. Sci. U.S.A.* **109**, 17845–17850 (2012).
16. D. E. Shaw *et al.*, *Science* **330**, 341–346 (2010).
17. R. B. Best, G. Hummer, W. A. Eaton, *Proc. Natl. Acad. Sci. U.S.A.* **110**, 17874–17879 (2013).
18. S. J. Hagen, J. Hofrichter, A. Szabo, W. A. Eaton, *Proc. Natl. Acad. Sci. U.S.A.* **93**, 11615–11617 (1996).
19. J. Kubelka, J. Hofrichter, W. A. Eaton, *Curr. Opin. Struct. Biol.* **14**, 76–88 (2004).
20. S. T. R. Walsh, H. Cheng, J. W. Bryson, H. Roder, W. F. DeGrado, *Proc. Natl. Acad. Sci. U.S.A.* **96**, 5486–5491 (1999).
21. Y. Zhu *et al.*, *Proc. Natl. Acad. Sci. U.S.A.* **100**, 15486–15491 (2003).
22. D. U. Ferreiro, E. A. Komives, P. G. Wolynes, *Q. Rev. Biophys.* **47**, 285–363 (2014).
23. H. S. Chung *et al.*, *J. Phys. Chem. A* **115**, 3642–3656 (2011).
24. I. V. Gopich, A. Szabo, *J. Phys. Chem. B* **111**, 12925–12932 (2007).
25. I. V. Gopich, A. Szabo, *J. Phys. Chem. B* **113**, 10965–10973 (2009).
26. A. Ansari, C. M. Jones, E. R. Henry, J. Hofrichter, W. A. Eaton, *Science* **256**, 1796–1798 (1992).
27. D. E. Sagnella, J. E. Straub, D. Thirumalai, *J. Chem. Phys.* **113**, 7702–7711 (2000).
28. H. S. Chung, T. Cellmer, J. M. Louis, W. A. Eaton, *Chem. Phys.* **422**, 229–237 (2013).
29. Materials and methods are available as supplementary materials on *Science* Online.
30. J. C. F. Schulz, L. Schmidt, R. B. Best, J. Dzubiella, R. R. Netz, *J. Am. Chem. Soc.* **134**, 6273–6279 (2012).
31. G. S. Jas, W. A. Eaton, J. Hofrichter, *J. Phys. Chem. B* **105**, 261–272 (2001).
32. T. Cellmer, E. R. Henry, J. Hofrichter, W. A. Eaton, *Proc. Natl. Acad. Sci. U.S.A.* **105**, 18320–18325 (2008).
33. B. G. Wensley *et al.*, *Nature* **463**, 685–688 (2010).
34. B. G. Wensley, L. G. Kwa, S. L. Shammas, J. M. Rogers, J. Clarke, *J. Mol. Biol.* **423**, 273–283 (2012).
35. B. G. Wensley *et al.*, *Proc. Natl. Acad. Sci. U.S.A.* **109**, 17795–17799 (2012).
36. A. Borgia *et al.*, *Nat. Commun.* **3**, 1195 (2012).
37. J. J. Portman, S. Takada, P. G. Wolynes, *J. Chem. Phys.* **114**, 5082–5096 (2001).
38. D. de Sancho, A. Sirur, R. B. Best, *Nat. Commun.* **5**, 4307 (2014).
39. W. Zheng, D. De Sancho, T. Hoppe, R. B. Best, *J. Am. Chem. Soc.* **137**, 3283–3290 (2015).
40. I. Echeverria, D. E. Makarov, G. A. Papoian, *J. Am. Chem. Soc.* **136**, 8708–8713 (2014).
41. G. Ciccotti, M. Ferrario, J. T. Hynes, R. Kapral, *J. Chem. Phys.* **93**, 7137–7147 (1990).
42. R. G. Mullen, J. E. Shea, B. Peters, *J. Chem. Theory Comput.* **10**, 659–667 (2014).
43. S. H. Northrup, J. T. Hynes, *J. Chem. Phys.* **73**, 2700–2714 (1980).

REPORTS

QUANTUM SIMULATION

Observation of chiral edge states with neutral fermions in synthetic Hall ribbons

M. Mancini,[1] G. Pagano,[1] G. Cappellini,[2] L. Livi,[2] M. Rider,[3,4] J. Catani,[5,2] C. Sias,[6,2] P. Zoller,[3,4] M. Inguscio,[6,1,2] M. Dalmonte,[3,4] L. Fallani[1,2]*

Chiral edge states are a hallmark of quantum Hall physics. In electronic systems, they appear as a macroscopic consequence of the cyclotron orbits induced by a magnetic field, which are naturally truncated at the physical boundary of the sample. Here we report on the experimental realization of chiral edge states in a ribbon geometry with an ultracold gas of neutral fermions subjected to an artificial gauge field. By imaging individual sites along a synthetic dimension, encoded in the nuclear spin of the atoms, we detect the existence of the edge states and observe the edge-cyclotron orbits induced during quench dynamics. The realization of fermionic chiral edge states opens the door for edge state interferometry and the study of non-Abelian anyons in atomic systems.

Ultracold atoms in optical lattices represent an ideal system for studying the physics of condensed matter problems in a fully tunable, controllable environment (*1*, *2*). One of the notable achievements in recent years has been the realization of synthetic background gauge fields, akin to magnetic fields in electronic systems. By exploiting light-matter interaction, it is possible to imprint a Peierls phase onto the atomic wave function. This phase is analogous to the Aharanov-Bohm phase experienced by a charged particle in a magnetic field (*3–5*). These gauge fields, first synthesized in Bose-Einstein condensates (*6*), have recently allowed for the realization of the Harper-Hofstadter Hamiltonian in ultracold bosonic two-dimensional (2D) lattice gases (*7*, *8*), whereas, following a complementary route based on accurate engineering of the single-particle Hamiltonian, Chern insulators have been also realized (*9*) in systems that lack a net magnetic field (*10*). These works are paving the way toward the investigation of different forms of bulk topological matter in atomic systems (*5*, *11*). In the present work, we are instead interested in the edge properties of fermionic systems under the effects of a synthetic gauge field. Fermionic edge states

are a fundamental feature of 2D topological states of matter, such as quantum Hall and chiral spin liquids (*12*, *13*). Moreover, they are robust against changing the geometry of the system and can be observed even on Hall ribbons (*14*). In addition, fermionic edge states offer appealing prospects in quantum science, such as the realization of robust quantum information buses (*15*), and they are ideal starting points for the realization of non-Abelian anyons akin to Majorana fermions (*16*, *17*).
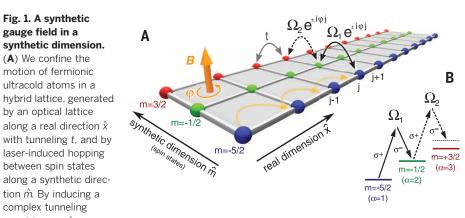
Here we report the observation of chiral edge states in a system of neutral fermions subjected to a synthetic magnetic field. We exploit the high level of control in our system to investigate the emergence of chirality as a function of the Hamiltonian couplings. These results have been enabled by an innovative approach, proposed in (*18*), where an internal (nuclear spin) degree of freedom of the atoms is used to encode a lattice structure lying in an "extra dimension" (*14*), providing direct access to edge physics. We synthesize a system of fermionic particles in an atomic Hall ribbon of tunable width pierced by an effective gauge field. One dimension is realized by an optical lattice, which induces a real tunneling t between different sites along direction $\hat{x}$ (Fig. 1A). The different internal spin states are coupled by a two-photon Raman transition, which provides a coherent controllable coupling $\Omega e^{i\varphi x}$ between different spin components. This can be interpreted as a complex tunneling amplitude between adjacent sites of an extra-dimensional lattice along a synthetic direction $\hat{m}$ (*14*, *19*). Furthermore, the phase imprinting laid out by the Raman beams amounts to the synthesis of an effective magnetic field for effectively charged particles (*4*) with flux $\varphi/2\pi$ (in units of the magnetic flux quantum)

[1]Department of Physics and Astronomy, University of Florence, I-50019 Sesto Fiorentino, Italy. [2]European Laboratory for Non-Linear Spectroscopy (LENS), I-50019 Sesto Fiorentino, Italy. [3]Institute for Quantum Optics and Quantum Information of the Austrian Academy of Sciences, A-6020 Innsbruck, Austria. [4]Institute for Theoretical Physics, University of Innsbruck, A-6020 Innsbruck, Austria. [5]Istituto Nazionale di Ottica del Consiglio Nazionale delle Ricerche (INO-CNR), Sezione di Sesto Fiorentino, I-50019 Sesto Fiorentino, Italy. [6]Istituto Nazionale di Ricerca Metrologica (INRIM), I-10135 Torino, Italy.
*Corresponding author. E-mail: fallani@lens.unifi.it

per plaquette (20). The Hamiltonian describing the system is

$$H = \sum_j \sum_\alpha [-t(c_{j,\alpha}^\dagger c_{j+1,\alpha} + \text{h.c.}) + \mu_j n_{j,\alpha}] +$$

$$\sum_j \sum_\alpha \left[\frac{\Omega_\alpha}{2} (e^{i\varphi j} c_{j,\alpha}^\dagger c_{j,\alpha+1} + \text{h.c.}) + \xi_\alpha n_{j,\alpha} \right] \quad (1)$$

where $c_{j,\alpha}^\dagger (c_{j,\alpha})$ are fermionic creation (annihilation) operators on the site (j,α) in the real (j) and synthetic $(\alpha = 1,2,3)$ dimensions, and $n_{j,\alpha} = c_{j,\alpha}^\dagger c_{j,\alpha}$. The first term describes the dynamics along $\hat{x}$, where t can be tuned by changing the intensity of the optical lattice beams. The dynamics along $\hat{m}$ is encoded in the second term: Ω_α can be con-trolled by changing the power of the Raman beams, whereas φ can be tuned by changing their angle (20). In Eq. 1, μ_j describes a weak trapping potential along $\hat{x}$, whereas ξ_α accounts for a state-dependent light shift, providing an energy offset along $\hat{m}$. h.c. stands for Hermitian conjugate. In our experiment, we produced large synthetic magnetic fields corresponding to $\varphi \simeq 0.37\pi$ per plaquette. For fermionic particles, we use alkaline-earth–like ^{173}Yb atoms, initially prepared in a degenerate Fermi gas. The sites of the synthetic dimension (Fig. 1B) are encoded in a subset of spin states $\{m\}$ out of the $I = 5/2$ nuclear spin manifold, thus providing fermionic "ladders" with up to six "legs." These atoms show SU(N)-invariant interactions [SU(N), special unitary group of degree N] (21), inhibiting the redistribution of the atoms amon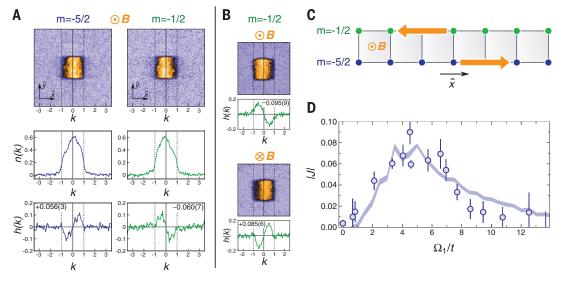g the different synthetic sites by collisional processes (22, 23). The effect of these interactions—which is not fundamental for explaining the observations reported in this manuscript—has been taken into account in the theoretical model as a renormalization of the trap frequency (20). This is possible because the maximum filling fraction is $\eta \simeq 0.8$ atoms per site of the real-space lattice: For larger filling fractions commensurate with the lattice, possible insulating phases can be stabilized.

The key advantage offered by the implementation in a lattice that combines real and synthetic spaces is the possibility to work with a finite-sized system with sharp and addressable edges. Specifically, we focus on elementary configurations made up of fermionic ladders with a small number of legs connected by a tunnel coupling between them. A leg is constituted by a 1D chain of atoms trapped in the sites of the real lattice in a specific spin state, whereas the ladder "rungs" are provided by the synthetic tunneling (Fig. 1A). The number of legs can be set by controlling the light shifts ξ_α in such a way as to choose the number of spin states that are coupled by the Raman lasers (20).
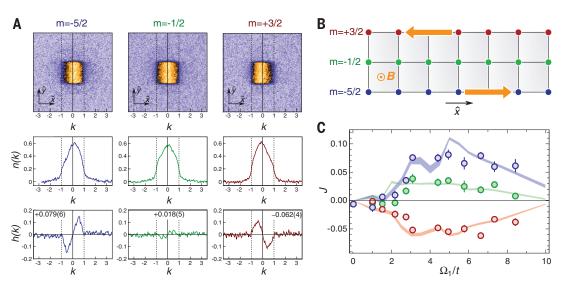
We first consider the case of a two-leg ladder constituted by the nuclear spin states $m = -5/2$ and $m = -1/2$. A quantum degenerate ^{173}Yb Fermi gas with 1.6×10^4 atoms and an initial temperature $T \simeq 0.2 T_F$ (where T_F is the Fermi temperature) is first spin-polarized in $m = -5/2$. By slowly turning on the intensity of the optical lattice along $\hat{x}$ (and of an additional strong lattice along $\hat{y}$ and $\hat{z}$ to suppress the dynamics along the other two real directions), we prepare a system of ladders in which all atoms occupy the $m = -5/2$ leg with less than one atom per site (i.e., in a conductive metallic state). Then, by controlling the intensity and frequency of the Raman beams (20), we slowly activate the tunnel

Fig. 1. A synthetic gauge field in a synthetic dimension.
(**A**) We confine the motion of fermionic ultracold atoms in a hybrid lattice, generated by an optical lattice along a real direction $\hat{x}$ with tunneling t, and by laser-induced hopping between spin states along a synthetic direction $\hat{m}$. By inducing a complex tunneling $\Omega_{1,2} e^{i\varphi j}$ along $\hat{m}$, the atom wave function acquires a phase φ per plaquette, mimicking the effect of a transverse magnetic field **B** on effectively charged particles. (**B**) Scheme of the ^{173}Yb nuclear spin states and Raman transitions used in the experiment.

Fig. 2. Chiral dynamics in two-leg ladders. (**A**) (Top) False-color time-of-flight images of the atoms in the $m = -5/2$ and $m = -1/2$ legs (averages of ~30 realizations). (Middle) Integrated lattice momentum distribution $n(k)$. (Bottom) $h(k) = n(k) - n(-k)$ [numerical values within the plots are the net momentum unbalance J determined from $h(k)$]. Experimental parameters: $\Omega_1 = 2\pi \times 489$ Hz, $t = 2\pi \times 134$ Hz, $\Omega_1/t = 3.65$, and $\varphi = 0.37\pi$. (**B**) Time-of-flight images and $h(k)$ of the $m = -1/2$ leg for opposite directions of the effective magnetic field. Experimental parameters: $\Omega_1 = 2\pi \times 394$ Hz, $t = 2\pi \times 87$ Hz, $\Omega_1/t = 4.53$, and $\varphi = \pm 0.37\pi$. (**C**) Sketch of the two-leg ladder configuration realized for this experiment. The arrows are a pictorial representation of the chiral currents. (**D**) Circles show experimental values of $|J|$ for the $m = -1/2$ leg as a function of Ω_1/t (averages of data sets taken for $\varphi = \pm 0.37\pi$). The error bars are obtained with a bootstrapping method applied on ~30 different measurements. The shaded area depicts the result of a numerical simulation that includes thermal fluctuations (20).

Fig. 3. Chiral edge currents in a three-leg ladder. (A) Experimental time-of-flight images (top), $n(k)$ (center), and $h(k) = n(k) - n(-k)$ (bottom) for each of the three legs $m = -5/2$, $m = -1/2$, and $m = +3/2$ constituting the ladder, respectively [numbers shown in the bottom panels are the values of J determined from $h(k)$]. Experimental parameters: $\Omega_1 = 2\pi \times 620$ Hz, $t = 2\pi \times 94$ Hz, $\Omega_1/t = 6.60$, and $\varphi = 0.37\pi$. **(B)** Sketch of the three-leg ladder configuration realized for this experiment. **(C)** Circles show experimental values of the net momentum unbalance J for each leg as a function of Ω_1/t.

The shaded areas illustrate the results of a numerical simulation (20). For both experimental and simulation data, blue, green, and red correspond to $m = -5/2$, $m = -1/2$, and $m = 3/2$, respectively.

coupling between the legs so as to adiabatically load the fermionic system in the lowest band of both the lattice and the Raman-dressed energy spectrum.

Despite the absence of a real bulk region, this two-leg configuration is expected to support chiral currents with atoms flowing in opposite directions along the legs (Fig. 2C), as investigated recently in bosonic systems (24). To observe this, we measured the relative motion of the atoms in the two legs by spin-selective imaging of the lattice momentum distribution, obtained by switching off the synthetic coupling and releasing the atoms from the lattice. In Fig. 2A (upper panel), we show two time-of-flight images corresponding to the $m = -5/2$ and $m = -1/2$ legs (Fig. 2C) for $\Omega_1 = 2\pi \times 489$ Hz and $t = 2\pi \times 134$ Hz ($\Omega_1/t = 3.65$). Here we are interested only in direction $\hat{x}$, which reflects the distribution of the lattice momenta k along the legs (in units of the real-lattice wave number $k_L = \pi/d$, where d is the real-lattice spacing). The lattice momentum distribution along $\hat{y}$ is a uniform square due to the presence of the strong optical lattice along the transverse (frozen) real directions (20). The central panel of Fig. 2A shows the lattice momentum distribution $n(k)$ after integration of the images along $\hat{y}$ and normalization according to $\int n(k)dk = 1$. We observe a clear asymmetry in $n(k)$ [similar to what was reported in experiments with spin-orbit coupling in harmonically trapped gases (25–27)], which we characterize by defining the function

$$h(k) = n(k) - n(-k) \qquad (2)$$

which is plotted in the lower panel of Fig. 2A. The expression $J = \int_0^1 h(k)dk$ provides a measurement of the lattice momentum unbalance and quantifies the strength of the chiral motion of the particles along the two legs. The values $J = +0.056(3)$ for $m = -5/2$ and $J = -0.060(7)$ for $m =$

$-1/2$ are approximately equal in intensity and opposite in sign, providing direct evidence for presence of chirality in the system. The small value of J is attributable to the fact that, in addition to states exhibiting chiral currents, fermions occupy other states at the bottom of the band, which do not display chiral features. We also performed the same experiment with a reversed direction of the synthetic magnetic field **B** (Fig. 2B), observing a change of sign in J, corresponding to currents circulating in the opposite direction. This behavior confirms the interpretation of our data in terms of chiral currents induced by a synthetic magnetic field in a synthetic 2D lattice.

The stability of chiral edge states in fermionic systems is of key importance, for example, for quantum information applications. In our system, the appearance of a chiral behavior is governed by several key parameters, including the ratio Ω_1/t, the Fermi energy E_F, and the flux φ. These parameters are easy to adjust, so they can be used to investigate the rise and fall of the edge currents as a function of the Hamiltonian parameters (24), as well as to identify which regimes exhibit stronger chiral features. By varying the tunneling rates along $\hat{x}$ and $\hat{m}$, we observe a phase transition between a chiral behavior and a nonchiral regime. The lattice momentum distribution is measured as a function of Ω_1/t without affecting other relevant parameters, such as E_F and T. Figure 2D illustrates the measurement of $|J|$ as a function of Ω_1/t (circles). As expected, no chirality is observed for vanishing Ω_1, when the legs are decoupled. Chirality is also suppressed for large inter-edge coupling $\Omega_1 \gg t$. In the latter regime, the largest energy scale in the system is the effective kinetic energy along the synthetic direction: This contribution is minimized when the fermions occupy the lowest energy state on each rung, which does not exhibit any chiral behavior. The measured values of $|J|$ compare well with the results of a numerical simulation

that includes thermal fluctuations (shaded area in Fig. 2D) (20).

We next considered a three-leg ladder, which is the minimal configuration for which chiral currents at the edges can be sharply distinguished from the behavior of the bulk. The experimental procedure is analogous to that employed for the two-leg case, with the Raman parameters adjusted to extend the synthetic coupling to $m = +3/2$, with $\Omega_2 \simeq 1.41 \, \Omega_1$ (20). Figure 3A shows measured $n(k)$ and $h(k)$ for each of the three legs for $\Omega_1 = 2\pi \times 620$ Hz and $t = 2\pi \times 94$ Hz ($\Omega_1/t = 6.60$). We observe strong chiral currents in the upper- and lower-edge chains, showing values of J with opposite sign, similar to the two-leg case [$J = +0.079(6)$ for $m = -5/2$ and $J = -0.062(4)$ for $m = +3/2$]. In contrast, the central leg shows a much-reduced asymmetry in $n(k)$ [$J = 0.018(5)$], signaling a suppressed net current in the bulk. This is direct evidence of the existence of chiral states propagating along the edges of the system, which leave the bulk mostly decoupled from the edges (Fig. 3C). This behavior is akin to what is expected for a fermionic system in a Harper-Hofstadter Hamiltonian. Bulk states exhibit only local circulations of current, which average to zero when all of the different states enclosed by the Fermi surface are considered. Only the edges of the system experience a nonzero current, because there the chiral nature of the states prevents this cancellation effect from occurring. In the ribbon geometry of the experiment, the bulk reduces to just a single central line. Nevertheless, the behavior discussed above is clearly present and detectable in the experimental signal. The small width of the ribbon favors the observation of edge states, given the large boundary-to-surface ratio of the system, which is reflected in a substantial population of states with edge character.

Figure 3C shows the values of J as a function of Ω_1/t for the three different legs of the ladder. The results illustrate the role of the bulk-edge coupling:
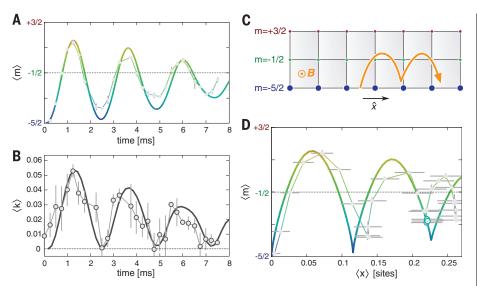
Fig. 4. Edge-cyclotron orbits. (**A**) Time dependence of the average position in the synthetic direction $\langle m \rangle$ after a quench on the synthetic tunneling. (**B**) Time dependence of the average lattice momentum $\langle k \rangle$ along the $\hat{x}$ direction. (**C**) Schematics of the edge-cyclotron orbits. (**D**) Average position in $\hat{m}$–$\hat{x}$ space. The circles in (A), (B), and (D) represent experimental data, the thin lines connect the points, and the thick lines illustrate the theoretical predictions (20). Experimental parameters: $\Omega_1 = 2\pi \times 490$ Hz and $t = 2\pi \times 94$ Hz. After the second orbit in (D), the mismatch between theory and experiment could possibly be ascribed to an accumulation of integration error in the data analysis, which amplifies the effects of the assumptions in the model (such as not accounting for interactions).

Similar to the two-leg case, chirality is very weak for small coupling and increases as Ω_1/t approaches ~3. The theoretical curves show that further increasing Ω_1/t eventually leads to attenuation of the signal because of effective coupling between the edges, which smoothens the chiral features of the system. We observe a substantial agreement between experiment and theory for the range of Ω_1/t that can be explored in our experimental setup. The nonzero current in the bulk ($J < 0.035$) can be ascribed to the different couplings (Ω_1 and Ω_2), as well as to a residual light shift that breaks the symmetry between the two edges (20).

Finally, we performed additional quench dynamics experiments that provide direct evidence of chiral transport properties along the edges. We prepared a system of lattice fermions in an initial state with zero average momentum on the lower $m = -5/2$ leg of a three-leg ladder. We then performed a quench by suddenly activating the complex tunneling in the synthetic direction. Figure 4A shows the time dependence of the average position in the synthetic direction $\langle m \rangle$, measured by optical Stern Gerlach detection (23). Figure 4B shows the time dependence of the average lattice momentum $\langle k \rangle$ along $\hat{x}$, measured by time-of-flight imaging of the whole cloud. Figure 4D shows an experimental reconstruction of the average orbit on the ribbon surface as a plot of $\langle m \rangle$ versus the average position in real space $\langle x \rangle$. The latter has been determined by evaluating the average velocity along $\hat{x}$, considering the knowledge of energy band dispersion versus lattice momentum, and then performing an integration in time (20). The dynamics displays a strong chiral character, demonstrated by the in-phase oscillations in Fig. 4, A and B, and the orbits in Fig. 4D. Under the effect of the synthetic magnetic field, the fermions move according to cyclotron-type dynamics, which is naturally truncated by the synthetic edge, giving rise to a skipping-type orbit, as expected for a quantum Hall system (12, 13). Furthermore, the experimental data are in reasonable agreement with the theoretical predictions, represented by the thick lines in Fig. 4, A, B, and D. These dynamics are effectively damped, even in the idealized case described by theory (Fig. 4, A and B), as a result of averaging over many different fermionic trajectories, which also causes a reduction of the average orbit radius to less than one real lattice site (Fig. 4D). This is markedly different from the behavior of a non-interacting Bose gas, which would occupy a single condensed wave packet undergoing undamped oscillations.

Our approach can be extended to wide ladder systems with as many as $2I + 1$ legs, providing a setting for the investigation of both edge and bulk 2D topological matter, complementary to recent works on Chern insulators (9). This would allow a controlled study of the combined effect of interactions and synthetic gauge fields, crucial for the realization of fractional quantum Hall physics, potentially leading to exotic states of matter (such as chiral Mott insulator states) in ladder systems. Moreover, the flexibility offered by the present scheme allows the engineering of arbitrary lattice patterns, including disorder and constriction, in ladder systems. This opens the door for the realization of interferometers for chiral liquids, investigation of their transport properties, and the possibility of implementing interfaces between chiral edges, which, in the presence of a molecular or superconducting reservoir (17), can potentially host exotic non-Abelian anyons such as Majorana-like states (16).

REFERENCES AND NOTES

1. M. Lewenstein, A. Sanpera, V. Ahufinger, *Ultracold Atoms in Optical Lattices: Simulating Quantum Many-Body Systems* (Oxford Univ. Press, Oxford, 2012).
2. I. Bloch, J. Dalibard, S. Nascimbène, *Nat. Phys.* **8**, 267–276 (2012).
3. D. Jaksch, P. Zoller, *New J. Phys.* **5**, 56 (2003).
4. J. Dalibard, F. Gerbier, G. Juzeliūnas, P. Öhberg, *Rev. Mod. Phys.* **83**, 1523–1543 (2011).
5. N. Goldman, G. Juzeliūnas, P. Öhberg, I. B. Spielman, *Rep. Prog. Phys.* **77**, 126401 (2014).
6. Y.-J. Lin, R. L. Compton, K. Jiménez-García, J. V. Porto, I. B. Spielman, *Nature* **462**, 628–632 (2009).
7. M. Aidelsburger *et al.*, *Phys. Rev. Lett.* **111**, 185301 (2013).
8. H. Miyake, G. A. Siviloglou, C. J. Kennedy, W. C. Burton, W. Ketterle, *Phys. Rev. Lett.* **111**, 185302 (2013).
9. G. Jotzu *et al.*, *Nature* **515**, 237–240 (2014).
10. F. D. M. Haldane, *Phys. Rev. Lett.* **61**, 2015–2018 (1988).
11. L. Duca *et al.*, *Science* **347**, 288–292 (2015).
12. X.-G. Wen, *Quantum Field Theory of Many-Body Systems* (Oxford Univ. Press, Oxford, 2004).
13. R. E. Prange, S. M. Girvin, *The Quantum Hall Effect* (Springer, New York, 1990).
14. A. Celi *et al.*, *Phys. Rev. Lett.* **112**, 043001 (2014).
15. N. Y. Yao *et al.*, *Nat. Commun.* **4**, 1585 (2013).
16. C. Nayak, S. H. Simon, A. Stern, M. Freedman, S. Das Sarma, *Rev. Mod. Phys.* **80**, 1083–1159 (2008).
17. N. H. Lindner, E. Berg, G. Refael, A. Stern, *Phys. Rev. X* **2**, 041002 (2012).
18. During the completion of this manuscript, we became aware of a closely related experimental work with Raman-coupled Bose-Einstein condensates (28).
19. O. Boada, A. Celi, J. I. Latorre, M. Lewenstein, *Phys. Rev. Lett.* **108**, 133001 (2012).
20. Full details on the experimental and theoretical procedures are available as supplementary materials on *Science* Online.
21. M. A. Cazalilla, A. M. Rey, *Rep. Prog. Phys.* **77**, 124401 (2014).
22. S. Taie, R. Yamazaki, S. Sugawa, Y. Takahashi, *Nat. Phys.* **8**, 825–830 (2012).
23. G. Pagano *et al.*, *Nat. Phys.* **10**, 198–201 (2014).
24. M. Atala *et al.*, *Nat. Phys.* **10**, 588–593 (2014).
25. Y.-J. Lin, K. Jiménez-García, I. B. Spielman, *Nature* **471**, 83–86 (2011).
26. P. Wang *et al.*, *Phys. Rev. Lett.* **109**, 095301 (2012).
27. L. W. Cheuk *et al.*, *Phys. Rev. Lett.* **109**, 095302 (2012).
28. B. K. Stuhl, H.-I Lu, L. M. Aycock, D. Genkina, I. B. Spielman, *Science* **349**, 1514–1518 (2015).

QUANTUM SIMULATION

Visualizing edge states with an atomic Bose gas in the quantum Hall regime

B. K. Stuhl,[1]* H.-I. Lu,[1]* L. M. Aycock,[1,2] D. Genkina,[1] I. B. Spielman[1]†

Bringing ultracold atomic gases into the quantum Hall regime is challenging. We engineered an effective magnetic field in a two-dimensional lattice with an elongated-strip geometry, consisting of the sites of an optical lattice in the long direction and of three internal atomic spin states in the short direction. We imaged the localized states of atomic Bose-Einstein condensates in this strip; via excitation dynamics, we further observed both the skipping orbits of excited atoms traveling down the system's edges, analogous to edge magnetoplasmons in two-dimensional electron systems, and a dynamical Hall effect for bulk excitations. Our technique involves minimal heating, which will be important for spectroscopic measurements of the Hofstadter butterfly and realizations of Laughlin's charge pump.

I n solids, the quantum Hall effects represent an extreme quantum limit, at which a system's behavior defies description by classical physics. The integer quantum Hall effect (IQHE) for two-dimensional (2D) electronic systems in magnetic fields (1) was the first topo-

[1]Joint Quantum Institute (JQI), National Institute of Standards and Technology (NIST) and University of Maryland, Gaithersburg, MD 20899, USA. [2]Department of Physics, Cornell University, Ithaca, NY 14850, USA.
*These authors contributed equally to this work. †Corresponding author. E-mail: ian.spielman@nist.gov

logical insulator (2): a bulk insulator with conducting edge states, always present in finite-sized topological systems, which produce the IQHE's signature quantized Hall resistance (3).

In classical systems, the magnetic field acts entirely through the Lorentz force, whereas in quantum systems, a particle with charge q in a uniform field B additionally acquires an Aharonov-Bohm phase $\phi_{AB}/2\pi = AB/\Phi_0$, after its path encircles an area A normal to B. (Here, $\Phi_0 = 2\pi\hbar/q$ is the flux quantum, and $2\pi\hbar$ is Planck's constant.) We generated an effective magnetic field in a system of cold

atoms, following (4), which yielded an elongated 2D square lattice formed from the sites of an optical lattice in the long direction and three internal atomic spin states in the short direction (a synthetic "spatial" dimension). We directly controlled the phases acquired as atoms traversed the lattice, creating an aggregate tunneling phase $\phi_{AB}/2\pi \approx 4/3$ around each lattice plaquette. These phases take the place of the Aharonov-Bohm phases produced by true magnetic fields and suffice to fully define the effective magnetic field. Aharonov-Bohm phases of order unity in the Harper-Hofstadter Hamiltonian, currently realized in engineered materials (5, 6) and in atomic (7–12) and optical (13) settings, fragment the low-field Landau levels into the fractal energy bands of the Hofstadter butterfly (14). Such Hofstadter bands are generally associated with a nonzero topological index, the Chern number (3).

Topologically nontrivial bulk properties are reflected by the presence of edge channels, composed of edge states, with quantized conductance. In fermionic systems, the number of edge channels is fixed by the aggregate topological index of the filled bands (2, 3, 15); this ultimately gives rise to phenomena such as the IQHE for electrons. Conceptually, the constituent edge states can be viewed as skipping orbits (2, 16, 17): In the presence of a strong magnetic field, nascent cyclotron orbits near the boundary reflect from the hard wall before completing a revolution, leading to skipping trajectories that follow the system's boundary. In contrast, localized bulk states correspond to closed cyclotron orbits.

By applying large effective fields to atomic Bose-Einstein condensates (BECs), we directly imaged individual, deterministically prepared bulk and edge eigenstates. In IQHE systems, these states
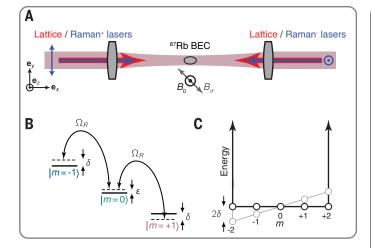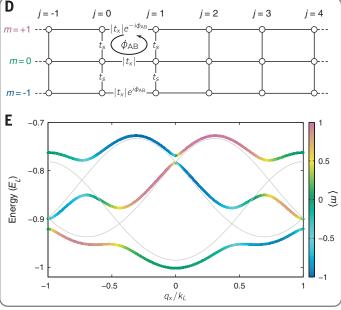

Fig. 1. Hybrid 2D lattice. (**A**) [87]Rb BECs (containing 10^5 atoms), confined in a 1D optical lattice with a bias magnetic field $B_0\mathbf{e}_z$, were illuminated either by a pair of counterpropagating Raman lasers with crossed linear polarization or by an rf magnetic field B_{rf}. (**B**) The Raman or rf field linking the three internal $|m\rangle$ states with Rabi frequency Ω_R was detuned by δ from the Zeeman splitting ($g\mu_B B_0/h \approx 0.817$ MHz or 1.35 MHz; g, the Landé g-factor; h, Planck's constant). The corresponding quadratic Zeeman shift lowered $|m = 0\rangle$ by $\varepsilon = 0.05E_L$ (for the data in Fig. 3) or $0.13E_L$ (for the data in Fig. 4). The Raman lasers' relative phases were actively stabilized at a beam combiner adjacent to the optical-lattice retroreflection mirror (24). (**C**) The lattice along $\mathbf{e}_s$ can be considered as a square well with hard walls at $m = \pm2$, for which $\delta \neq 0$ tilts the potential. (**D**) The 2D hybrid lattice, where the nonspatial dimension is built from the internal states $|m\rangle$, with an effective magnetic flux per plaquette of $\Phi/\Phi_0 = \phi_{AB}/2\pi$. (**E**) The three lowest magnetic bands (rainbow colors), computed for our full lattice without making the tight-binding approximation, with parameters $(\hbar\Omega_R, V, \delta, \varepsilon) = (0.141, 6, 0, 0.05)E_L$. The pale curves represent computations for $\hbar\Omega_R = 0$.

would govern the conductivity, but as individual eigenstates, they exhibit no time dependence. The corresponding dynamical entities are edge magnetoplasmons, consisting of superpositions of edge eigenstates in different Landau levels (18, 19) or, in this case, magnetic bands. We launched these excitations and recorded their full motion, observing both a chiral drift along the system's edge and the underlying skipping motion.

The Harper-Hofstadter Hamiltonian

$$H = -\sum_{j,m} [t_x |j+1,m\rangle \langle j,m| +$$

$$t_s |j, m+1\rangle \langle j,m| + \text{h.c.}] \qquad (1)$$

governs the motion of charged particles moving in a 2D lattice (14, 20)—i.e., the situation that we engineered for our neutral atoms—with complex hopping amplitudes t_x (long direction) and t_s (short direction) and sites labeled by j and m (h.c., Hermitian conjugate). Analogous to the Landau gauge in continuum systems, we describe our ex-

periment with real t_s (no phase) and with complex $t_x = |t_x|\exp(-i\phi_{AB} m)$, dependent on m. The sum of the tunneling phases around any individual plaquette is ϕ_{AB} (Fig. 1D).

We created a 2D lattice by combining a conventional optical lattice (21) to define the long axis of our system ($\mathbf{e}_x$ direction, sites labeled by j) with three sequentially coupled internal spin states to define the short axis ($\mathbf{e}_s$ direction, three sites labeled by $m \in \{-1,0,+1\}$); in parallel to the work described here, an analogous scheme has been realized for fermionic ytterbium (12). This system effectively has an infinite repulsive potential for $|m| \geq 2$ (Fig. 1C), allowing for the formation of robust edge states. In each band of our engineered lattice (Fig. 1E), the momentum along $\mathbf{e}_x$ specifies the position in $\mathbf{e}_s$ (denoted by color on the curves), as for 2D electrons in Landau levels.

We used ^{87}Rb BECs in the $f = 1$ ground-state hyperfine manifold (22), confined in an optical dipole potential from two 1064-nm laser beams aligned along $\mathbf{e}_x$ and $\mathbf{e}_y$, with trap frequencies $(\omega_x, \omega_y, \omega_z)/2\pi = (50, 40, 110)$ Hz (Fig. 1, A and B). We adiabatically (23) loaded these BECs onto the

sites of the 1D optical lattice, formed by a pair of laser beams (wavelength, $\lambda_L = 1064.46$ nm) counterpropagating along $\mathbf{e}_x$. The motion of atoms along $\mathbf{e}_y$ and $\mathbf{e}_z$ within each 2D layer formed by the 1D optical lattice was largely unaltered by the presence of the lattice, which only affected motion along $\mathbf{e}_x$. The lattice lasers' wavelength defines the single-photon recoil momentum $\hbar k_L = 2\pi\hbar/\lambda_L$ and recoil energy $E_L = \hbar^2 k_L^2/2m_{Rb}$, where $\hbar$ is the reduced Planck's constant, and m_{Rb} is the atomic mass. The lattice depth $V \approx 6E_L$ gave a hopping strength $|t_x| \approx 0.05E_L$ along $\mathbf{e}_x$.

We then coupled the three $|m\rangle$ sublevels, either with two-photon Raman transitions or with a radio-frequency (rf) magnetic field. The Raman lasers ($\lambda_R = 790.04$ nm) also counterpropagated approximately along $\mathbf{e}_x$ (24), with wavenumber $k_R = \pm 2\pi/\lambda_R$; the rf coupling effectively had a k_R of 0. Either field produced a laboratory-tunable effective tunneling strength $|t_s| \sim |t_x|$ along $\mathbf{e}_s$, proportional to the Rabi frequency Ω_R. The $2\hbar k_R$ momentum imparted from these transitions resulted in a spatially periodic phase factor $\exp(i2k_R x) = \exp(i\phi_{AB} j)$ accompanying the change in m, where $\phi_{AB}/2\pi = k_R/k_L \approx \pm 4/3$ for Raman coupling, and $\phi_{AB}/2\pi = 0$ for rf coupling (25, 4). The sign of ϕ_{AB} was controlled by reversing the relative detuning of the Raman lasers (Fig. 1, A and B), effectively swapping the laser directions.
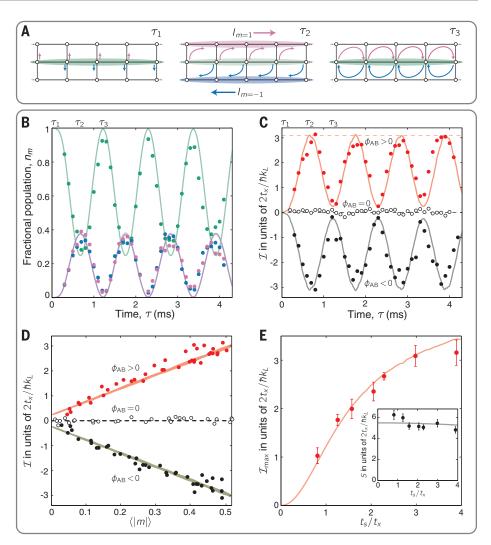
Figure 1E shows the band structure for our system, featuring the three Hofstadter bands expected for $\phi_{AB}/2\pi \sim 4/3$, with our boundary conditions. The system is most easily understood after making the local gauge transformation $|j,m\rangle \rightarrow \exp(-i\phi_{AB} jm) |j,m\rangle$, which transfers the Peierls phase from t_s into t_x. This fully maps our system to Eq. 1 and results in an effective flux $\Phi/\Phi_0 = \phi_{AB}/2\pi$ per plaquette (Fig. 1D).

We began our experiments by directly imaging adiabatically loaded eigenstates of the ground Hofstadter band with either $\phi_{AB}/2\pi = 0$ or $\phi_{AB}/2\pi \approx 4/3$, in an isotropic lattice with $|t_x| \approx |t_s|$. After preparation, we used a measurement procedure common to all experiments: We simultaneously removed all potentials and coupling fields (with a turnoff time $t_{off} < 1$ μs), which returned the atoms to bare spin and momentum states. The atomic cloud expanded for an ~18-ms time-of-flight (TOF) period (21). During TOF, a 2-ms magnetic gradient pulse was applied, and Stern-Gerlach spin separation was used to separate the three $|m\rangle$ states. The resulting 2D column density was recorded using standard absorption imaging techniques, giving the normalized momentum distributions $n_m(k_x)$ with perfect single-lattice site resolution along $\mathbf{e}_s$.

Figure 2A shows typical data for $\phi_{AB} = 0$, under which conditions we adiabatically loaded the BEC into the ground state and observed $n_m(k_x)$. The fractional population $n_m = \int dk_x n_m(k_x)$ (Fig. 2B) resembles that of a particle in a discretized box along $\mathbf{e}_s$, whereas the momentum distributions, typical for atoms in an optical lattice (26), have the same profile for each m site. This demonstrates that the two directions are uncoupled at $\phi_{AB} = 0$. The data in Fig. 2, C to E, for which $\phi_{AB} \neq 0$, are qualitatively different as a function of both k_x
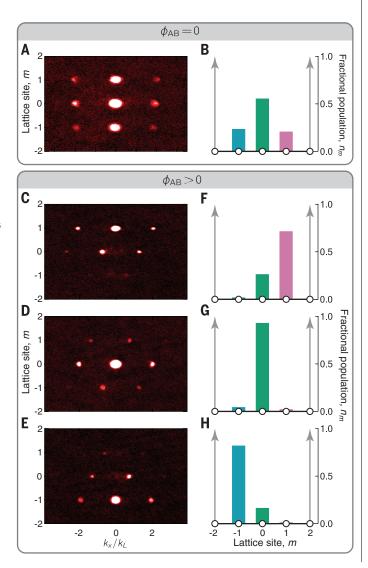

Fig. 2. Adiabatically loaded eigenstates.
(Left panels) Site-resolved normalized momentum distributions $n_m(k_x)$ obtained by absorption imaging. (Right panels) Fractional population n_m. (**A** and **B**) Atoms loaded into the single ground state present for $\phi_{AB} = 0$ show the expected separable behavior along $\mathbf{e}_x$ and $\mathbf{e}_s$. (**C** to **H**) Atoms loaded into the upper-edge, bulk, and lower-edge states (top, middle, and bottom panels, respectively) present for $\phi_{AB}/2\pi \approx 4/3$ demonstrate the coupling between $\mathbf{e}_x$ and $\mathbf{e}_s$ and the localization along $\mathbf{e}_s$.

Fig. 3. Chiral edge currents. (**A**) Schematic of system dynamics: A system prepared on site $m = 0$ at time $\tau_1 = 0$ obtains a chiral edge current at τ_2, which returns to zero at τ_3. (**B**) Measured fractional population versus time for atoms initialized on $m = 0$ at time $\tau = 0$. The dynamics are the same for positive and negative values of ϕ_{AB}. Colors in (A) and (B) correspond to m sites, as in Figs. 1 and 2. (**C**) Chiral edge current $\mathcal{I}$ versus time. Data shown in red, black, and open circles correspond to positive, negative, and zero values of ϕ_{AB}, respectively. (**D**) $\mathcal{I}$ plotted against $\langle|m|\rangle$. The solid curves (theory) use parameters $(\hbar\Omega_R, V, \delta, \varepsilon) = (0.52, 6, 0.001, 0.05)E_L$, determined from the data in (B) for $\phi_{AB} \neq 0$ and giving $t_s = 0.14E_L$, and parameters $(\hbar\Omega_R, V, \delta, \varepsilon) = (0.33, 6, -0.01, 0.05)E_L$ for $\phi_{AB} = 0$. (**E**) Maximum edge current versus asymmetry (t_s/t_x). (Inset) Slope S [taken from data as in (D)] is nearly independent of t_s/t_x.

and m. These differences can be understood by analogy with a 2D electron system in a perpendicular magnetic field, confined in one dimension with hard walls. Along the confined direction, the wavefunction is localized to the scale of the magnetic length $\ell_B = \sqrt{\hbar/qB}$, with the center position at $k_x\ell_B^2$ in the bulk state, and where $\hbar k_x$ is the electron's canonical momentum. At large $|k_x|$, the electron becomes localized near the edges, lifting the degeneracy of the otherwise macroscopically degenerate Landau levels. Each of these points has an analog in our observations (Fig. 1E and Fig. 2, F to H). In our system, the magnetic length $\ell_B^* \sim \sqrt{3/2\pi} \approx 0.7$, in units of lattice period, was of order unity (23); this considerably narrowed the bulk state (Fig. 2G), as compared with conditions in which $\phi_{AB} = 0$ (Fig. 2B). In addition, we observed the appearance of states that were localized at the system's edges (Fig. 2, F and H), which were completely absent when $\phi_{AB} = 0$. These localized edge states are the analog to the current-carrying edge states in fermionic IQHE systems (27).

Having described the static properties of this system, we now turn to dynamics. We loaded our system onto different m sites with $t_s = 0$ and then abruptly (24) turned on t_s, allowing tunneling along $\mathbf{e}_s$. The resulting initial states all consisted of coherent superpositions of magnetic-band eigenstates with crystal momentum $q_x/k_L = -m\phi_{AB}/\pi$, which began to coherently tunnel along $\mathbf{e}_s$ and to move along $\mathbf{e}_x$ as a result of the associated Lorentz force. Atoms initialized on the bulk $m = 0$ site exhibited a dynamic Hall effect. Those starting on the edge sites became cold-atom analogs to edge magnetoplasmons: They began cyclotron orbits, were reflected from the hard wall, and skipped down one edge or the other.

The dynamics of atoms initialized in the bulk state (on the $m = 0$ site) are presented in Fig. 3. As schematically illustrated in Fig. 3A and plotted in Fig. 3B, a balanced population oscillated in and out of the originally empty $m = \pm1$ sites, as a function of time τ. When $\phi_{AB} \neq 0$, this motion drove transverse (i.e., Hall) edge currents $I_{m=\pm1}(\tau) = n_m(\tau)\langle V_m\rangle$ along $\mathbf{e}_x$ (Fig. 3A), where $\langle V_m\rangle$ is the mean velocity of atoms on site m along $\mathbf{e}_x$.

A chiral current $\mathcal{I} = I_1 - I_{-1}$ developed, with its overall sign following that of ϕ_{AB} (Fig. 3C). As atoms tunneled to the edges, they acquired a transverse velocity controlled by two parameters: ϕ_{AB} determined the crystal momentum acquired while tunneling, and t_x set the natural unit of velocity $2t_x/\hbar k_L$. This led to the observed in-phase oscillation of $\mathcal{I}$ and the combined $m = \pm1$ populations $\langle|m|\rangle$.

This synchronous oscillation implies a linear dependence of $\mathcal{I}$ on $\langle|m|\rangle$, the slope S of which is plotted in red and black symbols in Fig. 3D. We confirmed the system's chirality by inverting ϕ_{AB} and verifying that S changed in sign. For comparison, we repeated the experiment with $\phi_{AB} = 0$ and observed no chiral current (open symbols). These data are in good agreement with our theory (solid curves in Fig. 3D), which uses parameters obtained from fits to Fig. 3B (24).

The dependence of the chiral current on the tunneling anisotropy t_s/t_x (Fig. 3E) is reminiscent of the optical lattice experiments in (28). The chiral current remained linear in $\langle|m|\rangle$, with an essentially constant slope $S \approx 2t_x\lambda_L\sin(\phi_{AB})/\hbar$; this demonstrates a dynamic Hall effect (29) governed by the magnetic flux and the optical lattice strength and period (24). In contrast, the peak edge current $\mathcal{I}_{max}$ (pink dashed line in Fig. 3C) strongly depends on t_s/t_x (Fig. 3E), increasing from zero and then reaching saturation. For small t_s/t_x, few atoms tunneled, giving a correspondingly small
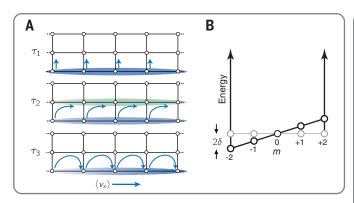
Fig. 4. Skipping orbits. (**A** and **B**) Schematic of dynamics, starting from $m = -1$ (indicated by the blue ellipse) and including a nonzero detuning that tilted the lattice along $\mathbf{e}_s$. (**C**) Mean displacement $\langle m \rangle$ versus time τ for excitations on both edges. Data for systems initialized on $m = 1$ ($m = -1$) are depicted by pink (blue) circles. (**D**) Group velocity along $\mathbf{e}_x$ versus time for both edge excitations. Numerical simulations (solid curves) use parameters $(\hbar\Omega_R, V, \delta, \varepsilon) = (0.41, 5.2, \pm 0.087, 0.13)E_L$ from fits to population dynamics, such as those shown in (C). In both cases, the potential gradient along $\mathbf{e}_s$ from δ was selected so that the initial site ($m = \pm 1$) had the lowest energy. (**E**) Edge-magnetoplasmon trajectories, where the displacement $\langle \delta j(\tau) \rangle$ was obtained by integrating $\langle v_x(\tau)/a \rangle$.

$\mathcal{I}_{max}$; as t_s/t_x increased, $\mathcal{I}_{max}$ began to saturate as essentially all atoms tunneled (27).

We then shifted our focus from bulk excitations to edge excitations, which we studied by launching edge magnetoplasmons, or superpositions of edge states across magnetic bands with crystal momentum $q_a/k_L = \mp \phi_{AB}/\pi$. We created them on either edge, with the potential tilted along $\mathbf{e}_s$ (Fig. 4, A and B), so that the initially occupied site was at the potential minimum. The time-evolving average position $\langle m(\tau) \rangle$ along $\mathbf{e}_s$ and the velocity $\langle v_x(\tau) \rangle = \sum_m I_m$ along $\mathbf{e}_x$ are shown in Fig. 4, C and D. Data shown in pink and blue solid circles are for initial sites $\langle m(\tau = 0) \rangle = \pm 1$, both of which evolved periodically in time but with opposite velocities. The spatial trajectories are illustrated in Fig. 4E; we obtained the displacement $\langle \delta j(\tau) \rangle$ by directly integrating $\langle v_x(\tau)/a \rangle$, where $a = \lambda_L/2$ is the lattice period. These data show edge magnetoplasmons with their chiral longitudinal motion and constitute an experimental observation of their edge localization and transverse skipping motion.

This and related approaches (12) have a practical advantage over other techniques for creating artificial gauge fields, in that minimal Raman-laser coupling is required [typically 10 to 50 times less than in previous experiments using Raman coupling (30)], thereby minimizing heating from spontaneous emission and enabling many-body experiments that require negligible heating rates. Lifetimes from spontaneous emission with this technique are in excess of 10 s (corresponding to a heating rate of $<10^{-3}$ $t_x/2\pi\hbar$), whereas other approaches for creating large artificial gauge fields have lifetimes well below 1 s (8–10, 31).
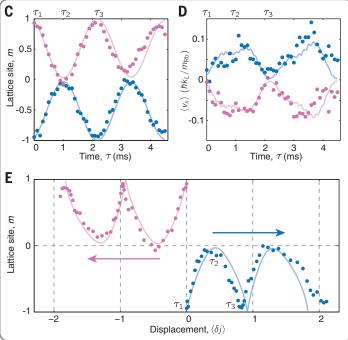
The experiments described here used nearly pure BECs, either in adiabatically prepared eigen-states or evolving after sudden changes to the Hamiltonian. In the former case, interactions did not affect our measurements, whereas in the latter case, collisions during the dynamical evolution gradually populated additional states and contributed to considerable dephasing within 10 ms. Because our approach of using the internal atomic spin states as lattice sites involves different "synthetic sites" residing in the same location in space, the interactions between atoms are anisotropic—short-ranged along $\mathbf{e}_x$ but long-ranged along $\mathbf{e}_s$. In (32), it was shown theoretically that even such anisotropic systems can support fractional quantum Hall states.

With our hard-wall potential, a realization of the Laughlin charge pump (33) is straightforward: As particles accelerate along $\mathbf{e}_x$, mass moves from one edge to the other in the orthogonal direction $\mathbf{e}_s$. Extending our technique to periodic boundary conditions—i.e., coupling the $|m = \pm 1\rangle$ states—should produce systems exhibiting a fractal Hofstadter spectrum (4), even with only a three-site extent along $\mathbf{e}_s$. Going beyond conventional condensed-matter realities, the flexibility afforded by directly laser-engineering the hopping enables the creation of Möbius strip geometries, or topological systems with only one edge (34).

REFERENCES AND NOTES

1. K. von Klitzing, G. Dorda, M. Pepper, *Phys. Rev. Lett.* **45**, 494–497 (1980).
2. M. Z. Hasan, C. L. Kane, *Rev. Mod. Phys.* **82**, 3045–3067 (2010).
3. D. J. Thouless, M. Kohmoto, M. P. Nightingale, M. den Nijs, *Phys. Rev. Lett.* **49**, 405–408 (1982).
4. A. Celi *et al.*, *Phys. Rev. Lett.* **112**, 043001 (2014).
5. M. C. Geisler *et al.*, *Phys. Rev. Lett.* **92**, 256801 (2004).
6. B. Hunt *et al.*, *Science* **340**, 1427–1430 (2013).
7. D. Jaksch, P. Zoller, *New J. Phys.* **5**, 56 (2003).
8. M. Aidelsburger *et al.*, *Phys. Rev. Lett.* **111**, 185301 (2013).
9. H. Miyake, G. A. Siviloglou, C. J. Kennedy, W. C. Burton, W. Ketterle, *Phys. Rev. Lett.* **111**, 185302 (2013).
10. G. Jotzu *et al.*, *Nature* **515**, 237–240 (2014).
11. M. Aidelsburger *et al.*, *Nat. Phys.* **11**, 162–166 (2015).
12. M. Mancini *et al.*, *Science* **349**, 1510–1513 (2015).
13. M. Hafezi, S. Mittal, J. Fan, A. Migdall, J. M. Taylor, *Nat. Photonics* **7**, 1001–1005 (2013).
14. D. R. Hofstadter, *Phys. Rev. B* **14**, 2239–2249 (1976).
15. W. Beugeling, N. Goldman, C. Morais Smith, *Phys. Rev. B* **86**, 075118 (2012).
16. M. Büttiker, *Phys. Rev. B* **38**, 9375–9389 (1988).
17. G. Montambaux, *Eur. Phys. J. B* **79**, 215–224 (2011).
18. K. Kern, D. Heitmann, P. Grambow, Y. H. Zhang, K. Ploog, *Phys. Rev. Lett.* **66**, 1618–1621 (1991).
19. R. C. Ashoori, H. L. Stormer, L. N. Pfeiffer, K. W. Baldwin, K. West, *Phys. Rev. B* **45**, 3894–3897 (1992).
20. P. G. Harper, *Proc. Phys. Soc. A* **68**, 879–892 (1955).
21. O. Morsch, M. Oberthaler, *Rev. Mod. Phys.* **78**, 179–215 (2006).
22. Y.-J. Lin, A. R. Perry, R. L. Compton, I. B. Spielman, J. V. Porto, *Phys. Rev. A* **79**, 063631 (2009).
23. Because all physics is 2π-periodic in the acquired phase, our flux $\phi_{AB}/2\pi \approx 4/3$ is equivalent to $\phi_{AB} \approx 2\pi/3$. For the purpose of estimating the magnetic length, which is a continuum concept, it is suitable to use $\ell_B^* \approx \sqrt{3/2\pi}$.
24. Materials and methods are available as supplementary materials on *Science* Online.
25. O. Boada, A. Celi, J. I. Latorre, M. Lewenstein, *Phys. Rev. Lett.* **108**, 133001 (2012).
26. M. Greiner, I. Bloch, O. Mandel, T. Hänsch, T. Esslinger, *Phys. Rev. Lett.* **87**, 160405 (2001).
27. D. Hügel, B. Paredes, *Phys. Rev. A* **89**, 023619 (2014).
28. M. Atala *et al.*, *Nat. Phys.* **10**, 588–593 (2014).
29. L. J. LeBlanc *et al.*, *Proc. Natl. Acad. Sci. U.S.A.* **109**, 10811–10814 (2012).
30. Y. J. Lin, R. L. Compton, K. Jiménez-García, J. V. Porto, I. B. Spielman, *Nature* **462**, 628–632 (2009).
31. J. Struck *et al.*, *Phys. Rev. Lett.* **108**, 225304 (2012).
32. A. Petrescu, K. Le Hur, *Phys. Rev. B* **91**, 054520 (2015).
33. R. Laughlin, *Phys. Rev. B* **23**, 5632–5633 (1981).
34. O. Boada, A. Celi, J. Rodríguez-Laguna, J. I. Latorre, M. Lewenstein, *New J. Phys.* **17**, 045007 (2015).

NANOMATERIALS

Atomically thin two-dimensional organic-inorganic hybrid perovskites

Letian Dou,[1,2]* Andrew B. Wong,[1,2]* Yi Yu,[1,2,3]* Minliang Lai,[1] Nikolay Kornienko,[1,2] Samuel W. Eaton,[1] Anthony Fu,[1,2] Connor G. Bischak,[1] Jie Ma,[2] Tina Ding,[1,2] Naomi S. Ginsberg,[1,2,4,5,6] Lin-Wang Wang,[2] A. Paul Alivisatos,[1,2,5,7] Peidong Yang[1,2,5,7]†

Organic-inorganic hybrid perovskites, which have proved to be promising semiconductor materials for photovoltaic applications, have been made into atomically thin two-dimensional (2D) sheets. We report the solution-phase growth of single- and few-unit-cell-thick single-crystalline 2D hybrid perovskites of $(C_4H_9NH_3)_2PbBr_4$ with well-defined square shape and large size. In contrast to other 2D materials, the hybrid perovskite sheets exhibit an unusual structural relaxation, and this structural change leads to a band gap shift as compared to the bulk crystal. The high-quality 2D crystals exhibit efficient photoluminescence, and color tuning could be achieved by changing sheet thickness as well as composition via the synthesis of related materials.

The organic-inorganic hybrid perovskites, especially $CH_3NH_3PbI_3$, have recently been used in solution-processable photovoltaic devices that have reached 20% power conversion efficiency (1–4). These layered materials have a general formula of $(RNH_3)_2(CH_3NH_3)_{m-1}A_mX_{3m+1}$, where R is an alkyl or aromatic moiety, A is a metal cation, and X is a halide. The variable m indicates the number of the metal cation layers between the two layers of the organic chains (5–11). In the extreme case where $m = \infty$, the structure becomes a three-dimensionally bonded perovskite crystal with a structure similar to $BaTiO_3$. In the opposite extreme where $m = 1$, the structure becomes an ideal quantum well with only one atomic layer of AX_4^{2-} separated by organic chains, in which the adjacent layers are held together by weak van der Waals forces.

This arrangement is fundamentally different from transition metal dichalcogenides, in which one layer of the metal ions is sandwiched between two hexagonal layers of S or Se atoms, affording a rigid backbone. In contrast, the lay-

ered hybrid perovskites normally have a tetragonal or orthorhombic structure and are inherently more flexible and deformable (5–11). By varying the value of m, the thickness and the related optoelectronic properties of the quantum well can be tuned. To date, many organic amines, metal cations (Cu^{2+}, Mn^{2+}, Cd^{2+}, Ge^{2+}, Sn^{2+}, Pb^{2+}, Eu^{2+}, etc.) and halides (Cl, Br, and I) have been used to construct such layered materials ($m = 1 \sim 3$), and their corresponding optoelectronic properties have been well studied (12–15). Previous reports have claimed that the organic layers effectively isolate the two-dimensional (2D) quantum wells in each layer from electronic coupling, if the organic chain is longer than propyl amine (16). This means that the properties of the atomically thin 2D quantum well should be the same as those of the bulk layered material (microscopic crystal, powder, or film). This hypothesis, as well as the technical difficulty of separating individual layers, has probably delayed investigation of freestanding single layers of such 2D materials. Very recently, attempts to obtain ultrathin 2D perovskite samples by spin coating, chemical vapor deposition, or mechanical exfoliation methods have been made with limited success (17–19).

Here we report the direct growth of atomically thin 2D hybrid perovskites $[(C_4H_9NH_3)_2PbBr_4]$ and derivatives from solution. Uniform square-shaped 2D crystals on a flat substrate with high yield and excellent reproducibility were synthesized by using a ternary co-solvent. We investigated the structure and composition of individual 2D crystals using transmission electron microscopy (TEM), energy-dispersive spec-

troscopy (EDS), grazing-incidence wide-angle x-ray scattering (GIWAXS), and Raman spectroscopy. Unlike other 2D materials, a structural relaxation (or lattice constant expansion) occurred in the hybrid perovskite 2D sheets that could be responsible for emergent features. We investigated the optical properties of the 2D sheets using steady-state and time-resolved photoluminescence (PL) spectroscopy and cathodoluminescence microscopy. The 2D hybrid perovskite sheets have a slightly shifted band edge emission that could be attributed to the structural relaxation. We further demonstrated that the as-grown 2D sheets exhibit high PL quantum efficiency as well as wide composition and color tunability.

A structural illustration of a monolayer 2D perovskite (Fig. 1A) shows the case with six Br atoms surrounding each Pb atom, and the four in-plane Br atoms are shared by two octahedrons, forming a 2D sheet of $PbBr_4^{2-}$. The negative charges are compensated for by the butylammonium that caps the surfaces of the 2D sheet. This structure is amenable to facile solution synthesis. The ionic character of such materials is stronger than the transition metal disulfides and diselenides, and the bulk solid is soluble in polar organic solvents such as dimethylformamide (DMF) (20). To grow 2D sheets, a very dilute precursor solution was dropped on the surface of a Si/SiO_2 substrate and dried under mild heating [see the supplementary materials (21)]. A DMF and chlorobenzene (CB) co-solvent was initially investigated, because CB helps to reduce the solubility of $(C_4H_9NH_3)_2PbBr_4$ in DMF and promote crystallization. Because CB has a similar boiling point and evaporation rate as DMF, the drying of the solvents and the crystallization process were uniform across the whole substrate.

We examined the products of this reaction by optical microscopy and atomic force microscopy (AFM), but instead of monolayers, thick particles with random shapes formed on the substrate (fig. S1). Hybrid perovskites have limited solubility in acetonitrile, and the solvent has been used previously for making microscopic hybrid perovskite single crystals (22). In this case, acetonitrile evaporates more quickly and helps induce the formation of the ultrathin 2D hybrid perovskite sheets. When acetonitrile was combined with DMF and CB, uniform square sheets grew on the substrate (Fig. 1B). The edge length of the square crystals ranged from 1 to 10 μm, with an average of 4.2 μm (the size distribution statistics can be found in fig. S2). The detailed synthetic procedure and discussion of the role of each solvent can be found in the supplementary text (21).

[1]Department of Chemistry, University of California, Berkeley, CA 94720, USA. [2]Materials Sciences Division, Lawrence Berkeley National Laboratory, Berkeley, CA 94720, USA. [3]School of Physical Science and Technology, ShanghaiTech University, Shanghai, 201210, China. [4]Department of Physics, University of California, Berkeley, CA 94720, USA. [5]Kavli Energy NanoScience Institute, Berkeley, CA 94720, USA. [6]Physical Biosciences Division, Lawrence Berkeley National Laboratory, Berkeley, CA 94720, USA. [7]Department of Materials Science and Engineering, University of California, Berkeley, CA 94720, USA.
*These authors contributed equally to this work. †**Corresponding author. E-mail: p_yang@berkeley.edu**

The thickness of the square sheets was quantified with AFM. The thickness of the crystals varied from a few to tens of nanometers; the thinnest sheets were ~1.6 nm (±0.2 nm). The AFM images of several monolayer and double-layer sheets show thicknesses of 1.6 and 3.4 nm (±0.2 nm) (Fig. 1, C and D), whereas the d spacing in the bulk crystal was 1.4 nm (20). AFM tapping mode (noncontact) was used to avoid sample damage, which can lead to a minor overestimation. For the separated monolayer, the organic chain may also relax, and the apparent thickness of the monolayer may increase slightly. Additional AFM images of other similar 2D sheets can be seen in fig. S3.

By combining AFM and optical microscopy, we correlated the appearance of the sheets in the optical image with their thickness as shown in fig. S4. The thinnest sheet on Si/SiO_2 that we could distinguish in an optical microscope was a double layer. We also prepared large single crystals of $(C_4H_9NH_3)_2PbBr_4$ and investigated the conventional mechanical exfoliation method using tape and the solvent exfoliation method using hexane to disperse the thin sheets (23). Unfortunately, the majority of the products from mechanical exfoliation were very thick flakes (fig. S5A) and from solvent exfoliation they were randomly shaped particles (fig. S5, B and C). The monolayer-thick particles obtained were very small (less than 1 μm), which suggests that these hybrid perovskite layers are mechanically brittle.

To determine the crystal structure of the 2D hybrid perovskites, x-ray diffraction (XRD) and TEM were used. The XRD pattern revealed that the (001) plane grew parallel to the substrate, and the out-of-plane d spacing was 1.42 nm (fig. S6), which is consistent with reported data for this material (16). The in-plane structural information was revealed by selected-area electron diffraction (SAED) in a TEM. F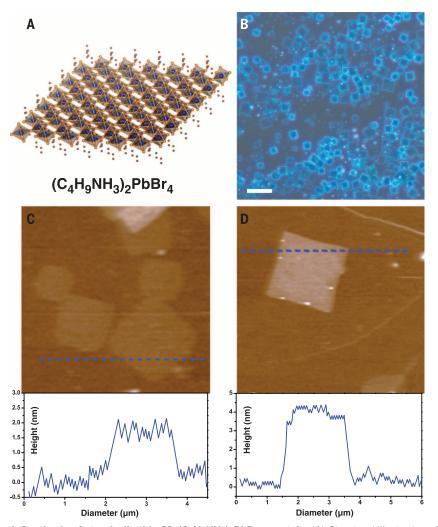igure 2A shows a TEM image of a 2D sheet grown on a lacy carbon grid. After examining more than 20 individual sheets by TEM, we found that they all showed similar shape and identical diffraction patterns (additional TEM images are shown fig. S7); Fig. 2B shows the SAED pattern of another sheet. The calculated average in-plane lattice constants are $a = 8.41$ Å and $b = 8.60$ Å from five sheets, which are slightly greater than the lattice constants in the bulk crystal measured by single-crystal XRD [$a = 8.22$ Å and $b = 8.33$ Å, see (15) and tables S1 and S2]. The electron diffraction patterns were consistent with structural simulations, which further confirm the structure of the atomically thin 2D sheets (see figs. S8 and S9 for more discussion on the simulations/experiments on the bulk and few-layer hybrid perovskites).
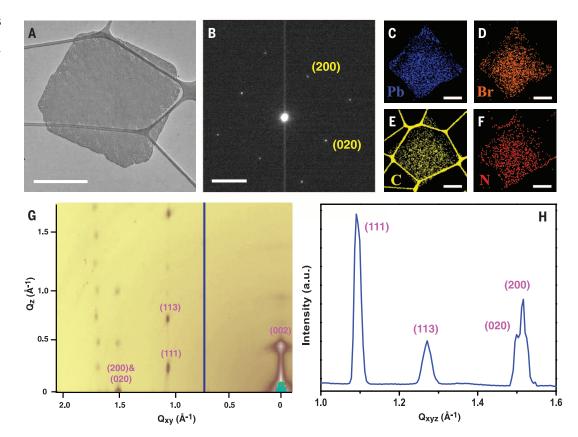
We observed rapid radiation damage of the sheets under the strong electron beam. After exposing the 2D sheets to the electron beam for a few seconds, Pb was reduced and precipitated, which caused the sample to be irreversibly damaged (fig. S10). This phenomenon is similar to that observed in alkali halides (24). More examples of SAED patterns of individual sheets and their corresponding TEM images demonstrating the degradation can be found in fig. S11. Figure 2, C to F, shows the elemental distribution in the thin sheets; lead, bromine, carbon, and nitrogen are all present in the square.

The lattice expansion in the 2D sheets was further confirmed through macroscopic GIWAXS measurements. Figure 2G shows the GIWAXS image and Fig. 2H shows the integrated pattern. In addition, to the (200) and (020) peaks observed in TEM diffraction, many other peaks can be assigned. The d spacing of the (200), (020), (111), and (113) planes is 4.19 (lattice constant $a = 8.38$ Å), 4.25 (lattice constant $b = 8.50$ Å), 5.81, and 5.00 Å; respectively. These values are all greater than those of the bulk crystals and are consistent with our TEM measurements of single 2D sheets.

In addition, we examined the Raman spectra of the bulk crystal and the thin sheet as shown in fig. S12. The peaks found at 57.7 and 43.6 cm^{-1} for the bulk crystal shifted to 55.2 and 41.3 cm^{-1} for the 2D sheet, respectively. These peaks can be attributed to Pb-Br stretching and librational motions of both inorganic and organic ions (25), indicating that relaxation of the crystal lattice occurs in the thin sheets. Meanwhile, the peak at 122.2 cm^{-1} (from -CH_3 group torsional motion and insensitive to lattice distortion) did not change. The peaks for the 2D sheet became narrower, suggesting better-defined vibrational states in the thin sheet. Furthermore, our density functional theory (DFT) calculation indicates a small lattice expansion of around 0.1 Å for the monolayer as compared to the bulk $(C_4H_9NH_3)_2PbBr_4$ crystal (see the supplementary materials for details about DFT simulation).

Strong crystal lattice distortions are common for hybrid perovskites (5–10). Structural distortion–induced optical and electronic changes have been reported in bulk hybrid perovskites (26–29). Single-crystal XRD data of the bulk crystal of $(C_4H_9NH_3)_2PbBr_4$ revealed that the $PbBr_4^{2-}$ layer in the bulk crystal is highly distorted, with a

Fig. 1. Synthesis of atomically thin 2D $(C_4H_9NH_3)_2PbBr_4$ crystals. (**A**) Structural illustration of a single layer $(C_4H_9NH_3)_2PbBr_4$ (blue balls, lead atoms; large orange balls, bromine atoms; red balls, nitrogen atoms; small orange balls, carbon atoms; H atoms were removed for clarity). (**B**) Optical image of the 2D square sheets. Scale bar, 10 μm. (**C**) AFM image and height profile of several single layers. The thickness is around 1.6 nm (±0.2 nm). (**D**) AFM image and height profile of a double layer. The thickness is around 3.4 nm (±0.2 nm).

$(C_4H_9NH_3)_2PbBr_4$

Fig. 2. TEM, EDS, and GIWAXS studies. (**A**) TEM image of a thin $(C_4H_9NH_3)_2PbBr_4$ sheet. Scale bar, 1 μm. (**B**) Electron diffraction pattern of a thin sheet of $(C_4H_9NH_3)_2PbBr_4$. Scale bar, 2 nm^{-1}. (**C** to **F**) EDS analysis showing the elemental distribution of lead, bromide, carbon, and nitrogen, respectively. Scale bars, 1 μm. (**G**) GIWAXS image of the 2D thin sheets. Q, wave vector in reciprocal space. (**H**) Integrated GIWAXS spectrum of the 2D thin sheets. a.u., arbitrary units.

Pb-Br-Pb bond angle of 152.94° (see fig. S13 and tables S3 and S4 for more details), which may provide driving forces for lattice relaxation in the 2D thin sheet. In other reported 2D materials, the in-plane crystal structure does not change from the bulk crystal to isolated sheets; and the optical and electronic properties change because of electronic decoupling between adjacent layers.

We investigated the PL properties of individual 2D crystals under 325-nm laser excitation. Figure 3A shows the PL spectra of the bulk $(C_4H_9NH_3)_2PbBr_4$ crystal and 2D sheets with different thickness (22, 8, and 3 layers thick, see fig. S14 for AFM images), and Fig. 3, B to E, shows the corresponding PL image of each sheet. Both the bulk materials and the sheets exhibit similar strong purple-blue light emission. The bulk crystal has an emission peak at 411 nm (2.97 eV), and the 2D sheets have slightly blue-shifted peaks at ~406 nm (3.01 eV). The slightly increased optical band gap for the ultrathin 2D sheets is probably induced by the lattice expansion. Our DFT simulation also suggests a 20-meV blue shift in PL for the single-layer 2D sheets, which is a trend consistent with the experimental observation. The 2D sheets with different thickness (from 22 to 3 layers) have similar PL spectra, the peak position shift is within 1 nm, and any lattice constant difference is within the experimental error from SAED observed between these samples. More discussion about the PL can be found in the supplementary text (21).

Cathodoluminescence microscopy, a technique that provides a map of the light emitted from a sample when excited by a focused electron beam with excellent lateral resolution, was used to determine the spatial distribution of emissive sites on the 2D sheets. As shown in Fig. 3G, the cathodoluminescence mapping from 395 to 435 nm shows a square shape identical to the corresponding scanning electron microscopy (SEM) images as shown in Fig. 3F, indicating that the emission is from the whole square. The PL internal quantum efficiency (QE) of the 2D sheets was estimated by comparing the integrated PL intensity (from 390 to 450 nm) of the band edge emission at room temperature (298 K) and helium cryogenic temperature (6 K), and the results are shown in Fig. 3H (30). There is a small red shift of the main peak from 406 to 412 nm as the temperature decreases. The emission at 421 nm (2.91 eV) at 6 K is known from the Γ_1^- state, which cannot be distinguished from the Γ_2^- state at room temperature (26). The PL QE for the 2D sheet is calculated to be ~26%, which is much higher than the QE of the bulk crystal (<1%), indicating the high quality of the single-crystalline 2D sheets. The PL intensity increased linearly as the excitation power increased (fig. S15), suggesting that the PL QE was constant within our measurement range. The PL lifetime of the 2D sheets was measured by time-resolved PL. As shown in Fig. 3I, the decay curve showed a bi-exponential feature with lifetimes of 0.78 ns (67%) and 3.3 ns (33%), which are near the reported data for the bulk crystals (15).

The chemistry of synthesizing these ultrathin 2D sheets was extended to other hybrid perovskites (8). We prepared $(C_4H_9NH_3)_2PbCl_4$, $(C_4H_9NH_3)_2PbI_4$, $(C_4H_9NH_3)_2PbCl_2Br_2$, $(C_4H_9NH_3)_2PbBr_2I_2$, and $(C_4H_9NH_3)_2(CH_3NH_3)Pb_2Br_7$ ultrathin 2D sheets using similar methods, and their PL spectra and optical images are shown in Fig. 4 (see fig. S16 for XRD and fig. S17 for AFM images). For the $(C_4H_9NH_3)_2PbCl_4$ sheet (i), the band edge emission was in the ultraviolet at ~340 nm, which was beyond our detection range for the single-sheet measurement. Three states in the visible region were observed at 486, 568, and 747 nm, which made the sheets appear nearly white. This emission is attributed to the transient formation of self-trapped excitons (31). For the $(C_4H_9NH_3)_2PbI_4$ sheet (iii), the band edge emission was at 514 nm, which is blue-shifted by 9 nm as compared to the bulk (5). This blue shift is consistent with the bromide case (ii) discussed above. For the chloride-bromide alloy crystal, $(C_4H_9NH_3)_2PbCl_2Br_2$ (iv), the band edge emission peak was at 385 nm, and a broad self-trapped exciton emission appeared at longer wavelength. However, the bromide-iodide alloy (v) showed only one peak at 505 nm. In the case of $(C_4H_9NH_3)_2(CH_3NH_3)Pb_2Br_7$, no well-defined squares were observed, and the thickness of the plates was ~10 nm. Preliminary PL study indicates a band edge emission at 453 nm, which is red-shifted slightly as compared to the bulk. These results indicate that the 2D hybrid perovskites have excellent composition and color tunability.

The direct growth of atomically thin sheets overcomes the limitations of the conventional exfoliation and chemical vapor deposition methods, which normally produce relatively thick perovskite plates (17–19, 32, 33). In contrast to other 2D materials, the structural framework of
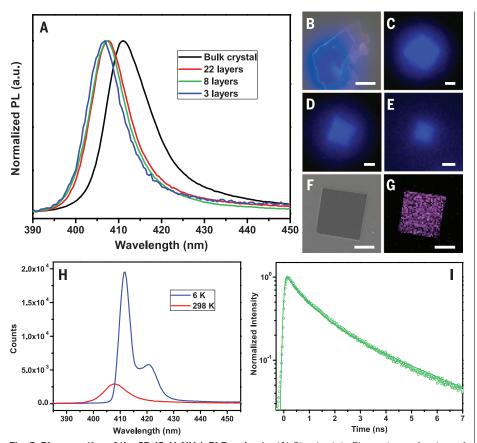
Fig. 3. PL properties of the 2D (C$_4$H$_9$NH$_3$)$_2$PbBr$_4$ sheets. (**A**) Steady-state PL spectrum of a piece of bulk crystal and several 2D sheets. (**B**) The corresponding optical image of the bulk crystal under excitation. Scale bar, 20 μm. (**C** to **E**) Optical images of the 2D sheets with 22 layers, 8 layers, and 3 layers. Scale bars, 2 μm. (**F**) SEM image of a 2D sheet. Scale bar, 2 μm. (**G**) The corresponding cathodoluminescence image showing the emission (with a 40-nm bandpass filter centered at 415 nm). (**H**) PL spectra of a 2D sheet at 298 and 6 K. (**I**) Time-resolved PL measurements showing a bi-exponential decay.
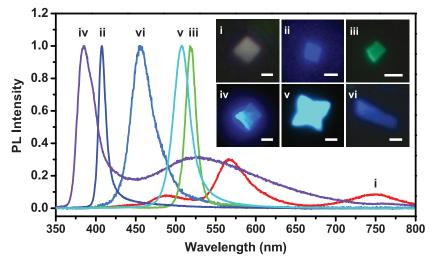

Fig. 4. Photoluminescence of different 2D hybrid perovskites. (C$_4$H$_9$NH$_3$)$_2$PbCl$_4$ (i), (C$_4$H$_9$NH$_3$)$_2$PbBr$_4$ (ii), (C$_4$H$_9$NH$_3$)$_2$PbI$_4$ (iii), (C$_4$H$_9$NH$_3$)$_2$PbCl$_2$Br$_2$ (iv), (C$_4$H$_9$NH$_3$)$_2$PbBr$_2$I$_2$ (v), and (C$_4$H$_9$NH$_3$)$_2$(CH$_3$NH$_3$)Pb$_2$Br$_7$ (vi) 2D sheets demonstrate that the solution-phase direct growth method is generalizable. The corresponding optical PL images are shown in the inset. Scale bars, 2 μm for (i) to (v) and 10 μm for (vi).

brid perovskites and introduces a new family of 2D solution-processed semiconductors for nanoscale optoelectronic devices.

REFERENCES AND NOTES

1. M. M. Lee, J. Teuscher, T. Miyasaka, T. N. Murakami, H. J. Snaith, *Science* **338**, 643–647 (2012).
2. J. Burschka *et al.*, *Nature* **499**, 316–319 (2013).
3. L. Dou *et al.*, *Nat. Commun.* **5**, 5404 (2014).
4. H. Zhou *et al.*, *Science* **345**, 542–546 (2014).
5. D. B. Mitzi, *Prog. Inorg. Chem.* **48**, 10–15 (2007).
6. G. C. Papavassiliou, *Prog. Solid State Chem.* **25**, 192–243 (1997).
7. D. B. Mitzi, *J. Chem. Soc., Dalton Trans.* **1**, 1–12 (2001).
8. G. Lanty *et al.*, *J. Phys. Chem. Lett.* **5**, 3958–3963 (2014).
9. I. Borriello, G. Cantele, D. Ninno, *Phys. Rev. B* **77**, 235214 (2008).
10. A. Meresse, A. Daoud, *Acta Crystallogr. C* **45**, 194–196 (1989).
11. T. Ishihara, J. Takahashi, T. Goto, *Solid State Commun.* **69**, 933–936 (1989).
12. R. Willett, H. Place, M. Middleton, *J. Am. Chem. Soc.* **110**, 8639–8650 (1988).
13. J. Calabrese *et al.*, *J. Am. Chem. Soc.* **113**, 2328–2330 (1991).
14. D. B. Mitzi, S. Wang, C. A. Feild, C. A. Chess, A. M. Guloy, *Science* **267**, 1473–1476 (1995).
15. N. Kawano *et al.*, *J. Phys. Chem. C* **118**, 9101–9106 (2014).
16. Y. Takeoka, K. Asai, M. Rikukawa, K. Sanui, *Bull. Chem. Soc. Jpn.* **79**, 1607–1613 (2006).
17. K. Gauthron *et al.*, *Opt. Express* **18**, 5912–5919 (2010).
18. W. Niu, A. Eiden, G. V. Prakash, J. J. Baumberg, *Appl. Phys. Lett.* **104**, 171111 (2014).
19. S. T. Ha *et al.*, *Adv. Opt. Mater.* **2**, 838–844 (2014).
20. M. A. Green, A. Ho-Baillie, H. J. Snaith, *Nat. Photonics* **8**, 506–514 (2014).
21. Materials and methods are available as supplementary materials on *Science* Online.
22. N. Mercier, S. Poiroux, A. Riou, P. Batail, *Inorg. Chem.* **43**, 8361–8366 (2004).
23. G. Cunningham *et al.*, *ACS Nano* **6**, 3468–3480 (2012).
24. L. W. Hobbs, in *Introduction to analytical electron microscopy*, J. J. Hren, J. I. Goldstein, D. C. Joy, Eds. (Plenum, New York, 1979).
25. Y. Abid, *J. Phys. Condens. Matter* **6**, 6447–6454 (1994).
26. K. Tanaka *et al.*, *Jpn. J. Appl. Phys.* **44**, 5923–5932 (2005).
27. S. Sourisseau *et al.*, *Chem. Mater.* **19**, 600–607 (2007).
28. M. R. Filip, G. E. Eperon, H. J. Snaith, F. Giustino, *Nat. Commun.* **5**, 5757 (2014).
29. E. R. Dohner, A. Jaffe, L. R. Bradshaw, H. I. Karunadasa, *J. Am. Chem. Soc.* **136**, 13154–13157 (2014).
30. D. J. Gargas, H. Gao, H. Wang, P. Yang, *Nano Lett.* **11**, 3792–3796 (2011).
31. X. Wu *et al.*, *J. Am. Chem. Soc.* **137**, 2089–2096 (2015).
32. K. S. Novoselov *et al.*, *Science* **306**, 666–669 (2004).
33. K. F. Mak, C. Lee, J. Hone, J. Shan, T. F. Heinz, *Phys. Rev. Lett.* **105**, 136805 (2010).

hybrid perovskites is flexible and deformable; and unlike the bulk crystal, the thin 2D sheets exhibit new features such as structural relaxation and PL shift. This study opens up opportunities for fundamental research on the synthesis and characterization of atomically thin 2D hy-

ASTROPHYSICS

Gravitational waves from binary supermassive black holes missing in pulsar observations

R. M. Shannon,[1,2]* V. Ravi,[3]* L. T. Lentati,[4] P. D. Lasky,[5] G. Hobbs,[1] M. Kerr,[1] R. N. Manchester,[1] W. A. Coles,[6] Y. Levin,[5] M. Bailes,[3] N. D. R. Bhat,[2] S. Burke-Spolaor,[7] S. Dai,[1,8] M. J. Keith,[9] S. Osłowski,[10,11] D. J. Reardon,[5] W. van Straten,[3] L. Toomey,[1] J.-B. Wang,[12] L. Wen,[13] J. S. B. Wyithe,[14] X.-J. Zhu[13]

Gravitational waves are expected to be radiated by supermassive black hole binaries formed during galaxy mergers. A stochastic superposition of gravitational waves from all such binary systems would modulate the arrival times of pulses from radio pulsars. Using observations of millisecond pulsars obtained with the Parkes radio telescope, we constrained the characteristic amplitude of this background, $A_{c,yr}$, to be $<1.0 \times 10^{-15}$ with 95% confidence. This limit excludes predicted ranges for $A_{c,yr}$ from current models with 91 to 99.7% probability. We conclude that binary evolution is either stalled or dramatically accelerated by galactic-center environments and that higher-cadence and shorter-wavelength observations would be more sensitive to gravitational waves.

Studies of the dynamics of stars and gas in nearby galaxies provide strong evidence for the ubiquity of supermassive ($>10^6$ solar masses) black holes (SMBHs) (1). Observations of luminous quasars indicate that SMBHs are hosted by galaxies throughout the history of the universe (2) and affect global properties of the host galaxies (3). The prevailing dark energy–cold dark matter cosmological paradigm predicts that large galaxies are assembled through the hierarchical merging of smaller galaxies. The remnants of mergers can host gravitationally bound binary SMBHs, with orbits decaying through the emission of gravitational waves (GWs) (4).

GWs from binary SMBHs, with periods between ~0.1 and 30 years (5), can be detected or constrained by monitoring, for years to decades, a set of rapidly rotating millisecond pulsars (MSPs) distributed throughout our galaxy. Radio emission beams from MSPs are observed as pulses that can be time-tagged with precision as fine as 20 ns (6). When traveling across the pulsar-Earth line of sight, GWs induce variations in the arrival times of the pulses (7).

The superposition of GWs from the binary SMBH population is a stochastic background (GWB), which is typically characterized by the strain-amplitude spectrum $h_c(f) = A_{c,yr}[f/(1 \text{ year}^{-1})]^{-2/3}$, where f is the GW frequency; $A_{c,yr}$ is the characteristic amplitude of the GWB measured at $f = 1 \text{ year}^{-1}$, predicted to be $>10^{-15}$ (5, 8–12); and $-2/3$ is the predicted spectral index (5, 8–12). The GWB is expected to add low-frequency perturbations to pulse arrival times. Although the detection of the GWB would confirm the presence of a cosmological population of binary SMBHs, limits on its amplitude constrain models of galaxy and SMBH evolution (8).

As part of the Parkes Pulsar Timing Array (PPTA) project to detect GWs (6), we have been monitoring 24 pulsars with the 64-m Parkes radio telescope. Using observations taken at a central wavelength of 10 cm and previously reported methods (6, 8), we have produced a new data set that spans 11 years, which is 3 years longer than previous data sets analyzed at this wavelength. In addition to having greater sensitivity to the GWB than previous data sets because of its longer duration, this new data set was improved by identifying and correcting for some instrumental offsets [supplementary text S1 (13)].

[1]Commonwealth Science and Industrial Research Organization (CSIRO) Astronomy and Space Science, Australia Telescope National Facility, Post Office Box 76, Epping, New South Wales 1710, Australia. [2]International Centre for Radio Astronomy Research, Curtin University, Bentley, Western Australia 6102, Australia. [3]Centre for Astrophysics and Supercomputing, Swinburne University of Technology, Post Office Box 218, Hawthorn, Victoria 3122, Australia. [4]Astrophysics Group, Cavendish Laboratory, JJ Thomson Avenue, Cambridge CB3 0HE, UK. [5]Monash Centre for Astrophysics, School of Physics and Astronomy, Monash University, Post Office Box 27, Victoria 3800, Australia. [6]Department of Electrical and Computer Engineering, University of California–San Diego, La Jolla, CA 92093, USA. [7]National Radio Astronomical Observatory, Array Operations Center, Post Office Box O, Socorro, NM 87801-0387, USA. [8]Department of Astronomy, School of Physics, Peking University, Beijing 100871, China. [9]Jodrell Bank Centre for Astrophysics, University of Manchester, Manchester M13 9PL, UK. [10]Department of Physics, Universitat Bielefeld, Universitatsstrasse 25, D-33615 Bielefeld, Germany. [11]Max-Planck-Institut für Radioastronomie, Auf dem Hügel 69, 53121 Bonn, Germany. [12]Xinjiang Astronomical Observatory, Chinese Academy of Sciences, 150 Science 1-Street, Urumqi, Xinjiang 830011, China. [13]School of Physics, University of Western Australia, Crawley, Western Australia 6009, Australia. [14]School of Physics, University of Melbourne, Parkville, Victoria 3010, Australia.
*Corresponding author. E-mail: ryan.shannon@csiro.au (R.S.); v.vikram.ravi@gmail.com (V.R.)
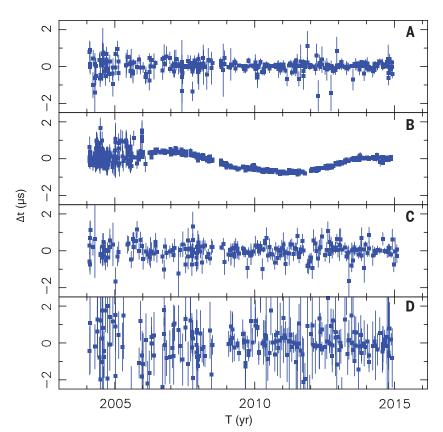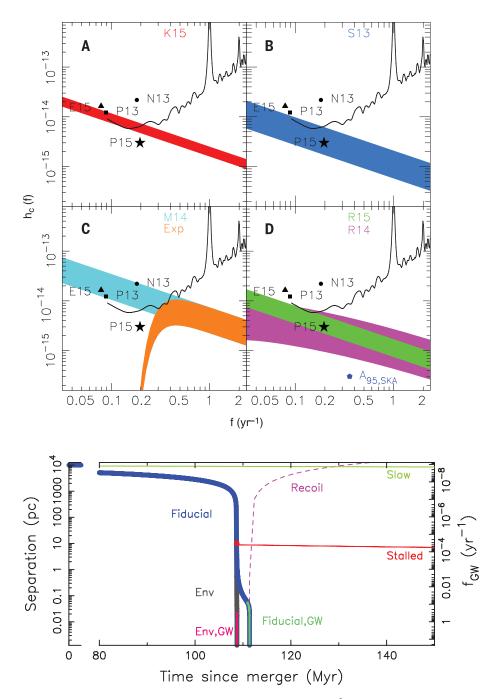
Fig. 1. Residual pulse times of arrival, Δt, for the four pulsars used in our analysis. These include (**A**) PSR J1909-3744, (**B**) PSR J0437-4715, (**C**) PSR J1713+0747, and (**D**) PSR J1744-1134.

We searched for the GWB in observations of the four pulsars (Fig. 1) that have the highest timing precision and therefore would be most sensitive to it. Observations of these pulsars at other wavelengths contain excess noise that is inconsistent with the 10-cm observations, and they were therefore excluded from this analysis (supplementary text S2.1). This exclusion does not bias our analysis, because GWs produce achromatic variations in arrival times. Observations of other pulsars are not presented here because they have insufficient timing pre-

cision, relative to the best pulsars, to influence the search (supplementary text S2). We also have not corrected for chromatic arrival-time variations associated with propagation through a varying column of interstellar plasma, because these effects are small in the 10-cm band (14). Additionally, using uncorrected observations can only have reduced our sensitivity to the GWB, making our analysis conservative.

We used a Bayesian methodology (15) to marginalize over the pulsar rotational ephemerides and to search for stochastic contributions to the

arrival times. The stochastic terms include excess white noise associated with intrinsic pulse-shape changes and instrumental distortions uncorrelated between observations. They also include excess low-frequency timing noise that is uncorrelated between pulsars, which could be intrinsic to the pulsars or caused by interstellar propagation effects. In addition, the model includes the GWB, which produces timing perturbations that are correlated between the pulsars (7). The methodology also enables us to quantitatively compare models by providing evidence, in the form of a probability,

Fig. 2. Predictions and limits on the GWB strain spectrum. The black stars (labeled P15) show the 95% confidence limit that we obtained, assuming $h_c(f) = A_{c,yr}[f/(1\ year^{-1})]^{-2/3}$. The other symbols show previously published limits from the European Pulsar Timing Array (triangles labeled E15) (20), the North American Nanohertz Observatory for Gravitational Waves collaboration (circles labeled N13) (29), and our previous limit (squares labeled P13) (8). Each panel shows a different prediction for the GWB, based on four models for SMBH evolution that predict a power-law form for $h_c(f)$: (**A**) K15 (12), (**B**) S13 (9), (**C**) M14 (10), and (**D**) R15 (11). Predictions are shown as shaded regions (correspondingly colored) that represent the 1σ uncertainty. Also shown in (C) and (D) are models Exp (supplementary text S2.2) and R14 (22), respectively, which include the effects of environmentally driven binary evolution and therefore predict more complex strain spectra. The black curve in each panel shows the nominal single-frequency sensitivities of our observations (supplementary text S2.2), and it is above our limit because of the statistical penalties applied when searching individual frequencies. In (D), the blue pentagon (labeled $A_{95,SKA}$) shows the projected upper limit on $A_{c,yr}$ obtained by a single-pulsar timing campaign conducted with a next-generation radio telescope (the SKA) (supplementary text S2.2); it excludes all considered models with > 98% probability.

Fig. 3. Illustrative evolutionary paths for a pair of 10^9–solar-mass SMBHs in a galaxy merger. The figure shows the pair separation and the GW emission frequency f_{GW}, assuming the binary is in a circular orbit. The blue curve shows the evolution of the separation of the SMBHs using fiducial assumptions, which results in a GWB that is inconsistent with our data. The cyan curve (labeled Fiducial, GW) is the portion of the evolution that occurs when GW emission dominates orbital decay. We also show scenarios that could explain our GWB limit. First, the galaxy merger rate could be lower, as represented by the slow merger curve (green). Alternatively, after the SMBHs form a binary (red circle), the orbital evolution may stall before emitting GWs (red curve). The gray curve (labeled Env) shows a scenario in which a dense binary SMBH environment drives orbital decay through the GW frequency band at which our observations

are sensitive. In this case, GW emission dominates only for $f_{GW} > 0.5\ year^{-1}$ (pink curve labeled Env,GW). Last, it is possible that the post-coalescence SMBH could undergo gravitational recoil and escape its host galaxy (purple dashed curve), negating the possibility of it forming a binary SMBH again. Myr, millions of years.

that can be used to select a preferred model (supplementary text S2).

We found no evidence for the GWB in our data set. We therefore placed an upper limit on the amplitude of the GWB by analyzing its posterior distribution. The pulsar that individually provides the best limit on the GWB, PSR J1909–3744 (Fig. 1), shows no evidence for excess low-frequency timing noise. The pulsar that provides the third-most constraining limit, PSR J0437-4715 (Fig. 1), shows evidence for a low-frequency signal that is inconsistent both with the predicted GWB spectral shape (99.0% probability) and, in amplitude, with the limit derived from PSR J1909–3744 (99.4% probability).

For the power-law GWB strain-amplitude spectrum, we found $A_{c,yr}$ to be $<1.0 \times 10^{-15}$ with 95% probability (Fig. 2). This corresponds to an upper limit on the fractional closure density of the universe (Ω_{GW}) of 2.3×10^{-10} at a frequency of 0.2 year^{-1} (supplementary text S2.2). This is a factor of 6 lower than any previous limit (Fig. 2). Other pulsar timing array experiments with comparable data spans, but with longer-wavelength observations, do not achieve the same sensitivity to GWs (16) because of the higher timing precision in our observations and the presence of low-frequency noise in theirs. Our data are inconsistent with current models for the GWB (9–12) with between 91 and 99.7% probability (13).

Our results therefore suggest that at least one of the physical assumptions underlying these GWB models are incorrect. Models for the binary SMBH population rely on measurements of the galaxy merger rate. They also assume that all galaxy mergers form binary SMBHs that coalesce well before a subsequent galaxy merger, and that binary orbital decay is driven only by losses of energy to GWs when radiating in the pulsar-timing frequency band (Fig. 3, black curve).

Figure 3 shows schematically the evolution of a binary SMBH, in which each component has a mass of 10^9 solar masses, evolving under standard assumptions (Fig. 3, blue curve) and in other ways that produce a weaker GWB.

Longer galaxy-merger time scales would result in a lower inferred merger rate (Fig. 3, green curve), fewer binary SMBHs, and hence a lower GWB amplitude. Although predictions for merger time scales vary by a factor of 3 (17), models that include this uncertainty (9, 11) are in tension with our limit. Shorter predicted time scales result from the inclusion of more sophisticated physical mechanisms and are therefore favored (17). Therefore, galaxy mergers are expected to rapidly form gravitationally bound binaries.

Models for the GWB also assume that all large galaxies host SMBHs. A low SMBH-occupation fraction beyond the local universe (redshifts $z > 0.3$) could result from exceedingly rare, high-redshift SMBH-seed formation (18). For this to be the case, seed SMBHs would have to occupy ~1% of the most massive galaxies at $z \sim 6$ (19). The models also assume that, post-coalescence, SMBHs remain gravitationally bound to their host galaxies. However, it is unlikely that the acceleration of post-coalescence SMBHs beyond galactic escape velocities through gravitational-radiation recoil (Fig. 3, purple dashed curve) results in a substantial number of galaxies without central SMBHs (20).

The GWB amplitude would also be reduced if SMBH binaries do not efficiently reach the GW-emitting stage (Fig. 3, red curve). Dynamical friction is expected to bring the SMBHs in a merging galaxy pair close enough to form a bound binary (4), with an orbital major axis $a_{form} \sim 60\, M_9^{0.54}$ pc, where M_9 is the mass of the larger SMBH in units of 10^9 solar masses (supplementary text S4). The time to coalescence through GW emission is $t_{GW} = 18\, M_9^{-3}[a_{form}/(1\text{ pc})]^4$ billion years in the lower-limiting case of an equal-mass binary, which is longer than the age of the universe. Hence, another mechanism in addition to GW emission is required to drive binaries to coalescence.

Observations and theoretical models, however, indicate that binary SMBHs can coalesce within the age of the universe through the coupling of binary SMBHs to their environments (21). Proposed coupling mechanisms include the three-body scattering of stars on radial orbits and viscous friction against circumbinary gas. The actions of environments (Fig. 3, gray curve) would cause binaries to spend less time emitting GWs, reducing the GWB amplitude at low frequencies. Our nondetection of the GWB may therefore result from the efficient coupling of binary SMBHs to their environments (10, 22, 23).

Modeling of the stellar environments of the cosmological population of binary SMBHs (22) indicates that the GWB characteristic-strain spectrum may be attenuated at frequencies up to 0.3 year^{-1} (Fig. 2); similar results are obtained when the possible gas-rich environments of binary SMBHs are considered (23). Our GWB constraint, placed at 0.2 year^{-1}, is consistent with some models that predict the extreme efficiency of environments in shrinking SMBH binary orbits (model R14, Fig. 2). However, other environmentally driven models that include higher galaxy merger rates (10) are inconsistent with our limit (model Exp, Fig. 2)

Distinguishing between explanations for our limit requires further observations and better models of SMBH evolution. The characterization of a substantial population of binary or recoiling SMBHs (24) would better delineate the coalescence rate. The coalescence events themselves may produce strong millihertz-frequency GWs that could be detected by space-based laser interferometers (5). The detection of the GWB at frequencies ≳0.2 year^{-1} with the currently predicted amplitude would provide strong evidence for the high efficiency of binary environments in shrinking orbits (25). This hypothesis also predicts an enhanced prospect for detecting low-frequency GWs from the most massive individual binary SMBHs, which are less affected by their environments (22, 23). The alternate explanation for our limit is that the rate of coalescence between SMBHs is lower than current estimates suggest; in this case, the GWB may still have a power-law spectrum.

This limit implies that a change in observational strategy could increase the sensitivity of pulsar timing arrays to GWs. One approach is to obtain more observations of pulsars with comparable sensitivity to those of our four best pulsars. If the observed excess noise at longer radio wavelengths is astrophysical, observations will need to be conducted at shorter wavelengths (≲10 cm). In this case, GWB detection may require observations with a sensitive radio telescope such as the Square Kilometre Array [SKA (26)], because MSP emission is weaker at these wavelengths. If binary SMBH environments are driving orbital evolution, a high-cadence campaign is required to detect the GWB at frequencies ≳0.2 year^{-1}. Alternatively, the GWB could have a power-law spectrum but be weak in amplitude. Our limit implies that there is a 50% probability that $A_{c,yr} < 2.4 \times 10^{-16}$. If this is the case, the first evidence for the GWB will be low-frequency perturbations to timing observations of the most stable pulsar, PSR J1909–3744, when longer data spans are achieved. In all cases, the predicted time to detection of the GWB with pulsar timing arrays (27) has been underestimated.

It is also possible that there is a more exotic reason for our nondetection. We have not yet tested GWBs expected from alternate theories of gravity. Our limit is consistent with GWs being absorbed on cosmological scales (28). Until GWs are detected, our limits will continue to improve with data span, as more pulsars are added into the sample and improved data analysis methods are developed (Fig. 2, blue pentagon). These limits will provide even stronger constraints on models of SMBH formation and evolution.

REFERENCES AND NOTES

1. J. Kormendy, L. Ho, *Annu. Rev. Astron. Astrophys.* **51**, 511–653 (2013).
2. F. Shankar, D. H. Weinberg, J. Miralda-Escudé, *Mon. Not. R. Astron. Soc.* **428**, 421–446 (2013).
3. A. Fabian, *Annu. Rev. Astron. Astrophys.* **50**, 455–489 (2012).
4. M. Begelman, R. Blandford, M. Rees, *Nature* **287**, 307–309 (1980).
5. J. S. B. Wyithe, A. Loeb, *Astrophys. J.* **590**, 691–706 (2003).
6. R. N. Manchester et al., *Publ. Astron. Soc. Aust.* **30**, e017 (2013).
7. R. W. Hellings, G. S. Downs, *Astrophys. J.* **265**, L39 (1983).
8. R. M. Shannon et al., *Science* **342**, 334–337 (2013).
9. A. Sesana, *Class. Quantum Gravity* **30**, 224014 (2013).
10. S. T. McWilliams, J. P. Ostriker, F. Pretorius, *Astrophys. J.* **789**, 156 (2014).
11. V. Ravi, J. S. B. Wyithe, R. M. Shannon, G. Hobbs, *Mon. Not. R. Astron. Soc.* **447**, 2772–2783 (2015).
12. A. Kulier, J. P. Ostriker, P. Natarajan, C. N. Lackner, R. Cen, *Astrophys. J.* **799**, 178 (2015).
13. Supplementary materials are available on *Science* Online.
14. M. J. Keith et al., *Mon. Not. R. Astron. Soc.* **429**, 2161–2174 (2013).
15. L. Lentati et al., *Phys. Rev. D Part. Fields Gravit. Cosmol.* **87**, 104021 (2013).
16. L. Lentati et al., *Mon. Not. R. Astron. Soc.* **453**, 2576–2598 (2015).
17. C. Conselice, *Annu. Rev. Astron. Astrophys.* **52**, 291–337 (2014).
18. K. Menou, Z. Haiman, V. K. Narayanan, *Astrophys. J.* **558**, 535–542 (2001).
19. T. L. Tanaka, *Class. Quantum Gravity* **31**, 244005 (2014).
20. A. Gerosa, A. Sesana, *Mon. Not. R. Astron. Soc.* **446**, 38–55 (2015).
21. M. Colpi, *Space Sci. Rev.* **183**, 189–221 (2014).
22. V. Ravi, J. S. B. Wyithe, R. M. Shannon, G. Hobbs, R. N. Manchester, *Mon. Not. R. Astron. Soc.* **442**, 56–68 (2014).
23. B. Kocsis, A. Sesana, *Mon. Not. R. Astron. Soc.* **411**, 1467–1479 (2011).
24. M. Eracleous, T. A. Boroson, J. P. Halpern, J. Liu, *Astrophys. J.* **201**, 23 (2012).
25. L. Sampson, N. J. Cornish, S. T. McWilliams, *Phys. Rev. D Part. Fields Gravit. Cosmol.* **91**, 084055 (2015).
26. G. H. Janssen et al., in *Advancing Astrophysics with the Square Kilometer Array*, T. L. Bourke et al., Eds. (Proceedings of

Science, Trieste, Italy, 2015); http://pos.sissa.it/archive/conferences/215/037/AASKA14_037.pdf.
27. X. Siemens, J. Ellis, F. Jenet, J. D. Romano, *Class. Quantum Gravity* **30**, 224015 (2013).
28. S. W. Hawking, *Astrophys. J.* **145**, 544 (1966).
29. P. B. Demorest *et al.*, *Astrophys. J.* **762**, 94 (2013).

BIOCATALYSIS

Conversion of alcohols to enantiopure amines through dual-enzyme hydrogen-borrowing cascades

Francesco G. Mutti,[1,2]*† Tanja Knaus,[2]† Nigel S. Scrutton,[2]
Michael Breuer,[3] Nicholas J. Turner[1]*

α-Chiral amines are key intermediates for the synthesis of a plethora of chemical compounds at industrial scale. We present a biocatalytic hydrogen-borrowing amination of primary and secondary alcohols that allows for the efficient and environmentally benign production of enantiopure amines. The method relies on a combination of two enzymes: an alcohol dehydrogenase (from *Aromatoleum* sp., *Lactobacillus* sp., or *Bacillus* sp.) operating in tandem with an amine dehydrogenase (engineered from *Bacillus* sp.) to aminate a structurally diverse range of aromatic and aliphatic alcohols, yielding up to 96% conversion and 99% enantiomeric excess. Primary alcohols were aminated with high conversion (up to 99%). This redox self-sufficient cascade possesses high atom efficiency, sourcing nitrogen from ammonium and generating water as the sole by-product.

Amines are among the most frequently used chemical intermediates for the production of active pharmaceutical ingredients, fine chemicals, agrochemicals, polymers, dyestuffs, pigments, emulsifiers, and plasticizing agents (*1*). However, the requisite amines are scarce in nature, and their industrial production mainly relies on the metal-catalyzed hydrogenation of enamides (i.e., obtained from related ketone precursors). This process requires transition metal complexes, which are expensive and increasingly unsustainable (*2*). Moreover, the asymmetric synthesis of amines from ketone precursors requires protection and deprotection steps that generate copious amounts of waste. As a consequence, various chemical processes for the direct conversion of alcohols into amines have been developed during the past decade. The intrinsic advantage of the direct amination of an alcohol is that the reagent and the product are in the same oxidation state; therefore, theoretically, additional redox equivalents are not required. However, many of these methods have low efficiency and high environmental impact (e.g., Mitsunobu reaction) (*3*). The amination of simple alcohols such as methanol and ethanol via heterogeneous catalysis requires harsh conditions (>200°C), and more structurally diverse alcohols are either converted with extremely low chemoselectivity or not converted at all (*4*). Furthermore, most of the work in this field involves nonchiral substrates, whereas 40% of the commercial optically active drugs are chiral amines (*2*). Increasingly, biocatalytic methods are applied for the production of optically active amines [e.g., the lipase-catalyzed resolution of racemic mixtures of amines or the ω-transaminase process; a recent example uses an engineered enzyme applied to the industrial manufacture of the diabetes medication Januvia (sitagliptin)] (*5–7*).

Multistep chemical reactions in one pot avoid the need for isolation of intermediates and purification steps. This approach offers economic as well as environmental benefits, because it eliminates the need for time-consuming intermediate work-ups and minimizes the use of organic solvents for extraction and purification as well as energy for evaporation and mass transfer (*8*). As a consequence, cascade reactions generally possess elevated atom efficiency and potentially lower environmental impact factors (*9*). The major challenge is to perform cascade reactions wherein an oxidative and a reductive step are running simultaneously. Even more challenging is to carry out a simultaneous interconnected redox-neutral cascade wherein the electrons liberated in the first oxidative step are quantitatively consumed in the subsequent reductive step [(*8*); for a recent detailed study, see (*10*)]. This concept is the basis for the hydrogen-borrowing conversion of alcohols (primary or secondary) into amines. The reducing equivalents (i.e., hydride) liberated in the first step—the oxidation of the alcohol to the ketone—are directly consumed in the second interconnected step—reductive amination of the ketone.

A number of chemocatalytic hydrogen-borrowing methods have recently been developed using ruthenium as well as iridium catalysts (*11*, *12*). However, the required reaction conditions (e.g., high catalyst and cocatalyst loading, low substrate concentration, moderate chemoselectivity, moderate or total lack of stereoselectivity, the requirement of an excess of substrate, and stringent temperature and elevated pressure requirements) complicate the application of these methods on a large scale (*13*). Another recently developed hydrogen-borrowing chemical method involves the stoichiometric use of Ellman's enantiopure sulfinamide auxiliary as the nitrogen donor in combination with a Ru-Macho catalyst (*14*). Besides the requirement of the expensive chiral auxiliary, the maximum diastereomeric excess was 90%. A reported biocatalytic hydrogen-borrowing amination of alcohols combining three enzymes—a ω-transaminase (ωTA), an alcohol dehydrogenase (ADH), and the alanine dehydrogenase from *Bacillus subtilis* (AlaDH)—also lacks efficiency because of the requirement for at least 5 equivalents of L- or D-alanine as the sacrificial amine donor and also as a result of the lower conversion and chemoselectivity for the amination of secondary alcohols (*15*, *16*). Another redox-neutral biocatalytic cascade was applied for the deracemization of mandelic acid to enantioenriched L-phenylglycine. However, the method was limited to the conversion of this specific α-hydroxy acid (*17*).

Here, we present a highly enantioselective catalytic hydrogen-borrowing amination of primary

[1]School of Chemistry, University of Manchester, Manchester Institute of Biotechnology, Manchester M1 7DN, UK. [2]Manchester Institute of Biotechnology, Faculty of Life Sciences, University of Manchester, Manchester M1 7DN, UK. [3]BASF SE, White Biotechnology Research, GBW/B-A030, 67056 Ludwigshafen, Germany.
*Corresponding author. E-mail: nicholas.turner@manchester.ac.uk (N.J.T.); f.mutti@uva.nl (F.G.M.) †Present address: Van 't Hoff Institute for Molecular Sciences, University of Amsterdam, Science Park 904, 1098 XH Amsterdam, Netherlands.

as well as secondary alcohols that requires only two biocatalysts, namely an ADH and an amine dehydrogenase (AmDH) (Fig. 1). The redox self-sufficient cycle uses ammonium ion/ammonia as the source of the nitrogen and generates only water as the by-product. The cascade requires only catalytic quantities of a nicotinamide coenzyme that shuttles hydride from the oxidative step to the reductive step. The method has been successfully applied to amination of optically active secondary alcohols with inversion of configuration, amination of the corresponding enantiomeric secondary alcohols with retention of configuration, asymmetric amination of racemic secondary alcohols, and amination of primary alcohols.

Initially, we examined the catalytic activity of the amine dehydrogenase variant that was recently obtained by protein engineering of the wild-type phenylalanine dehydrogenase from *B. badius* (Ph-AmDH) (18, 19). The substrate scope of the Ph-AmDH variant K78S-N277L for the conversion of a broad range of ketone substrates has not been reported; only the reductive amination of *para*-fluorophenylacetone (**2b**) was previously described, using glucose and glucose dehydrogenase (GDH) for cofactor regeneration, and very recently three other ketones were also tested (20). Hence, the Ph-AmDH variant K78S-N277L was expressed and purified as histidine (His)–tagged protein. The activity of the enzyme was initially studied using **2b** as the test substrate in ammonium buffer systems with a range of different counterions (chloride, sulfate, acetate, phosphate, borate, citrate, oxalate, and formate). The pH was also varied from 4 up to 11.5, depending on the ammonium buffer used (fig. S5). The highest catalytic activity was observed at pH 8.2 to 8.8, whereas the optimal buffer was ammonium chloride. In contrast, previous studies with this enzyme were carried out at pH 9.6 (18). Reductive amination of **2b** (20 mM) was carried out at varying concentrations of NH4Cl/NH3 buffer at pH 8.7 using GDH and glucose for cofactor regeneration. Quantitative conversion (>99%) was achieved after 12 hours using ~0.7 M ammonium buffer (table S1 and fig. S6).

ADHs have been extensively used in biocatalysis for the interconversion of ketones and alcohols, and hence a wealth of data is available for these enzymes (21). Because of the dependence of Ph-AmDH on nicotinamide adenine dinucleotide (oxidized form; NAD) as cofactor, we searched for suitable stereocomplementary NAD-dependent secondary ADHs that might exhibit high stability and activity toward a wide range of secondary alcohols at pH >8.5 as well as tolerance of high concentrations of ammonium ions. The NAD-dependent Prelog ADH from *Aromatoleum aromaticum* (AA-ADH, previously named as denitrifying bacterium strain EbN1; PDB 2EW8 and 2EWM) (22) and an engineered anti-Prelog ADH from *Lactobacillus brevis* (LBv-ADH; PDB 1ZK4 for the wild-type enzyme) were selected for this study (23–25). Analysis of the crystal structures of the ADHs with bound NAD(P)H (reduced NAD phosphate) as well as previous docking studies (i.e., substrate bound to the enzyme) revealed that the active sites of AA-ADH and LBv-ADH possess a

very similar amino acid arrangement, but in an inverted conformation. In particular, a tyrosine residue (Tyr[93] for AA-ADH, Tyr[189] for LBv-ADH) is crucial for the stereoselectivity, as it protrudes into the active site and forces the substrates to bind with the larger group in the opposite direction. This Tyr residue is in a mirror-image position in the active site of the two ADHs (22, 25).

The amination of alcohol substrate (R)-**1a** (20 mM) was carried out initially by combining a crude cell extract of LBv-ADH with purified His-tagged Ph-AmDH in the presence of catalytic NAD+ [1 mM; 5 mole percent (mol %)] and in the pres-

ence of buffer systems ranging from pH 7 to 8.7. Although formation of the amine product (R)-**3a** was observed, the maximum conversion was 6%. In particular, accumulation of the ketone intermediate **2a** was observed (from 61% to 97%; table S2). However, under these conditions, the concentration of ketone **2a** cannot exceed the concentration of the cofactor NAD+ (1 mM), and hence the accumulation of high levels of **2a** was attributed to the presence of at least one NAD oxidase from the host organism (*Escherichia coli*) used for the expression of the ADH, as previously observed by other groups (26). The NADH oxidase competed
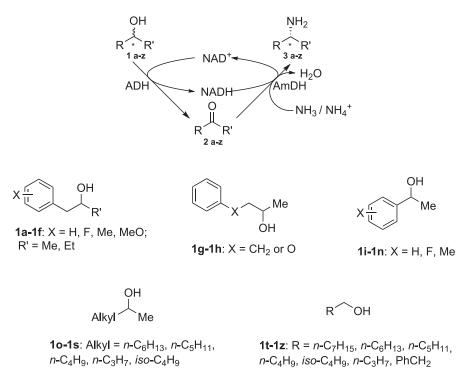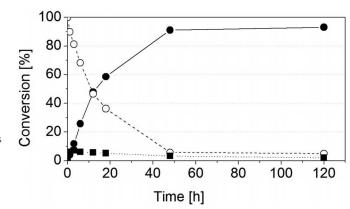

Fig. 1. Two-enzyme cascade for the hydrogen-borrowing amination of alcohols. In the first oxidative step, the Prelog AA-ADH and the anti-Prelog LBv-ADH were applied for the oxidation of the (S)- and (R)-configured alcohol substrates, respectively. The AmDHs used in this study afforded the (R)-configured amines in the second reductive step. Structures of the alcohol substrates explored in this study are shown below the schematic catalytic cycle. Me, methyl; Et, ethyl. See (27) for detailed structural representations of the alcohol substrates.

Fig. 2. Kinetics of asymmetric hydrogen-borrowing biocatalytic amination. The reaction of (S)-**1a** (20 mM) gives inverted (R)-**3a** using AA-ADH and Ph-AmDH with catalytic NAD+ (1 mM; 5 mol %). Concentrations of the amine product (solid line, black circles), ketone intermediate (dotted line, black squares), and alcohol substrate (dashed line, white circles) were monitored over time. As expected, the concentration of the ketone intermediate **2a** remained constant and below the concentration of the nicotinamide coenzyme. See (27) for details.

with the AmDH in the amination step for the oxidation of the NADH, leading to accumulation of **2a** (*27*) (fig. S3). Therefore, the LBv-ADH was purified by ion exchange chromatography and size exclusion chromatography and was then recombined with the purified His-tagged Ph-AmDH for the alcohol amination reaction (**1a** concentration 20 mM, NAD$^+$ 5 mol %). Under these conditions, the concentration of the ketone **2a** at the end of the reaction was between 1.6 and 2.9 (less than the maximum theoretical value of 5%). Unfortunately, the final concentration of the amine product **3a** was also very low (<1%) (table S3). Replacing LBv-ADH with AA-ADH for the amination of (*S*)-**1a** led to the same results.

During the course of these preliminary experiments, we noticed that solutions containing the ADH (LBv-ADH or AA-ADH) together with the His-tagged Ph-AmDH tended to become cloudy after a few minutes of the reaction, generating an enzyme precipitate. However, no precipitation occurred even after more than 24 hours when

the ADHs and the His-tagged Ph-AmDH were separately incubated in the same buffer under the same conditions. AA-ADH and LBv-ADH belong to the family of the short-chain dehydrogenases/reductases (SDRs). Both ADHs are homotetramers and possess the characteristic Ser-Tyr-Lys catalytic triad of the SDRs. Additionally, the LBv-ADH has two Mg^{2+} sites that are placed at the interphase between the monomeric units and are crucial for its stability (*25*). Although the crystal structure of AA-ADH was reported without an evident metal ion, a high homolog was crystallized in a stable form with six additional divalent cations (*28*). Furthermore, we noticed that the stability of LBv-ADH was significantly improved during purification when Mg^{2+} was added into the buffer, indicating a reversible dissociation process of the cation from the enzyme (*27*). Therefore, we speculated that enzyme precipitation in the dual-enzyme cascade might have been caused by coordination of free divalent cations, coming from the ADHs, to the His-terminal

tag of the Ph-AmDH. As a consequence, enzyme aggregation and precipitation occurred. We then used a highly selective recombinant thrombin to cleave the His tag from the Ph-AmDH (*27*) (fig. S7). Incubation of the two purified ADHs with the Ph-AmDH devoid of a His tag resulted in visually more stable systems wherein enzyme aggregation and precipitation were not observed even after 24 hours.

The hydrogen-borrowing cascade was then repeated by combining AA-ADH with the Ph-AmDH (devoid of His tag) in ammonium chloride buffer at pH 8.7. AA-ADH is selective for (*S*)-**1a**, whereas Ph-AmDH shows (*R*)-selectivity in the reduction of the intermediate **2a**; hence, the overall cascade was expected to proceed with inversion of configuration. The reaction was tested at various concentrations of ammonium ions to ascertain the impact on the conversion. Under reaction conditions of (*S*)-**1a** = 20 mM, NAD$^+$ = 1 mM, and NH$_4^+$/NH$_3$ = 2 M, the conversion of alcohol to amine reached 85% after 24 hours, with an enantiomeric excess (ee) of >99% (*R*) (table S4).

Table 1. Asymmetric hydrogen-borrowing amination of enantiopure aromatic secondary alcohols 1a to 1n. Reactions were carried out at 30°C for 48 hours. See (*27*) for experimental details.

	Amination of aromatic chiral secondary alcohols 1a to 1n with inversion of configuration				Amination of aromatic chiral secondary alcohols 1a to 1n with retention of configuration				Asymmetric amination of aromatic racemic secondary alcohols 1a to 1n		
Entry	Substrate	Conversion (%)	ee (%)	Entry	Substrate	Conversion (%)	ee (%)	Entry	Substrate	Conversion (%)	ee (%)
1	(*S*)-**1a**	95	>99(*R*)	15	(*R*)-**1a**	93	>99(*R*)	29	Rac-**1a**	81	>99(*R*)
2	(*S*)-**1b**	93	>99(*R*)	16	(*R*)-**1b**	36	>99(*R*)	30	Rac-**1b**	66	>99(*R*)
3	(*S*)-**1c**	55	97(*R*)	17	(*R*)-**1c**	27	97(*R*)	31	Rac-**1c**	47	97(*R*)
4	(*S*)-**1d**	65	>99(*R*)	18	(*R*)-**1d**	24	>99(*R*)	32	Rac-**1d**	78	>99(*R*)
5	(*S*)-**1e**	31	82(*R*)	19	(*R*)-**1e**	14	82(*R*)	33	Rac-**1e**	30	82(*R*)
6	(*S*)-**1f**	80	>99(*R*)	20	(*R*)-**1f**	85	>99(*R*)	34	Rac-**1f**	87	>99(*R*)
7	(*S*)-**1g**	92	82(*R*)	21	(*R*)-**1g**	92	83(*R*)	35	Rac-**1g**	92	83(*R*)
8	(*S*)-**1h**	96	>99(*R*)	22	(*R*)-**1h**	94	>99(*R*)	36	Rac-**1h**	84	>99(*R*)
9	(*S*)-**1i**	17	>99(*R*)	23	(*R*)-**1i**	30	>99(*R*)	37	Rac-**1i**	16	>99(*R*)
10	(*S*)-**1j**	14	>99(*R*)	24	(*R*)-**1j**	17	>99(*R*)	38	Rac-**1j**	16	>99(*R*)
11	(*S*)-**1k**	26	>99(*R*)	25	(*R*)-**1k**	33	>99(*R*)	39	Rac-**1k**	20	>99(*R*)
12	(*S*)-**1l**	12	>99(*R*)	26	(*R*)-**1l**	18	>99(*R*)	40	Rac-**1l**	12	>99(*R*)
13	(*S*)-**1m**	14	>99(*R*)	27	(*R*)-**1m**	27	>99(*R*)	41	Rac-**1m**	19	>99(*R*)
14	(*S*)-**1n**	7	>99(*R*)	28	(*R*)-**1n**	14	>99(*R*)	42	Rac-**1n**	9	>99(*R*)

Table 2. Asymmetric hydrogen-borrowing amination of aliphatic secondary alcohols 1o to 1s. Reactions were carried out at 30°C for 48 hours. See (*27*) for experimental details.

	Amination of aliphatic chiral secondary alcohols with inversion of configuration				Amination of aliphatic chiral secondary alcohols with retention of configuration				Asymmetric amination of aliphatic racemic secondary alcohols		
Entry	Substrate	Conversion (%)	ee (%)	Entry	Substrate	Conversion (%)	ee (%)	Entry	Substrate	Conversion (%)	ee (%)
1	(*S*)-**1o**	94	99(*R*)	6	(*R*)-**1o**	91	>99(*R*)	11	Rac-**1o**	93	99(*R*)
2	(*S*)-**1p**	95	99(*R*)	7	(*R*)-**1p**	79	99(*R*)	12	Rac-**1p**	96	99(*R*)
3	(*S*)-**1q**	95	>99(*R*)	8	(*R*)-**1q**	83	>99(*R*)	13	Rac-**1q**	95	>99(*R*)
4	(*S*)-**1r**	74	>99(*R*)	9	(*R*)-**1r**	73	>99(*R*)	14	Rac-**1r**	66	>99(*R*)
5	(*S*)-**1s**	88	99(*R*)	10	(*R*)-**1s**	80	99(*R*)	15	Rac-**1s**	80	>99(*R*)

Monitoring the progress of the reaction revealed a maximum conversion in excess of 93% after 3 days (Fig. 2 and table S5). Increasing the concentration of ammonia up to 4 M led to a slight increase in conversion (95%; Table 1, entry 1, and tables S6 to S8). Addition of further aliquots of AA-ADH, Ph-AmDH, and NAD$^+$ after 2 days gave no further increase in conversion, indicating that the thermodynamic equilibrium had been reached. For improved catalytic efficiency of the cascade, the concentration of NAD$^+$ was reduced by a factor of 5, to 0.2 mM (1 mol %), which resulted in a slight drop in conversion to 76% (table S5 and figs. S9 and S10).

Surprisingly, when the same reaction conditions were applied to the amination of (R)-1a (20 mM) using LBv-ADH with the Ph-AmDH (minus His tag), the conversion to amine was <4% (table S9). We speculated that the instability of the LBv-ADH in ammonium chloride buffer at pH 8.7 might be the origin of the low conversion, so we investigated lower pH values. For ammonium chloride buffers, pH values of <8.5 cannot be attained; hence, ammonium formate buffer was investigated at various pH values (29). At pH 8 to 8.5, the amination of (R)-1a (20 mM) was achieved in 93% conversion and >99% ee (Table 1, entry 15). The cascade was then run by combining both of the stereocomplementary ADHs with the Ph-AmDH in one pot for the asymmetric amination of racemic 1a, affording (R)-3a in >99% ee and 81% conversion (Table 1, entry 29).

The hydrogen-borrowing cascade was initially tested on a limited number of 1-phenyl-2-propanol derivatives 1a to 1e (Table 1) for amination with inversion of configuration (entries 1 to 5), retention of configuration (entries 15 to 19), and asymmetric amination of racemic alcohols (entries 29 to 33). Conversion varied from moderate to excellent, whereas the ee was excellent in almost all cases.

Whereas ADHs generally possess broad substrate specificity, the Ph-AmDH accepts solely phenylacetone and phenylacetaldehyde derivatives with elevated turnover numbers. Nonetheless, the generation of chimeric enzymes through domain shuffling from different parents can rapidly lead to new enzymes with increased activity or different and extended substrate specificity. The

amino acid sequence of a stable chimeric AmDH (Ch1-AmDH) was recently published, although its substrate scope and stereoselectivity have not been elucidated (30). Thus, the Ch1-AmDH devoid of His tag was combined with the previously selected ADHs for the amination of a much broader panel of alcohols 1f to 1s. Aromatic substrates 1f to 1h bearing the phenyl ring in the α position (Table 1, entries 6, 20, and 34) and β position (Table 1, entries 7, 8, 21, 22, 35, and 36), relative to the secondary alcohol, as well as phenylethanol derivatives 1i to 1n with substituents in the ortho-, meta-, and para- positions (Table 1, entries 9 to 14, 23 to 28, and 37 to 42), were aminated with 99% ee (R) and conversions ranging from moderate to high. The only exception was alcohol 1g, which was aminated with lower enantioselectivity (82 or 83% ee; Table 1, entries 7, 21, and 35). For this particular substrate, the progress of ee was monitored as a function of time (table S14 and fig. S12). The enantiomeric excess of amine 3g remained constant, demonstrating that longer incubation times are not detrimental to the stereoselective outcome of the process. All the aliphatic secondary alcohols 1o to 1s examined (medium, long, and branched chain) were aminated with perfect ee and high conversions up to 96% (Table 2).

The hydrogen-borrowing amination is an extremely efficient and valuable method for the generation of optically active amines from alcohols. However, achiral terminal primary amines are also in high demand by the chemical industry, especially for the production of polymers and plasticizing agents (1). To demonstrate the broad applicability of the methodology, the amination of different primary alcohols was accomplished by combining the primary hT-ADH from Bacillus stearothermophilus (31) with either the Ch1-AmDH (Table 3, entries 1 to 6) or the Ph-AmDH (Table 3, entry 7). Quantitative conversion to the amine product was obtained with alcohols 1u to 1x.

To demonstrate the practical application of the methodology, we carried out bioaminations of five representative substrates—one for each structural category reported in Fig. 1—at a preparative scale. Starting from (S)-1a as the alcohol substrate, the conversion into the amine product (R)-3a reached 93% after 48 hours. The work-up consisted of extraction of the unreacted alcohol and ketone intermediate under acidic conditions, followed by the extraction of the amine product under basic conditions (27). The isolated yield of pure (R)-3a was 85% (99% ee). Following the same protocol, substrates (S)-1g, (S)-1i, (S)-1q, and 1u were converted to the corresponding amines with 89%, 31%, 95%, and >99% conversion, respectively. The isolated yields of pure (R)-3g, (R)-3i, (R)-3q, and 3u were 78%, 30%, 91%, and 91%, respectively. The enantiomeric excesses remained the same as for the experiments on an analytical scale.

Our dual-enzyme hydrogen-borrowing process enables the asymmetric amination of a broad range of secondary alcohols to afford the corresponding (R)-configured amines in high enantiomeric excess. Furthermore, in the majority of the cases, amination of primary alcohols proceeded in quantitative conversion. The biocatalytic

system uses ammonia as the simplest amine donor and generates water as the sole innocuous by-product. Ongoing studies are currently aimed at extending the substrate scope of the cascade through further protein engineering of AmDHs capable of aminating a wide range of more complex alcohols with elevated stereoselectivity. Although only enantiopure (R)-configured amines have been generated to date, the engineering of stereocomplementary AmDHs (S-selective) starting from D–amino acid dehydrogenases as scaffolds will complement the scope of our hydrogen-borrowing process. Finally, the use of lower concentrations of ammonia may be possible by the addition of further enzymes to derivatize the amine products and hence provide a thermodynamic driving force for the amination step.

REFERENCES AND NOTES

1. H. A. Wittcoff, B. G. Rueben, J. S. Plotkin, Industrial Organic Chemicals (Wiley- Interscience, New York, ed. 2, 2004).
2. T. C. Nugent, Ed., Chiral Amine Synthesis (Wiley-VCH, Weinheim, Germany, 2010).
3. E. Fabiano, B. T. Golding, M. M. Sadeghi, Synthesis 1987, 190–191 (1987).
4. H.-J. Arpe, Industrial Organic Chemistry (Wiley-VCH, Weinheim, Germany, ed. 5, 2010).
5. F. Balkenhohl, K. Ditrich, B. Hauer, W. Ladner, J. Prakt. Chem. 339, 381–384 (1997).
6. D. I. Sterling, in Chirality in Industry, A. N. Collins, G. N. Sheldrake, J. Crosby, Eds. (Wiley, Chichester, UK, 1992), pp. 209–222.
7. C. K. Savile et al., Science 329, 305–309 (2010).
8. J. H. Schrittwieser, J. Sattler, V. Resch, F. G. Mutti, W. Kroutil, Curr. Opin. Chem. Biol. 15, 249–256 (2011).
9. R. A. Sheldon, I. W. C. E. Arends, U. Hanefeld, Green Chemistry and Catalysis (Wiley-VCH, Weinheim, Germany, 2007).
10. T. Knaus, F. G. Mutti, L. D. Humphreys, N. J. Turner, N. S. Scrutton, Org. Biomol. Chem. 13, 223–233 (2015).
11. S. Imm et al., Angew. Chem. Int. Ed. 50, 7599–7603 (2011).
12. Y. Zhang, C.-S. Lim, D. S. B. Sim, H.-J. Pan, Y. Zhao, Angew. Chem. Int. Ed. 126, 1423–1427 (2014).
13. The amination with the Ru catalyst (7) requires 3 mol % of the metal catalyst, 150°C, ammonia gas under pressure and inert atmosphere; racemic amines are obtained. The amination with Ir catalyst (8) requires 5 mol % of the metal catalyst coordinated to an expensive chiral ligand, 10 mol % of binaphthalene phosphoric acid as cocatalyst; para-anisidine is the nitrogen source; at least 33% of the alcohol starting material is wasted.
14. N. J. Oldenhuis, V. M. Dong, Z. Guan, J. Am. Chem. Soc. 136, 12548–12551 (2014).
15. J. H. Sattler et al., Angew. Chem. Int. Ed. 51, 9156–9159 (2012).
16. When using (R)-selective ω-TAs, D-alanine must be used. D-alanine has a high cost and, moreover, a D-alanine dehydrogenase is not known. Only L-alanine would be produced during the reaction. Hence, in the case of (R)-selective ω-TAs, the system works via removal rather than recycling of the pyruvate.
17. V. Resch, W. M. F. Fabian, W. Kroutil, Adv. Synth. Catal. 352, 993–997 (2010).
18. M. J. Abrahamson, J. W. Wong, A. S. Bommarius, Adv. Synth. Catal. 355, 1780–1786 (2013).
19. M. J. Abrahamson, E. Vázquez-Figueroa, N. B. Woodall, J. C. Moore, A. S. Bommarius, Angew. Chem. Int. Ed. 51, 3969–3972 (2012).
20. S. K. Au, B. R. Bommarius, A. S. Bommarius, ACS Catal. 4, 4021–4026 (2014).
21. M. M. Musa, R. S. Phillips, Catal. Sci. Technol. 1, 1311–1323 (2011).
22. H. W. Höffken et al., Biochemistry 45, 82–93 (2006).
23. The wild-type Lactobacillus brevis ADH is a NADP-dependent ADH. This enzyme was previously engineered to accept NAD as cofactor, and this variant was applied in this study.
24. W. Hummel, B. Riebel, PCT Int. Appl. WO 9947684 (1999).

Table 3. Hydrogen-borrowing amination of primary alcohols 1t to 1z. Reactions were carried out at 30°C for 48 hours. See (27) for experimental details.

Entry	Substrate	Conversion (%)
1	1t	8
2	1u	99
3	1v	99
4	1w	99
5	1x	99
6	1y	61
7	1z	10

25. N. H. Schlieben et al., J. Mol. Biol. **349**, 801–813 (2005).
26. K. Tauber et al., Chemistry **19**, 4030–4035 (2013).
27. See supplementary materials on Science Online.
28. A. C. Price, Y.-M. Zhang, C. O. Rock, S. W. White, Structure **12**, 417–428 (2004).
29. The Ph-AmDH tolerates different buffers well (i.e., ammonium chloride, formate, borate, citrate, acetate, oxalate). However, the homotetrameric LBv-ADHs contains two Mg^{2+} centers; therefore, strong chelators such as oxalate, citrate, and acetate must be avoided as buffer salts. Removal of these Mg^{2+} ions inactivates the enzyme (32).
30. B. R. Bommarius, M. Schürmann, A. S. Bommarius, Chem. Commun. **50**, 14953–14955 (2014).
31. R. Cannio, M. Rossi, S. Bartolucci, Eur. J. Biochem. **222**, 345–352 (1994).
32. K. Niefind, J. Müller, B. Riebel, W. Hummel, D. Schomburg, J. Mol. Biol. **327**, 317–328 (2003).

BATTERIES

Alkaline quinone flow battery

Kaixiang Lin,[1] Qing Chen,[2] Michael R. Gerhardt,[2] Liuchuan Tong,[1] Sang Bok Kim,[1] Louise Eisenach,[3] Alvaro W. Valle,[3] David Hardee,[1] Roy G. Gordon,[1,2]* Michael J. Aziz,[2]* Michael P. Marshak[1,2]*

Storage of photovoltaic and wind electricity in batteries could solve the mismatch problem between the intermittent supply of these renewable resources and variable demand. Flow batteries permit more economical long-duration discharge than solid-electrode batteries by using liquid electrolytes stored outside of the battery. We report an alkaline flow battery based on redox-active organic molecules that are composed entirely of Earth-abundant elements and are nontoxic, nonflammable, and safe for use in residential and commercial environments. The battery operates efficiently with high power density near room temperature. These results demonstrate the stability and performance of redox-active organic molecules in alkaline flow batteries, potentially enabling cost-effective stationary storage of renewable energy.

T
he cost of photovoltaic (PV) and wind electricity has dropped so much that one of the largest barriers to getting most of our electricity from these renewable sources is their intermittency (1–3). Batteries provide a means to store electrical energy; however, traditional, enclosed batteries maintain discharge at peak power for far too short a duration to adequately regulate wind or solar power output (1, 2). In contrast, flow batteries can independently scale the power and energy components of the system by storing the electro-active species outside the battery container itself (3–5). In a flow battery, the power is generated in a device resembling a fuel cell, which contains electrodes separated by an ion-permeable membrane. Liquid solutions of redox-active species are pumped into the cell, where they can be charged and discharged, before being returned to storage in an external storage tank. Scaling the amount of energy to be stored thus involves simply making larger tanks (Fig. 1A). Existing flow batteries are based on metal ions in acidic solution, but challenges with corrosivity, hydrogen evolution, kinetics, materials cost and abundance, and efficiency thus far have prevented large-scale commercialization. The use of anthraquinones in an acidic aqueous flow battery can dramatically

[1]Department of Chemistry and Chemical Biology, Harvard University, 12 Oxford Street, Cambridge, MA 02138, USA. [2]Harvard John A. Paulson School of Engineering and Applied Sciences, 29 Oxford Street, Cambridge, MA 02138, USA. [3]Harvard College, Cambridge, MA 02138, USA.
*Corresponding author. E-mail: aziz@seas.harvard.edu (M.J.A.); gordon@chemistry.harvard.edu (R.G.G.); michael.marshak@colorado.edu (M.P.M.)
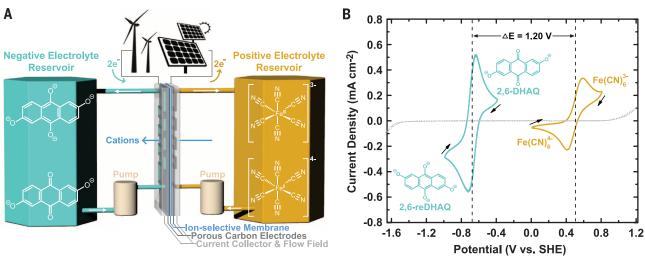
Fig. 1. Cyclic voltammetry of electrolyte and cell schematic. (A) Schematic of cell in charge mode. Cartoon on top of the cell represents sources of electrical energy from wind and solar. Curved arrows indicate direction of electron flow and white arrows indicate electrolyte solution flow. Blue arrow indicates migration of cations across the membrane. Essential components of electrochemical cells are labeled with color-coded lines and text. The molecular structures of oxidized and reduced species are shown on corresponding reservoirs. **(B)** Cyclic voltammogram of 2 mM 2,6-DHAQ (dark cyan curve) and ferrocyanide (gold curve) scanned at 100 mV/s on glassy carbon electrode; arrows indicate scan direction. Dotted line represents CV of 1 M KOH background scanned at 100 mV/s on graphite foil electrode.

reduce battery costs (6, 7); however, the use of bromine in the other half of the system precludes deployment in residential communities owing to toxicity concerns.

We demonstrate that quinone-based flow batteries can be adapted to alkaline solutions, where hydroxylated anthraquinones are highly soluble and bromine can be replaced with the nontoxic ferricyanide ion (8, 9)—a food additive (10). Functionalization of 9,10-anthraquinone (AQ) with electron-donating groups such as OH has been shown to lower the reduction potential and expand the battery voltage (6). In alkaline solution, these OH groups are deprotonated to provide solubility and greater electron donation capability, which results in an increase in the open-circuit voltage (OCV) of 47% over the previously reported system. Because functionalization away from the ketone group provides molecules with the highest solubility (11, 12), we initially targeted commercially available 2,6-dihydroxyanthraquinone (2,6-DHAQ),

which we find exhibits a room-temperature solubility of >0.6 M in 1 M KOH. This system can achieve power densities of >0.45 W cm^{-2} at room temperature and 0.7 W cm^{-2} at 45°C.

The use of alkaline electrolyte exploits pH as a parameter to shift the thermodynamic potentials of proton-dependent reactions to more negative values. In acid solutions, AQ undergoes a two-electron two-proton reduction at a single potential, which shifts to more negative values as the pH increases (6). When the pH exceeds 12, the reduction potential of 2,6-DHAQ becomes pH-independent because the reduced species is generated in its fully deprotonated form (fig. S1). In contrast with the pH-dependent electrochemical behavior of quinones (negative terminal), the ferro/ferricyanide redox couple (positive terminal) has a pH-independent redox potential. This contrasting pH dependence can be exploited through the development of low–reduction potential quinones at high pH. The cyclic voltammograms

(CVs) of 2,6-DHAQ and ferro/ferricyanide predict an equilibrium cell potential of 1.2 V upon combination of these two half-reactions (Fig. 1B). A quantitative analysis of the CV of 2,6-DHAQ at pH 14 (fig. S2) revealed redox behavior consistent with two one-electron reductions at potentials separated by only 0.06 V, with a rapid kinetic rate similar to that of quinones in acid (6). This behavior raises interesting questions about the relationship between quinone redox and hydrogen bonding (13).

Cell testing was performed at 20°C with solutions of 0.5 M 2,6-DHAQ dipotassium salt and 0.4 M K$_4$Fe(CN)$_6$, both dissolved in 1 M KOH. These solutions were pumped through a flow cell constructed from graphite flow plates and carbon paper electrodes, which were separated by a Nafion membrane. A charging current of 0.1 A cm^{-2} was applied to charge the cell, and polarization curves were measured at 10, 50, and 100% states of quinone charge (SOC). The OCV is 1.2 V at 50%
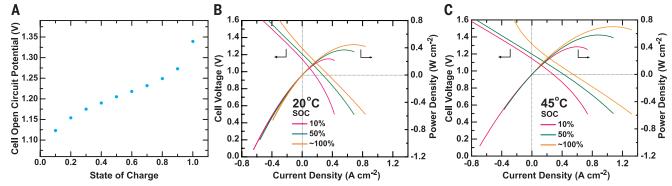

Fig. 2. Cell performance. (A) Cell open-circuit voltage versus state of charge. All potentials were taken when cell voltage stabilized to within ±1 mV. One hundred percent SOC was reached by potentiostatic holding at 1.5 V until the current decreased to below 20 mA/cm². (B and C) Cell voltage and power density versus current density at 20° and 45°C, respectively, at 10, 50, and ~100% SOC. Electrolyte composition: At 20°C, 0.5 M 2,6-DHAQ and 0.4 M ferrocyanide were used in negative electrolyte and positive electrolyte, respectively. At 45°C, both concentrations were doubled. In both cases, potassium hydroxide content started at 1 M for both sides in the fully discharged state.
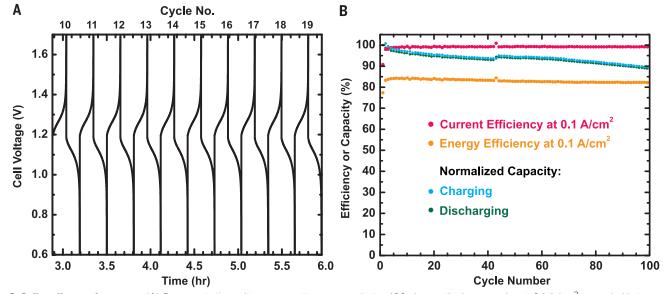

Fig. 3. Cell cycling performance. (A) Representative voltage versus time curves during 100 charge-discharge cycles at 0.1 A/cm², recorded between the 10th and 19th cycles. (B) Capacity retention, current efficiency, and energy efficiency values of 100 cycles. Normalized capacity is evaluated based on the capacity of the first charge and discharge cycle.

SOC; its dependence on SOC is shown in Fig. 2A. The polarization curves (Fig. 2B) show no sign of redox kinetic limitations and exhibit a peak galvanic power density exceeding 0.4 W cm^{-2}.
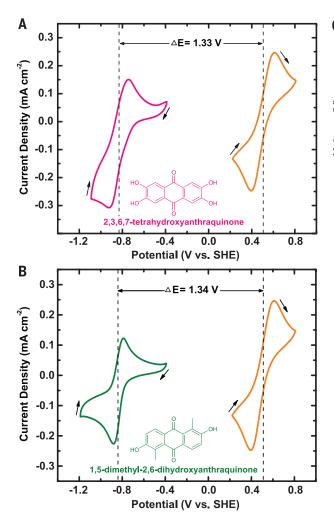
The cell was cycled at a constant current density of ±0.1 A cm^{-2} for 100 cycles (Fig. 3A). The current efficiency exceeded 99%, with a stable round-trip energy efficiency of 84%. A 0.1% loss in capacity per cycle was observed during cycling, which appears to be a continuous loss of electrolyte over the 100 cycles. Three possible loss mechanisms were explored: chemical decomposition, electrolyte crossover through the membrane, and leakage from the pumping system. Chemical and electrochemical stability studies showed that the negative electrolyte is stable. Ten millimolar 2,6-DHAQ was heated in 5 M KOH solution at 100°C for 30 days and was characterized by proton nuclear magnetic resonance (NMR). Cycled negative electrolyte was also collected and characterized by the same method; both studies showed no degradation product at the sensitivity level of 1% (fig. S3). Membrane crossover contamination has been a common challenge in acid-based redox flow batteries, where most electro-active molecules are either neutral or positive and tend to migrate through proton-conductive membranes (5). In this alkaline system,

however, all the electro-active molecules remain negatively charged in all charge states, leading to a dramatic decrease in the degree of crossover during cell cycling. Cyclic voltammetry of the ferro/ferricyanide electrolyte collected at the end of cycling showed no evidence of the presence of 2,6-DHAQ. This observation places an upper limit on crossover of 0.8% of the DHAQ, implying a crossover current density of <2.5 μA cm^{-2} (fig. S4). Finally, hydraulic leakage was investigated because an apparent but unquantifiable small decrease in fluid levels was observed in the reservoirs. After cell cycling, the cell was washed with deionized water until no coloration of eluent could be observed. The cell was then disassembled; coloration was found on the gaskets, indicating the likely site of electrolyte leakage (fig. S5). This source of capacity loss—equivalent to roughly eight drops in our system—is expected to become negligible as system size is scaled up.

By increasing the temperature to 45°C, the peak galvanic power density increases from 0.45 to ~0.7 W cm^{-2} (Fig. 2C), as the cell area-specific resistance (ASR) decreases from about 0.878 to 0.560 ohm cm^2, estimated from the linear parts of the polarization curves in Fig. 2. Most of this ASR decrease comes from a change in the high-frequency ASR (r_{hf}) measured by electrochemical

impedance spectroscopy (fig. S6). In both cases, the r_{hf} contributes more than 70% of the ASR and is indeed the limiting factor to the cell current and power outputs. The r_{hf} is dominated by the resistance of the membrane, which is an order of magnitude higher than the resistance of the same membrane in a pH 0 acid solution (14).

The sluggish kinetics of the hydrogen evolution reaction in alkaline solution on carbon electrodes results in a larger practical stability window in base rather than in acid (fig. S7). Consequently, quinones with substantially more negative reduction potentials are feasible as negative electrolyte materials. Preliminary investigations into the synthesis of different hydroxy-substituted anthraquinones suggest that further increases in cell potential are possible. Self-condensation reactions of substituted benzene yield 2,3,6,7-tetrahydroxy-AQ (THAQ) (15) and 1,5-dimethyl-2,6-DHAQ (15-DMAQ) (figs. S8 and S9). The CVs of these species in 1 M KOH suggest cell potentials versus ferri/ferrocyanide approaching 1.35 V (Fig. 4, A and B), which exceeds that of many aqueous rechargeable batteries (Fig. 4C).

The cyanide ions in both ferro- and ferricyanide are bound too tightly to be released under most conditions. Consequently, it is nontoxic in both oxidized and reduced forms and is even
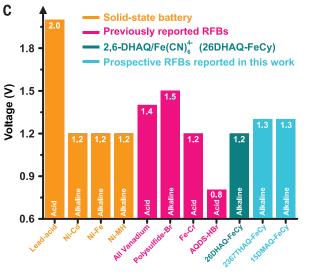

Fig. 4. Molecular structure and cyclic voltammetry of 2,6-DHAQ derivatives. (**A** and **B**) Molecular structures and CV of 2,3,6,7-THAQ (pink) and 1,5-DMAQ (olive), respectively, plotted along with ferrocyanide (orange curve) scanned at 100 mV/s on glassy carbon electrode. Both 2,6-DHAQ derivatives/ferrocyanide couples showed higher equilibrium potential than 2,6-DHAQ/ferrocyanide. (**C**) Selected aqueous secondary batteries showing voltage and flow status. Literature data from (3) and (16).

permitted for use as a food additive (*10*). The use of ferrocyanide offers notable advantages over bromine because it is nonvolatile and noncorrosive, allowing simpler and less expensive materials of construction. In addition, these tri- and tetra-anionic organometallic molecules exhibit low crossover rates through cation-exchange membranes.

The results reported herein highlight the ability of hydroxy-substituted anthraquinone and ferrocyanide to function as stable flow battery electrolytes in alkaline solution. The use of organic and organometallic coordination complexes in base, rather than aqueous metal ions in acid, resolves serious cost, corrosion, and safety concerns of previous flow battery chemistries. Alkaline flow batteries can compensate for higher membrane resistance with higher voltage, leading to performance similar to that of their acidic counterparts. In addition, quinone-ferrocyanide alkaline chemistry avoids the membrane crossover, corrosivity, toxicity, and regulations associated with bromine. This reduced corrosivity can lead to a substantially lower materials cost because many components can be made of inexpensive polyolefin or poly(vinyl chloride) plastics.

REFERENCES AND NOTES

1. B. Dunn, H. Kamath, J.-M. Tarascon, *Science* **334**, 928–935 (2011).
2. Z. Yang et al., *Chem. Rev.* **111**, 3577–3613 (2011).
3. T. Nguyen, R. F. Savinell, *Electrochem. Soc. Interface* **19**, 54–56 (2010).
4. D. Biello, *Sci. Am.* **311**, 66–71 (November 2014).
5. M. Skyllas-Kazacos, M. H. Chakrabarti, S. A. Hajimolana, F. S. Mjalli, M. Saleem, *J. Electrochem. Soc.* **158**, R55–R79 (2011).
6. B. Huskinson et al., *Nature* **505**, 195–198 (2014).
7. R. M. Darling, K. G. Gallagher, J. A. Kowalski, S. Ha, F. R. Brushett, *Energy Env. Sci.* **7**, 3459–3477 (2014).
8. G. G. I. Joseph, A. J. Gotcher, G. Sikha, G. J. Wilson, High performance flow battery (2011); www.google.com/patents/US20110244277.
9. J. R. Goldstein, Novel flow battery and usage thereof (2015); www.google.com/patents/US20150048777.
10. "Seventeenth Report of the Joint FAO/WHO Expert Committee on Food Additives. Report No. 539," *Wld Hlth Org. Techn. Rep. Ser.* (World Health Organization, Geneva, 1974).
11. H. Pal, T. Mukherjee, J. P. Mittal, *J. Chem. Soc., Faraday Trans.* **90**, 711–716 (1994).
12. S. Er, C. Suh, M. P. Marshak, A. Aspuru-Guzik, *Chem. Sci.* **6**, 885–893 (2015).
13. M. Quan, D. Sanchez, M. F. Wasylkiw, D. K. Smith, *J. Am. Chem. Soc.* **129**, 12847–12856 (2007).
14. Q. Chen, M. R. Gerhardt, L. Hartle, M. J. Aziz, *J. Electrochem. Soc.* **163**, A5010–A5013 (2015).
15. T. S. Balaban, A. Eichhöfer, M. J. Krische, J.-M. Lehn, *Helv. Chim. Acta* **89**, 333–351 (2006).
16. D. Linden, T. B. Reddy, *Handbook of Batteries* (McGraw-Hill, New York, 2002).

H-BONDING CATALYSIS

O–H hydrogen bonding promotes H-atom transfer from α C–H bonds for C-alkylation of alcohols

Jenna L. Jeffrey,* Jack A. Terrett,* David W. C. MacMillan†

The efficiency and selectivity of hydrogen atom transfer from organic molecules are often difficult to control in the presence of multiple potential hydrogen atom donors and acceptors. Here, we describe the mechanistic evaluation of a mode of catalytic activation that accomplishes the highly selective photoredox α-alkylation/lactonization of alcohols with methyl acrylate via a hydrogen atom transfer mechanism. Our studies indicate a particular role of tetra-*n*-butylammonium phosphate in enhancing the selectivity for α C–H bonds in alcohols in the presence of allylic, benzylic, α-C=O, and α-ether C–H bonds.

Complex molecules, such as medicinal agents and natural products, often possess multiple types of C–H bonds, each with a different inherent reactivity. This intrinsic reactivity depends on a multifaceted interplay of steric effects, inductive and conjugative influences, as well as innate strain (*1, 2*). The intermolecular catalytic functionalization of C(sp³)–H bonds in a selective manner represents a long-standing challenge that has inspired decades of effort within the synthetic community. Notable early studies by Bergman (*3*), as well as recent advances in selective intermolecular transition metal catalyzed C(sp³)–H activation—including, among others, Hartwig's rhodium-catalyzed borylation of terminal methyl groups (*4*) and White's iron-catalyzed oxidation of both secondary (2°) and tertiary (3°) aliphatic C–H bonds (*5*)—highlight the importance of catalyst structure on site selectivity.

Catalyst structure has also proven critical to the selectivity of C(sp³)–H functionalization via hydrogen atom transfer (HAT) catalysis. HAT—the effective movement of a hydrogen atom between two molecular sites—represents a ubiquitous elementary reaction step in organic chemistry (*6–8*). The rate of hydrogen abstraction from a C–H bond depends not only on the C–H bond dissociation enthalpy (BDE) but also on polar effects in the transition state. In 1987, Roberts noted that certain electrophilic radicals (such as *t*-butoxyl) preferentially abstract hydrogen from electron-rich C–H bonds, whereas nucleophilic radicals (such

as amine-boryl) selectively cleave electron-deficient C–H bonds (*9*). The generality of this concept was subsequently delineated through the broad application of polarity reversal catalysis (PRC), which takes advantage of favorable polar effects to control the regioselectivity of HAT from multiple C–H groups of similar strength (*10*).

We questioned whether the basic principles of PRC could be integrated into a catalytic system for the selective activation of alcohol α-C–H bonds in the presence of a wide range of other C–H bonds (such as α-C=O, α-ether, or allylic or benzylic C–H) (*11, 12*). Specifically, we postulated that the selective C-alkylation of alcohols could be achieved via a photoredox-catalyzed, H-bond–assisted bond activation strategy (Fig. 1) (*13–15*), in which the hydroxyalkyl C–H bond is selectively polarized and weakened via O–H hydrogen bonding.

It is well known that the strength of α C–H bonds of alcohols decreases upon deprotonation of the alcohol O–H group. This so-called "oxy anionic substituent effect" (*16, 17*) leads to the acceleration of a wide range of organic reactions [such as oxyanionic [1,3] and [3,3] sigmatropic rearrangements and HAT from alkoxides (*18*)]. More recently, it has been shown that intermolecular hydrogen bonding between alcohols and various acceptor molecules gives rise to a similar polarization and weakening of the adjacent C–H bond (*19*), the strength of which is reflected in the ¹³C nuclear magnetic resonance (NMR) chemical shift and the one-bond ¹³C–¹H coupling constant ($^1J_{CH}$) (*20, 21*). In particular, it was found that a 1 kJ/mol increase in the enthalpy of the H-bond resulted in a 0.2-Hz decrease in $^1J_{CH}$ for hexafluoroisopropanol complexed to various amines (*20*). On the basis of these studies, we reasoned that the efficiency and selectivity of alcohol C–H activation

Merck Center for Catalysis, Princeton University, Princeton, NJ 08544, USA.
*These authors contributed equally to this work. †Corresponding author. E-mail: dmacmill@princeton.edu

Fig. 1. Proposed hydrogen bond–assisted C–H activation of alcohols. BDE values are available in (13–15).
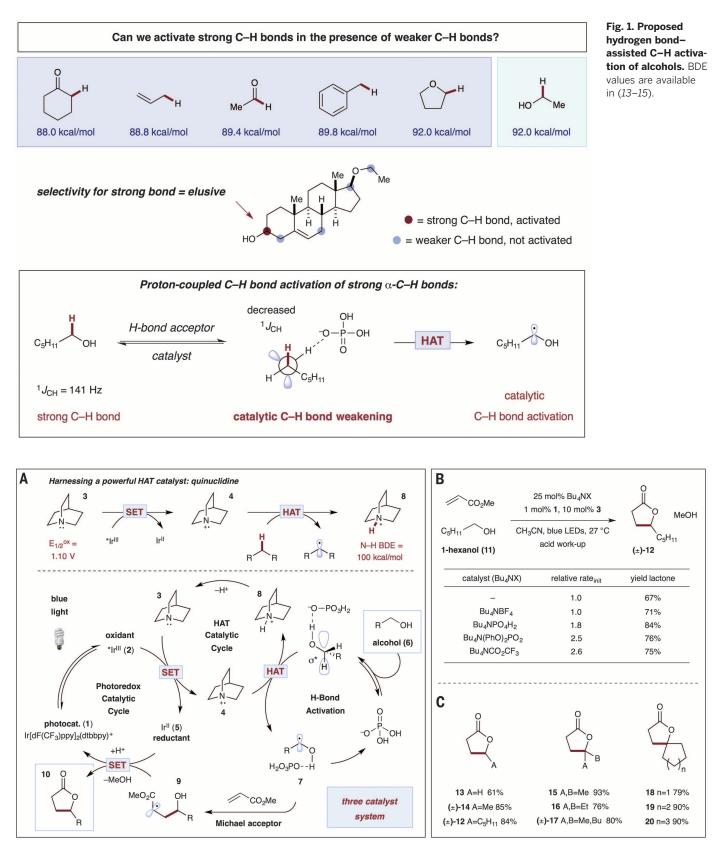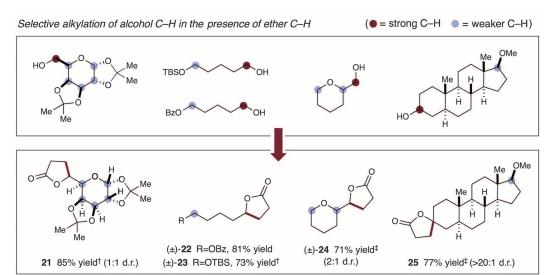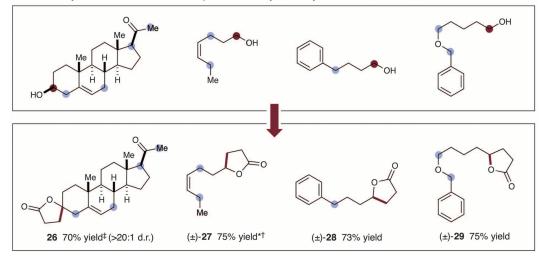

Fig. 2. Reaction development. (**A**) H-bond–assisted C–H activation of alcohols. Shown is a proposed mechanistic pathway for the C-alkylation of alcohols with Michael acceptors. SET, single-electron transfer. (**B**) Evaluation of hydrogen-bonding catalysts. Yield determined by means of ^{1}H NMR, using an internal standard. (**C**) Selected scope of simple alcohol addition to methyl acrylate. Only products are shown; experimental conditions are as in (B). Isolated yields are reported.

Fig. 3. Selected alcohol scope for H-bond–assisted C–H activation. Additions to methyl acrylate were carried out at 27°C for 24 hours, unless otherwise noted. Isolated yields are reported. Detailed experimental procedures and full scope of alcohols/Michael acceptors are provided in the supplementary materials. Dagger symbol indicates 40 hours reaction time; double-dagger symbol indicates 48 hours reaction time; and asterisk indicates 1:1 mixture of E/Z isomers. No alkylation of positions marked with blue circles was observed in any case.

could be enhanced by catalytic complexation with a suitable hydrogen-bond acceptor. In particular, interaction of the hydroxyl group of an alcohol with a hydrogen-bond acceptor catalyst should increase n–σ* delocalization of the oxygen lone pair, rendering the α C–H bond more hydridic (more polarized) and more susceptible to HAT by an electrophilic radical species.

We demonstrate the selective α-activation of alcohol C–H bonds in the presence of allylic, benzylic, α-oxy, and α-acyl C–H groups via a photoredox protocol, which relies on the cooperation of three distinct catalysts: an iridium-based photoredox catalyst; a HAT catalyst; and tetra-n-butylammonium phosphate (or TBAP), which is a hydrogen-bonding catalyst. On the basis of kinetic analyses, NMR structural data, and kinetic isotope effects (KIEs), we demonstrate the role of TBAP in facilitating the highly selective α hydrogen atom abstraction from alcohols.

The past several years have witnessed a dramatic increase in the application of photoredox catalysis—the use of visible light–activated organic dyes or metal complexes to facilitate single-

electron transfer events—to the development of organic transformations (22). By combining photoredox activation with organocatalysis (23, 24) and nickel catalysis (25), we have recently highlighted the potential of photoredox catalysis to achieve bond constructions that are not possible with more traditional methods.

We became interested in the selectivity and efficiency of C–H bond activation in the context of our ongoing campaign to merge visible-light photoredox catalysis with HAT catalysis (26–29). We have previously demonstrated the utility of thiols (S–H BDE = 87 kcal/mol) as HAT catalysts in the photoredox coupling of benzylic ethers (C–H BDE = 86 kcal/mol) with arenes (26) and imines (27). We recognized that the ability to catalytically activate stronger C–H bonds, such as those present in aliphatic alcohols and ethers (α C–H BDE > 90 kcal/mol), would hinge on the identification of a catalyst that satisfies two critical requirements: (i) homolytic cleavage of a strong substrate C–H bond must be counterbalanced by formation of a stronger H–[catalyst] bond, and (ii) selective activation of hydridic C–H bonds (bonds that are

substantially polarized because of oxygen lone pair donation) must be realized. With these criteria in mind, we questioned whether it might be possible to transiently generate a hydridophilic amine radical cation from quinuclidine (Figs. 2A and 3)—which would be particularly suited to abstraction of relatively strong, hydridic C–H bonds—while resisting α-deprotonation because of poor H–C–N orbital overlap in this rigid bicyclic structure (30, 31). As outlined in Fig. 2A, we envisioned an initial excitation of the well-known photocatalyst Ir[dF(CF$_3$)ppy]$_2$(dtbbpy)PF$_6$ [dF(CF$_3$)ppy = 2-(2,4-difluorophenyl)-5-(trifluoromethyl)pyridine, dtbbpy = 4,4'-di-$tert$-butyl-2,2'-bipyridine] (1) to *Ir[dF(CF$_3$)ppy]$_2$(dtbbpy)$^+$ (2) with visible light. Reductive quenching of 2 [reduction potential ($E_{1/2}^{red}$) = +1.21 V versus saturated calomel electrode (SCE) in CH$_3$CN] (32) via oxidation of 3 ($E_{1/2}^{ox}$ = +1.1 V versus SCE in CH$_3$CN) (33, 34) would then afford radical cation 4 and Ir(II) (5). At this stage, the electrophilic quinuclidinium radical 4 should abstract a hydrogen atom from an alcohol (6) to afford α-hydroxy radical 7 and quinuclidinium ion 8 [H–N$^+$ BDE = 100 kcal/mol
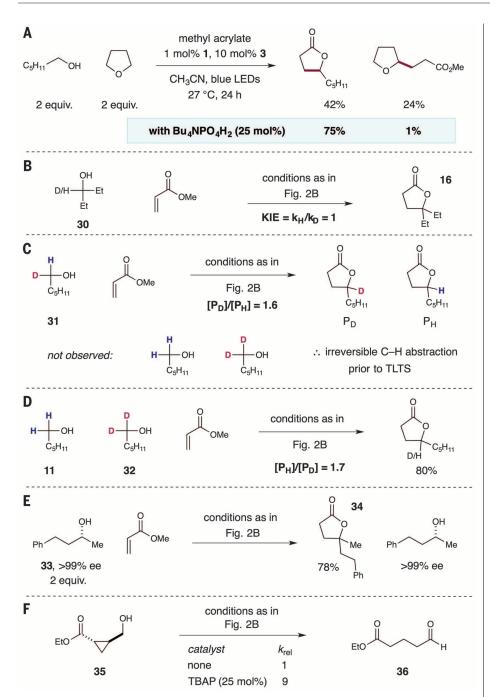
Fig. 4. Mechanistic studies. (**A**) H-bond–dependent selectivity of α-oxy C–H alkylation. (**B**) Kinetic isotope effect determined from two parallel kinetic analyses. (**C**) Kinetic isotope effect determined from intramolecular competition experiment. (**D**) Kinetic isotope effect determined from intermolecular competition experiment. (**E**) Evaluation of the enantiomeric excess of unreacted alcohol under standard C-alkylation conditions. (**F**) Effect of TBAP on the rate of C–H abstraction from **35**.

phosphate (Fig. 2B). Superior levels of product formation were achieved with catalytic TBAP (25 mol %), which provided the desired lactone in 84% yield. Initial rate kinetic analysis of the alkylation/lactonization of **11** revealed rate enhancements in the presence of each hydrogen-bonding catalyst examined, with the largest initial rate acceleration from use of $Bu_4NCO_2CF_3$ or $Bu_4N(PhO)_2PO_2$ [relative rate (r_{rel}) = 2.6 and 2.5, respectively].

We next demonstrated that a wide range of 1° and 2° alcohols undergo selective α-hydroxy alkylation with methyl acrylate in good to excellent yields using TBAP catalysis (Fig. 2C). As outlined in Fig. 3, these conditions clearly enable the selective activation of alcohol C–H bonds in the presence of various α-oxy C–H groups, including cyclic and acyclic alkyl ethers (**21**, **24**, and **25**, 85, 71, and 77% yield, respectively), silyl ethers (**23**, 73% yield), and esters (**22**, 81% yield). Moreover, excellent selectivity was achieved in the presence of both allylic and benzylic hydrogens (for example, **26** to **29**, 70 to 75% yield). The selectivity of this H-bond–assisted C–H activation platform was further demonstrated via the C–H alkylation/lactonization of bifunctional steroid derivatives, which provided the corresponding lactone products in good levels of efficiency (**25** and **26**, 77 and 70%, respectively). Electron-deficient α-benzoyloxy and α-acyl C–H bonds (**22** and **26**) are expected to be inherently deactivated toward HAT with respect to electrophilic radical HAT systems (10), such as quinuclidinium radical cation. In the absence of TBAP, higher levels of substrate concentration were required to achieve useful efficiencies. However, under those conditions nonselective C–H abstraction of weaker, less hydridic C–H bonds was observed. In all cases outlined in Fig. 3, we only observed alkylation products arising from the activation of the hydroxyalkyl C–H bonds present in the various substrates.

We next turned our attention to defining the capacity for selective α-hydroxy C–H functionalization in the presence of C–H bonds that have similar polarity and strength. Specifically, we selected tetrahydrofuran (THF) as a prototypical ether substrate, which would normally undergo C–H activation via HAT with rates similar to those of alcohol substrates. We found that the dual catalytic system involving quinuclidine and photoredox catalyst **1** enabled the efficient alkylation of THF with rates that were competitive with 1-hexanol in competition experiments, affording a 1.7:1 mixture of lactone and ether products (Fig. 4A) (37). However, the addition of 25 mol % of TBAP catalyst enabled a dramatic increase in overall reaction selectivity to afford almost exclusively the alcohol C–H alkylation product (75% lactone, 1% ether).

To further understand the role of hydrogen bonding in this H-bond–assisted C-alkylation process, a series of computational calculations and NMR experiments were undertaken. These studies were to evaluate the interaction of 1-hexanol with various hydrogen-bonding catalysts (highlighted in Fig. 2B) and to determine their accompanying effect on the α-hydroxy C–H bond strength. We performed density functional theory (DFT)

(33)]. Nucleophilic addition of α-oxy radical **7** to an electron-deficient alkene would furnish alkyl radical **9**. Single-electron reduction of this electron-deficient radical **9** by Ir(II) (**5**) ($E_{1/2}^{red}$ = –1.37 V versus SCE in CH_3CN) would then afford the α-alkylated product **10** after protonation and lactonization, while simultaneously regenerating both the photocatalyst (**5→1**) and the HAT catalyst (**8→3**) (35, 36).

We initially validated our proposed alkylation protocol by subjecting 1-hexanol (**11**) and methyl acrylate to blue light in the presence of amine **3** [10 mole percent (mol %)] and photocatalyst **1**, which afforded after 24 hours γ-nonalactone (**12**) in 67% yield after acidic work-up (Fig. 2B). We next evaluated a range of hydrogen-bond acceptor catalysts, including the tetra-*n*-butylammonium salts of phosphate, trifluoroacetate, and diphenyl

calculations using an unrestricted B3LYP functional with a 6–31G basis set. In the presence of either phosphate, diphenyl phosphate, or trifluoroacetate tetrabutylammonium salts, a BDE weakening of ~3 kcal/mol was calculated (supplementary materials). Although this represents a change in the α-C–H BDE of 1-hexanol from 94.1 kcal/mol to 91.0 kcal/mol when bonded to the TBAP catalyst, it clearly demonstrates that BDE is not the only factor defining this HAT selectivity, and bond polarization effects are likely important.

We also performed NMR experiments to explore the influence of both quinuclidine and TBAP as hydrogen-bonding catalysts for 1-hexanol. In the absence of either additive, the ^{13}C NMR chemical shift of the α carbon of 1-hexanol (δC1) in CDCl$_3$ (38) appeared at 63.1 parts per million (ppm) with $^{1}J_{CH[hexanol]}$ = 141.1 Hz. Addition of an equimolar amount of quinuclidine resulted in a 0.4-ppm upfield shift (δC1$_{hexanol:3}$ = 62.7 ppm) and a slight decrease in the one-bond ^{13}C–^{1}H coupling constant ($^{1}J_{CH[hexanol:3]}$ = 140.4 Hz). For comparison, a 1:1 mixture of 1-hexanol and TBAP gave rise to a similarly upfield shift in the ^{13}C signal for C1 of 1-hexanol (δC1$_{hexanol:TBAP}$ = 62.6 ppm; $\Delta\delta$C1=0.5 ppm), with $^{1}J_{CH(hexanol:TBAP)}$ = 140.3 Hz. These data clearly indicate that both quinuclidine and TBAP can induce bond weakening of the α-C1–H of 1-hexanol via hydrogen bonding. These data are also consistent with decreased s-character in the hybrid carbon orbitals of the C–H bond (increased hydridicity) of hexanol upon H-bond formation (39).

To more thoroughly outline the factors governing both the rate and selectivity of the C-alkylation of alcohols, we performed a suite of mechanistic experiments. The initial rate of the reaction of 1-hexanol with methyl acrylate showed first-order dependence on [hexanol]$_{init}$ and [acrylate]$_{init}$. The observed increase in the initial rate of reaction in the presence of TBAP (Fig. 2B), coupled with first-order dependence on both reactants, implies that TBAP serves to lower the energy barrier of (i) the C–H abstraction step (owing to α-C–H bond weakening); (ii) the C–C bond forming step, that is, addition of radical **9** to methyl acrylate (owing to enhanced nucleophilicity of the H-bonded α-hydroxy radical); or (iii) a combination of both of these steps.

In order to distinguish between these three possibilities, we conducted a series of experiments to assess potential deuterium kinetic isotope effects on the C–H abstraction step of the proposed catalytic cycle. First, the rate constants for the coupling of methyl acrylate with either 3-pentanol or D-3-pentanol (**30**→**16**) (Fig. 4B) were found to be identical—KIE = 1—clearly demonstrating that C–H/D abstraction from the alcohol **30** does not occur during the turnover-limiting transition state (TLTS) of our proposed catalytic cycle (Fig. 2A). However, an intramolecular competition experiment of monodeuterated alcohol **31** afforded a mixture of deuterated and undeuterated lactones (P$_D$ and P$_H$) with a 1.6:1 ratio (Fig. 4C). This result demonstrates that even though C–H/D abstraction is not rate-limiting, it represents the selectivity-determining step of the C-alkylation of hexanol **31**. The recovered starting material from this exper-

iment did not contain any fully protonated 1-hexanol or d_2-hexanol, confirming that C–H/D abstraction is irreversible in this process. The irreversibility of the C–H abstraction step was further confirmed through two additional experiments: first, in an intermolecular competition between 1-hexanol and dideuterated hexanol **32** (Fig. 4D), in which no amount of monodeuterated alcohol **31** was detected during the process; and second, in the C-alkylation of enantiopure alcohol **33** (Fig. 4E), in which no racemization of starting material was observed upon recovery of excess starting material (40). Taken together, these results are consistent with the mechanistic scenario (iii): a dual role of TBAP in both accelerating the C–H abstraction from alcohols and enhancing the rate of addition of the resulting radical to Michael acceptors (41).

Last, compelling experimental evidence for our proposed C–H activation pathway was attained in the form of initial rate data for the conversion of cyclopropyl radical clock alcohol **35** to aldehyde **36** in the presence and absence of TBAP catalyst (Fig. 4F). Specifically, we reasoned that C–H abstraction from **35** to generate the 2-(alkoxycarbonyl) cyclopropylcarbinyl radical [rate constant for rearrangement = 5×10^{10} to 8×10^{10} s^{-1} at 25°C (42–44)] would be rate-limiting. As such, enhancement in the rate of C–H abstraction via H-bond–assisted C–H activation should be clearly manifested in the observed rate of conversion of **35** to **36** in the presence and absence of TBAP catalyst. Indeed, under our photoredox/HAT conditions, a ninefold rate enhancement in the rate of conversion of alcohol **35** to aldehyde **36** was observed upon addition of 25 mol % TBAP (45). This result clearly corroborates our mechanistic proposal, in which TBAP facilitates C–H abstraction from alcohols via hydrogen bond activation. The activation concept presented here is likely pertinent to a wide range of C–H abstraction reactions.

REFERENCES AND NOTES

1. D. Balcells, E. Clot, O. Eisenstein, *Chem. Rev.* **110**, 749–823 (2010).
2. T. Newhouse, P. S. Baran, *Angew. Chem. Int. Ed.* **50**, 3362–3374 (2011).
3. B. A. Arndtsen, R. G. Bergman, T. A. Mobley, T. H. Peterson, *Acc. Chem. Res.* **28**, 154–162 (1995).
4. J. D. Lawrence, M. Takahashi, C. Bae, J. F. Hartwig, *J. Am. Chem. Soc.* **126**, 15334–15335 (2004).
5. M. S. Chen, M. C. White, *Science* **327**, 566–571 (2010).
6. E. A. Mader, E. R. Davidson, J. M. Mayer, *J. Am. Chem. Soc.* **129**, 5153–5166 (2007).
7. J. J. Warren, J. M. Mayer, *Proc. Natl. Acad. Sci. U.S.A.* **107**, 5282–5287 (2010).
8. J. M. Mayer, *Acc. Chem. Res.* **44**, 36–46 (2011).
9. V. Paul, B. P. Roberts, *J. Chem. Soc. Chem. Commun.* (17): 1322 (1987).
10. B. P. Roberts, *Chem. Soc. Rev.* **28**, 25–35 (1999).
11. A Ti-catalyzed conjugate addition protocol enabled by complexation-induced N–H bond-weakening was recently reported (12).
12. K. T. Tarantino, D. C. Miller, T. A. Callon, R. R. Knowles, *J. Am. Chem. Soc.* **137**, 6440–6443 (2015).
13. F. G. Bordwell, J. A. Harrelson Jr., *Can. J. Chem.* **68**, 1714–1718 (1990).
14. S. J. Blanksby, G. B. Ellison, *Acc. Chem. Res.* **36**, 255–263 (2003).
15. L. J. J. Laarhoven, P. Mulder, D. D. M. Wayner, *Acc. Chem. Res.* **32**, 342–349 (1999).
16. M. L. Steigerwald, W. A. Goddard III, D. A. Evans, *J. Am. Chem. Soc.* **101**, 1994–1997 (1979).

17. D. A. Evans, D. J. Baillargeon, *Tetrahedron Lett.* **19**, 3315–3318 (1978).
18. J. A. Cradlebaugh et al., *Org. Biomol. Chem.* **2**, 2083–2086 (2004).
19. E. Gawlita et al., *J. Am. Chem. Soc.* **122**, 11660–11669 (2000).
20. N. C. Maiti, Y. Zhu, I. Carmichael, A. S. Serianni, V. E. Anderson, *J. Org. Chem.* **71**, 2878–2880 (2006).
21. U. Pal, S. Sen, N. C. Maiti, *J. Phys. Chem. A* **118**, 1024–1030 (2014).
22. C. K. Prier, D. A. Rankic, D. W. C. MacMillan, *Chem. Rev.* **113**, 5322–5363 (2013).
23. D. A. Nicewicz, D. W. C. MacMillan, *Science* **322**, 77–80 (2008).
24. M. T. Pirnot, D. A. Rankic, D. B. C. Martin, D. W. C. MacMillan, *Science* **339**, 1593–1596 (2013).
25. Z. Zuo et al., *Science* **345**, 437–440 (2014).
26. K. Qvortrup, D. A. Rankic, D. W. C. MacMillan, *J. Am. Chem. Soc.* **136**, 626–629 (2014).
27. D. Hager, D. W. C. MacMillan, *J. Am. Chem. Soc.* **136**, 16986–16989 (2014).
28. J. Jin, D. W. C. MacMillan, *Angew. Chem. Int. Ed.* **54**, 1565–1569 (2015).
29. J. D. Cuthbertson, D. W. C. MacMillan, *Nature* **519**, 74–77 (2015).
30. The importance of polar effects in reactions of electrophilic radicals, such as aminium cation radicals, is well documented. An early example of selectivity in radical C–H functionalization is provided in (31).
31. F. Minisci, R. Galli, A. Galli, R. Bernardi, *Tetrahedron Lett.* **8**, 2207–2209 (1967).
32. M. S. Lowry et al., *Chem. Mater.* **17**, 5712–5719 (2005).
33. W.-Z. Liu, F. G. Bordwell, *J. Org. Chem.* **61**, 4778–4783 (1996).
34. S. F. Nelsen, P. J. Hintz, *J. Am. Chem. Soc.* **94**, 7114–7117 (1972).
35. We cannot currently rule out the possibility that radical chain mechanisms are operative, in addition to the proposed closed catalytic cycle. A recent report on the characterization of radical chain processes in visible light photoredox reactions is provided in (36).
36. M. A. Cismesia, T. P. Yoon, *Chem. Sci.* **6**, 5426–5434 (2015).
37. In a related experiment using d_8-THF in place of THF, no deuterium exchange was observed between d_8-THF and 1-hexanol.
38. The propensity of CD$_3$CN to form H-bonds with 1-hexanol precluded its use as a solvent for the measurement of changes in $^{1}J_{CH}$ as a function of H-bond formation with **3** or TBAP. However, small changes in δC1 were measured: δC1$_{hexanol}$ = 62.7 ppm, δC1$_{hexanol:3}$ (1:1) = 62.6 ppm, and δC1$_{hexanol:TBAP}$ (3:1) = 62.6 ppm.
39. M. Balci, *Basic ^{1}H-^{13}C NMR Spectroscopy* (Elsevier B. V., Amsterdam, 2005), pp. 325–332.
40. For comparison, an intermolecular competition experiment between THF and d_8-THF gave rise to a 2:1 ratio of products, with the undeuterated ether as the major product.
41. A reaction coordinate diagram depiction of scenario (iii) is provided in the supplementary materials on *Science* Online.
42. M. Newcomb, S. Y. Choi, *Tetrahedron Lett.* **34**, 6363–6364 (1993).
43. S. Y. Choi, M. Newcomb, *Tetrahedron* **51**, 657–664 (1995).
44. M. Newcomb, P. H. Toy, *Acc. Chem. Res.* **33**, 449–455 (2000).
45. As expected, when the same experiment was conducted in the presence of methyl acrylate (1 equivalent), none of the corresponding C-alkylation product was observed. Experimental details are provided in the supplementary materials on *Science* Online.

PALEOCEANOGRAPHY

Synchronous centennial abrupt events in the ocean and atmosphere during the last deglaciation

Tianyu Chen,[1]* Laura F. Robinson,[1] Andrea Burke,[2] John Southon,[3] Peter Spooner,[1] Paul J. Morris,[1]† Hong Chin Ng[1]

Antarctic ice-core data reveal that the atmosphere experienced abrupt centennial increases in CO_2 concentration during the last deglaciation (~18 thousand to 11 thousand years ago). Establishing the role of ocean circulation in these changes requires high-resolution, accurately dated marine records. Here, we report radiocarbon data from uranium-thorium–dated deep-sea corals in the Equatorial Atlantic and Drake Passage over the past 25,000 years. Two major deglacial radiocarbon shifts occurred in phase with centennial atmospheric CO_2 rises at 14.8 thousand and 11.7 thousand years ago. We interpret these radiocarbon-enriched signals to represent two short-lived (less than 500 years) "overshoot" events, with Atlantic meridional overturning stronger than that of the modern era. These results provide compelling evidence for a close coupling of ocean circulation and centennial climate events during the last deglaciation.

Paleo-records have shown that warming during the transition from the Last Glacial Maximum (LGM) [~22 thousand to 18 thousand years ago (ka)] to the Holocene occurred in several abrupt events, which were not synchronous between hemispheres (1). The warming in the Southern Hemisphere was accompanied by millennial-scale atmospheric CO_2 concentration increases during the Younger Dryas (YD) (12.9 to 11.5 ka) and Heinrich Stadial 1 (HS1) (~18 to 14.6 ka) (2). Together, the timing of interhemispheric temperature and CO_2 changes at millennial scales point to a critical role for Atlantic Meridional Overturning Circulation (AMOC) through its "seesaw" behavior (3, 4). Reduced AMOC strength decreased heat transport from the south to the north during the YD and HS1 (5). At the same time, increased Southern Ocean upwelling likely enhanced the release of CO_2 (6, 7). Recently, a new, high-resolution Antarctic ice-core record (8) has revealed three abrupt centennial-scale atmospheric CO_2 increases superimposed on the millennial-scale deglacial CO_2 rise, each of 10 to 15 parts per million by volume (ppmv), contributing a substantial portion of the total 90 ppmv deglacial CO_2 increase. Within the constraints of the ice-age and gas-age offsets, the timings of the latter two of these centennial changes are coincident with abrupt Northern Hemisphere warming at the end of the YD and HS1. These two abrupt centennial CO_2 rises have been interpreted as being driven from the north by reinvigoration of AMOC (8).

In order to establish direct links between the atmosphere and ocean at centennial time scales, it is necessary to have well-dated, high-resolution marine records that are comparable with ice-core records. Deep-sea fossil corals have the particular advantage that they can be precisely dated with U-series disequilibrium methods (9). The aragonite skeletons of scleractinian corals also record the radiocarbon (^{14}C) content of dissolved inorganic carbon (DIC) at the time of growth, so that coupled ^{14}C/^{12}C analysis and U-series dating of deep-sea corals provides the reconstruction of past deep-ocean ^{14}C/^{12}C ratios. Radiocarbon is produced in the upper atmosphere by cosmic ray–induced nuclear reaction and has a decay half-life of 5730 years. Once introduced into the deep sea from the surface ocean, it is isolated from the atmosphere and decays away. Variability of ^{14}C in the deep ocean thus provides a proxy that is related to the isolation and geometry of deepwater masses and the rate of deep circulation both in the modern and the geological past. In this study, we have generated a detailed deglacial radiocarbon history in the Equatorial Atlantic mainly at depths from 750 to 2100 m [Intermediate/Deep waters (EAI/DW)] and at locations within modern-day Southern Ocean Upper Circumpolar Deep Water (UCDW) (700 to 1800 m) from the Drake Passage on an absolute time scale based on deep-sea corals. We use these data to put new constraints on the millennial to centennial mechanisms connecting the Atlantic, the Southern Ocean, and the atmosphere.

The Equatorial Atlantic coral samples (5 to 15°N) were recovered from depths of 750 to 2800 m from the Sierra Leone Rise, the Mid-Atlantic Ridge, and Researchers Ridge (10). The modern hydrography is mainly composed of North Atlantic Deep Water (NADW), Antarctic Intermediate Water (AAIW) (core depth of 700 to 800 m), and a lesser contribution from subtropical surface wa-

ters (fig. S1) (10). Samples of interest with ages less than 25 thousand years (ky) were selected and dated precisely with isotope-dilution methods (9). Radiocarbon analyses were made on samples with U-Th ages that passed our screening criteria (10). We have calculated Δ^{14}C, $\Delta\Delta^{14}$C, and B-Atmosphere age (11) for each sample based on IntCal13 (12). The deglacial ^{14}C evolution of UCDW has been reported before, but with lower sampling resolution (13). In this study, we have filled important gaps in the earlier record and increased the number of samples from 31 to 55, allowing a comparison of ^{14}C ventilation between the Southern Ocean and EAI/DW at submillennial time scales (Fig. 1, B and D).

Holocene Δ^{14}C values of EAI/DW corals agree well with Δ^{14}C of the modern-day seawater DIC (fig. S2). Strong advection of ^{14}C-enriched NADW and relatively ^{14}C-depleted AAIW in the modern Atlantic results in increasing Δ^{14}C with depth between 1000 and 2000 m (14), which is reflected in the coral ^{14}C reconstruction (fig. S2). The deepest sample, recovered from 2800 m water depth, has a calendar age of 10.4 ky and has almost the same Δ^{14}C as that of other early Holocene samples in the EAI/DW (Fig. 1C, star).

The Δ^{14}C values of the shallow EAI/DW layers (750 to 1162 m) (Fig. 1A) decreased from ~365 per mil (‰) during the early LGM to ~−110‰ in the late Holocene, with a slightly larger offset from the contemporary atmosphere ($\Delta\Delta^{14}$C) in the glacial period (~−140‰ to −200‰ around 25 to 18 ka) than in the Holocene (~−100‰). At the end of HS1 and YD, the ^{14}C gradient between deep and shallow depths was eroded (Fig. 1C). One glacial coral has a Δ^{14}C similar to that of the contemporary atmosphere (fig. S3 and table S2). However, without more data to confirm the ^{14}C-enriched signature, we do not interpret this ^{14}C result as a signature of ventilation in the EAI/DW.

New ^{14}C data from the Drake Passage (Fig. 1, B and D) support previous findings (13) and further constrain the timing of ^{14}C evolution toward a smaller $\Delta\Delta^{14}$C during late HS1. A rapid return to a relatively ^{14}C-depleted condition during the early Bølling-Allerød (B-A) (14.6 to 12.9 ka) was followed by a second abrupt $\Delta\Delta^{14}$C increase during the YD-to-Holocene transition (Fig. 1D) (13).

Observations from nutrient proxies indicate that a strong chemical gradient existed between 2000 and 2500 m depth in the Atlantic during the LGM (15). Glacial reconstructions also show ^{14}C-depleted signatures in the deep Atlantic, thus supporting a more isolated deep ocean (16–18). However, data in the intermediate ocean are more challenging to interpret. For example, geostrophic reconstructions from the Florida Straits point to a reduced Gulf Stream (19), whereas evidence from sedimentary Pa/Th ratios suggests that glacial Atlantic upper-ocean circulation (<2000 m) was at least as strong as the modern deep overturning (20). Our ^{14}C data (Fig. 2C and fig. S4) from intermediate depths (750 to 1492 m) as well as a published record from thermocline waters (500 to 600 m) (21) indicate that the upper Equatorial Atlantic during the glacial period was filled with ^{14}C-enriched water similar to that of

[1]Bristol Isotope Group, School of Earth Sciences, University of Bristol, Bristol, UK. [2]Department of Earth and Environmental Sciences, University of St Andrews, St. Andrews, UK. [3]School of Physical Sciences, University of California, Irvine, Irvine, CA, USA.
*Corresponding author. E-mail: tc14502@bristol.ac.uk †Present address: Department of Nuclear Sciences and Applications, International Atomic Energy Agency, Monaco.

the modern era, supporting relatively strong circulation in the upper ocean. However, the ^{14}C age differences between UCDW and the shallow layer (750 to 1162 m) of EAI/DW were much larger during LGM (~800 to 1000 years) than the present (~500 years) (Fig. 2C). Mechanisms that could maintain these large glacial ^{14}C gradients might be related to water mass mixing and advection rates, as well as more extreme ^{14}C end-member compositions during the glacial period (10).

In the early HS1 (18.0 to 16.0 ka), deep sedimentary Pa/Th ratios indicate a substantial reduction in AMOC rates (5), which coincided with the initiation of the deglacial atmospheric CO_2 rise (8) as well as the decrease in atmospheric Δ^{14}C (Fig. 2, A, B, and E) (12). During this time period, the mid-depth North Atlantic and Brazil Margin (1500 to 2000 m) both saw a major decrease in benthic δ^{13}C (a measure of the ratio of stable isotopes ^{13}C:^{12}C) (22, 23), with a coincident decrease in North Atlantic [CO_3^{2-}] concentration (~1800 m) (24). These changes in the carbon chemistry of the mid-depth Atlantic may have been due to the weakened AMOC and its associated effects (such as respired carbon accumulation in mid-depth waters) rather than upwelling in the deep South Atlantic (>2500 m) (22, 23, 25). Under this scenario, an additional, well-ventilated North Atlantic water mass at shallower depths (such as <1200 m) is required to
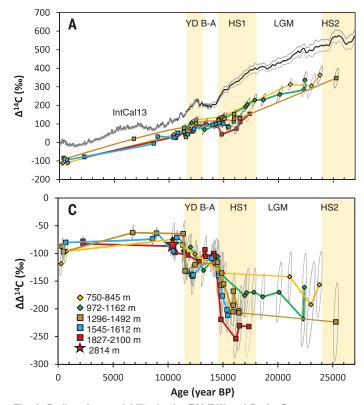
explain the early HS1 Atlantic benthic δ^{13}C and δ^{18}O (a measure of the ratio of stable isotopes ^{18}O:^{16}O) data (23). In support of this hypothesis, our ^{14}C data from 972 to 1162 m do not show any substantial decrease during the initial transition from glacial to the early HS1 (18 to 17.0 ka) (fig. S4). This result can be best explained by a persistent North Atlantic shallow overturning (26) fed by relatively ^{14}C-enriched waters from the north, as observed during the LGM. There is also no evidence in the Equatorial Atlantic for the extremely ^{14}C-depleted signals during HS1 that have been observed at other locations in intermediate waters of the Pacific, Atlantic, and Indian Oceans (27–29). Given that extremely depleted ^{14}C waters do not seem to pass through the intermediate depths of the Southern Ocean or Equatorial Atlantic (13, 21, 30), those ^{14}C depletions are likely to be regional or localized features.

In the deeper waters of the Equatorial Atlantic (1827 to 2100 m), the early part of HS1 is characterized by a decreasing Δ^{14}C trend from 17.4 to 16.2 ka (Fig. 1A). The B-atmosphere age at 17.4 ka was more than 400 ^{14}C years older than the intermediate waters (972 to 1162 m), which is in marked contrast with the Holocene (Fig. 2C) and is consistent with a reduced presence of ^{14}C-rich NADW. From the LGM to the early HS1 (Fig. 1D), the $\Delta\Delta^{14}$C of UCDW in the Drake Passage increased by ~90‰. However, by 16.6 ka this trend

was reversed, with $\Delta\Delta^{14}$C decreasing by ~80‰, which is consistent with increased mixing of ^{14}C-depleted waters from below (13) and potentially associated with a reduction in AMOC. At the same time, between 18 and 16 ka, Greenland remained cold (31), whereas Antarctic δ^{18}O indicates continuous warming under a background of increasing CO_2 forcing (Fig. 2F). These changes in the early HS1 suggest a reduced/shoaled AMOC (Fig. 2E) and a comparatively low efficiency of heat transport from the Southern to the Northern Hemisphere.

Throughout HS1, the water column of the equatorial Atlantic was characterized by low-Δ^{14}C deep waters underlying shallower, more ^{14}C-enriched waters. Although we find no evidence for enhanced ^{14}C ventilation in the 1827-to-2100-m layer, our records show that the Drake Passage records and Equatorial Atlantic mid-depth (1296 to 1612 m) waters started to shift toward a higher Δ^{14}C value as compared with that of the early HS1 (Fig. 2C). Therefore, it is unlikely that this shift was caused by upwelling of ^{14}C-enriched waters from below, but rather from increased lateral advection of a relatively well-ventilated intermediate water mass. We cannot distinguish the exact source of ventilation [for example, Northern Component Water (NCW) from the North Atlantic, Southern Component Water (SCW) from the Southern Ocean, or both] here, but the better ventilation of mid-depth waters in late HS1 is a distinct feature
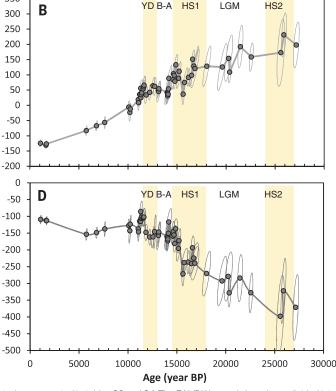

Fig. 1. Radiocarbon variability in the EAI/DW and Drake Passage reconstructed from deep-sea corals. (**A** and **B**) Reconstructed relative ^{14}C activity (Δ^{14}C) of the (A) EAI/DW and (B) Drake Passage. (**C** and **D**) The Δ^{14}C offset ($\Delta\Delta^{14}$C) of the sample from the contemporary atmosphere of (C) EAI/DW and (D) Drake Passage. Included are 2σ error ellipses reconstructed from deep-sea corals (11). Part of the Drake Passage data have been reported in (13), and the new data of this study are reported in tables S3 and S4. The EAI/DW records have been divided into five different layers according to the sample depths. The black line in (A) represents the IntCal13 (12) atmosphere radiocarbon curve (±2σ uncertainties, gray lines). The red star in (C) represents the sample from 2.8 km depth. One LGM data point from 1097 m depth is not shown because it lies directly on the atmospheric curve and has not been replicated (fig. S3). Before Present (BP) is defined as before 1950 AD.

of our records. Foraminifera Nd isotopes from the tropical Atlantic have previously highlighted a two-phase HS1 water-mass provenance shift at intermediate water depths (~1000 m) (32). In contrast, Pa/Th ratios and Nd isotopes from the deep subtropical North Atlantic (5, 33) did not show a mid HS1 shift, which is consistent with our observation that the deeper Equatorial At-

lantic remained in a poorly ¹⁴C-ventilated condition throughout HS1. Together, these results suggest that increased ¹⁴C ventilation and the potential increase in AMOC strength in the late HS1 might have been restricted to the upper ocean (such as <2000 m), whereas the abyssal Atlantic remained less affected (5, 22). This mid-HS1 shift in ¹⁴C ventilation was accompanied by

major reorganization of the atmosphere and the North Atlantic climate system (10, 31, 34, 35). At around the same time, a reversal in the early HS1 temperature decline at Northern Greenland (NGRIP) initiates Northern Hemisphere deglacial warming (Fig. 3B).

Deglacial warming in the Northern Hemisphere is characterized by two abrupt warming events of ~10°C at Northern Greenland, occurring at the HS1-to–B-A transition and YD-to-Holocene transition (31), which were synchronous with the rapid intensification of Asian monsoons (Fig. 2D) (35). During both events, CO_2 increased by ~12 ppmv (Figs. 2B and 3) (8), and two coincident abrupt resumptions of deep AMOC are indicated by sedimentary Pa/Th ratios (Fig. 3E) (5).

The two distinct centennial-scale events toward a ¹⁴C-enriched water column in both EAI/DW and the Southern Ocean (14.8 to 14.6 ka and 11.7 to 11.5 ka) (Fig. 3) provide strong support for an AMOC-related mechanism driving the abrupt increases in atmosphere CO_2 concentration (8) and Northern Hemisphere warming (31). The atmospheric CO_2 concentration increased at the same time as the ¹⁴C gradient was eroding, suggesting that CO_2 was released into the atmosphere when excess respired carbon in the deep ocean was being flushed out by newly formed, high-Δ¹⁴C NCW. Meanwhile, changes in the solubility of CO_2 may have played a role in modulating atmospheric CO_2 as deep waters became warmer (less soluble) and fresher (more soluble). In contrast, the first centennial CO_2 increase at ~16.3 ka occurred during a period of reduced AMOC and with no notable changes in North Greenland temperature (Fig. 3C). Therefore, mechanisms other than sudden AMOC changes are likely to dominate this first centennial CO_2 increase, such as a rapid shift in ocean fronts driving the degassing of CO_2 from mid-depth waters of the Southern Ocean (36).

At the beginning of the B-A and Holocene, the Drake Passage records were even more ¹⁴C-enriched than in the modern day, by some 400 to 500 ¹⁴C years at ~14.3 and ~11.3 ka, respectively (Fig. 2C and fig. S4). Each of the two high-¹⁴C peaks in the Drake Passage are well constrained by coral samples from similar depths and locations (13), adding confidence that these ¹⁴C shifts reflected changes in deep-ocean circulation. We propose that rapid and deepened advection of well-ventilated NCW homogenized the ¹⁴C composition of the water column during these two pronounced "flushing" events. The presence of NCW at abyssal depths during the B-A and Holocene is also supported by the distinctive unradiogenic Nd isotopic shift and enriched ¹⁴C signatures in the deep North Atlantic (17, 33).

A subsequent rapid return to a modern-like ¹⁴C water column after both flushing events, highlighted by the rapid decrease in Drake Passage Δ¹⁴C (Fig. 1B), adds weight to the idea of an "AMOC overshoot," a transient stronger AMOC than that of the modern ocean. This AMOC overshoot during B-A has been previously proposed in (16) on the basis of benthic ¹⁴C data, in which it was described as a transient expansion of the NADW cell and a better ventilated deep
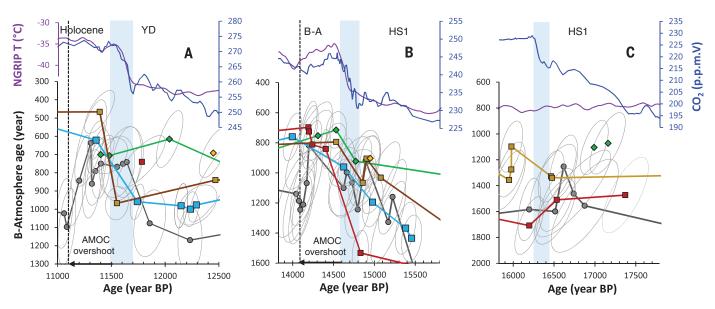

Fig. 2. Radiocarbon age variability in the EAI/DW of the past 25 ky in comparison with other climate records. (**A**) Δ¹⁴C of the atmosphere from the IntCal13 compilation (12). (**B**) New high-resolution CO_2 concentration record from the West Antarctic Ice Sheet Divide ice core (WDC) (8). (**C**) B-Atmosphere age reconstructed from ¹⁴C data of EAI/DW and Drake Passage (700 to 1800 m) (13). For clarity, the 2σ error ellipses of Drake Passage records are not shown. The green arrow illustrates the modern radiocarbon age difference between EAI/DW and the atmosphere, and the gray arrow illustrates the modern radiocarbon age difference between UCDW and the atmosphere (14). The red star represents the sample from 2.8 km depth. (**D**) δ¹⁸O (an Asian monsoon index) record from the Hulu speleothem (35, 40). (**E**) ²³¹Pa/²³⁰Th ratios (an AMOC strength index) of a subtropical North Atlantic deep sediment core (OCE326-GGC5, water depth 4550 m) (5). The age model has been revised on the basis of IntCal13 (12). (**F**) δ¹⁸O (a temperature index) record of the Northern Greenland (NGRIP) (41) and Antarctic (WDC) (8) ice cores. Gray lines in (F) represent five-point moving average. Light yellow bands indicate cold stadials, and light blue bands indicate periods of sudden centennial atmosphere CO_2 increases.

Fig. 3. Comparison of new 14C records with ice-core records during three key intervals of the last deglaciation. (**A** to **C**) Detailed comparison during (A) 11.0 to 12.5 ka, (B) 15.8 to 13.8 ka, and (C) 17.8 to 15.8 ka between B-Atmosphere ages of EAI/DW and UCDW (colors and symbols are as in Fig. 2C, with 2σ error ellipses), reconstructed temperature of North Greenland NGRIP (thin purple line) (31), and high-resolution atmosphere CO_2 concentration from WDC (thin blue line) (8). Abrupt centennial CO_2 increases are highlighted with light blue bands. Dashed lines in (A) and (B) mark the return of UCDW to reduced 14C ventilation condition. The arrows indicate periods of AMOC overshoot.

ocean as compared with the modern ocean (16, 18). In contrast to but not necessarily at odds with those studies that suggest an overshoot throughout B-A (10), our data indicate that the return to poorer ventilation of the Southern Ocean occurred within 500 years after the start of B-A (14.6 ka) and Holocene (11.5 ka) (Fig. 3, A and B). The rapid return thus suggests that the timing of decline in peak AMOC strength occurred in less than 500 years, which is more consistent with AMOC predictions from modeling studies (16, 37). These results therefore provide evidence for the existence of short-lived deep-ocean flushing events during the last deglaciation.

After the AMOC overshoot in the early B-A, the water-column structure of the EAI/DW was similar to that of the Holocene (Fig. 2C) (16, 17), providing support for the modern-like advection in the Atlantic. At the start of YD, the EAI/DW water column is characterized by high B-Atmosphere ages in the deeper layer and low B-Atmosphere ages in the shallow layer (Fig. 2C and fig. S5). However, the 14C gradient during the YD was not as large as during the early HS1, probably because the 14C-depleted water that built up over the glacial period had been largely flushed out by the start of the B-A. Although the data are not well resolved during the Holocene, we do not see any evidence for substantial change in the water column structure of the EAI/DW during this time.

The millennial-scale atmosphere CO_2 increase during YD and HS1 has been suggested to be caused by a southward shift of the westerlies, with increased upwelling in the Southern Ocean (4, 6). At the same time, reduction of AMOC would lead to a decreased efficiency of the ocean's biological pump because NCW has lower preformed nu-

trients than that of SCW (25). These oceanic processes would perturb the deep-ocean alkalinity balance and facilitate further CO_2 release on millennial scales (24). For the centennial-scale abrupt changes, the first event at 16.3 ka may have been related to a southward shift of ocean fronts in the Southern Ocean (36), with a mechanism similar to that of the millennial-scale CO_2 rise. The processes driving the latter two CO_2 rise events are likely to be very different; they were related to enhanced AMOC and increased ventilation of the deep ocean with newly formed waters, as supported by the data presented here. Although the terrestrial carbon reservoir may have contributed to carbon release at 14.6 ka (38), the in-phase relationship between EAI/DW ventilation and atmosphere CO_2 concentration supports the fundamental role of ocean carbon release during the latter two events. Therefore, mechanisms that can counteract the effect of efficient nutrient utilization of NCW (for example, in contrast with the millennial mechanism) and that are faster than the alkalinity feedback are likely to play a more important role for these events. One of those mechanisms could be an increase in the preformed nutrient content of NCW associated with a shoaled organic matter remineralization depth during abrupt warming (39), combined with a fast oceanic overturning that rapidly releases respired CO_2 into the atmosphere.

REFERENCES AND NOTES

1. P. U. Clark et al., Proc. Natl. Acad. Sci. U.S.A. **109**, E1134–E1142 (2012).
2. E. Monnin et al., Science **291**, 112–114 (2001).
3. W. S. Broecker, Paleoceanography **13**, 119–121 (1998).
4. J. R. Toggweiler, D. W. Lea, Paleoceanography **25**, PA2212 (2010).
5. J. F. McManus, R. Francois, J. M. Gherardi, L. D. Keigwin, S. Brown-Leger, Nature **428**, 834–837 (2004).
6. R. F. Anderson et al., Science **323**, 1443–1448 (2009).
7. M. A. Martínez-Botí et al., Nature **518**, 219–222 (2015).
8. S. A. Marcott et al., Nature **514**, 616–619 (2014).
9. H. Cheng, J. Adkins, R. L. Edwards, E. A. Boyle, Geochim. Cosmochim. Acta **64**, 2401–2416 (2000).
10. Materials and methods are available as supplementary materials on Science Online.
11. Δ14C is the deviation in per mil units of sample 14C activity from (preindustrial) modern atmosphere after correction for both age-integrated decay and isotope fractionation. ΔΔ14C is the Δ14C difference between sample and the contemporary atmosphere. "B-Atmosphere age" represents the 14C age difference between sample and the contemporary atmosphere.
12. P. J. Reimer et al., Radiocarbon **55**, 1869–1887 (2013).
13. A. Burke, L. F. Robinson, Science **335**, 557–561 (2012).
14. R. M. Key et al., Global Biogeochem. Cycles **18**, 4031 (2004).
15. W. B. Curry, D. W. Oppo, Paleoceanography **20**, PA1017 (2005).
16. S. Barker, G. Knorr, M. J. Vautravers, P. Diz, L. C. Skinner, Nat. Geosci. **3**, 567–571 (2010).
17. L. F. Robinson et al., Science **310**, 1469–1473 (2005).
18. L. C. Skinner, S. Fallon, C. Waelbroeck, E. Michel, S. Barker, Science **328**, 1147–1151 (2010).
19. J. Lynch-Stieglitz, W. B. Curry, N. Slowey, Nature **402**, 644–648 (1999).
20. J. Lippold et al., Nat. Geosci. **5**, 813–816 (2012).
21. C. Cléroux, P. deMenocal, T. Guilderson, Quat. Sci. Rev. **30**, 1875–1882 (2011).
22. D. C. Lund, A. C. Tessin, J. L. Hoffman, A. Schmittner, Paleoceanography **30**, 477–494 (2015).
23. D. W. Oppo, W. B. Curry, J. F. McManus, Paleoceanography **30**, 353–368 (2015).
24. J. Yu et al., Science **330**, 1084–1087 (2010).
25. A. Schmittner, D. Lund, Clim. Past **11**, 135–152 (2015).
26. L. I. Bradtmiller, J. F. McManus, L. F. Robinson, Nat. Commun. **5**, 5817 (2014).
27. T. M. Marchitto, S. J. Lehman, J. D. Ortiz, J. Flückiger, A. van Geen, Science **316**, 1456–1459 (2007).
28. D. J. R. Thornalley, S. Barker, W. S. Broecker, H. Elderfield, I. N. McCave, Science **331**, 202–205 (2011).
29. S. P. Bryan, T. M. Marchitto, S. J. Lehman, Earth Planet. Sci. Lett. **298**, 244–254 (2010).
30. R. De Pol-Holz, L. Keigwin, J. Southon, D. Hebbeln, M. Mohtadi, Nat. Geosci. **3**, 192–195 (2010).
31. C. Buizert et al., Science **345**, 1177–1180 (2014).
32. K.-F. Huang, D. W. Oppo, W. B. Curry, Earth Planet. Sci. Lett. **389**, 200–208 (2014).

33. N. L. Roberts, A. M. Piotrowski, J. F. McManus, L. D. Keigwin, *Science* **327**, 75–78 (2010).
34. W. Broecker, A. E. Putnam, *Quat. Sci. Rev.* **57**, 17–25 (2012).
35. Y.-J. Wang *et al.*, *Science* **294**, 2345–2348 (2001).
36. K. A. Allen *et al.*, *Quat. Sci. Rev.* **122**, 180–191 (2015).
37. Z. Liu *et al.*, *Science* **325**, 310–314 (2009).
38. P. Köhler, G. Knorr, E. Bard, *Nat. Commun.* **5**, 5520 (2014).
39. K. Matsumoto, *Geophys. Res. Lett.* **34**, L20605 (2007).
40. J. Southon, A. L. Noronha, H. Cheng, R. L. Edwards, Y. J. Wang, *Quat. Sci. Rev.* **33**, 32–41 (2012).
41. K. K. Andersen *et al.* North Greenland Ice Core Project members, *Nature* **431**, 147–151 (2004).

EVOLUTIONARY ECOLOGY

Functional mismatch in a bumble bee pollination mutualism under climate change

Nicole E. Miller-Struttmann,[1,2]* Jennifer C. Geib,[3] James D. Franklin,[2] Peter G. Kevan,[4] Ricardo M. Holdo,[2] Diane Ebert-May,[5] Austin M. Lynn,[2] Jessica A. Kettenbach,[2,6] Elizabeth Hedrick,[7] Candace Galen[2]

Ecological partnerships, or mutualisms, are globally widespread, sustaining agriculture and biodiversity. Mutualisms evolve through the matching of functional traits between partners, such as tongue length of pollinators and flower tube depth of plants. Long-tongued pollinators specialize on flowers with deep corolla tubes, whereas shorter-tongued pollinators generalize across tube lengths. Losses of functional guilds because of shifts in global climate may disrupt mutualisms and threaten partner species. We found that in two alpine bumble bee species, decreases in tongue length have evolved over 40 years. Co-occurring flowers have not become shallower, nor are small-flowered plants more prolific. We argue that declining floral resources because of warmer summers have favored generalist foraging, leading to a mismatch between shorter-tongued bees and the longer-tubed plants they once pollinated.

L ong-tongued bumble bees have coevolved to pollinate plants that possess elongated corolla tubes in a mutualistic relationship. Recent declines in such long-tongued bee populations suggest that historical selection regimes in these systems are changing (*1–3*), yet the mechanisms driving these declines are unclear. Spatial and temporal discrepancies with food plants, habitat destruction, and pressure from invasive competitors have been implicated (*3–6*), but the details of these declines and their causes remain unresolved.

Matching of functional morphology between partners increases benefits and reduces costs in mutualisms (*7, 8*). The match between flower tube depth and pollinator tongue length influences resource acquisition and pollination effectiveness (*9, 10*). For bees, hummingbirds, bats, moths, and flies, morphological matching increases handling efficiency on flowers (*9–14*). Thus, changes that disrupt such matching can alter plant species recruitment and the trajectory of coevolution. Although the climate change impacts on phenological and spatial overlap of mutualists are well known, the role of climate change in generating functional discrepancies between them is less understood. Using historical data, we show that reduced flower abundance in bumble bee host-plants at the landscape scale has accompanied recent warming, leading to evolutionary shifts in foraging traits of two alpine bumble bee species (*Bombus balteatus* and *B. sylvicola*). Rapid evolution of shorter tongues in these species may inform our understanding of widespread declines in long-tongued *Bombus* specialists.

We measured the change in tongue length of *B. balteatus* and *B. sylvicola* using specimens collected from 1966–1980 and 2012–2014 in the central Rocky Mountains (*15*). These two species historically comprised 95 to 99% of bumble bees at our high-altitude field sites (*16–18*). *B. balteatus* workers were collected from three geographically isolated locations: Mount Evans (39°35.033′N, 105°38.307′W), Niwot Ridge (40°3.567′N, 105° 37.000′W), and Pennsylvania Mountain (39°15.803′N, 106°8.564′W).

B. sylvicola workers were collected from Niwot Ridge and Pennsylvania Mountain. Mean tongue length has decreased 0.61% annually and 24.4% cumulatively in these taxa ($F_{1,23}$ = 17.02, P = 0.0004 and $F_{1,67}$ = 46.14, P < 0.0001) (Fig. 1 and table S1). Using archived specimens and field surveys of bumble bees and host plants, we explored four potential mechanisms for this change in tongue length: (i) decreasing body size, (ii) coevolution with floral traits, (iii) competition from subalpine invaders, and (iv) diminishing floral resources.

Temporal changes in bumble bee tongue length are not explained by plasticity in body size. When phenotypic variance in tongue length is partitioned among underlying sources, size accounts for less than 20% of variation (table S1) (*15*). Size has declined in some populations (*B. balteatus*: $F_{2,96}$ = 8.61, P = 0.0004; *B. sylvicola*: $F_{1,76}$ = 29.01, P < 0.0001) (fig. S1 and table S1) and is phenotypically correlated with tongue length [correlation coefficient (r) = 0.50 to 0.60, P < 0.005] (fig. S1) but contributes little to its reduction over time. After removing variance explained by body size, analysis of covariance shows significant temporal changes in tongue length (*B. balteatus*: $F_{1,23}$ = 17.02, P = 0.0004; *B. sylvicola*: $F_{1,67}$ = 46.14, P < 0.0001) (Fig. 1 and table S1).

Selection to track the floral traits of host plants should favor short-tongued pollinators when flowers become shallower or deep flowers less common (*9, 10*). We tested this hypothesis by comparing flower depth of herbarium specimens collected from 1960–1982 and 2012–2013 near Mount Evans and Niwot Ridge (*15*). In six species that historically provided 88% of floral resources for *B. balteatus* and *B. sylvicola* (*18*), the change in flower depth over time varied among species ($F_{6,13}$ = 9.42, P = 0.0004). Species that now have shallower flowers received few (<10%) bumble bee visits historically (fig. S2A). On Pennsylvania Mountain and Niwot Ridge, short-tubed flowers show no systematic increase in abundance [coefficient of determination (R^2) = 0.227, $t_{1,4}$ = 1.21, P = 0.294; R^2 = 0.0004, $t_{1,9}$ = –0.62, P = 0.952, respectively] (fig. S2, B and C), suggesting that recent changes in floral trait distributions are insufficient to drive tongue length adaptation in bumble bees.

Alternatively, shifts in bumble bee tongue length may reflect competition from subalpine congeners moving upward with climate change.

[1]Biological Sciences Department, Natural Sciences Building Rm NS247, SUNY College at Old Westbury, Old Westbury, NY 11568, USA. [2]Division of Biological Sciences, University of Missouri, Columbia, MO 65211, USA. [3]Department of Biology, Appalachian State University, Boone, NC 28608, USA. [4]School of Environmental Sciences, University of Guelph, Guelph, ON, Canada N1G 2W1. [5]Department of Plant Biology, Michigan State University, East Lansing, MI 48824, USA. [6]Department of Biological Sciences, Zoology Program, North Carolina State University, Raleigh, NC 27695, USA. [7]Department of Life and Physical Sciences, Lincoln University, Jefferson City, MO 65101, USA.
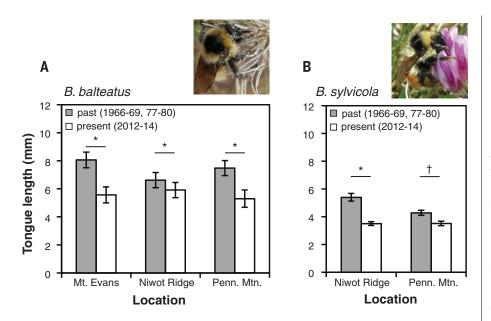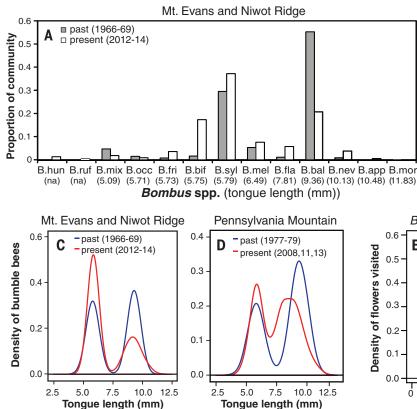*Corresponding author. E-mail: nmillstrutt@gmail.com

Fig. 1. Change in tongue length for *B. balteatus* and *B. sylvicola* on Mount Evans, Niwot Ridge, and Pennsylvania Mountain. (**A**) *B. balteatus*. (**B**) *B. sylvicola*. Bars represent least squares means ± SE. (*15*). Asterisks denote significant differences (*P* < 0.05) between means. Dagger denotes a trend (*P* < 0.06).

Comparisons of past (1960s and 1970s) (*16*, *17*) and present (2008 and 2011–2014) bumble bee communities on Pennsylvania Mountain and in the Front Range [Mount Evans and Niwot Ridge combined (*16*)] indicate increased species diversity (respectively, $\chi^2 = 293.4$, df = 7, and $\chi^2 = 579.4$, df = 12, $P < 0.001$) (Fig. 2, A and B), immigration of short-tongued species from lower altitudes, and a 24.1% decrease in the frequency of long-tongued bees (Front Range: $F_{1,1998} = 94,618$, $P < 0.0001$; Pennsylvania Mountain: $F_{1,1988} = 85.6$, $P < 0.0001$) (Fig. 2, C and D, and table S2) (*15*). With increasing competition from immigrant species, foraging breadth of resident bees should contract (*19*, *20*). Yet alpine bumble bee host choice shows the opposite trend. In 2012–2014, we resurveyed bumble bee visitation on Mount Evans and Niwot Ridge in accordance with historical observations (*18*). Despite a 10-fold difference between past (*n* = 4099 visits observed) and present (*n* = 519 visits observed) collection effort, surveys indicate that resident bumble bees have broadened their diet. Resampling historical visitation data to match present collection effort reveals that foraging breadth (Levin's niche breadth) (*15*) increased from 2.61 to 7.01 for *B. balteatus* [*z* score (*Z*) = 28.48, $P < 0.0001$] and 2.09 to 5.07
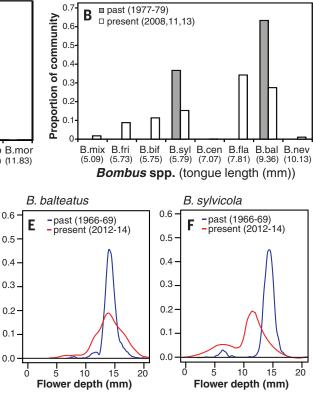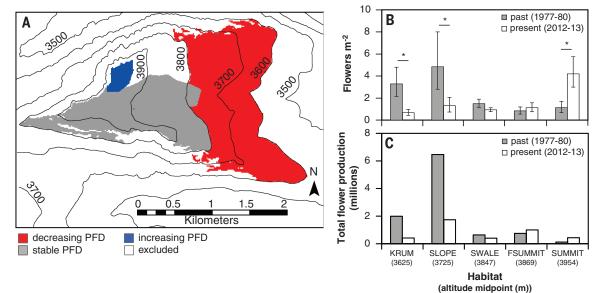

Fig. 2. Changing bumble bee community composition, bumble bee tongue length distributions, and tube depth distributions of visited flowers over time. (**A** and **B**) Bumble bee community composition. (**C** and **D**) Bumble bee tongue length. (**E** and **F**) Flower tube depth distribution. *Bombus* species abundance in alpine communities is indicated by the proportion of total foragers (*15*). Species are ordered by increasing tongue length [in (A), species' names follow (*18*)]. Bimodality of the density functions (*15*) indicates that bumble bee communities contain two predominant phenotypes, short-tongued and long-tongued [(C) and (D)]. (E) and (F) show the tube depth density functions for flowers visited by, respectively, *B. balteatus* and *B. sylvicola* in the Front Range [Mount Evans and Niwot Ridge (*15*)]. For tongue length [(C) and (D)] and tube depth [(E) and (F)], representative density functions for simulated communities (*15*) are shown.

Fig. 3. Change in flower abundance at landscape and local scales along a 400-m altitudinal gradient on Pennsylvania Mountain. (**A**) Map showing areas where PFD decreased (1.95 km²), is stable (1.29 km²), and increased (0.10 km²). Unshaded (excluded) areas contain cliff, talus, mining disturbance, and subalpine forest. (**B**) PFD (mean ± SE) for plots in krummholz (KRUM); tundra slopes (SLOPE); wet meadow (SWALE), false summit (FSUMMIT); and summit (SUMMIT) habitats ($N = 6$ species; $F_{4,385} = 5.55$, $P = 0.0002$). Asterisks indicate significant differences at $P < 0.05$. (**C**) Total flower production (in millions) is the product of total surface area for (A) each habitat (table S5) (15) and (B) mean PFD.

Fig. 4. Relative advantage of generalizing as a function of flower density and the proportion of deep flowers in the community. Outcomes with flight speed of 0.5 m s⁻¹ are shown (15). The generalist is favored when its relative advantage is >1 (pink shading).

for *B. sylvicola* ($Z = 19.78$, $P < 0.0001$). Bumble bees have added flowers with shorter and more variable tube depth to their diet (*B. balteatus*: $F_{1,1997} = 7554$, $P < 0.0001$; *B. sylvicola*: $F_{1,1997} = 64,851$, $P < 0.0001$) (Fig. 2, E and F, and table S3).

In response to warmer temperatures and drying soils, flowering has declined in alpine and arctic habitats worldwide (21–24). Optimal foraging theory predicts that foragers will expand their niche in response to such resource scarcity (25, 26). When bumble bees (*B. balteatus*) encounter low densities of preferred host plants, they incorporate shallower flowers into their diet ($F_{1,194} = 29.39$, $P < 0.0001$) (table S4) (15). The expansion of foraging breadth over time in Front Range bumble bees is congruent with this behavior (Fig. 2, E and F, and table S3). Climate

records from Niwot Ridge show warming summer minimum temperatures over the past 56 years (27). We see similar changes on Mount Evans ($R^2 = 0.383$, $t_{1,52} = 5.68$, $P < 0.0001$) and Pennsylvania Mountain ($R^2 = 0.341$, $t_{1,52} = 5.20$, $P < 0.0001$) (fig. S3, A and B), where summer minimums have increased ~2°C since 1960. We used a nonlinear model to characterize the relationship between peak flower density (PFD; flowers per square meter) and summer minimum temperature. For four bumble bee host species monitored in 6 years between 1977 and 2014 (15), average PFD on Pennsylvania Mountain rose as minimum summer temperature increased from 1.8°C to 3.25°C but declined above this value (quadratic $R^2 = 0.19$, $t_{1,17} = -2.18$, $P = 0.040$) (fig. S3C) (15). Temperatures that are associated with reduced flowering (greater than

3.25°C) have become more frequent, occurring on Pennsylvania Mountain in only 12% of years from 1960 to 1985 but 48% of years since 1985 ($\chi^2 = 8.19$, df = 1, $P < 0.0041$) (fig. S3B).

On Pennsylvania Mountain, alpine bumble bees forage over hundreds of meters to provision their nests (28). To ask how warming has affected floral resources at this scale, we measured PFD of six bumble bee host plants from 1977–1980 and 2012–2014 in five habitats along a 400-m altitudinal span (table S5). Land surface area decreases with altitude above tree line in the Rocky Mountains (29), declining by more than an order of magnitude on Pennsylvania Mountain, where 58% of habitable terrain is found below 3800 m and only 4% above 3938 m on the summit (Fig. 3A and table S5). Because bumble bees forage across the 400-m altitudinal range (28), we evaluated the temporal change in flower production at this landscape scale. For each habitat, we multiplied PFD (flowers per square meter) within sampling plots by surface area (square meters) to estimate of total flower production (15). PFD fell by 73 to 80% within krummholz and slope habitats below 3800 m, which occupy 1.95 km². Conversely, PFD increased by 75% in 0.10 km² of summit habitat ($F_{4,385} = 5.55$, $P = 0.0002$) (fig. 3B and table S6). Because declines in flowering occurred at low altitude, they affected the majority of the mountain landscape; in these extensive habitats, millions of flowers were lost. Thus, even with gains of a few thousand flowers on the summit, total food resources for alpine bumble bees on Pennsylvania Mountain have fallen by 60% since the 1970s (Fig. 3C).

Alpine regions are considered "canaries in the coal mine" for their sensitivity to global warming (29). Using a simple model adapted from (26), we tested whether reduced flowering in other ecosystems could drive the evolution of pollinator

foraging traits as indicated for alpine bumble bees (*15*). The model predicts changes in the energetic advantage of generalization with floral density. Long-tongued bumble bees exhibit greater specialization than that of short-tongued bees (*16*, *30*). Across a range of flight speed and plant community composition (*15*), the advantage of generalizing increases as flower density declines (Fig. 4). Theoretical and empirical studies alike suggest that with lower floral resources, fitness advantages of long-tongued specialist phenotypes have diminished, potentially driving the rapid evolution of shorter-tongued bees. We have documented decreases in bumble bee tongue length within species and communities on three peaks in the Rocky Mountains. Our analyses suggest that reduced flower density at the landscape scale is driving this shift in tongue length. Although populations of long-tongued bees are undergoing widespread decline (*1*, *3*), shifts foraging strategies may allow alpine bumble bees to cope with environmental change. We see broader bumble bee foraging niches, immigration by short-tongued bumble bees, and shorter tongue length within resident bee populations as floral resources have dwindled. In remote mountain habitats—largely isolated from habitat destruction, toxins, and pathogens (*31*)—evolution is helping wild bees keep pace with climate change.

REFERENCES AND NOTES

1. S. A. Cameron *et al.*, *Proc. Natl. Acad. Sci. U.S.A.* **108**, 662–667 (2011).
2. E. F. Ploquin, J. M. Herrera, J. R. Obeso, *Oecologia* **173**, 1649–1660 (2013).
3. R. Bommarco, O. Lundin, H. G. Smith, M. Rundlöf, *Proc. Biol. Sci.* **279**, 309–315 (2012).
4. J. C. Biesmeijer *et al.*, *Science* **313**, 351–354 (2006).
5. J. C. Grixti, L. T. Wong, S. A. Cameron, C. Favret, *Biol. Conserv.* **142**, 75–84 (2009).
6. C. Matsumura, J. Yokoyama, I. Washitani, *Glob. Environ. Res.* **8**, 51–66 (2004).
7. M. Stang, P. G. L. Klinkhamer, N. M. Waser, I. Stang, E. van der Meijden, *Ann. Bot. (Lond.)* **103**, 1459–1469 (2009).
8. D. P. Vázquez, N. Blüthgen, L. Cagnolo, N. P. Chacoff, *Ann. Bot. (Lond.)* **103**, 1445–1457 (2009).
9. M. A. Rodríguez-Gironés, A. L. Llandres, *PLOS ONE* **3**, e2992 (2008).
10. L. D. Harder, *Oecologia* **57**, 274–280 (1983).
11. N. Muchhala, J. D. Thomson, *Proc. R. Soc. Biol. Sci.* **276**, 2147–2152 (2009).
12. V. Grant, E. J. Temeles, *Proc. Natl. Acad. Sci. U.S.A.* **89**, 9400–9404 (1992).
13. R. B. Miller, *Evolution* **35**, 763–774 (1981).
14. F. S. Gilbert, *Ecol. Entomol.* **6**, 245–262 (1981).
15. Materials and methods are available as supplementary materials on *Science* Online.
16. N. E. Miller-Struttmann, C. Galen, *Oecologia* **176**, 1033–1045 (2014).
17. P. A. Byron, thesis, University of Colorado, Boulder (1980).
18. L. W. Macior, *Melandaria* **15**, 1–59 (1974).
19. R. MacArthur, R. Levins, *Am. Nat.* **101**, 377–385 (1967).
20. D. W. Inouye, *Ecology* **59**, 672–678 (1978).
21. C. W. Kopp, E. E. Cleland, *J. Veg. Sci.* **25**, 135–146 (2014).
22. A. J. Miller-Rushing, D. W. Inouye, *Am. J. Bot.* **96**, 1821–1829 (2009).
23. T. T. Høye, E. Post, N. M. Schmidt, K. Trojelsgaard, M. C. Forchhammer, *Nat. Clim. Change* **3**, 759–763 (2013).
24. D. W. Inouye, *Ecology* **89**, 353–362 (2008).
25. C. Fontaine, C. L. Collin, I. Dajoz, *J. Ecol.* **96**, 1002–1010 (2008).
26. C. J. Essenberg, *Am. Nat.* **180**, 153–166 (2012).
27. C. R. McGuire, C. R. Nufio, M. D. Bowers, R. P. Guralnick, *PLOS ONE* **7**, e44370 (2012).
28. J. C. Geib, J. P. Strange, C. Galen, *Ecol. Appl.* **25**, 768–778 (2015).
29. P. R. Elsen, M. W. Tingley, *Nat. Clim. Change* **5**, 772–776 (2015).
30. G. H. Pyke, D. W. Inouye, J. D. Thomson, *Environ. Entomol.* **41**, 1332–1349 (2012).
31. D. Goulson, E. Nicholls, C. Botías, E. L. Rotheray, *Science* **347**, 1255957 (2015).

MITOCHONDRIAL IMPORT

Molecular architecture of the active mitochondrial protein gate

Takuya Shiota,[1,2] Kenichiro Imai,[3] Jian Qiu,[4]* Victoria L. Hewitt,[1]† Khershing Tan,[1] Hsin-Hui Shen,[1] Noriyuki Sakiyama,[3]‡ Yoshinori Fukasawa,[3] Sikander Hayat,[5]§ Megumi Kamiya,[2] Arne Elofsson,[5] Kentaro Tomii,[3] Paul Horton,[3] Nils Wiedemann,[4,6] Nikolaus Pfanner,[4,6] Trevor Lithgow,[1]|| Toshiya Endo[2,7]||
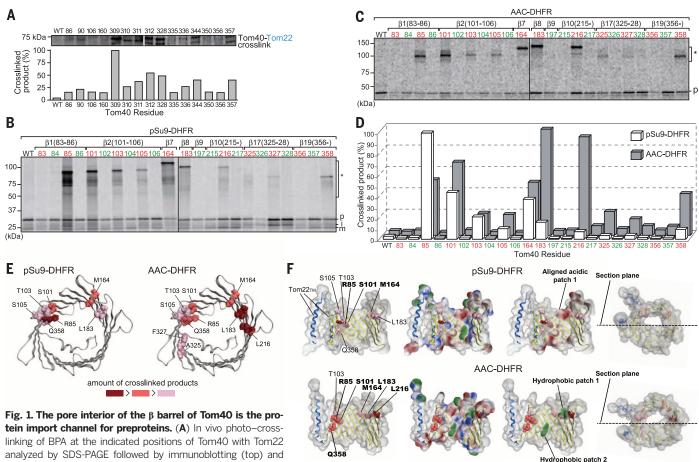
Mitochondria fulfill central functions in cellular energetics, metabolism, and signaling. The outer membrane translocator complex (the TOM complex) imports most mitochondrial proteins, but its architecture is unknown. Using a cross-linking approach, we mapped the active translocator down to single amino acid residues, revealing different transport paths for preproteins through the Tom40 channel. An N-terminal segment of Tom40 passes from the cytosol through the channel to recruit chaperones from the intermembrane space that guide the transfer of hydrophobic preproteins. The translocator contains three Tom40 β-barrel channels sandwiched between a central α-helical Tom22 receptor cluster and external regulatory Tom proteins. The preprotein-translocating trimeric complex exchanges with a dimeric isoform to assemble new TOM complexes. Dynamic coupling of α-helical receptors, β-barrel channels, and chaperones generates a versatile machinery that transports about 1000 different proteins.

Mitochondria are pivotal for cellular adenosine triphosphate (ATP) production, numerous metabolic pathways and regulatory processes, and programmed cell death. Most mitochondrial proteins are synthesized as preproteins in the cytosol and are imported into mitochondria. Preproteins either contain N-terminal targeting sequences (presequences) or internal targeting information in the mature part (*1–3*). The protein translocator of the outer membrane (the TOM complex) functions as the main entry gate of mitochondria (*1–3*). Over 90% of all mitochondrial proteins are imported by the TOM complex, followed by transfer to distinct translocators for individual classes of preproteins. Whereas all structurally known membrane protein complexes consist of either α-helical or β-barrel proteins, the TOM complex is composed of both α-helical and β-barrel integral membrane proteins. The complex consists of the channel-forming β-barrel protein Tom40 and six other subunits, each containing single α-helical transmembrane (TM) segments: the receptor proteins Tom20, Tom22, and Tom70 and the regulatory small Tom proteins (*1–3*). The molecular architecture of the complex has not been elucidated. How α-helical and β-barrel membrane proteins can be combined into a functional

[1]Biomedicine Discovery Institute and Department of Microbiology, Monash University, Melbourne, Victoria 3800, Australia. [2]Department of Chemistry, Graduate School of Science, Nagoya University, Chikusa-ku, Nagoya 464-8602, Japan. [3]Biotechnology Research Institute for Drug Discovery, National Institute of Advanced Industrial Science and Technology, 2-4-7 Aomi, Koto-ku, Tokyo 135-0064, Japan. [4]Institut für Biochemie und Molekularbiologie, Universität Freiburg, 79104 Freiburg, Germany. [5]Department of Biochemistry and Biophysics and Science for Life Laboratory, Stockholm University, Box 1031, 17121 Solna, Sweden. [6]Centre for Biological Signalling Studies, Universität Freiburg, 79104 Freiburg, Germany. [7]Faculty of Life Sciences, Kyoto Sangyo University, Kamigamo-motoyama, Kita-ku, Kyoto 603-8555, Japan.
*Present address: Swiss Federal Institute of Technology, 1015 Lausanne, Switzerland. †Present address: Department of Biomedical Science, The University of Sheffield, Sheffield S10 2TN, UK. ‡Present address: Biomedical Department Cloud Services Division, IT Infrastructure Services Unit, Mitsui Knowledge Industry Company, 2-5-1 Atago, Minato-ku, Tokyo 105-6215, Japan. §Present address: Computational Biology Program, Memorial Sloan-Kettering Cancer Center, New York, NY, USA.
||Corresponding author. E-mail: trevor.lithgow@monash.edu (T.L.); tendo@cc.kyoto-su.ac.jp (T.E.)

Fig. 1. The pore interior of the β barrel of Tom40 is the protein import channel for preproteins. (**A**) In vivo photo–cross-linking of BPA at the indicated positions of Tom40 with Tom22 analyzed by SDS-PAGE followed by immunoblotting (top) and quantification (bottom). (**B** and **C**) [³⁵S]pSu9-DHFR (Su9 presequence fused to dihydrofolate reductase) (B) or [³⁵S]AAC-DHFR (ADP-ATP carrier fused to DHFR) (C) was incubated with mitochondria [pretreated with valinomycin for (B)] with BPA-bearing Tom40 at 4°C (B) or 25°C in the presence of 1 μM methotrexate and 1 mM NADPH (C), for 10 min, and UV-irradiated. Affinity-purified cross-linked products (asterisk) were subjected to SDS-PAGE and radioimaging. Variation in the apparent molecular weight of the cross-linked products may reflect different configurations. β-strand numbers and BPA positions (red and green, side chain facing the pore interior or membrane, respectively) are indicated. The cross-links of the

neighboring residues 356 (weak) and 357 (strong) with Tom22 may suggest imperfections in the last β strand 19 around this position. p, precursor form; i, processing intermediate form; m, processed mature form. (**D**) Quantification of the cross-linked products in (B) and (C). (**E**) The side chains of the Tom40 residues cross-linked to pSu9-DHFR or AAC-DHFR are shown with color reflecting the amount of cross-linked products detected. (**F**) The acidic patches (red) and hydrophobic patches (green) are shown in the pore interior of Tom40, in relation to the position of Tom22_TM (Fig. 4, inset).

complex and how diverse classes of preproteins can be transported by the same TM channel is unclear.

To define the architecture of the functional TOM complex, we mapped the interactions of Tom40 with preproteins in transit and α-helical subunits by in vivo and in organello site-specific cross-linking. Photoactivatable *p*-benzoylphenylalanine (BPA) was introduced at 108 different positions in the 387-residue Tom40 in yeast cells (fig. S1) (*4–6*). A structural model based on homology and cysteine scanning shows 19 antiparallel β strands with the first and last β strands annealing in parallel arrangement (*7–9*) (fig. S2A). In TM β strands, every second residue faces the pore lumen, and alternate residues face outward. BPA cross-linking to Tom22 revealed outward orientation of side chains (Fig. 1A and fig. S1). Whether preproteins transit through the lumen of the Tom40 β barrel or via the interstitial space between multiple β barrels that make up the TOM complex has been con-

troversial (*10, 11*). To resolve this, we accumulated the model preproteins presequence of subunit 9-dihydrofolate reductase (pSu9-DHFR) and ADP-ATP carrier (AAC)–DHFR without a presequence, in the TOM complex (*10, 12, 13*) and irradiated it with ultraviolet (UV) light. Residues cross-linked to pSu9 and AAC were only found at positions facing the pore interior (Fig. 1, B to D; red residues face the pore). Similar results were obtained by sulfhydryl group (SH)–directed chemical cross-linking (fig. S2B). Thus, preproteins in transit are located inside the β-barrel pore of Tom40 and not in the interstitial space between Tom40 molecules.
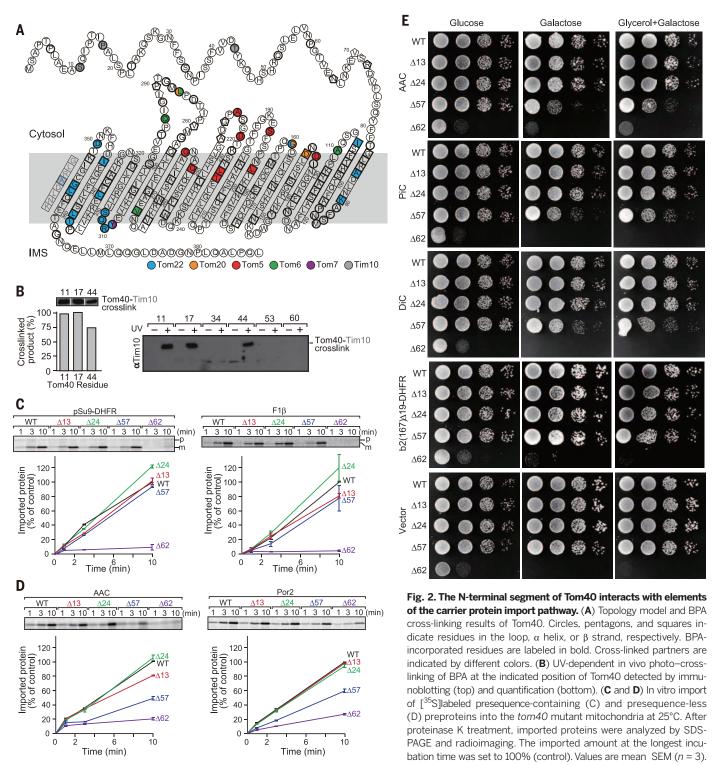
Do presequence-containing and carrier-family preproteins use the same path through the Tom40 channel? The cross-linking results revealed a nonidentical pattern for pSu9-DHFR and AAC-DHFR (Fig. 1, D and E, and fig. S2C). Negatively charged residues are aligned in the pore from the cytosolic side to the intermembrane space (IMS) side,

forming acidic patches near the cross-linked sites for pSu9-DHFR (red in Fig. 1F and fig. S3), whereas hydrophobic patches (green) are near the cross-linked sites for AAC-DHFR and partly for pSu9-DHFR [presequences form positively charged amphiphilic helices (*1–3*)]. Homology models for animal and plant Tom40 indicate similar acidic and hydrophobic patches inside the channel pore (fig. S4). We conclude that positively charged presequences follow an acidic path on the inner wall of the Tom40 pore, whereas carrier proteins interact with mostly hydrophobic residues. Thus, Tom40 can handle and chaperone (*14*) diverse classes of preproteins by providing distinct translocation paths.

Systematic analysis of the cross-linking partners of BPA-bearing Tom40 revealed that α-helical Tom proteins interact with the outside of the β barrel or loops of Tom40 (Fig. 2A and fig. S1). Unexpectedly, the IMS protein Tim10 was cross-linked to the N-terminal segment of Tom40 (Fig.

2, A and B), suggesting that this segment extends from the cytosolic side through the β-barrel pore of Tom40 to the IMS (8). We generated yeast mutants with N-terminal truncations of Tom40 and found that, whereas a 62-residue deletion (*tom40Δ62*) inhibited import of both presequence-containing and presequence-less preproteins, a 57-residue deletion selectively inhibited import of presequence-less preproteins (Fig. 2, C and D, and fig. S5). The *tom40Δ57* yeast strain became sensitive to overexpression of carrier proteins, not of a presequence-containing preprotein, being un-able to cope with the increased load of hydrophobic preproteins (Fig. 2E). Tim10 is a subunit of the hexameric Tim9-Tim10 (small TIM) chaperone in the IMS, functioning to guide presequence-less preproteins through the aqueous IMS (1–3). We thus conclude that the recruitment of these

Fig. 2. The N-terminal segment of Tom40 interacts with elements of the carrier protein import pathway. (**A**) Topology model and BPA cross-linking results of Tom40. Circles, pentagons, and squares indicate residues in the loop, α helix, or β strand, respectively. BPA-incorporated residues are labeled in bold. Cross-linked partners are indicated by different colors. (**B**) UV-dependent in vivo photo–cross-linking of BPA at the indicated position of Tom40 detected by immunoblotting (top) and quantification (bottom). (**C** and **D**) In vitro import of [^{35}S]labeled presequence-containing (C) and presequence-less (D) preproteins into the *tom40* mutant mitochondria at 25°C. After proteinase K treatment, imported proteins were analyzed by SDS-PAGE and radioimaging. The imported amount at the longest incubation time was set to 100% (control). Values are mean SEM (n = 3). (**E**) Serial dilutions of the Tom40 N-terminal truncation mutant cells with overexpression of the indicated proteins were spotted on SCD (-Ura, -Trp) (glucose), SCGal (-Ura, -Trp) (galactose), and SCGly + 0.05% D-glucose (-Ura, -Trp) (glycerol + galactose) media and grown at 30°C for 3 days (glucose and galactose) or 4 days (glycerol + galactose). WT, corresponding TOM40-(His)$_{10}$ strain; PiC, phosphate carrier; DiC, dicarboxylate carrier.

chaperones to the TOM channel exit promotes an efficient transfer of hydrophobic preproteins.

To define the subunit organization within the TOM complex, we probed the interactions of the Tom40 molecule with Tom40 itself and with the core receptor Tom22. We asked whether Tom40 molecules are close enough to make direct contact with each other, like bacterial β-barrel proteins (15), by chemical cross-linking with the SH-directed homobifunctional cross-linkers BMB or M2M. We introduced Cys at membrane-facing

positions as well as pore-facing positions of a Cys-free Tom40 variant (8). Cross-linked products were evident for the pairs of membrane-facing Cys residues in endogenous Tom40 (Fig. 3A) or imported Tom40 (fig. S6A). The distances between the Sγ atoms of cross-linked Cys are ~6.9 and ~12.0 Å for M2M and BMB cross-linking, respectively (16), indicating that two Tom40 molecules are located within a distance of ~6.9 Å (Fig. 3B).

Because the TM helix of Tom22 (Tom22$_{TM}$) interacts with two Tom40 molecules (17), we an-

alyzed the geometrical arrangement of Tom22 and Tom40. We introduced BPA into Tom40 at two of the positions 86, 309, 350, and 357 in the narrow vertical Tom22-interacting regions along the β-barrel axis (Fig. 3C and fig. S6B) simultaneously. UV irradiation generated cross-linked Tom40:[Tom22]$_2$ oligomers for BPA positions 86 and 309 (fig. S6B). Simultaneous introduction of BPA into Tom40 and Tom22 in their interacting regions (Fig. 3, C and D), generated cross-linked Tom40:[Tom22]$_2$ and [Tom40]$_2$:Tom22
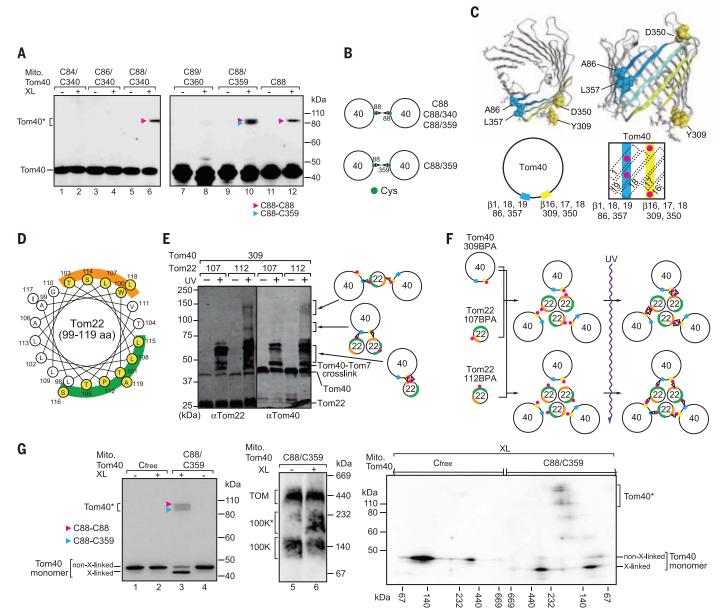
Fig. 3. The native TOM complex dynamically exchanges with the Tom40 dimeric complex. (**A**) Mitochondria with the indicated Tom40 Cys residues were treated with (+) or without (−) the cross-linker (1,4-bismaleimidobutane) [BMB (XL)]. Proteins were analyzed by SDS-PAGE and immunoblotting with antibodies to Tom40. Cross-linked products are indicated by the asterisk and arrowheads. (**B**) Schematic models for (A). (**C**) (Top) The Tom40 β barrel showing the residues cross-linked with Tom22. (Botom) Tom22-interacting regions of Tom40 (blue and yellow) with the Tom22-cross-linked residues

(pink circles). (**D**) Tom40-interacting regions of Tom22$_{TM}$ (orange and green) (18). (**E**) In vivo cross-linking of BPA in Tom40 and Tom22 was detected by immunoblotting. Cross-linked products are indicated. (**F**) Schematic models for (E). (**G**) Mitochondria with the Tom40 Cys mutations were treated with (+) or without (−) the cross-linker BMOE [bis(maleimido)ethane]. Proteins were analyzed by SDS-PAGE (lanes 1 to 4), BN-PAGE (lanes 5 and 6), or 2D-PAGE (first- BN-PAGE and second-dimensional SDS-PAGE) and immunoblotting. Cross-linked products are indicated by the asterisk and arrowheads.
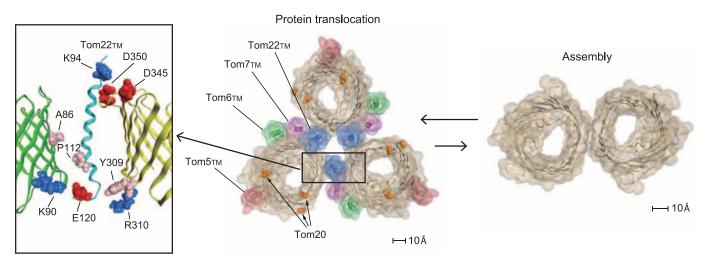
Fig. 4. Subunit organization of the TOM complex. Subunit arrangement of the Tom40 β barrel and TM α helices of Tom5, Tom6, Tom7, and Tom22, based on the BPA cross-linking results and the proposed model for the exchange of the Tom40-Tom22 trimeric complex with the Tom40 dimer. The inset shows possible interactions between Tom22$_{TM}$ and the Tom40 β barrel, with key residues suggested from fig. S8. Basic residues, acidic residues, and others are colored in blue, red, and pink, respectively. The Tom22$_{TM}$ α helix, possibly bent at Pro^{112}, tethers two Tom40 molecules through the interactions of its N-terminal and C-terminal parts with conserved residues of adjacent Tom40 molecules.

oligomers only for a specific combination of introduced BPA (Fig. 3E). These results pose a geometrical constraint that is consistent only with a threefold rotational symmetric arrangement of three molecules each of Tom40 and Tom22 (Fig. 3F), in which the distance between the Tom40 molecules bridged by Tom22 must be larger than 22 Å, which is incompatible with a distance of ~6.9 Å between the Tom40 molecules (fig. S6A).

How can the opposing cross-linking results be explained? We hypothesized that both dimeric and trimeric isoforms of TOM complexes, previously observed by single-particle electron microscopy analyses (*18–20*), exist in organello. Tom40 Cys mutant mitochondria were subjected to cross-linking and analyzed by SDS–polyacrylamide gel electrophoresis (PAGE) and blue native (BN)–PAGE (Fig. 3G). SDS-PAGE demonstrated the cross-linked dimers, and BN-PAGE revealed that the cross-linked Tom40 dimers arose from a ~100-kD (100K) subcomplex, not from the mature (large) TOM complex. The two Tom40 molecules are thus close together, bridged by short chemical cross-linkers only in the 100K complex (Fig. 3B). The 100K complex contains Tom40 and small Tom proteins, but not Tom22; it functions as a late assembly intermediate of newly imported Tom40 on the pathway to the mature TOM complex (*17, 21*). Thus, the 100K complex containing the dimer exchanges with the mature trimeric TOM complex. A dynamic exchange between dimeric and trimeric forms provides the means for template-driven assembly of new subunits through their exchange for old subunits.

The Tom22$_{TM}$ has been conserved through evolution, with an invariant Pro (Pro^{112}), flanked by basic residues on the cytosolic side and acidic residues on the IMS side (fig. S7). We generated yeast strains with mutant Tom22 and analyzed destabilization of the TOM complex and in vitro import of presequence-containing and presequence-

less preproteins by amino acid replacements of those residues (fig. S8). These analyses suggest that the full-sized mature TOM complex tethered by Tom22 (Fig. 4, inset) is required for efficient preprotein import. We also determined the interactions of Tom40 with the receptor Tom20 and the small subunits Tom5, Tom6, and Tom7 (summarized in Fig. 2A and figs. S1 and S9). A complete model of the subunit arrangement in the TOM core complex is shown in Fig. 4 (middle panel).

We conclude that the trimeric mature TOM complex dynamically exchanges with a dimeric Tom22-free form that provides an assembly platform for the integration of new subunits (Fig. 4, right panel). The dynamic α/β organization of the TOM complex favors both assembly of the complex and cooperative preprotein transfer from receptors to the import channel and IMS chaperones, ensuring the efficient translocation of different classes of preproteins into mitochondria.

REFERENCES AND NOTES

1. A. Chacinska, C. M. Koehler, D. Milenkovic, T. Lithgow, N. Pfanner, *Cell* **138**, 628–644 (2009).
2. W. Neupert, J. M. Herrmann, *Annu. Rev. Biochem.* **76**, 723–749 (2007).
3. T. Endo, K. Yamano, *Biol. Chem.* **390**, 723–730 (2009).
4. T. Shiota, S. Nishikawa, T. Endo, *Methods Mol. Biol.* **1033**, 207–217 (2013).
5. S. Chen, P. G. Schultz, A. Brock, *J. Mol. Biol.* **371**, 112–122 (2007).
6. J. W. Chin et al., *Science* **301**, 964–967 (2003).
7. R. Ujwal et al., *Proc. Natl. Acad. Sci. U.S.A.* **105**, 17742–17747 (2008).
8. J. Qiu et al., *Cell* **154**, 596–608 (2013).
9. S. W. Lackey et al., *J. Biol. Chem.* **289**, 21640–21650 (2014).
10. M. Harner, W. Neupert, M. Deponte, *EMBO J.* **30**, 3232–3241 (2011).
11. D. Rapaport, *J. Cell Biol.* **171**, 419–423 (2005).
12. T. Kanamori et al., *Proc. Natl. Acad. Sci. U.S.A.* **96**, 3634–3639 (1999).
13. N. Wiedemann, N. Pfanner, M. T. Ryan, *EMBO J.* **20**, 951–960 (2001).
14. M. Esaki et al., *Nat. Struct. Biol.* **10**, 988–994 (2003).
15. G. Meng, R. Fronzes, V. Chandran, H. Remaut, G. Waksman, *Mol. Membr. Biol.* **26**, 136–145 (2009).
16. N. S. Green, E. Reisler, K. N. Houk, *Protein Sci.* **10**, 1293–1304 (2001).
17. T. Shiota, H. Mabuchi, S. Tanaka-Yamano, K. Yamano, T. Endo, *Proc. Natl. Acad. Sci. U.S.A.* **108**, 15179–15183 (2011).
18. K. P. Künkele et al., *Cell* **93**, 1009–1019 (1998).
19. U. Ahting et al., *J. Cell Biol.* **147**, 959–968 (1999).
20. K. Model, C. Meisinger, W. Kühlbrandt, *J. Mol. Biol.* **383**, 1049–1057 (2008).
21. K. Model et al., *Nat. Struct. Biol.* **8**, 361–370 (2001).

TRANSPOSONS

Arrested replication forks guide retrotransposon integration

Jake Z. Jacobs, Jesus D. Rosado-Lugo, Susanne Cranz-Mileva, Keith M. Ciccaglione, Vincent Tournier, Mikel Zaratiegui*

Long terminal repeat (LTR) retrotransposons are an abundant class of genomic parasites that replicate by insertion of new copies into the host genome. Fungal LTR retrotransposons prevent mutagenic insertions through diverse targeting mechanisms that avoid coding sequences, but conserved principles guiding their target site selection have not been established. Here, we show that insertion of the fission yeast LTR retrotransposon Tf1 is guided by the DNA binding protein Sap1 and that the efficiency and location of the targeting depend on the activity of Sap1 as a replication fork barrier. We propose that Sap1 and the fork arrest it causes guide insertion of Tf1 by tethering the integration complex to target sites.

Retrotransposons are mobile genetic elements that replicate through an RNA intermediate that is reverse transcribed into a cDNA capable of insertion elsewhere in the genome. By virtue of this amplifying mechanism, retrotransposons constitute large portions of many eukaryotic genomes and have a critical influence on their evolution (1). Fungal LTR retrotransposons minimize their mutagenic potential by carefully selecting integration sites away from protein coding sequences (2). The different families of LTR retrotransposons employ a variety of strategies for this target site selection, but current models posit tethering interactions between retrotransposon proteins and host DNA binding factors.

The fission yeast genome shows signs of ancient and persistent colonization by the LTR retrotransposons Tf1 and Tf2, members of the Metaviridae/Ty3-gypsy–like group of transposable elements (3). Both Tf1 and Tf2 exhibit a preference for insertion into promoters of RNA polymerase (Pol) II–transcribed genes (4, 5) coinciding with the nucleosome-free region (NFR) that usually precedes the transcription start site. The main determinant of NFR presence in fission yeast promoters is Sap1 (6), which binds DNA as homopolymers to clusters of a 5– base pair (bp) sequence motif (7, 8). To determine whether Sap1 binding coincided with transposition hotspots, we performed high-throughput sequencing of transposon–host genome junctions in cultures overexpressing a genetically marked Tf1 transposon (4). Genome-wide correlation analysis shows a strong association of Sap1 enrichment (9) with insertion sites (Fig. 1, A and B, and fig. S1a). Sap1 is strongly enriched at the previously described Tf1 hotspots, such as the promoters of class II genes (Fig. 1A and fig. S1b). Peaks of significant Sap1 enrichment [MACS (10)] account for 63.1% of transposition

Department of Molecular Biology and Biochemistry, Rutgers, The State University of New Jersey, Nelson A133, 604 Allison Road, Piscataway, NJ 08854, USA.
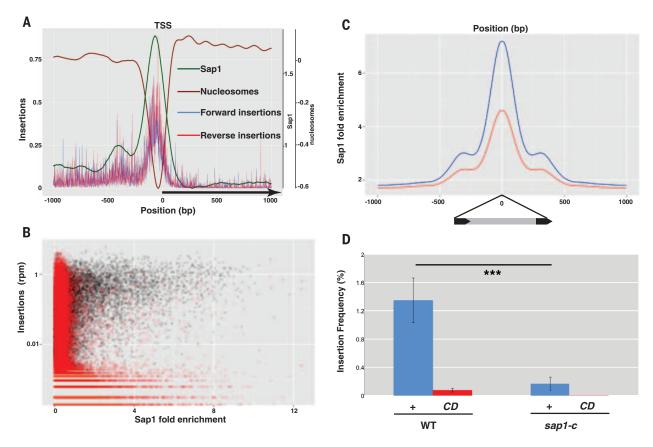*Corresponding author. E-mail: zaratiegui@dls.rutgers.edu

Fig. 1. Tf1 transposition into Sap1 binding regions. (**A**) Sap1, nucleosome positioning, and average insertion number in reads per million (rpm) at type II genes aligned at the transcription start site (TSS). (**B**) Genome-wide correlation between transposition (insertion number, rpm) and Sap1 binding in 500-bp windows. Black: genomic windows; red: randomized value pairs. (**C**) WT Sap1 enrichment around WT insertions (blue) and *sap1-c* insertions (red). (**D**) Transposition frequency in WT and *sap1-c* mutant of integrase + (+) and catalytic dead (CD) Tf1. Error bars represent SDs and asterisks depict statistically significant differences (***P < 0.001).

points, while covering only 5.1% of the host genome, and contain more efficient insertion points than the rest of the genome (fig. S1c). Logistic regression analysis revealed that Sap1 binding is a strong predictor of insertion position [area under the curve (AUC) – 0.5^{WT} = 0.217; fig. S2, a and b]. However, correlation between Sap1 fold enrichment and number of insertion points, though significant (Spearman's rho = 0.70, $P = 1 \times 10^{-10}$), shows a wide variability beyond the threshold of significant enrichment (fig. S1, a and b), suggesting that Sap1 binding is not the only factor affecting target site competence. Insertion points coincide precisely with a maximum of Sap1 enrichment (9), strongly indicating that Sap1 determines Tf1 target site selection (Fig. 1C). To investigate the involvement of Sap1 in Tf1 transposition, we performed high-throughput insertion analysis in a *sap1* mutant with a lower affinity for DNA (*sap1-c*) (9). *sap1-c* mutants exhibited a markedly reduced

transposition frequency (*t* test, $P < 0.001$, $n = 21$; Fig. 1D). Additionally, the strong association of insertion points with Sap1 was decreased (Fig. 1C), the portion of insertions in Sap1-enriched regions fell to 49.9%, and the accuracy of Sap1 binding as a predictor of insertion dropped (AUC – 0.5^{sap1-c} = 0.097, fig. S2a), indicating that transpositions are dispersed away from Sap1 binding peaks. The *sap1-c* background showed no defects in cDNA processing or altered levels of integrase, suggesting that the transposition defect is due to impaired integration (fig. S3). Together, these data show that Sap1 is a major determinant of Tf1 insertion target site selection.

Sap1 is essential for maintaining genome integrity during DNA replication (11). It has a demonstrated role in forming directional replication fork barriers (RFBs) (12, 13). We plotted Tf1 insertion density around Sap1 binding motifs, taking into account their orientation (Fig. 2A). Insertions

were enriched around Sap1 binding motifs, (Fig. 2B), indicating that Sap1 binding directs transposition but protects its footprint. Notably, most insertion events occurred 3′ of the Sap1 binding motif [Wilcoxon signed rank test (5, 99 < mu <7, 99), 95% confidence interval, $P < 2 \times 10^{-16}$, $n = 888$], displaying a prominent periodicity of peaks (Fig. 2B and fig. S4). Sap1-dependent RFBs have been shown to cause fork arrest on this side of the motif (8, 9, 12). Moreover, in both known Sap1-dependent RFBs, the replication terminator Ter1 located at ribosomal DNA (rDNA) (12, 13) and the solo LTR interspersed in the genome (9), most insertions occurred on the blocking side of the Sap1 barrier, suggesting that the RFB influences site selection (Fig. 2, C and D). Consistently, Tf1 insertion hotspots and Sap1 binding regions coincide with domains of phosphorylated histone H2A (γH2A) deposition and with DNA Pol ε (Cdc20) maxima in undisturbed S phase, both of which
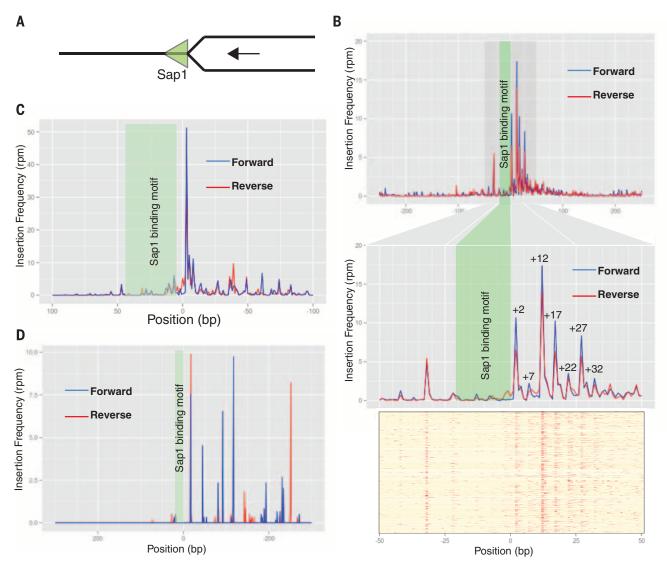

Fig. 2. Insertion profile around Sap1 binding motifs. (**A**) Sap1 binding motifs are oriented as blocking replication forks advancing in the right-to-left orientation. (**B**) Averaged transposition frequency around Sap1 binding motifs ($n = 888$). Upper panel: 500-bp window; middle panel: 100-bp zoom-in window; lower panel: 100-bp heat-map of individual motifs. (**C**) Averaged transposition frequency around Tf2 LTR ($n = 152$). (**D**) Averaged transposition frequency around Ter1 ($n = 3$).

are markers of replication fork arrest (*14*, *15*) (fig. S5). Because Sap1 fork barrier activity depends on binding site structure rather than on binding affinity (*8*), this observation could explain the variability in transposition competence of Sap1 binding sites (fig. S1, a and b) and why the *sap1-c* allele,

which only modestly lowers DNA binding but strongly affects RFB activity (*9*), decreases Tf1 transposition to such a notable extent (Fig. 1D).

To test the hypothesis that Sap1-dependent fork arrest guides Tf1 insertion, we assessed whether the transposition competence of Sap1 binding sites

correlates with the intensity of Sap1 binding signal or with their RFB activity. We examined the influence of Sap1 binding site orientation with respect to fork progression on transposition efficiency in wild-type (WT) cells, using three well-characterized Sap1 binding sites: (i) the rDNA replication
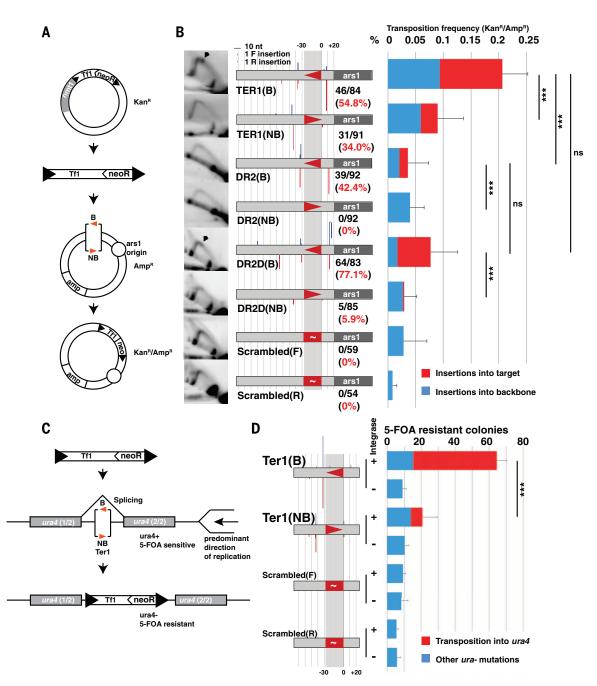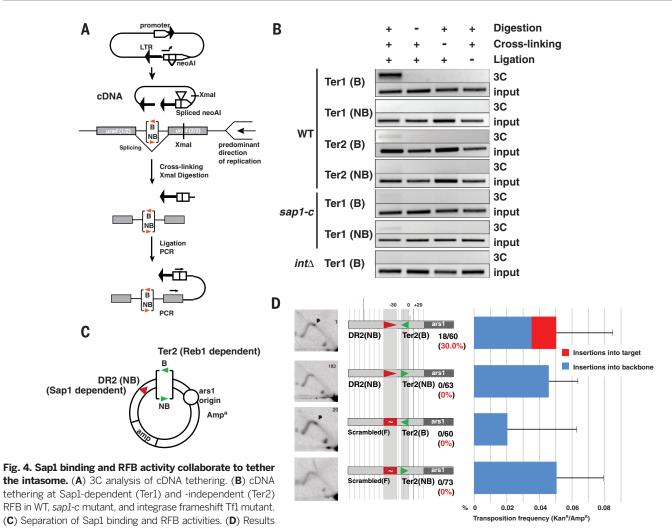
Fig. 3. Transposition competence of Sap1 binding sites depends on RFB activity. (**A**) Plasmid transposition trap strategy. (**B**) Transposition into Ter1, DR2, DR2D, and Scrambled binding motifs in plasmid transposition trap assay. Left column: 2D gel electrophoresis; RFB signals are marked with an arrowhead. Middle column: diagram of target site with insertion sites as columns (blue in forward, red in reverse orientation) at the insertion position of height proportional to number of insertions. Sap1 binding sites depicted by triangles, in blocking (B, pointing left) and nonblocking (NB, pointing right) orientations. Number of insertions into the target site (150-bp window around the Sap1 binding motif)

divided by the total number of insertions in black and percentage in red numbers. Right column: Frequency of transposition into the plasmid (Kan^R/Amp^R plasmids divided by Amp^R total plasmids), with insertions into the target site in red, and insertions into the plasmid backbone in blue. Error bars represent SDs. Asterisks depict statistically significant differences (***$P < 0.001$). ns, not significant ($P > 0.05$). (**C**) Intron transposition trap strategy. (**D**) Insertion into Ter1 and Scrambled binding motifs in intron transposition trap assay. Diagram of motif arrangement and insertions as in (B). Proportion of 5-FOA–resistant colonies due to transposition into *ura4* are shown in red; those due to other mutations are in blue.

Fig. 4. Sap1 binding and RFB activity collaborate to tether the intasome. (**A**) 3C analysis of cDNA tethering. (**B**) cDNA tethering at Sap1-dependent (Ter1) and -independent (Ter2) RFB in WT, *sap1-c* mutant, and integrase frameshift Tf1 mutant. (**C**) Separation of Sap1 binding and RFB activities. (**D**) Results of plasmid trap assay. Left column: 2D gel electrophoresis. Middle column: Diagram of arrangement of Sap1 (DR2 and Scrambled) and Reb1 (Ter2) binding motifs, insertion points, and frequency depicted as in Fig. 3B. Right panel: Transposition frequency into target plasmid as in Fig. 3B.

terminator Ter1 (*12, 13*), a very efficient RFB; (ii) the synthetic sequence DR2, derived from in vitro Sap1 binding selection (*16*) but an inefficient RFB; and (iii) DR2D, a mutation of DR2 that enhances its RFB activity (*8*). We introduced these Sap1 binding sites in one of the two orientations [blocking (B) or nonblocking (NB)] into autonomously replicating plasmids, in close proximity to a replication origin so as to control the predominant direction of fork progression over the motif. We then used these plasmids as transposition acceptors in a targeting assay (*17*) (Fig. 3A). The results are summarized in Fig. 3B. Two-dimensional (2D) native-native gel electrophoresis of replication intermediates confirmed that Ter1 and DR2D, but not DR2, are efficient RFBs in their blocking orientation (Fig. 3B). Chromatin immunoprecipitation (ChIP) analysis showed little difference in Sap1 enrichment between the two orientations of each motif but revealed that DR2 binds to Sap1 more strongly than do the other binding sites, with DR2D showing the lowest and Ter1 showing intermediate enrichment (fig. S6A). The results of the transposition trap experiment show that RFB competency (Ter1 and DR2D, but not DR2), as well as blocking ability (B orienta-

tion), determined higher transposition frequency into the target site ($n = 3$ biological replicates per condition, Tukey Range test, $P = 0.0006$). All insertions displayed 5-bp target site duplications (TSDs, not shown), indicating that they were integrase-mediated transpositions. These results indicate that transposition into Sap1 binding regions depends not on their Sap1 binding affinity but on their efficiency as RFBs.

We next examined if the effect of target site orientation extended to genomic positions. We set up a transposon trap system in which the target site is placed inside an artificial intron in the reporter gene *ura4*, allowing selection of insertions by treatment with the counterselection drug 5-fluoroorotic acid (5-FOA). *ura4* is passively replicated by forks approaching from two nearby replication origins on its centromeric side (*18*), which allowed us to correlate the target site efficiency with its competence as a RFB (Fig. 3C). Blocking or nonblocking orientations of Ter1 showed equal binding of Sap1 (fig. S6b). However, insertion frequency was 10-fold larger in the Ter1 motif placed in the blocking orientation (*t* test, $P < 0.001$, $n = 4$ biological replicates per condition). Again, all insertions exhibited TSD (not shown).

We conclude that the efficiency of insertion near a Sap1 binding motif depends on its ability to cause fork arrest.

These observations prompted us to examine how Sap1, the Tf1 intasome (integration complex), and the replication fork interact. We split Sap1 into functional domains and tested for interactions with the full-length Tf1 integrase with a yeast two-hybrid assay, which revealed that the Tf1 integrase interacts directly with the C-terminal dimerization domain of Sap1 (*16*) (fig. S7). To evaluate the role of this interaction and the arrested fork in Tf1 transposition, we used chromosome conformation capture (3C) to measure tethering of mature cDNA at Sap1-dependent and -independent RFBs (Fig. 4A). Sap1 bound to Ter1 in the blocking orientation led to prominent recruitment of Tf1 cDNA, whereas the non-blocking orientation was unable to recruit (Fig. 4B, Ter1 B/NB). Tethering to Ter1 was also dependent on WT Sap1 and the presence of Tf1 integrase in the intasome (Fig. 4B, *sap1-c*, *int*Δ panels). This suggests that the direct interaction of Sap1 with integrase (fig. S7) participates in intasome recruitment and that Sap1 bound to cDNA (fig. S8) through its cognate binding sequences in the

LTR (*9*) is not sufficient to localize the intasome by multimerization with genome-bound Sap1. A Sap1-independent RFB [Ter2, dependent on the DNA binding factor Reb1 (*19*)] did not tether the cDNA [Fig. 4B, Ter2 (B) and Ter2 (NB)]. This is consistent with our genome-wide observations that class III genes and other Sap1-independent RFBs are not hotspots for Tf1 transposition despite causing polar fork arrest (not shown) (*15, 19*). Combined, these results suggest that integrase, Sap1, and fork barrier activity must be present to tether Tf1 cDNA to the target site and guide insertion.

We next investigated whether the RFB and Sap1 binding requirements can be separated. If so, we could rescue insertion into a non-RFB Sap1 binding site by providing an independent RFB in cis. We cloned Ter2 next to the DR2 binding site placed in the nonblocking orientation (Fig. 4C and fig. S9). Ter2 rescued the targeting efficiency of DR2 only when placed in the blocking orientation (Mann-Whitney U test, $P < 0.001$, $n = 3$ biological replicates per condition, Fig. 4D). Part of the increase in targeting to DR2 could be caused by replication forks converging onto the Ter2 blocked fork to complete S phase, approaching DR2 in the blocking orientation. Accordingly, insertions were detectable on the blocking side of DR2 (Fig. 4D). However, transposition also occurred near Ter2 into the side of the motif where Reb1 stops the fork, suggesting that features of the arrested fork, and not the location of binding sites, are the major determinants of target site choice. Together, these results reveal that Tf1 transposition targeting requires two separable conditions—Sap1 binding and an active RFB—both of which are necessary but neither of which is sufficient by itself.

Insertion of Tf1 into an arrested replication fork could be a result of strand-transfer reactions between the cDNA and replication intermediates, like the insertion of the bacterial Tn7 transposon into the lagging-strand template at replication terminators (*20*). Alternatively, fork arrest or restart may fire DNA damage checkpoint and repair mechanisms that participate in insertion (*21*), or leave epigenetic marks to guide it (*22, 23*) (figs. S5 and S10). Other LTR retrotransposons may display a similar preference for RFBs. The *Saccharomyces cerevisiae* LTR retrotransposons Ty1 (Copia group) and Ty3 (Gypsy group) insert upstream of RNA Pol III–transcribed genes like tRNA and 5S (*22–25*), which are confirmed RFBs (*26*) (fig. S10). Similarly, other LTR retrotransposons with an insertion preference for heterochromatin might use fork stalling at satellite repeats in pericentromeric DNA (*27*).

REFERENCES AND NOTES

1. K. H. Burns, J. D. Boeke, *Cell* **149**, 740–752 (2012).
2. F. D. Bushman, *Cell* **115**, 135–138 (2003).
3. N. J. Bowen, I. K. Jordan, J. A. Epstein, V. Wood, H. L. Levin, *Genome Res.* **13**, 1984–1997 (2003).
4. Y. Guo, H. L. Levin, *Genome Res.* **20**, 239–248 (2010).
5. A. G. Chatterjee et al., *Nucleic Acids Res.* **42**, 8449–8460 (2014).
6. A. Tsankov, Y. Yanagisawa, N. Rhind, A. Regev, O. J. Rando, *Genome Res.* **21**, 1851–1862 (2011).
7. B. Arcangioli, M. Ghazvini, V. Ribes, *Nucleic Acids Res.* **22**, 2930–2937 (1994).
8. G. Krings, D. Bastia, *Mol. Cell. Biol.* **26**, 8061–8074 (2006).
9. M. Zaratiegui et al., *Nature* **469**, 112–115 (2011).
10. Y. Zhang et al., *Genome Biol.* **9**, R137 (2008).
11. R. de Lahondès, V. Ribes, B. Arcangioli, *Eukaryot. Cell* **2**, 910–921 (2003).
12. E. Mejía-Ramírez, A. Sánchez-Gorostiaga, D. B. Krimer, J. B. Schvartzman, P. Hernández, *Mol. Cell. Biol.* **25**, 8755–8761 (2005).
13. G. Krings, D. Bastia, *J. Biol. Chem.* **280**, 39135–39142 (2005).
14. S. Rozenzhak et al., *PLOS Genet.* **6**, e1001032 (2010).
15. N. Sabouri, J. A. Capra, V. A. Zakian, *BMC Biol.* **12**, 101 (2014).
16. M. Ghazvini, V. Ribes, B. Arcangioli, *Mol. Cell. Biol.* **15**, 4939–4946 (1995).
17. Y.-E. Leem et al., *Mol. Cell* **30**, 98–107 (2008).
18. S. Lambert, A. Watson, D. M. Sheedy, B. Martin, A. M. Carr, *Cell* **121**, 689–702 (2005).
19. A. Sánchez-Gorostiaga, C. López-Estraño, D. B. Krimer, J. B. Schvartzman, P. Hernández, *Mol. Cell. Biol.* **24**, 398–406 (2004).
20. A. D. Fricker, J. E. Peters, *Annu. Rev. Genet.* **48**, 167–186 (2014).
21. M. J. Curcio et al., *Mol. Cell. Biol.* **27**, 8874–8885 (2007).
22. L. Mularoni et al., *Genome Res.* **22**, 693–703 (2012).
23. J. A. Baller, J. Gao, R. Stamenova, M. J. Curcio, D. F. Voytas, *Genome Res.* **22**, 704–713 (2012).
24. A. Bridier-Nahmias et al., *Science* **348**, 585–588 (2015).
25. X. Qi et al., *Genome Res.* **22**, 681–692 (2012).
26. A. M. Deshpande, C. S. Newlon, *Science* **272**, 1030–1033 (1996).
27. M. Zaratiegui et al., *Nature* **479**, 135–138 (2011).

SUPPLEMENTARY MATERIALS

www.sciencemag.org/content/349/6255/1549/suppl/DC1
Figs. S1 to S10
Materials and Methods
Tables S1 to S3
References (*28–39*)

Gordon Research Conferences
frontiers of science

2016 "Session I" Meetings will be held between January 9 and March 25 in Ventura, CA and Galveston, TX in the United States, and internationally in the Tuscany region of Italy. A list of preliminary programs appears on the following 9 pages. For detailed programs, fees, site/travel information and online application, visit our web site at **www.grc.org**.

Gordon Research Conferences are different from other scientific conferences because. . .

. . .they contain one high caliber presentation after another, complemented by robust discussions of important scientific topics in our field, day after day. It's truly a unique experience.

(David E. Watson, Chair, 2014 Drug Safety GRC)

Image: Mouse embryonic fibroblasts treated with mTOR inhibitor plus lysosome inhibitor (Bafilomycin A1) to induce the accumulation of autolysosomes. Cells were stained with LAMP1 (green), LC3B (red) and DAPI (blue; DNA). Courtesy of David McEwan (University of Frankfurt Medical School). Submitted by Paolo Grumati & Anna Vainshtein, Chairs, Autophagy in Stress, Development & Disease GRS. The Autophagy GRS will take place March 19-20, 2016 at the Ventura Beach Marriott in Ventura, CA.

2016 "Session I" Preliminary Programs

The list of meetings, session topics and speakers begins below. Discussion leaders are noted in italics.

Note: Gordon Research Seminars (GRS) are listed below their associated Gordon Research Conference. GRSs are 2-day meetings that precede an associated GRC, designed for graduate students, post-docs, and other young scientists to present and exchange new data and cutting-edge ideas. Seed funding for new Gordon Research Seminars is provided by the Kenan Institute for Engineering, Technology & Science at North Carolina State University and Merck & Co., Inc.

- **Gene-Environment Interplay in Alcohol Actions**
  (*Michael Miles* / Joel Gerlenter / Kim Raab-Graham / Kazue Hashimoto-Torii / Jill Bettinger / Paul Kenny)
- **Are Ion Channels Key Molecular Substrates of Alcohol?**
  (*Leslie Morrow* / Paul Slesinger / Nigel Atkinson / Alex Dopico)
- **Drug Development -- How Close Are We to a Cure for Alcohol Use Disorders?**
  (*Tamara Phillips* / John Krystal / Jennifer Mitchell / Barbara Mason / Lorenzo Leggio / Gunter Schumann)
- **Alcohol and Decision Making**
  (*Kathleen Grant* / Gary Aston-Jones / John Woodward / David Lovinger)

- **The Brain RAS / Salt and Metabolism**
  (*Eric Lazartigues*, *Dominik Muller* / Yumei Feng / Javier Stern / Jens Titze / Jonathan Jantsch / Frederique Yannikouris)
- **Technical Advances in Genome Editing and Optogenetics**
  (*Mingyu Liang* / Aron Geurts / Michael Bader / Sergey Kasparov)
- **Recent Advances in Tissue RAS**
  (*Toshiro Fujita*, *Rhian Touyz* / Mark Chappell / Kenneth Gross / Shigeru Shibata / Sadashiva Karnik / Eric Krause)
- **MicroRNAs: Regulation, Function and Therapeutic Targets in Cardiovascular Diseases**
  (*Michael Bader* / Mingyu Liang / Thomas Thum / Andrew Baker)

Alcohol & the Nervous System
Breakthroughs in Alcohol Neuroscience Research at the Level of Molecules, Cells, Synapses, and Behavior
Feb 7-12, 2016
Hotel Galvez, Galveston, TX
Chair: Dorit Ron
Vice Chairs: Jeff L. Weiner & C. Fernando Valenzuela

- **Keynote Session: New Insights into the Neurocircuitry of Psychiatric Disorders**
  (*David Lovinger* / Karl Deisseroth)
- **The Dark Side of Addiction**
  (*Howard Becker* / George Koob / Jeff Weiner / Klaus Miczek / Sheena Josselyn / Jonathan Brigman)
- **Addiction to Alcohol and Other Substances: Common Neural Substrates?**
  (*Lawrence Judson Chandler* / Brigitte Kieffer / John Dani / Yavin Shaham)
- **Circuitry of Motivated Behaviors**
  (*John Crabbe* / Antonello Bonci / Stephan Lammel / Roh-Yu Shen / Christina Gremel / Rita Goldstein / Olivier George)
- **Neuroscience Innovations for Alcohol Research**
  (*Changhai Cui* / Bruce Hope / Bryan Roth / Kevin Bender)

Angiotensin
Angiotensin: From Cell Biology and Signaling Networks to Novel Physiological Paradigms and Therapeutics
Feb 21-26, 2016
Renaissance Tuscany Il Ciocco, Lucca (Barga), Italy
Chair: Curt D. Sigmund
Vice Chair: Toshiro Fujita

- **Keynote Session: Regulation and Genetics of the Renin-Angiotensin-Aldosterone System**
  (*Curt Sigmund* / Armin Kurtz / Xavier Jeunemaitre)
- **Renin Angiotensin Aldosterone Blockers: Are Dual Specificity Inhibitors the Next Great Thing?**
  (*Jan Danser* / Massimo Volpe / John Burnett / Natalia Nalivaeva-Turner)
- **Regulatory Networks and Clinical Relevance**
  (*Akira Nishiyama* / Pedro Jose / Michaela Kuhn / Youhua Liu)
- **New Roles for Renin, Renin Receptor and ACE in the Kidney**
  (*Thomas Coffman*, *Rodrigo Fraga-Silva* / Maria Louisa Sequiera-Lopez / Jorge Giani / Minolfa Prieto-Carrasquero)
- **Immunity and Inflammation**
  (*Ulrich Wenzel* / Steven Crowley / Duska Dragun / Daniela Carnevale)

Angiotensin (GRS)
The Renin Angiotensin System in Health and Disease: Latest Advances and New Technologies
Feb 20-21, 2016
Chairs: Kirsty G. Pringle & Rodrigo Fraga-Silva

Antibody Biology & Engineering
Connecting Antibody Biology, Structure and Function to Future Applications
Mar 20-25, 2016
Hotel Galvez, Galveston, TX
Chairs: Richard Blumberg & Janine Schuurman
Vice Chair: Mark Hogarth

- **Keynote Session: Perspectives on Antibody Biology and Engineering**
  (*Omid Vafa*, *Derry Roopenian* / Sally Ward / Paul Carter)
- **Antibody Structure and Dynamics in Relation to Function**
  (*Brian Sutton*, *John Desjarlais* / Sarel Fleishman / Gary Gilliland / Floyd Romesberg / Clarissa Jakob)

- **Modeling Antibody Diversity - Its Generation and Uses**
(*George Georgiou, David King* / Jamie Scott / Sachdev Sidhu / Francois Vigneault)
- **The Functionality of Antibodies and the Receptors Through Which They Operate: Functional Consequences**
(*Paul Parren, Falk Nimmerjahn* / Peter Sun / Leo James / Brian Sutton / Falk Nimmerjahn)
- **The Functionality of Antibodies and the Receptors Through Which They Operate: Translation to Therapeutic Applications**
(*Paul Parren, Falk Nimmerjahn* / David Szymkowski)
- **Development and Mechanisms of Pathogenic or Protective Antibodies**
(*Antonio Lanzavecchia, Michel Nussenzweig* / Erica Ollmann Saphire / Louis Weiner / Antonio Lanzavecchia / Michel Nussenzweig)
- **Unique Therapeutic Vistas in Antibody Engineering: Bispecifics**
(*Paul Carter* / Teemu Junttila)
- **Co-Opting Antibodies as a Delivery Vehicle**
(*John Lambert* / Christopher Scott / Christian Klein / Xiuxia Sun / K. Dane Wittrup)
- **Therapeutic Challenges and Opportunities in the Application of Antibodies to Modifying Disease**
(*Louis Weiner* / Sergio Quezada / Paul Parren)

GRS **Antibody Biology & Engineering**
Modulation and Mechanisms of Antibody Activity
Mar 19-20, 2016
Chairs: Kristi Baker & Anja Lux

Autophagy in Stress, Development & Disease
From the Basics in the Signaling and Molecular Aspect of Autophagy to the Identification of Therapeutic Targets
Mar 20-25, 2016
Ventura Beach Marriott, Ventura, CA
Chairs: Fulvio Reggiori & Patrice Codogno
Vice Chairs: Katja Simon & David C. Rubinsztein

- **Keynote Session: Proteasome and Autophagy: Two Faces of Proteostasis: Implication for Human Disease**
(*Patrice Codogno* / Fred Goldberg / Herbert Virgin / Tamotsu Yoshimori)
- **Mechanism of Autophagy**
(*Tamotsu Yoshimori* / James Hurley / Noboru Mizushima / Hitoshi Nakatogawa / Sharon Tooze)
- **Regulation of Autophagy**
(*Beth Levine* / Kun-Liang Guan / Adi Kimchi / Li Yu)
- **Autophagy in Model Organisms and Plants**
(*Malene Hansen* / Eric Baehrecke / Diane Bassham / Miguel Penalva / Hong Zhang)
- **Autophagy in Development and Differentiation**
(*Ana Maria Cuervo* / Charleen Chu / Mondira Kundu / Beth Levine)
- **Autophagy in Infection and Immunity**
(*Herbert Virgin* / Ken Cadwell / Vojo Deretic / Ivan Dikic / Christian Munz)
- **Drug Discovery and Potential Therapeutic Targets**
(*David Rubinsztein* / Bear Nyfeler / Natalie Roy D'Amore / Junying Yuan)
- **Genetic Diseases**
(*Katja Simon* / Andrea Ballabio / Augustine Choi / Alec Kimmelman / Mihai Netea)
- **Autophagy in Metabolism and Ageing**
(*Vojo Deretic* / Ana Maria Cuervo / Malene Hansen / Guido Kroemer)

GRS **Autophagy in Stress, Development & Disease**
Autophagy: From the Bench to the Bedside, Basic Science Translated
Mar 19-20, 2016
Chairs: Paolo Grumati & Anna Vainshtein

Basal Ganglia
Emerging Views of Cellular and Circuit Diversity Within the Basal Ganglia
Feb 28 - Mar 4, 2016
Four Points Sheraton / Holiday Inn Express, Ventura, CA
Chair: Nicole Calakos
Vice Chair: Mark Bevan

- **Keynote Session: Striatal Adaptations in Parkinson's Disease: When Homeostasis Goes Astray**
(*Nicole Calakos* / D. James Surmeier)
- **Basal Ganglia Circuit Interactions and the Behaviors They Shape**
(*Thomas Wichmann* / Laszlo Acsady / Michele Basso / Helen Bronte-Stewart / Juan Mena-Segovia)
- **What the Basal Ganglia Do: Perspectives from Computational Neuroscience**
(*XJ Wang* / Kim Blackwell / Mark Humphries / Henry Yin)
- **From Good Habits to Bad: Insights from the Dorsal and Ventral Striatum**
(*Ann Graybiel* / Veronica Alvarez / Christian Luscher / John O'Doherty)
- **Basal Ganglia Dysfunction in Neurodegenerative Disease: New Insights and Opportunities**
(*William Dauer* / X. William Yang / Huaibin Cai)
- **Cellular and Molecular Diversity of the Basal Ganglia: Technical Innovations and Functional Insights**
(*Bernardo Sabatini* / Savio Chan / Jens Hjerling Leffler / Tibor Koos / Anne Schaefer)
- **Basal Ganglia and Action**
(*Rui Costa* / Joshua Berke / Michael Frank / Anatol Kreitzer)
- **Synaptic Plasticity: Mechanisms and Behavioral Consequences**
(*Robert Malenka* / Haruo Kasai / David Lovinger / Raffaella Tonini)
- **Signal Transduction in Basal Ganglia**
(*Rosario Moratalla* / Marc Caron / Jean Antoine Girault / Miriam Heiman)

GRS **Basal Ganglia**
Emerging Views of Cellular and Circuit Diversity Within the Basal Ganglia
Feb 27-28, 2016
Chairs: Julia C. Lemos & Justin K. O'Hare

Batteries
Fundamental Tools for Designing the Next Generation of Electrochemical Energy Storage
Feb 21-26, 2016
Four Points Sheraton / Holiday Inn Express, Ventura, CA
Chair: Dean Wheeler
Vice Chair: Nina Balke

- **Lessons from Industry**
(*Marten Behm* / Mark Verbrugge / Thomas Barrera)
- **Nanoscale Materials Design**
(*Bryan McClosky* / Yi Cui / Ying Shirley Meng / Yury Gogotsi)
- **From Lithium to Sodium**
(*Candace Chan* / Jurgen Janek / Linda Nazar)
- **Interfaces and Interphases**
(*Yue Qi* / Jeff Dahn / Robert Kostecki / Perla Balbuena)
- **Fundamental Mechanisms Governing Battery Performance**
(*Gleb Yushin* / Doron Aurbach / Rachid Yazami)
- **Tools for Studying Lifetime Phenomena**
(*Stephen Harris* / Daniel Abraham / John Turner / Craig Carter)
- **Reducing the Cost per kWh**
(*Corie Cobb* / Linda Gaines / Dan Steingart)
- **New Chemistries**
(*Haleh Ardebili* / M. Stanley Whittingham / Yukinori Koyama / Jeffery Read)
- **Battery Reformat**
(*Nina Balke* / Hector Abruna / Fikile Brushett)

GRS **Batteries**
Building Better Batteries: Materials, Interfaces and Devices
Feb 20-21, 2016
Chairs: Martin Ebner & Rose E. Ruther

Biology of Acute Respiratory Infection
Host-Pathogen Interactions in Acute Respiratory Tract Infection: From Basic Mechanisms to Human Disease
Feb 21-26, 2016
Hotel Galvez, Galveston, TX
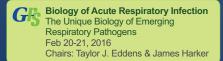Chairs: Theodore J. Standiford & Peter Openshaw
Vice Chairs: Chad Steele & Dawn Bowdish

- **Pathogen Recognition and Cellular Participants in Lung Immunity: Novel Mechanisms**
(*Chad Steele* / Bart Lambrecht / Samithamby Jeyaseelan / Jean-Claude Sirard)
- **Novel Effector Antimicrobial Mechanisms**
(*Scott Evans* / Vojo Deretic / Paul Kubes / Christopher Evans)
- **Control of Injury and Repair in Acute Respiratory Infection**
(*Samithamby Jeyaseelan* / Jahar Bhattacharya / Hal Chapman / Amanda Jamieson)
- **Molecular Mechanisms of Microbial Pathogenesis**
(*Alice Prince* / Anders Hakansson / Pradeep Singh / Andreas Wack)
- **The Lung Microbiome in Health and Disease**
(*David Corry* / Benjamin Marsland / Robert Dickson / Michael Surette)
- **Evolving Concepts in Immune Memory of the Lung**
(*Bart Lambrecht* / Mihai Netea / Joseph Mizgerd / Andre Ballesteros-Tato)
- **Emerging Microbial Pathogens: Animal Modeling to Human Disease**
(*Dawn Bowdish* / Stacey Schultz-Cherry / Matthew Frieman / Frank Deleo)
- **The Host Response in Lung Infection: Genes and Environment**
(*Joseph Mizgerd* / Michael Ciancanelli / Benjamin Suratt / David Corry)
- **Prevention of Lung Infection: Novel Vaccination Approaches**
(*Jay Kolls* / Christopher Chiu / Dawn Bowdish / Alfredo Torres)

GRS **Biology of Acute Respiratory Infection**
The Unique Biology of Emerging Respiratory Pathogens
Feb 20-21, 2016
Chairs: Taylor J. Eddens & James Harker

Conferees at the Epithelial Differentiation and Keratinization GRC enjoy a mountain hike at Sunday River in Maine.

Bones & Teeth
Translating Local Tissue Interactions and Systemic Interplays into New Therapies for Bones and Teeth
Feb 14-19, 2016
Hotel Galvez, Galveston, TX
Chair: Maurizio Pacifici
Vice Chair: Fanxin Long

- **Progenitors in Bone Development and Repair**
  (*Henry Kronenberg* / Christa Maes / Vicki Rosen / Deneen Wellik)
- **Bone Marrow Constituents and Bone Homeostasis**
  (*Pamela Robey* / Ralf Adams / Laurie McCauley / Thomas Clemens)
- **Osteocyte Dynamics and Communication**
  (*Lynda Bonewald* / Sarah Dallas / Mitch Shaffler)
- **Regeneration of the Dentition**
  (*Ophir Klein* / Pascal Schneider / Samuel Stupp / Jukka Jernwall / Jeffrey Streelman)
- **Osteoclasts and Subchondral Bone in Joint Disease**
  (*Vicki Rosen* / Xu Cao / Yousef Abu-Amer)
- **Rare Musculoskeletal Diseases and Possible Therapies**
  (*Kevin Jones* / Brendan Lee / Paolo Bianco / Jacqueline Hecht)
- **Adult Stem Cells and Dental Repair and Renewal**
  (*Yang Chai* / Frederic Michon / Ophir Klein)
- **Systemic Bone Biology: Energy Metabolism, Obesity and Diabetes**
  (*Steven Teitelbaum* / Gerard Karsenty / Clifford Rosen / Fanxin Long)
- **Keynote Session: VEGF Biology in Bone Health and Disease**
  (*Eileen Shore* / Bjorn Olsen)

GRS **Bones & Teeth**
Building on Solid Foundations: From Mechanisms to Bone Tissue Repair
Feb 13-14, 2016
Chairs: Nunzia Di Maggio & Shai Eyal

Colloidal, Macromolecular & Polyelectrolyte Solutions
Non-Equilibrium and Bio-Inspired Systems
Feb 7-12, 2016
Four Points Sheraton / Holiday Inn Express, Ventura, CA
Chairs: Maria M. Santore & Frederick C. MacKintosh
Vice Chairs: Eric M. Furst & Wilson K. Poon

- **Colloidal and Nanoparticle Assembly on Surfaces and in Solution**
  (*William Ducker* / Paul Chaikin / Carol Hall / James Gilchrist)
- **Fundamentals of Colloidal and Macromolecular Interactions: Deformable Interfaces and Elasticity**
  (*Howard Stone* / Joelle Frechette / Tobias Baumgart)
- **Glassy and Constrained Phases**
  (*David Weitz* / Ludwik Leibler / Gregory McKenna)
- **Polyelectrolytes and Active/Biomimetic Gels**
  (*Chi Wu* / Eugenia Kharlampieva / Ping Sheng / Krystyn Van Vliet)
- **Coacervates and Solution Phase Assemblies**
  (*Michael Rubinstein* / Sarah Perry / Prabhu Vivek)
- **Rheology in Concentrated Suspensions**
  (*Eric Weeks* / Matteo Pasquali / Peter Schall)
- **Cooperative Systems: Active and Living Colloids**
  (*Igor Aronson* / Michael Cates / Jacinta Conrad / Gerard Wong)
- **Interactions and Functional Assemblies of Biological Nanoparticles and Colloids**
  (*Francesco Stellacci* / Trevor Douglas / Ralf Richter)
- **Translating Assemblies: From Fundamental Concepts to Applications**
  (*Monica Olvera de la Cruz* / Frank Caruso / Ronald Larson)

GRS **Colloidal, Macromolecular & Polyelectrolyte Solutions**
Emergent Behavior in Complex Fluids
Feb 6-7, 2016
Chairs: Michelle Calabrese & John K. Riley

Cornea, Biology & Pathobiology of the
Function of the Ocular Surface and Tear Film in Health and Disease
Feb 28 - Mar 4, 2016
Ventura Beach Marriott, Ventura, CA
Chairs: Darlene A. Dartt & Robert M. Lavker
Vice Chairs: Shigeto Shimmura & Julie T. Daniels

- **Keynote Session: Setting Our Sights: Future of Ocular Surface and Tear Film Research**
  (*Ilene Gipson* / Tung-Tien Sun / Dimitri Azar)
- **Establishment of Tissue Boundaries: Implications for Cornea and Conjunctiva**
  (*Sophie Deng*, *Friedrich Kruse* / David Wilkinson / Spiro Getsios / Kohji Nishida / Nick Di Girolamo)
- **Maintenance of Corneal Homeostasis**
  (*Mary Ann Stepp*, *Alexander Ljubimov* / Richard Carthew / Stephen Sugrue / Ruby Shalom-Fuerstein / Susan Menko)
- **Mechanism of Tear Film Formation by the Lacrimal Gland, Meibomian Glands, and Conjunctiva**
  (*Margarita Calonge*, *Alison McDermott* / Sarah Hamm-Alvarez / James Jester / Sharmila Masli / Edit Tóth-Molnár)
- **Ocular Surface Pain: Etiology and Treatments**
  (*Yolanda Diebold*, *Micheal Stern* / Diana Bautista / David Borsook / Juana Gallar / Blanka Golebiowski)
- **What We Can Learn from Common Diseases of Skin, Salivary Glands and Other Tissues**
  (*Esen Akpek*, *David Woodley* / Denise Faustman / M. Peter Marinkovitch / Irwin McLean / Ammon Peck)
- **Diseases of the Ocular Surface (Cornea and Conjunctiva)**
  (*Deborah Jacobs*, *Mark Rosenblatt* / Ali Djalillian / George Ousler / Danielle Robertson / Fushin Yu)
- **Ocular Surface Responses to Infection and Inflammation**
  (*Shukti Chakravarti*, *Michael Zegans* / Suzanne Fleiszig / Mihaela Gadjeva / Daniel Saban / Melanie Scott)
- **Mechanisms of Corneal Repair**
  (*Natalie Afshari*, *José Gomes* / Karsten Gronert / David Kaplan / Bruce Ksander / Sangbum Park)

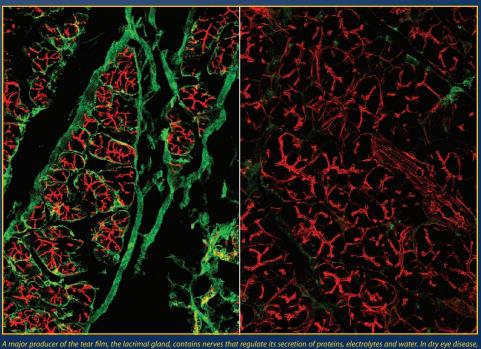**GRS** **Cornea, Biology & Pathobiology of the**
Future Challenges and Directions of Ocular Surface Research
Feb 27-28, 2016
Chairs: Laura Contreras Ruiz & Jong Kook Park

A major producer of the tear film, the lacrimal gland, contains nerves that regulate its secretion of proteins, electrolytes and water. In dry eye disease, lacrimal gland secretion is impaired. Shown here are lacrimal gland acinar cells (red, phalloidin directly conjugated to a fluorphore) surrounded by nerves (green, anti-beta3 tubulin antibody). Left image is from a 24 week old wild type mouse. Right image is from a 24 week old thrombospondin-1 (TSP-1) knock out mouse, a model of dry eye disease. Note dramatic loss of nerves in the lacrimal gland from the TSP-1 knock out mouse. Submitted by Darlene A. Dartt, Chair, Biology & Pathobiology of the Cornea GRC.

Craniofacial Morphogenesis & Tissue Regeneration
Insights into Gene Networks, Disease Models and Evolutionary Mechanisms in Craniofacial Morphogenesis
Mar 13-18, 2016
Four Points Sheraton / Holiday Inn Express, Ventura, CA
Chair: Patrick Tam
Vice Chair: Ophir D. Klein

- **Keynote Session: Phenomics and Mutagenesis Screen; Epithelial and Mesenchymal Morphogenesis: Genomics and Imaging**
  (*Ophir Klein* / Lee Niswander / Mark Krasnow)
- **Functional Genomics and Clinical Genetics**
  (*Paul Trainor* / Richard Maas / Bernice Morrow)
- **Evolution and Functional Anatomy**
  (*Jeffrey Streelman* / Anne Huysseune / Craig Miller)
- **Modelling Developmental Errors**
  (*Paul Sharpe* / Jeffrey Bush / Joan Richtmeier)
- **Formshaping: Skull and Face**
  (*James Martin* / Sevan Hopyan / Ralph Marcucio)
- **Tissue Patterning: Cellular Mechanisms**
  (*Marianne Bronner* / Carole LaBonne / James Martin)
- **Organ Formation**
  (*Yang Chai* / Clare Baker / Matthew Hoffmann)
- **Tissue Engineering and Repairs**
  (*Irma Thesleff* / Warren Grayson / Derk Joester)
- **Gene Network and Molecular Switches**
  (*Ralph Marcucio* / Robert Cornell / Tatjana Sauka-Spengler)

GRS Craniofacial Morphogenesis & Tissue Regeneration
From Bench to Bedside in Craniofacial Biology
Mar 12-13, 2016
Chairs: Sandra Gonzalez-Malagon & Alice Goodwin

DNA Damage, Mutation & Cancer
Genome Instability from Environmental and Inherent Sources of DNA Damage
Mar 13-18, 2016
Ventura Beach Marriott, Ventura, CA
Chair: Sergei M. Mirkin
Vice Chair: Richard D. Wood

- **Keynote Session: Inherent Genomic Stability and Instability**
  (*Richard Wood* / Philip Hanawalt / Stephen Kowalczykowski)
- **Genome Weak Links**
  (*Sergei Mirkin* / Catherine Freudenreich / Karen Vasquez / Evgeny Nudler / Thomas Petes / Susan Lovett / Richard Wood)
- **Environmental Genomic Damage**
  (*Nicholas Geacintov* / Johannes Walter / Isao Kuraoka / Mitch McVey / Nicholas Geacintov)
- **RNA-DNA Interplay in Genome Instability**
  (*Hannah Klein* / Mark Bedford / Francesca Storici / Andres Aguilera / Sue Jinks-Robertson / Hannah Klein)
- **Oxidative DNA Damage and Base Excision Repair**
  (*Samuel Wilson* / Cynthia McMurray / Sylvie Doublie / Yuan Liu / Guoliang Xu / Yves Pommier)
- **Mutagenesis in Response to Arrested Replication**
  (*Wei Yang* / Frederick Alt / Simon Boulton / Massimo Lopes / Naoko Shima / Wei Yang)
- **Checkpoints and Strand-Break Repair**
  (*Karlene Cimprich* / Nancy Maizels / Lee Zou / Dale Ramsden / Karlene Cimprich)
- **FoSTeS, Kataegis and Chromothripsis**
  (*Anna Malkova* / James Lupski / Thanos Halazonetis / David Pellman / Youri Pavlov / Anna Malkova)
- **Emerging Chemotherapies Based on Cancer Genomics**
  (*Thomas Helleday* / Lawrence Loeb / Andrea Ventura / Tarun Kapoor / James Ford / Thomas Helleday)

GRS DNA Damage, Mutation & Cancer
Genome Instability from Environmental and Inherent Sources of DNA Damage
Mar 12-13, 2016
Chair: Jane C. Kim
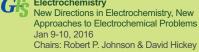
Electrochemistry
New Directions in Electrochemistry, New Approaches to Electrochemical Problems
Jan 10-15, 2016
Four Points Sheraton / Holiday Inn Express, Ventura, CA
Chair: Philip N. Bartlett
Vice Chair: Shelley Minteer

- **Spectroelectrochemistry**
  (*Carol Korzeniewski* / Jacek Lipkowski / Andrea Russell)
- **Molecular Catalysis and Energy**
  (*Mark Spitler* / Jillian Dempsey / Sharon Hammes-Schiffer / John Keith)

- **Electrodeposition**
  (*John Stickney* / Jan Fransaer / Stephen Maldonado)
- **Bioelectrochemistry**
  (*Yann Astier* / Christophe Leger / Janine Mauzeroll / David Waldeck)
- **Cooperative Behaviour**
  (*Richard Crooks* / Viola Birss / Katharina Krischer)
- **Nanoscale Electrochemistry**
  (*Nongjian Tao* / Joaquin Rodriguez-Lopez / Henry White / Andrew Hillier)
- ***In Situ* Studies**
  (*Daniel Scherson* / Hector Abruna / Keith Stevenson)
- **Electrocatalysis**
  (*Andrea Russell* / Yan Xia Chen / Timo Jacob / Michael Janik)
- **Late-Breaking Topics**
  (*Shelley Minteer*)

GRS Electrochemistry
New Directions in Electrochemistry, New Approaches to Electrochemical Problems
Jan 9-10, 2016
Chairs: Robert P. Johnson & David Hickey

Geobiology
Reconstructing Processes from Genes to the Geologic Record
Jan 31 - Feb 5, 2016
Hotel Galvez, Galveston, TX
Chair: David A. Fike
Vice Chair: Tanja Bosak

NEW!

- **Keynote Session: Cryptic Microbial Cycles**
  (*Alexandra Turchyn* / Bo Barker Jorgensen / Orit Sivan)
- **Microbial Ecology in Surface Environments**
  (*Victoria Orphan* / Alexis Templeton / Eric Boyd / Sara Pruss)
- **Nitrogen in Marine Environments**
  (*Karen Casciotti* / Brian Popp / Julie Granger)
- **Microbial Ecology and Evolution Through the Lens of Bioinformatics**
  (*Anne-Kristin Kaster* / Gregory Fournier / Laura Hug / Adam Arkin)
- **Biosignature Generation: Who, How, and Where**
  (*Dianne Newman* / Paula Welander / Ann Pearson)
- **Depositional Constraints on Geobiological Signals**
  (*Robert Aller* / William Berelson / Rachel Wood / Itay Halevy)
- **Metals as Biogeochemical Proxies**
  (*Alex Halliday* / Jeff Catalano / Stefan Lalonde)
- **Deep Time Records**
  (*Kurt Konhauser* / David Rowley / Shanan Peters / John Higgins)
- **Novel Tools and Techniques**
  (*Woodward Fischer* / Kenneth Williford / Jena Johnson)

Glycolipid & Sphingolipid Biology
Glycolipid and Sphingolipid Homeostasis and Function in Health and Disease
Mar 6-11, 2016
Renaissance Tuscany Il Ciocco, Lucca (Barga), Italy
Chair: Howard Riezman
Vice Chair: Mark Kester

- **Keynote Session: Understanding Complex Networks in Membranes and Sphingolipid Homeostasis**
  (*Walter Holleran* / Kai Simons / Yusuf Hannun)

- **Enzymology and Regulation of Glycolipids and Sphingolipids**
  (*Yasuyuki Igarashi* / Joost Holthuis / Jonathan Weissman / Giovanni D'Angelo)
- **Glycolipid and Sphingolipid Metabolism and Traffic**
  (*Kentaro Hanada* / Anthony Futerman / Pietro De Camilli / Akio Kihara)
- **Glycolipid and Sphingolipids in Infection**
  (*Besim Ogretman* / Erich Gulbins / Urs Greber / Giulio Superti-Furga)
- **Glycolipid and Sphingolipid Tool Box**
  (*Alfred Merrill* / Xianlin Han / Berend Snijder)
- **Sphingosine 1 Phosphate Signaling in Inflammation and Cell Migration**
  (*Richard Proia* / Sarah Spiegel / Timothy Hla / Julie Saba)
- **Glycolipid and Sphingolipid Related Diseases**
  (*James Shayman* / Frances Platt / Thorsten Hornemann / Scott Summers)
- **Genetic Disorders of Glycolipids and Sphingolipids / Neurobiology**
  (*Alessandro Prinetti* / Yoshio Hirabayashi / Vittorio Maglione)
- **Translational Aspects of Glycolipid and Sphingolipid Biology**
  (*Lina Obeid* / Richard Kolesnick / Leah Siskind)

Ligand Recognition & Molecular Gating
Molecular Basis of Ligand Recognition and Gating in Transmembrane Signaling and Transport
Jan 31 - Feb 5, 2016
Renaissance Tuscany Il Ciocco, Lucca (Barga), Italy
Chair: Crina Nimigean
Vice Chair: Edmund Kunji

- **G Protein Coupled Receptors**
  (*Benjamin Kaupp* / Klaus Hofmann / Andreas Pluckthun / Gebhard Schertler / Kurt Wuthrich)
- **Physiology of Transporters and Channels**
  (*Edmund Kunji* / Geoffrey Abbott / Frances Ashcroft / Nancy Carrasco / Benjamin Kaupp)
- **Ion Channel Permeation and Gating Mechanisms**
  (*Kenton Swartz* / Francisco Bezanilla / Bert de Groot / Ann McDermott / Jian Payandeh)
- **Dual Function and Exotic Channels and Transporters**
  (*Dirk Jan Slotboom* / Alessio Accardi / Christopher Miller)
- **Ligand-Gated Ion Channels**
  (*Anna Moroni* / Pierre-Jean Corringer / Peter Hegemann)
- **Technique Innovation**
  (*Simon Scheuring* / Maxime Dahan / Werner Kuhlbrandt / Carol Robinson)
- **Transporter Mechanism**
  (*Lucy Forrest* / Olga Boudker / Jose Faraldo-Gomez / Dirk Jan Slotboom)
- **Calcium Release Channels**
  (*Christopher Miller* / Steve Long / Irina Serysheva / Nieng Yan)
- **Late-Breaking Topics**
  (*Alessio Accardi* / Eduardo Perozo)

GRS Ligand Recognition & Molecular Gating
Molecular Basis of Ligand Recognition and Gating in Transmembrane Signaling and Transport
Jan 30-31, 2016
Chairs: Cristina Paulino & Mingfeng Tsai

Lymphatics
Basic Science and Disease Mechanisms in Multiple Organ Systems
Mar 20-25, 2016
Four Points Sheraton / Holiday Inn Express, Ventura, CA
Chair: Gwendalyn J. Randolph
Vice Chairs: Mihaela Skobe & Gou Young Koh

- **Building Lymphatics**
  (*Anne Eichmann* / Benjamin Hogan / Mark Kahn / Guillermo Oliver)
- **The Interstitial Microenvironment and Recent Focus on Interstitial Flow in the Brain**
  (*Melody Swartz* / Jens Titze / Norman Miller / Helge Wiig / Maiken Nedergaard / Jonathan Kipnis / Kari Alitalo)
- **Collecting Lymphatic Vessels and Mechanics**
  (*David Zawieja* / Tatiana Petrova / Michael Davis / Brandon Dixon)
- **The Lymph Node and Lymphatics in Immunity**
  (*Nancy Ruddle* / Melody Swartz / Shannon Turley / James Moore / Reinhold Forster / Lijun Xia / Jason Cyster)
- **Genetics and Lymphedema**
  (*Stanley Rockson* / Miikka Vikkula / Sahar Mansour / Babak Mehrara)
- **Signals that Regulate the Lymphatic Vasculature in Development, Health, and Disease**
  (*Gou Young Koh* / Anne Eichmann / Steve Watson / Martin Schwartz / Michael Detmar / Mihaela Skobe)
- **Lymphangioleiomyomatosis (LAM)**
  (*Mark Kahn* / Frank McCormack / Lisa Henske / Kuniaki Seyama)
- **Lymphatics in the Intestine, Mesentery, and Visceral Fat**
  (*Gwendalyn Randolph* / Natasza Kurpios / Taija Makinen / Karine Clement / Gou Young Koh)
- **Lymphatics in the Cardiovascular System**
  (*Mihaela Skobe* / Kathleen Caron / Seppo Yla-Herttuala / Donald McDonald)

> **GRS** **Lymphatics**
> Perspectives on Lymphatic Vascular Signaling, Development and Function
> Mar 19-20, 2016
> Chairs: Amelie Sabine & Joshua P. Scallan

Marine Natural Products
Insights into Marine Natural Products from the Field, Lab and Clinic
Mar 6-11, 2016
Four Points Sheraton / Holiday Inn Express, Ventura, CA
Chair: Julia Kubanek
Vice Chair: Paul R. Jensen
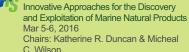
- **Genetically Encoded Small Molecules from Marine Organisms**
  (*Shigeki Matsunaga* / Bradley Moore)

A lymphatic collecting vessel in red passing through an adipose tissue depot. Leaf-like valves are apparent in the collecting lymphatic vessel. There is a growing appreciation for the cross-regulation between lymphatics and adipose tissue, but many mysteries remain. Staining in red is for podoplanin; white is collagen type IV, which surrounds every adipocyte. Submitted by Gwendalyn J. Randolph, Chair, Lymphatics GRC.

- **Synthetic Biology of Natural Products**
  (*Mohamed Donia* / Emily Balskus / Sarah O'Connor / Eric Schmidt)
- **Microbial Signaling in a Vast Ocean**
  (*David Rowley* / Tracy Mincer / Roman Stocker)
- **Organismal Interactions in Wet and Not-so-Wet Worlds**
  (*Amy Lane* / Danielle Dixson / Martin Kaltenpoth / Toshiyuki Wakimoto)
- **Antibiotic Discovery and Microbial Secondary Metabolism**
  (*Brian Murphy* / Stefan Schulz / Mohammad Seyedsayamdost)
- **Creative Chemical Solutions to Mysterious Molecules**
  (*Daniel Romo* / Kirk Gustafson / Tadeusz Molinski / Richmond Sarpong)
- **Molecular Targets and Omics Approaches**
  (*Roberto Berlinck* / Carole Bewley / Leticia Costa-Lotufo)
- **Targeting Human Disease with Natural Products**
  (*Yali Fu* / Robert Capon / Victoria Knight-Connoni / John MacMillan)
- **Keynote Session: Development of Marine Natural Products as Pharmaceuticals and Tools for Research**
  (*Paul Jensen* / Eduardo Esquinazi / Ronald Quinn)

> **GRS** **Marine Natural Products**
> Innovative Approaches for the Discovery and Exploitation of Marine Natural Products
> Mar 5-6, 2016
> Chairs: Katherine R. Duncan & Micheal C. Wilson

Mechanical Systems in the Quantum Regime
Mechanical Quantum Systems: From Fundamental Physics to Real World Applications
Mar 6-11, 2016
Ventura Beach Marriott, Ventura, CA
Chairs: Oskar Painter & Eva M. Weig
Vice Chairs: John Teufel & Markus Aspelmeyer

- **Opto- and Electro-Mechanics of Low Dimensional Materials**
  (*Shahal Ilani* / Gary Steele / Wolfgang Wernsdorfer)
- **Mechanical Transducers as Quantum Interfaces**
  (*Andrew Cleland* / Cindy Regal / Yasunobu Nakamura)
- **Hybrid Quantum Systems**
  (*Ania Bleszynski Jayich* / Michel Devoret / Aashish Clerk / Marko Loncar)
- **Nonlinear Dynamics and Multi-Moded Systems**
  (*Jakob Taylor* / Warwick Bowen / Vittorio Peano / Hiroshi Yamaguchi)
- **Nanoscale Devices**
  (*Ivan Favero* / Alex Fainstein / John Davis / Johannes Fink)
- **Cold-Atom Optomechanics**
  (*Monika Schleier-Smith* / Dan Stamper-Kurn / Philipp Treutlein)

- **Precision Measurement and Fundamental Physics**
  (*Klemens Hammerer* / Jun Ye / Jess Riedel / Roman Schnabel)
- **Levitated Mechanical Objects**
  (*Peter Barker* / Jack Harris / Lukas Novotny)
- **Electro-Mechanical Quantum Systems**
  (*Konrad Lehnert* / Pertti Hakonen / Michael Tobar)

> **GRS** **Mechanical Systems in the Quantum Regime**
> Beyond Standard Optomechanics: Exploring New Mechanical Interactions
> Mar 5-6, 2016
> Chairs: Anja Metelmann & Norberto D. Lanzillotti Kimura

Metals in Biology
How to Solve Biologically-Inspired, Metal-Related Problems
Jan 24-29, 2016
Four Points Sheraton / Holiday Inn Express, Ventura, CA
Chair: Joanne Stubbe
Vice Chairs: R. David Britt & Yi Lu

- **Copper Reactivity: Models to Enzymes**
  (*Leslie Murray* / Edward Solomon / Kenneth Karlin)
- **Protein Design**
  (*Donald Hilvert* / Anastassia Alexandrova / Akif Tezcan / Frances Arnold / Donald Hilvert)
- **Metal Sensors: Design, Issues and What We Have Learned**
  (*Amy Palmer* / Stephen Lippard / Yi Lu / Christopher Chang)
- **Non-Heme Iron Chemistry**
  (*Aimin Lu* / Wilfred van der Donk / Pinghua Liu / Wenjun Zhang)
- **Metals and Innate Immunity**
  (*Katherine Franz* / Elizabeth Nolan)
- **Metals in the Enviroment: Biology, Engineering, and Remediation**
  (*Michelle Chang* / Daniel Nocera / Gemma Reguera / Arash Komeili / Kenneth Nealson)
- **New B$_{12}$ Chemistry**
  (*Catherine Drennan* / David Leys / Vahe Bandarian)
- **Paramagnetic and Biochemical Methods to Study Metallo-Enzymes**
  (*Joan Broderick* / Marina Bennati / Brian Hoffman / R. David Britt)
- **Joint Session with the Gordon Research Seminar: RNRs Diverse Metallo-Cofactors Essential Deoxynucleotide Biosynthesis**
  (*Joseph Martin Bollinger* / Amie Boal / Britt-Marie Sjoberg)

Note: Unlike other GRSs, the Bioinorganic Chemistry GRS begins on a Thursday, sharing an evening session with the associated Metals in Biology GRC.

> **GRS** **Bioinorganic Chemistry**
> Exploring All Facets of the Inorganic Chemistry of Life
> Jan 28-31, 2016
> Chair: Kelly Chacon

Molecular & Ionic Clusters
Molecular Clusters from Bimolecular Complexes to the Onset of Bulk Matter
Jan 17-22, 2016
Four Points Sheraton / Holiday Inn Express, Ventura, CA
Chairs: Mathias Weber & Otto Dopfer
Vice Chairs: Gary Douberly & Ruth Signorell

- **Chiral Interactions in Clusters**
  (*Yunjie Xu* / Laurent Nahon / Anne Zehnacker-Rentien)
- **Biomolecular Clusters**
  (*Sonia Melandri* / Jose Alonso / Steen Brondsted Nielsen / Gert Von Helden)
- **Giant Clusters and Liquids**
  (*Julia Laskin* / Stephen Bradforth / Thomas Moeller)

- **Theoretical Treatment of Structures and Excitations in Clusters**
  (*Anne McCoy* / Stefan Grimme / Pavel Jungwirth / Roland Mitric)
- **Atmospheric Clusters and Aerosols**
  (*Veronica Vaida* / Henrik Kjaergaard / Kimberly Prather)
- **H-Bonded Networks and Microsolvation**
  (*Mark Johnson* / Knut Asmis / Takayuki Ebata / Evan Williams)
- **Ultracold Clusters**
  (*Frank Stienkemeier* / Stephan Schlemmer / Andrey Vilesov)
- **Metal-Containing and Inorganic Clusters**
  (*Michael Duncan* / Caroline Chick Jarrold / Etienne Garand / Lai-Sheng Wang)
- **Dynamics in Clusters**
  (*Oliver Gessner* / Masaaki Fujii / Marie-Pierre Gaigeot)

G S **Molecular & Ionic Clusters**
New Developments in Unraveling Cluster Nucleation and Structure
Jan 16-17, 2016
Chairs: Aude Bouchet & Bernadette M. Broderick

Multifunctional Materials & Structures   `NEW!`
The Science of Autonomic, Adaptive and Self-Sustaining Systems
Jan 31 - Feb 5, 2016
Four Points Sheraton / Holiday Inn Express, Ventura, CA
Chairs: B. L. (Les) Lee & Scott R. White
Vice Chairs: James P. Thomas & Nancy R. Sottos

- **Sensing and Self-Diagnosis**
  (*Donald Leo* / Fu-Kuo Chang / Yong Chen)
- **Self-Healing, Remodeling and Regeneration**
  (*Ellen Arruda* / Richard Weinkamer / Thomas Speck / Jeffrey Moore)
- **Modeling and Simulation**
  (*Kaushik Bhattacharya* / Anna Balazs / Sharon Glotzer)
- **Self-Cooling and Thermal Management**
  (*George Lesieutre* / Abraham Stroock / Nancy Sottos / Aaron Esser-Kahn)
- **Self-Powered Systems**
  (*Minoru Taya* / Eric Wetzel / Leif Erik Asp)
- **Adaptive Materials**
  (*Ray Baughman* / Richard Vaia / Andre Studart / Chiara Daraio)
- **Actuation and Morphing**
  (*Jayanth Kudva* / Daniel Inman / Graham Taylor)
- **Multifunctional Design Optimization**
  (*James Thomas* / Somnath Ghosh / Ioannis Chasiotis / James Guest)
- **Processing and Manufacturing Issues**
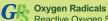 (*Jeffery Baur* / Daniel Therriault / H. Jerry Qi)

Natural Gas Hydrate Systems
Interfacial Science Advances Towards Understanding and Monitoring Gas Hydrate Systems
Feb 28 - Mar 4, 2016
Hotel Galvez, Galveston, TX
Chair: Marta Torres
Vice Chair: Carolyn A. Koh

- **Keynote Session: Processes at the Interface: From Micro to Macro Scales**
  (*Judith Schicks* / Zachary Aman / Andrzej Falenty)
- **Interface Science in Methane Transport: Pipes, Sediment and Water**
  (*Jefferson Creek* / Scott Socolofsky / Daniel McGinnis / Jason Lachance)
- **Gas Hydrates and Energy: New Production Strategies**
  (*Yongkoo Seol* / Erik Spangeberg / Pushpendra Kumar)

- **Sediment-Hydrate-Water Interface: Geomechanics**
  (*Carlos Santamarina* / Jocelyn Grozic / Tae-Hyuk Kwon / Nabil Sultan)
- **Sediment-Hydrate-Water Interface: Slope Stability**
  (*Brandon Dugan* / Matthew Hornbach / Joshu Mountjoy)
- **Challenges and Opportunities for Sensor Technology Applications**
  (*Robert Collier* / Giora Proskurowski / Miriam Roemer / Heike Ebendorff-Heidepriem)
- **New OOI Node on Hydrate Ridge**
  (*Andrew Thurber* / Deborah Kelley / Michael Riedel)
- **Recent Results from the Field**
  (*Peter Linke* / Giuliana Panieri / Heiko Sahling)
- **Microbiology at the Interfaces**
  (*Tina Treude* / Fumio Inagaki / Victoria Orphan)

G S **Natural Gas Hydrate Systems**
New Frontiers in Gas Hydrate Behavior at the Macro- and Micro-Scales
Feb 27-28, 2016
Chairs: Zachary M. Aman & Marco Terzariol

Conferees at the Mycotoxins and Phycotoxins GRC take a break from their soccer game to pose for a group photo at sunny Stonehill College.

New Antibacterial Discovery & Development
Enabling the Next Generation of Antibacterial Drugs
Mar 13-18, 2016
Renaissance Tuscany Il Ciocco, Lucca (Barga), Italy
Chairs: Heike Broetz-Oesterhelt & Jennifer A. Leeds
Vice Chairs: Richard E. Lee & Terry Roemer

- **Keynote Session: The Role of Government in Enabling New Antibacterial Discovery and Development**
  (*Laura Piddock* / Sally Davies / Sumathi Nambiar)
- **New Antibacterial Targets: Focusing on Likelihood of Success**
  (*Hans-Georg Sahl* / Sarah McLeod / Tanja Schneider / Sarah Ades / Rolf Mueller)
- **Technologies to Enable Antibacterial Discovery and Development**
  (*Terry Roemer* / Domingo Gargallo-Viola / Mariana Pinho / Joe Pogliano)
- **Identifying High-Value Chemical Starting Points: Hit Finding Revisited**
  (*Michael Barbachyn* / Christina Spry / Olga Genilloud / Matthew Cooper / Folkert Reck)
- **Addressing the Gap Between *In Vitro* (Target) and *In Vivo* (Cellular) Potency: Strategies to Enable the Latter**
  (*Charles Dean* / Athanasios Typas / Paolo Ruggerone / Olga Lomovskaya)
- **Learning from Clinical Experience with Validated Targets**
  (*Jared Silverman* / John Rex / Mary Motyl / Joyce Sutcliffe / Daniel Ritz)
- **Learning from Clinical Experience with Novel Targets**
  (*Ursula Theuretzbacher* / Antonio DiGiandomenico / Frederick Wittke / Lorraine Hernandez)
- **Alternative Mechanisms of Action and Antibacterial Modalities**
  (*Robert Hancock* / Man-Wah Tan / Cristina Landeta / Aileen Rubio)

- **The Future of Antibacterial Diagnostics: How Will New Diagnostics Enable Clinical Trial Design and Clinical Use of New Antibacterials?**
  (*Herman Goossens* / David Ecker / Linda Miller / Debra Goff)

G S **New Antibacterial Discovery & Development**
Enabling the Next Generation of Antibacterial Drugs
Mar 12-13, 2016
Chairs: David F. Bruhn & Daniel Hoagland

Origins of Life
Bridging Disciplinary Perspectives to See Further Into Life's Origins
Jan 17-22, 2016
Hotel Galvez, Galveston, TX
Chair: Stephen Freeland
Vice Chair: Matthew A. Pasek

- **Keynote Session: How Have We Arrived at Today's Questions?**
  (*Stephen Freeland* / Antonio Lazcano Araujo / Brian Hayes)
- **What Are the Earliest Life-Forms About Which We Can Be Confident?**
  (*Joseph Onyilagha* / Nigel Goldenfeld / Paul Higgs)
- **Advances in Understanding Simpler, Earlier Biospheres**
  (*Timothy Lenz* / Burckhard Seelig / Klara Hlouchova)
- **Connecting Life's Building Blocks: The Challenges of Biopolymers**
  (*Christopher Bennett* / Ramanarayana Krishnamurthy / David Deamer / Gonen Ashkenasy)
- **What Do Computers Bring to the Study of Life's Origins?**
  (*Markus Merringer* / Marco Saitta / Eugene Koonin / Markus Merringer)
- **The Exogenous Influence: What Did Extraterrestrial Sources Contribute to Life's Origins?**
  (*Patrick Gasda* / Aaron Burton)
- **Origins Beyond Earth: Where Else in Our Solar System Might We Expect to Study Life's Origins?**
  (*Heather Kaluna* / Britney Schmidt / Kevin Hand)
- **Future Funding Directions and Implications for Life Origin Research**
  (*Matthew Pasek* / Mary Voytek)
- **Selected Poster Presentations / Young Investigator Presentations**
  (*Omer Markovitch*)

G S **Origins of Life**
Understanding Life's Origin by Diving Outside of the Pool
Jan 16-17, 2016
Chair: Omer Markovitch

Oxygen Radicals
Oxygen Radicals as Effectors of Redox Biology
Feb 7-12, 2016
Ventura Beach Marriott, Ventura, CA
Chairs: Rakesh P. Patel & Ana Denicola
Vice Chairs: Douglas D. Thomas & Michael J. Davies

- **Keynote Session: Sleep Apnea, Oxygen Radicals and Hypertension**
  (*Rakesh Patel* / Gregg Semenza)
- **Pathophysiologic Roles of Oxidized Lipids**
  (*Henry Jay Forman, Homero Rubbo* / Bruce Freeman / David Ford / Anna-Liisa Levonen / Valerie O'Donnell / Christopher Cooper)
- **Sirtuins, Aging and Redox**
  (*Rick Domann, Sruti Shiva* / Raul Mostoslavsky / Carlos Escande / Paul Brookes)

- **Emerging Paradigms in Redox Signaling**
(*Victor Darley-Usmar*, *Douglas Thomas* / Raj Soorappan / Tobias Dick / Yvonne Hanssen Heininger / Daniel Rudic / Daniela Salvemini)
- **New Detection Methods and Probes for Reactive Species**
(*Balaraman Kalyanaraman*, *Paul Winyard* / Kate Carroll / Yang Dan / Cristina Furdui / Ashutosh Kumar)
- **Oxygen Radicals and Mechanisms of Disease**
(*Victor Thannickal* / Karen Bernard / Carola Neumann / Francisco Laurindo / Douglas Spitz / Manisha Patel)
- **Infectious Diseases and Free Radicals**
(*Michael Davies*, *Christine Winterbourn* / Rafael Radi / Michelle Raniere / Lars Dietrich)
- **Role for CO and H$_2$S in Oxygen Radicals Biology**
(*Neil Hogg*, *Jon Lundberg* / Beatriz Alvarez / Christopher Kevil / Takaaki Akaike / Roland Stocker / Roberto Motterlini)
- **Keynote Session: Mitochondrially Targeted Antioxidants and Signaling**
(*Ana Denicola* / Michael Murphy)

Peptides, Chemistry & Biology of
Crossing Barriers by Peptide Science for Health and Wellness
Feb 21-26, 2016
Ventura Beach Marriott, Ventura, CA
Chairs: Philip E. Dawson & Anna Maria Papini
Vice Chairs: Jennifer R. Cochran & James S. Nowick

- **Keynote Session: Crossing the Barrier from Academics to Industry (and Back)**
(*Philip Dawson*, *Anna Maria Papini* / Richard Dimarchi / Peter Kim)
- **Critical Analysis of Cell Penetrating Peptides**
(*Joel Schneider* / Niels Geijsen / Loren Walensky / Yao-Cheng Leo Li)
- **Peptides in the Immune System**
(*Charles Deber* / Huib Ovaa / Yehuda Shoenfeld / Michael Chorev)
- **Peptide Discovery: Biological and Chemical Libraries**
(*Kit Lam* / Thomas Kodadek / Dehua Pei / James Heath)
- **Challenges in Peptide Vaccine Development**
(*Peter Kim* / Elisabetta Bianchi / Michael Zwick)
- **Peptide Discovery: Where to Look Next**
(*Paul Alewood* / Richard Lewis / Mohamed Marahiel)
- **Posttranslationally Modified Proteins**
(*Jeffery Kelly*, *Geoffrey Wahl* / Hilal Lashuel / Matthew Pratt / Christian Becker)
- **Peptides in Epigenetic Regulation**
(*Huib Ovaa* / Champak Chatterjee / Danica Galonic / Beat Fierz / Brian Strahl)
- **Intelligent Materials**
(*Jennifer Cochran*, *James Nowick* / Nicole Steinmetz / Ian Hamley)

Photoionization & Photodetachment
Emerging Techniques for the Study of the Ejection of Photoelectrons as Probes of Dynamics, and Their Application to Exotic Systems in the Gas and Condensed Phases
Feb 7-12, 2016
Renaissance Tuscany Il Ciocco, Lucca (Barga), Italy
Chair: Katharine L. Reid
Vice Chair: Stephen T. Pratt

- **Emerging Techniques and Exotic Systems: Frontiers**
(*Jochen Kuepper* / Francesca Calegari / Bernd Winter)
- **Clusters and Complex Molecules**
(*Caroline Dessent* / Robert Continetti / Jan Verlet / Anna Krylov / Lai-Sheng Wang)
- **Matter in Intense Fields**
(*Fernando Martin* / Christoph Bostedt / Lorenz Cederbaum)
- **Microjets and Nanoparticles**
(*Helen Fielding* / Ruth Signorell / Stephen Southworth / Katrin Siefermann / Toshinoro Suzuki)
- **Novel Probes of Chirality**
(*Laurent Nahon* / Ivan Powis / Olga Smirnova / Yann Mairesse)
- **Capabilities with Ultrashort Laser Pulses**
(*Marc Vrakking* / Thomas Pfeifer / Caterina Vozzi / Albert Stolow)
- **Probing Dynamics at Interfaces**
(*Martin Wolf* / Isabella Gierz / Julia Staeler)
- **New Avenues with Free Electron Lasers**
(*Kiyoshi Ueda* / Nora Berrah / Oliver Gessner / Kevin Prince / Oriol Vendrell)
- **Complementary Techniques**
(*Danielle Dowek* / Reinhard Doerner / Majed Chergui / Ann Orel)
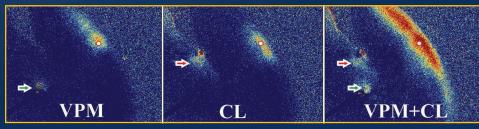
Photosensory Receptors & Signal Transduction
Natural and Synthetic Photoreceptor Systems: From Microbes to Man
Jan 24-29, 2016
Hotel Galvez, Galveston, TX
Chair: John Christie
Vice Chair: Katrina Forest

- **Keynote Session: Light-Gated Ion Channels: Function and Application**
(*Peter Hegemann* / Ehud Isacoff / Anna Moroni / Peter Hegemann)
- **Opsin Structure and Diversity**
(*Hideki Kandori* / John Spudich / Oliver Ernst / Robert Lucas / Adam Cohen / Hideki Kandori)
- **Responses to UV Irradiation**
(*Roman Ulm* / Xiaojing Yang / Takahiro Yamashita / Roman Ulm)

- **LOV to BLUF: Flavoprotein Photosensors**
(*Kevin Gardner* / Masamitsu Wada / John Kennis / Aba Losi / Lukas Kapitein / Kevin Gardner)
- **Cryptochrome Structure and Function**
(*Brian Crane* / Todd Holmes / Margaret Ahmad / Brian Crane)
- **Bilin-Based Photosensory Systems**
(*J. Clark Lagarias* / Sarah Mathews / Richard Vierstra / Emina Stojkovic / J. Clark Lagarias)
- **Microbial Light Sensing and Function**
(*Klaas Hellingwerf* / Sean Crosson / Beronda Montgomery / Klaas Hellingwerf)
- **Light Regulation of Signaling Networks**
(*Peter Quail* / Joanne Chory / Donald Bryant / Karen Halliday / Matias Zurbriggen / Peter Quail)
- **Light Inputs to Biological Rhythms**
(*Jennifer Loros* / Stacey Harmer / Ethan Buhr / Jennifer Loros)

Plant Volatiles
Diversity of Targets, Effects and Applications of Plant Volatiles
Jan 31 - Feb 5, 2016
Ventura Beach Marriott, Ventura, CA
Chairs: Martin Heil & Dorothea D. Tholl
Vice Chairs: Harro J. Bouwmeester & Florian Schiestl

- **The Multiple Effects of Plant VOCs on Other Organisms**
(*Martin Heil*, *Dorothea Tholl* / Juerg Gertsch / Linda Walling / Consuelo De Moraes)
- **The Value and Use of VOCs in Agronomy**
(*Marcel Dicke* / Ted Turlings / Jocelyn Millar / Felix Waeckers / G.U. Sofia Orre-Gordon / Allard Cose)
- **Essential Oils and Other VOCs in Biocontrol and the Industry**
(*Mark Lange* / Toby Bruce / Ravinder Kohli / Elena Stashenko)
- **Plant VOC Metabolism, Biosynthetic Diversity and Mechanisms of Release**
(*Jonathan Gershenzon* / Gregg Howe / Natalia Doudareva / Mark Lange / Paul O'Maille)
- **Plant VOCs as Flavor and Biorenewable Products**
(*Harro Bouwmeester* / Harry Klee / Efraim Lewinsohn / Joerg Bohlmann)
- **VOCs in Plant-Microbe Interactions**
(*Birgit Piechulla* / Luis Herrera-Estrella / Choong-Min Ryu / Elizabeth Quintana-Rodriguez / Maaria Rosenkranz)
- **Plant VOCs in a Changing Environment**
(*Joerg-Peter Schnitzler* / Francesco Loreto / Josep Penuelas)
- **Perception of Plant VOCs in Animals and Plants**
(*Rick Karban* / Anandasankar Ray / Kenji Matsui / Robert Schuurink / Johannes Stratmann)
- **VOCs in the Triangle Between Plants, Herbivores and Pollinators**
(*Florian Schiestl* / Robert Raguso / Andre Kessler)

VPM CL VPM+CL

Core and matrix: Flavoprotein autofluorescent imaging (FAI) in a mouse thalamocortical slice preparation in which connections between thalamus (VPM, core and CL, matrix) and barrel cortex are preserved. The FAI shows postsynaptic activity, and the arrows show the sites of thalamic stimulation via laser uncaging of glutamate. The response to conjoint stimulation of VPM and CL shows massive supralinear summation. Submitted by S. Murray Sherman, Chair, Thalamocortical Interactions GRC.

Gordon Research Conferences are different from other scientific conferences because. . .

...they are small and intimate and allow for scientists at every stage of their career to connect and collaborate. (Laura Sanchez, Chair, 2014 Marine Natural Products GRC)

Plasminogen Activation & Extracellular Proteolysis

Novel Biological Functions of Plasminogen Activation and Extracellular Proteolysis, from Basic Mechanisms to Translational Science
Feb 14-19, 2016
Four Points Sheraton / Holiday Inn Express, Ventura, CA
Chairs: Lindsey A. Miles & Michael Ploug
Vice Chair: Manuel Yepes

- **Extracellular Proteolysis and Women's Health**
  (*Robert Medcalf, Tor Ny* / Zena Werb / Karin List / Qingyu Wu)
- **Neurobiology: From Synaptic Function to Neurological Disease**
  (*Sidney Strickland* / Wendy Campana / Joachim Herz / Jae Kyu Ryu / Stella Tsirka / Manuel Yepes)
- **Structure-Function of Proteases, Receptors and Inhibitors**
  (*Cynthia Peterson* / Christian Heinis / Ruby Law / Nicolai Sidenius / Morten Beck Trelle)
- **Proteolysis in Cancer Dissemination**
  (*David Waisman* / Thomas Bugge / Charles Craik / Elena Deryugina / Steven Gonias / Malgorzata Wygrecka)
- **New Insights into Protease Functions in the Cardiovascular System**
  (*William Fay, Andre Samson* / Nicola Mutch / Edward Plow / Dudley Strickland / Imre Varju)
- **Inflammation and Infection**
  (*David Ginsburg* / Tione Buranda / Frank Castellino / David Corry / Jay Degen / Lirlândia Pires de Sousa)
- **Late-Breaking Topics: The Cutting Edge**
  (*Daniel Lawrence, Victoria Ploplis*)
- **Therapeutics / New Technologies**
  (*Peter Andreasen* / Paul Declerck / Haibo Jiang / Colin Kretz / Robert Lazarus / Toshio Miyata)
- **Role of Extracellular Proteolysis in Senescence and Aging**
  (*Michael Ploug* / Toni Antalis / Pura Munoz-Canoves / Katherine Hajjar / Douglas Vaughan)

GRS — Plasminogen Activation & Extracellular Proteolysis
Novel Biological Functions of Plasminogen Activation and Extracellular Proteolysis, from Basic Mechanisms to Translational Science
Feb 13-14, 2016
Chairs: Andre L. Samson & Colin A. Kretz

Predator-Prey Interactions

New Frontiers in Understanding Predator-Prey Interactions in a Human-Altered World
Jan 24-29, 2016
Ventura Beach Marriott, Ventura, CA
Chair: Andy Sih
Vice Chairs: Evan Preisser & Jacqueline Blundell

- **Keynote Session: Predator-Prey Interactions in a Changing World**
  (*Liana Zanette* / Joseph LeDoux / Thomas Schoener)
- **Climate Change and Predator-Prey Interactions**
  (*David Vasseur* / Kristy Kroeker / Mary O'Connor / Daniel Schindler / Hannu Ylonen)
- **Genetics and Neurobiology of Fear**
  (*Benno Roozendaal* / Alison Bell / Patrizia Campolongo)
- **Novel Predator-Prey Interactions**
  (*Jennifer Rehage* / Mark Hixon / Ben Phillips / Anthony Ricciardi / Julien Cucherousset)
- **The Chemistry of Predator-Prey Interactions**
  (*Douglas Chivers* / Tomas Brodin / Jennifer Thaler)
- **Predator-Prey Interactions, Conservation and Ecosystem Management**
  (*Ellen Pikitch* / Francesca Cagnacci / Mark Hebblewhite / Fiorenza Micheli / Mary Power)

- **Human Perceptions of Predation Risk**
  (*Jacqueline Blundell* / Dean Mobbs / Randolph Nesse)
- **Parasites and Predator-Prey Interactions**
  (*Ryan Hechinger* / Kevin Lafferty / Jason Rohr / Ajai Vyas / Joanne Webster)
- **Ecoevolutionary Responses of Predators and Prey to Environmental Change**
  (*Andrew Hendry* / David Reznick / Nelson Hairston)

A two-photon live image of the invaginating tooth germ at E12.5, which is labelled by membrane GFP that is Z-coded with pseudo-color. Courtesy of Jimmy Hu (UCSF). Submitted by Patrick Tam and Ophir D. Klein, Chair and Vice Chair, Craniofacial Morphogenesis & Tissue Regeneration GRC.

Protein Folding Dynamics

Folding: The Landscapes of Natural and Synthetic Life
Jan 10-15, 2016
Hotel Galvez, Galveston, TX
Chair: Peter G. Wolynes
Vice Chair: Benjamin Schuler

- **Keynote Session: The Atomistic Basis of Folding Energy Landscapes**
  (*Angel Garcia* / Robert Best / Klaus Schulten)
- **The Rights and Wrongs of Folding**
  (*Jose Onuchic* / Alan Fersht / Sheena Radford / Paul Whitford)
- **Fast Folding**
  (*Martin Gruebele* / Gerhard Hummer / Victor Munoz)
- **Folding the Chromosome**
  (*Bin Zhang* / Andrew Belmont / Erez Lieberman Aiden / Masaki Sasai)
- **Towards Synthetic Life: The World of Foldamers**
  (*Jeffrey Hartgerink* / Samuel Gellman / Ivan Huc)
- **Folding One Molecule at a Time**
  (*William Eaton* / Jane Clarke / Ashok Deniz / Michael Woodside)
- **Folding Membrane Proteins**
  (*Daniel Otzen* / Paula Booth / James Bowie)
- **Misfolding Landscapes**
  (*Yaakov Lelvy* / Tuomas Knowles / Pernilla Wittung-Stafshede / Martin Zanni)
- **Frustration and the Evolution of the Folding Landscape**
  (*Elizabeth Komives* / Faruck Morcos / Diego Ferreiro)

Protein Transport Across Cell Membranes

Protein Transport Across Cell Membranes: Mechanism, Structure, and Regulation
Mar 6-11, 2016
Hotel Galvez, Galveston, TX
Chairs: Steven M. Theg & Shu-Ou Shan
Vice Chairs: William R. Skach & Trevor Lithgow

- **General Principles of Protein Targeting to Different Cellular Locations**
  (*Tassos Economou* / Nikolaus Pfanner / Paul Jarvis / Linda Randall)
- **Targeting to Membranes**
  (*Matthias Muller* / Irmgard Sinning / Robert Keenan / Gunnar Von Heijne)
- **Protein Translocation Across Membranes**
  (*William Skach* / Arnold Driessen / Toshiya Endo / Peter Rehling)
- **Insertion into Membranes**
  (*Ross Dalbey* / Thomas Miller / Andreas Kuhn)
- **Dislocation and Quality Control**
  (*Randolph Hampton* / Malaiyalam Mariappan)
- **Protein Import into Organelles**
  (*Carla Koehler* / Ralf Erdman / Ben Berks / Elizabeth Craig)
- **Regulation of Translocation**
  (*Bil Clemens* / Hsou-Min Li / Chris Meisinger / Ming Liu)
- **Pathogenic Secretion**
  (*Harris Bernstein* / Gabriel Waksman / Patricia Clark / Daniel Wall)
- **New Paradigms in Translocation**
  (*Trevor Lithgow* / Feng Shao / Siegfried Musser / Mei Hong)

GRS — Protein Transport Across Cell Membranes
Mechanism, Structure, and Regulation of Protein Targeting and Translocation Across Diverse Biological Membranes
Mar 5-6, 2016
Chairs: Meera Rao & Iniyan Ganesan

Renewable Energy: Solar Fuels

Converting Sunlight into Chemical Energy
Feb 28 - Mar 4, 2016
Renaissance Tuscany Il Ciocco, Lucca (Barga), Italy
Chairs: Fraser A. Armstrong & Heinz Frei
Vice Chairs: Gary W. Brudvig & James R. Durrant

- **Closing the Photosynthetic Cycle: Progress Toward Complete Integrated Systems**
  (*Fraser Armstrong, Heinz Frei* / Michael Graetzel / Erwin Reisner)
- **Recent Advances in Understanding the Elementary Processes of Solar Fuel Production**
  (*Piotr Piotrowiak* / Alexander Cowan / Tanja Cuk)
- **Principles of Electrocatalysts for CO_2 Reduction to Fuels**
  (*Mei Wang* / Marc Koper / Judy Hirst / Jens Norskov)
- **New Catalysts for Fuel Generation**
  (*Marcella Bonchio* / Wendy Shaw / Matthew Kanan / Guido Mul)
- **Challenges for Building Integrated Systems: New Architectures for Hierarchical Structures**
  (*Joseph Hupp* / Harry Atwater / Tohru Setoyama)
- **Biological Fuels Production, Nature's Design Principles for Application in Artificial Photosystems**
  (*Brian Dyer* / Thomas Happe / Daniel Nocera)
- **New Materials for Light Capture and Catalysis**
  (*Xile Hu* / Kyoung-Shin Choi)
- **New Physico-Chemical Methods for Artificial Photosynthesis Research**
  (*Wolfgang Lubitz* / Petra Fromme / Richard van der Sanden / Haimei Zheng / Shannon Boettcher)

- **New Directions in Solar Fuel Technologies**
  (*Mei Wang, Gary Brudvig, James Durrant* / Clifford Kubiak)

GRC **Renewable Energy: Solar Fuels**
Solar Energy Conversion to Fuels
Feb 27-28, 2016
Chairs: Andreas Bachmeier & Lena Trotochaud

Sensory Transduction in Microorganisms
Signaling Diversity in Microbial Systems
Jan 17-22, 2016
Ventura Beach Marriott, Ventura, CA
Chair: John Kirby
Vice Chair: Igor Zhulin

- **Chemosensory Systems**
  (*Gerald Hazelbauer* / Brian Crane / Tino Krell)
- **Community Behavior**
  (*Peggy Cotter* / William Loomis / Christopher Hayes / Caroline Roper / Joao Xavier)
- **Biofilms and Pathogens**
  (*Tracy Raivio* / Christine Josenhans / Birgit Scharf / Zemer Gitai)
- **Cell Surfaces**
  (*Tarek Msadek* / Cynthia Whitchurch / Suckjoon Jun / Nassos Typas)
- **Signaling Networks**
  (*Gladys Alexandre* / Craig Ellermeier / Sean Crosson / Monica Gerth)
- **Synthetic and Systems Biology of Signaling Networks**
  (*Christopher Rao* / Victor Sourjik / Judith Armitage / Amy Schmid / Ann Stock)
- **Energy Monitoring**
  (*John Helmann* / Jacqueline Barton / Rebecca Parales / Dianne Newman)
- **Mechanisms of Motility**
  (*Grant Jensen* / Nicolas Biais / Ken Jarrell / Howard Berg / Lotte Sogaard-Andersen / Douglas Weibel)
- **Small Molecule Signaling**
  (*Fitnat Yildiz* / Joanne Santini / Michael Fischbach / Urs Jenal)

GRC **Sensory Transduction in Microorganisms**
Novel Ideas on Bacterial Sensing of Environmental Cues and Functional Responses
Jan 16-17, 2016
Chairs: Dan Bretl & Cynthia L. Darnell

Sleep Regulation & Function
Functions of Sleep in Body and Brain
Mar 13-18, 2016
Hotel Galvez, Galveston, TX
Chair: Craig Heller
Vice Chair: Chiara Cirelli
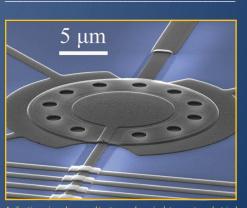
- **Rhythms of the Brain**
  (*Janet Mullington* / Gyorgy Buzsaki)
- **Sleep Disruption, Pain, and Fatigue**
  (*Lydic Ralph* / Ron Davis / Monica Haack / Mark Opp)
- **Sleep as a Window to Study Consciousness**
  (*Giulio Tononi* / Yukiyasu Kamitani / Francesca Siclari / Ursala Voss)
- **Neurophysiology of Memory Consolidation During Sleep**
  (*Gina Poe* / Karim Benchanane / Jan Born / Matthew Wilson)
- **Sleep Aging and Neurodegeneration**
  (*David Dinges* / Jose Cantero / David Holtzman / Clifford Saper)
- **New Circuits that Regulate Sleep**
  (*Barbara Jones* / Christelle Anaclet / Iior Appelbaum / Jeffrey Donlea / Pierre-Herve Luppi)
- **The Role of Sleep in Peripheral Systems**
  (*David Gozal* / Carol Everson / Fareed Hakim / Asya Rolls)

- **Sleep and Epigenetics**
  (*Ted Abel* / Mary Carskadon / Valerie Mongrain / Paolo Sassone-Corsi)
- **Sleep and the Microbiome**
  (*Derk-Jan Dijk* / Eran Elinav / Kenneth Wright)

GRC **Sleep Regulation & Function**
Sleep: Brain, Genes, Behavior and Function
Mar 12-13, 2016
Chairs: Allison J. Brager & Jared M. Saletin

A vibrating micro-drum used to store and manipulate quantum electrical signals. Courtesy of Adam Reed (Lehnert Lab at JILA/CU-Boulder). Submitted by Oskar Painter & Eva M. Weig, Chairs, Mechanical Systems in the Quantum Regime GRC.

Spirochetes, Biology of
Spirochetes: Environmental, Endosymbiotic, Invasive, and Persistent
Jan 10-15, 2016
Ventura Beach Marriott, Ventura, CA
Chair: Justin D. Radolf
Vice Chair: Jenifer L. Coburn

- **Spirochetes: Diverse and Unique**
  (*Linda Bockenstedt* / Jorge Benach / Ben Adler)
- **Interactions of Spirochetes with the Host**
  (*David Haake* / Elsio Wunder / Tara Moriarty / Patricia Rosa / Utpal Pal)
- **Immune Evasion and Persistence**
  (*Janis Weis* / Peter Kraiczy / Nicole Baumgarth / Adriana Marques)
- **Environmental Sensing and Responses**
  (*Scott Samuels* / Mathieu Picardeau / Richard Marconi / Paula Schlax / Brian Stevenson)
- **Physiology, Membrane Biology, and Structural Biology**
  (*Melissa Caimano* / Alejandro Buschiazzo / Christine Jacobs-Wagner / Michael Norgard)
- **Attachment, Invasion, Dissemination, and Persistence**
  (*Sven Bergstrom* / John Leong / Jenny Hyde / Job Lopez / David Haake)
- **Pathogen Recognition and Inflammation**
  (*Peter Kraiczy* / Catherine Werts / Kishore Alugupalli / Joao Pedra)
- **Spirochete Interception and Disease Prevention**
  (*Adriana Marques* / Linden Hu / Caroline Cameron / Kathryn Hacker / Joppe Hovius)
- **Spirochetes as Members of Microbial Consortia**
  (*Jared Leadbetter* / David Hampson / Chris Li / Sukanya Narasimhan)

GRC **Spirochetes, Biology of**
Spirochete Diversity and Pathogenesis: Spanning the Globe
Jan 9-10, 2016
Chairs: Robert B. Lochhead & Azad Eshghi

Thalamocortical Interactions
NEW!
Cell and Circuit Properties of Thalamocortical Interactions
Feb 14-19, 2016
Ventura Beach Marriott, Ventura, CA
Chair: Murray Sherman
Vice Chair: W. Martin Usrey

- **Evolution and Function of Thalamocortical Interactions in Primates**
  (*William Guido* / Jon Kaas / Nikos Logothetis)
- **Thalamic Circuits**
  (*William Guido* / Michael Beierlein / Martha Bickford / Chinfei Chen / Judith Hirsch / Lee Cox)
- **Thalamocortical Processing**
  (*William Guido* / Laszlo Acsady / Jose-Manuel Alonso / Francisco Clasca / W. Martin Usrey)
- **Corticothalamic Processing**
  (*Vivien Casagrande* / Helen Barbas / Farran Briggs / Solange Brown / Massimo Scanziani / Murray Sherman)
- **Computation and Theory**
  (*Eric Shea-Brown* / Larry Abbott / Ken Miller / Terry Sejnowski / Fritz Sommer)
- **Thalamus and Schizophrenia**
  (*John Csernansky* / Alan Anticevic / Monte Buchsbaum / Judith Ford / Anthony Grace / John Lisman)
- **Thalamus and Epilepsy**
  (*Vincenzo Crunelli* / John Huguenard / Nathalie Laresche / Jason Maclean / Jeanne Paz)
- **Thalamocortical Interactions and Behavior**
  (*Tania Pasternak* / Yogita Chudasama / Sonja Hofer / Harvey Swadlow / Bob Vertes / Robert Wurtz)
- **Behavioral Correlates of Higher Order Thalamic Relays**
  (*Tania Pasternak* / Suzanne Haber / Sabine Kastner / David Leopold / Anna Mitchell)

Ultrafast Phenomena in Cooperative Systems
Revealing Coupled Interactions in Complex Matter – Towards Control of Material Properties
Feb 14-19, 2016
Renaissance Tuscany Il Ciocco, Lucca (Barga), Italy
Chair: Martin Wolf
Vice Chair: Robert Schoenlein
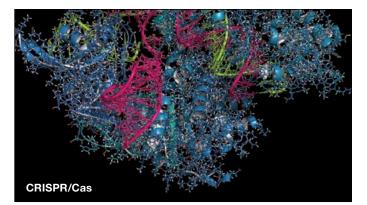
- **Topological Insulators and 2D Systems**
  (*Tony Heinz* / Nuh Gedik / Feng Wang)
- **Electronic Ordering and Correlation Phenomena**
  (*Andrea Cavalleri* / Peter Abbamonte / Urs Staub / Robert Kaindl)
- **Theory of Ultrafast Non-Equilibrium Processes**
  (*Takashi Oka* / Philipp Werner / Peter Oppeneer)
- **THz Excitation and Control of Collective Phenomena**
  (*Richard Averitt* / Alexej Pashkin / Ryo Shimano / Thomas Elsaesser)
- **Non-Equilibrium Dynamics in Superconductors**
  (*Steven Johnson* / Thomas Devereaux / Matteo Mitrano)
- **Photoinduced Phase Transitions**
  (*Dragan Mihailovic* / Julia Staehler / Bradley Siwick / Markus Raschke)
- **Ultrafast Dynamics and X-Ray Diffraction**
  (*Antoinette Taylor* / Margaret Murnane / Henry Chapman)
- **Many Body Physics and Non-Linear Spectroscopy**
  (*Alfred Leitenstorfer* / Immanuel Bloch / David Hsieh / Claudio Masciovecchio)
- **Young Investigator Presentations**
  (*Robert Schoenlein*)

GRC **Ultrafast Phenomena in Cooperative Systems**
Observing and Controlling the Nonequilibrium Properties of Quantum Matter
Feb 13-14, 2016
Chairs: Sebastian F. Maehrlein & Giacomo Coslovich

CRISPR/Cas

Synthetic biology's clinical applications

Engineered systems of genes and other molecular components created through synthetic biology make medical treatments more effective and promise cures for a range of health problems. Perhaps equally important, recent technologies make it easier for a broader range of scientists to apply synthetic-biology approaches that drive expanding clinical applications, from designing new diagnostics and building molecularly engineered tissues to developing new drugs and vaccines. **By Mike May**

Synthetic biology provides scientists with an arsenal of new tools to accurately and efficiently modify the molecular workings of cells to gain medical advantages. According to Jim Collins, Termeer Professor of Medical Engineering and Science at Massachusetts Institute of Technology (MIT) in Cambridge, "Synthetic biology brings together engineering and molecular biology to model, design, and build synthetic gene circuits and other biomolecular components and uses them to rewire and reprogram organisms for a variety of purposes." The clinical uses of synthetic biology already cover a wide range of areas, including diagnostics and treatments. Further, these clinical applications will likely expand more rapidly over the next few years because of the easy-to-use gene editing tools now available.

In 2012, molecular biologist Martin Jinek (now at the University of Zurich in Switzerland) and his colleagues published an article about clustered regularly interspaced short palindromic repeats (CRISPR)/CRISPR-associated (Cas) systems, which make it possible for any molecular biologist to edit an organism's DNA (scim.ag/1piiXv7). This system has quickly supplanted previous editing modalities such as zinc finger nucleases. "This is the most widely used genome editing tool," says Collins. "It's starting to move synthetic

biology toward nonexperts, and it caught on because it works remarkably well in many organisms and is very easy to use."

Synthetic biology is already playing a role in new clinical applications. For example, Collins and his colleagues have modified the genetic machinery from a cell using synthetic biology and embedded it in paper that can be freeze-dried for storage. This process has made possible the development of a paper-based diagnostic that detects pathogens in saliva or blood. Collins points out that the genetic elements embedded in the paper work just like they would in a living cell. He adds that these paper-based diagnostics can be engineered to "detect antibiotic resistance or viral infections such as Ebola." Such diagnostics could be quickly engineered to track public-health concerns. Going beyond diagnostics, the examples below highlight a variety of clinical research projects and emerging treatment options based on synthetic biology—a field that continues to expand into new therapeutic areas.

Two-stage twist

The value of a more efficient means for engineering DNA cannot be overemphasized in synthetic biology. In the United Kingdom, for example, scientists at **Touchlight Genetics** developed a two-step process to synthesize DNA that can be used in biological products. "This enzymatic process enables large-scale, high-yield synthesis of DNA—in the grams per liter range—without bacterial fermentation," says Lisa Caproni, group leader of research applications at Touchlight. The resulting product is called "doggybone DNA" (dbDNA) because of its shape.

Caproni emphasizes that this process overcomes several shortcomings of traditional DNA synthesis. For example, the method provides a ready-to-use product in which DNA does not need to be manufactured in and separated from bacterial material, such as *E. coli*. This is advantageous because DNA produced in bacteria can include genetic information that spurs antibiotic resistance—which is not at all desirable for medical treatments—and as Caproni says, may present "unnecessary practical and regulatory hurdles when used [in humans]." She adds that "some desired DNA sequences are found to be incompatible with growth in bacteria." For example, toxic genes cannot be produced inside any cell. The Touchlight technology sidesteps these challenges.

This technology can be used in several clinically related applications. "The process produces stabilized linear DNA that can be used both in the biomanufacturing of therapeutic DNA products, such as DNA vaccines and DNA-based gene therapy products, and in the creation of a variety of biological products, including therapeutic antibodies and viral vectors," Caproni explains. "In both cases, large quantities of highly pure DNA are required, and it is apparent that the provision of DNA at this scale and purity is expensive, and is often a bottleneck in product development." Because no bacterial steps are

required, large amounts of dbDNA can be made quickly, which makes it easier and more economical to create therapeutic products.

Working together

The breadth of synthetic biology, especially when applied clinically, makes teamwork a necessity for this field. For example, geneticist George Church of Harvard University, synthetic biologist Drew Endy of Stanford University, and microelectronics expert Joseph Jacobson of MIT founded **Gen9**, a company in Cambridge, Massachusetts that advertises itself as a "high-throughput supplier of synthesized genes."

Historically, scientists synthesized genes in pieces composed of 200 or less base pairs—the four building blocks of DNA—largely to reduce the odds of errors. Church, Endy, and Jacobson teamed up to create the BioFab platform, a chip-based process for gene synthesis that can synthesize hundreds of thousands of base pairs. This process allows researchers to work with non-ribosomal peptide-synthetase (NRPS) enzymes, for example. These enzymes come from a long gene cluster that is "critical in identifying new antibiotics," says molecular biologist Devin Leake, vice president of R&D at Gen9. Developing new antibiotics is especially important to Leake because he is allergic to the old standby, penicillin.

Researchers can also apply the Gen9 technology to other clinical opportunities. "We're seeing a lot of interest in protein engineering, like engineering antibodies," Leake says, noting that Gen9 enables researchers to precisely define DNA content that is then synthesized to make antibody variants. "Researchers can modify the amino acids that they want, like maybe including a hydrophobic region in a pocket of an antibody," Leake explains. "Then, changing just one amino-acid residue might give the antibody new properties, and we can explore the entire sequence space." That sort of control could be used to engineer compounds to custom fit disease targets, for example. Moreover, many drug candidates can be tested because the BioFab platform can build gene libraries of millions of variants that can then be screened for safety and effectiveness.

Building the tools

Some of the most intriguing clinical uses of synthetic biology are still in their infancy. For instance, scientists at UK-based **GlaxoSmithKline** (GSK) plan to use synthetic biology to create living systems that make small molecules, like aspirin, that typically come from chemical rather than biological processes. To enhance this capability, GSK licensed CodeEvolver, a protein-engineering technology from California-based **Codexis**. GSK uses this synthetic-biology platform to create unique enzymes for use in manufacturing drugs that work faster or more efficiently.

"We are focused on engineering biology as an improvement or replacement of traditional chemistry in the manufacture of our medicines," says Doug Fuerst, GSK's technology development leader. Using biological systems to

Vibrio cholerae

A microbe could be genetically engineered to detect a particular pathogen and kill it, for example, the bacteria *Vibrio cholerae* that causes cholera.

make chemical compounds, Fuerst explains, can improve the quality of the compounds and reduce the cost. "Using this enzyme evolution approach opens the chemical reaction space that is difficult to access with traditional chemical approaches," explains Mark Buswell, head of GSK's advanced manufacturing technologies. In fact, the biological approach is the only way to catalyze some reactions.

Once a reaction process is engineered through the enzymes, it can be put into cells, so that each cell performs like a drug-making factory. "We start with the ability to control the enzymes," Buswell says. Eventually, he hopes to use that enzyme knowledge to harness biochemical pathways to make drugs in cells instead of reactors.

Eventually, this approach might be used in human cells. Buswell calls this "blue-sky thinking," but a person's own cells might one day be engineered to make the drug required to treat an illness. As Buswell points out, "We're not actively doing that."

Living therapies

Some companies, however, are already turning synthetic biology into cell-based treatments. As MIT's Collins explains, "The field is beginning to expand toward engineering therapeutic microbes—living therapeutics." For example, a microbe could be genetically engineered to detect a particular pathogen and kill it, for example, the bacteria *Vibrio cholerae* that causes cholera. "Such a microbe would function both as a living diagnostic and a living therapeutic," Collins says.

Similarly, a bacteriophage—a virus that infects bacteria—could be engineered to treat bacterial infections. Such a virus might also be used to resensitize a bacterium that had grown resistant to antibiotics. As a result, the bacteria could be made susceptible once again to the antibiotic treatment. With the growing problem of antibiotic resistance, this synthetic-biology technique would be very useful in treating infectious diseases.

Although Collins says that these applications

are "very early on and more on the promising side than execution," he sees them moving ahead, and he plays several roles in advancing such technologies. For instance, **Synlogic** in Cambridge, Massachusetts (where Collins is a scientific cofounder), is engineering microbes to treat phenylketonuria, an inherited disease that results in high blood levels of the amino acid phenylalanine and can cause mental disorders if not treated.

In addition, Cambridge-based **EnBiotix**, where Collins is also a scientific founder, is engineering EPP-001, a bacteriophage that causes target bacteria to secrete an enzyme that destroys a bacteria-based biofilm. Collins and his colleagues hope to use EPP-001 to treat infections in prosthetic joints.

Subverting *Salmonella*

It turns out that bacteria can have both good and bad sides. For example, the Centers for Disease Control and Prevention reports that *Salmonella* infects about 1 million people every year in the United States, 380 of them fatally—but this bacterium is not all bad. Scientists at **Prokarium** in the United Kingdom use genetically altered *Salmonella* to deliver vaccines. "We've tamed the *Salmonella*. We have engineered it to retain its ability to enter the body's immune cells but also to prevent it from causing diseases," says Prokarium's chief executive officer Ted Fjällman. Prokarium uses the bacteria to deliver a vaccine orally. "It enters through the gut lining, is engulfed by immune cells, and then it starts making vaccine," Fjällman says. "It's like a bioreactor in your body."

So far, this technology has been tested in humans in the United Kingdom, the United States, and Vietnam. In addition, it has been tested as a vaccine against diarrhea, hepatitis B, and typhoid—however, it remains in clinical testing. Nevertheless, Fjällman says that this platform "can deliver almost any protein vaccine."

Despite the promise of this platform, much work lies ahead for Fjällman and his colleagues. Although Prokarium purchased the typhoid vaccine from **Emergent Biosolutions** in Gaithersburg, Maryland, this vaccine-*Salmonella* combination must still undergo proper clinical testing.

If this technology proves safe and effective, it will offer many benefits. In addition to the advantage of oral delivery, the *Salmonella*-based vaccine could be thermally stable at 37°C for weeks. "That is very helpful for developing regions," Fjällman says. "This is a huge displacement technology if we can make it happen."

Tailoring tissues

The basis of synthetic biology goes beyond genes and proteins. For instance, **OxSyBio** in the United Kingdom developed 3D printing technologies to construct biological materials or to make materials that mimic them. In 2013, Hagan Bayley and his colleagues at the University of Oxford described these tissue mimics (scim.ag/10ClLDf). The 3D process can control the size of the droplets, which are 30–50 µm across. By printing tens of thousands of droplets only picoliters in volume, Bayley and his colleagues generated cell-like compartments separated by lipid bilayers. Modification with proteins made the bilayers behave like biological membranes, which even allowed electrical communication similar to that occurring in neurons. The authors concluded that "printed droplet networks might be interfaced with tissues, used as tissue engineering substrates, or developed as mimics of living tissues."

Bayley's printing technology can be extended to include living cells that produce functional tissues for use in medical research and, eventually, in clinical applications. This research is being pursued at OxSyBio. "These printed tissues are very similar to biological tissues, and we anticipate that they can be used in toxicology or drug screening," says OxSyBio's director Mike Molinari. In addition, the cells in these tissues can be genetically engineered to further specify tissue properties.

The most advanced clinical applications for printed tissues lie in the future, but Molinari sees several possibilities for the near-term. For example, he says, "Tissue patches might be used to repair damaged heart tissue." He adds, "While the printing of complete synthetic organs cannot be dismissed, organ repair is a more plausible prospect. We will start with small pieces and then migrate to larger and more complex tissues." Eventually, Molinari hopes for even more grandiose applications: "One day," he says, "we might even provide on-demand printing in the operating theater."

The ultimate scope of clinical applications for synthetic biology remains to be seen. Today's application in diagnostics, drug discovery, and tissue engineering should soon grow more extensive and spawn opportunities that are currently unimaginable. Indeed, synthetic biology has the potential to radically change the way clinicians manage disease and to help us live, longer, healthier lives.

miRNA Profiling Assays

A new range of multiplex microRNA (miRNA) profiling assays is now available for high-throughput validation of miRNA biomarkers, based on the new Firefly particle technology. The new Multiplex Cellular miRNA Assay and Multiplex Circulating miRNA Assay allow researchers to rapidly and cost-effectively profile up to 68 miRNAs in each well of a 96-well plate, with readout on a standard flow cytometer. These assays offer an easier workflow for larger sample numbers compared to alternative methods such as quantitative polymerase chain reaction (qPCR), microarray, and sequencing, which can be resource intensive or require challenging data analysis. The Multiplex Circulating miRNA Assay enables profiling of miRNAs from small volumes of crude biofluids including serum and plasma, with no need for RNA purification, while the Multiplex Cellular miRNA Assay is optimized to work with purified RNA. The Multiplex Circulating miRNA Assay is particularly suited for studies targeting low-abundance miRNAs or studies in which the amount of each sample is limiting.

Abcam
For info: 888-772-2226
www.abcam.com

NGS Library Preparation

ThruPLEX Plasma-seq is powered by ThruPLEX chemistry to generate high performance next-generation sequencing (NGS) libraries from cell-free DNA isolated from plasma. The chemistry is optimized specifically for cell-free DNA to maximize the library complexity and to preserve the guanine-cytosine (GC) representation of the input DNA. Starting from less than 1 ng to 30 ng of cell-free DNA, ThruPLEX Plasma-seq generates indexed Illumina NGS libraries that are highly reproducible and consistent in performance between replicates and across different input amounts. ThruPLEX Plasma-seq is ideally suited for applications such as liquid biopsy, circulating tumor DNA (ctDNA) analysis, targeted sequencing, and noninvasive prenatal testing (NIPT).

Rubicon Genomics
For info: 734-677-4845
www.rubicongenomics.com

Real-Time PCR System

The real-time polymerase chain reaction (PCR) system qTOWER 2.0 not only wins with its modern design, but also allows quantitative PCR in the established 96-well format, thus providing an open platform for each kind of qPCR plasticware, from 0.2 mL single tubes to 96-well microplates. The high-grade silver sample block of qTOWER 2.0 also guarantees a temperature homogeneity of 0.2°C over the entire block and is thus suited for any real-time PCR application, with up to six fluorescent dyes. In combination with the available gradient function, additional adaptation to different assays becomes easily possible. Furthermore, the qTOWER 2.0 is equipped with a patented fiber-optic shuttle system for optimal excitation and detection of a variety of known fluorescent dyes. The PC-based system also contains a wide spectrum of optimized analysis tools, including absolute and relative quantification, delta-delta cycle threshold (Ct) method, PCR efficiency, allelic discrimination, endpoint detection, and protein determination.

Analytik Jena
For info: +49-(0)-36-41-77-70
www.analytik-jena.com

Exon Arrays

CytoSure Constitutional v3 arrays deliver the most advanced, high-resolution developmental disorder arrays currently available. Oxford Gene Technology has optimized the arrays via a proprietary probe design algorithm and experimental validation, enabling the selection of highly targeted, specific probes throughout the genome. Using an informed, sophisticated approach to array design, more of these optimized probes have been placed in regions of the genome that are most likely to detect a biologically relevant aberration. The result of this careful design procedure means that regions with the highest priority are covered at exon-level resolution on the arrays, enabling single-exon copy-number variation (CNV) detection in up to 502 prioritized genes of interest. Through combining superior array design capabilities with the latest research-led gene content, the most advanced array design is now available for accurately and easily identifying the causal aberrations underlying developmental delay. Providing straightforward analysis, all CytoSure arrays come with CytoSure Interpret software and full on-site training, streamlining data analysis, and interpretation.

Oxford Gene Technology
For info: +44-(0)-1865-856826
www.ogt.com

Oligonucleotide Column

The AdvanceBio oligonucleotide column is the first high-pH, stable, superficially porous particle-based liquid chromatography (LC) column for oligonucleotide analysis. It builds on Agilent's innovations in superficially porous, silica-based columns for biomolecule separations, which began with the Poroshell 300 in 2001, and includes AdvanceBio peptide-mapping, glycan-mapping, and reversed phase-monoclonal antibody (RP-mAb) columns. The right particle design gives researchers the flexibility to use high-performance or ultra-high-performance LC systems. AdvanceBio's increased flexibility also allows more efficient use of existing laboratory resources, thus reducing costs. AdvanceBio oligonucleotide columns and oligonucleotide standards improve the reliability of results and reduce costs for therapeutic oligonucleotide analysis.

Agilent Technologies
For info: 877-424-4536
www.agilent.com

Electronically submit your new product description or product literature information! Go to www.sciencemag.org/products/newproducts.dtl for more information.

Newly offered instrumentation, apparatus, and laboratory materials of interest to researchers in all disciplines in academic, industrial, and governmental organizations are featured in this space. Emphasis is given to purpose, chief characteristics, and availability of products and materials. Endorsement by *Science* or AAAS of any products or materials mentioned is not implied. Additional information may be obtained from the manufacturer or supplier.

TIANJIN UNIVERSITY
A Fertile Land for International Talents

The national strength relies primarily on the pooling of talents, which requires the encouragement and development of education. 120 years ago, Peiyang University was founded on October 2, 1895 in Tianjin, China. Learning from the educational model of modern western universities, it was to pursue national independence and prosperity. The University was renamed Tianjin University (TJU) in 1951.

Charles D. Tenney, an American educator, was commissioned by Sheng Xuanhuai, founder of the University who played a significant role in the Westernization Movement, to draw up the first university charter in China, and was hired as the University's first acting president. Since then, he started exploring the integration of theory and practice in the development of a modern university that fostered high-caliber scientific talents. Peiyang University harvested its first graduates in 1899 and granted the first collegiate diploma in China in early 1900.

At the beginning of its establishment, most courses were taught by distinguished foreign scholars from the United States, Russia, Britain, France, and Japan. These teachers included Chemist H. V. Fuller, who was a close friend of Albert Einstein, and N. F. Drake, an expert in mining and metallurgy. A number of elites who has been trained overseas, including Zhao Tianlin, Mao Yisheng, Cai Yuanze, Li Shutian, Zhang Hanying, successively served as President of the University.

The University has cultivated and nurtured a number of famous graduates, including "No. 1 expert in modern law" Wang Ch'ung-hui, "Antimony King" Wang Chungyu and "Founding Father of the Olympic Games in China" Wang Zhengting. They have made outstanding contributions not only to the establishment of modern systems of jurisprudence and industry, but also to the development of modern education in China.

Nowadays, TJU is committed to the mission of revitalizing this country through education and upholds the motto "Seeking Truth from Facts" while the faculty follows the guideline of precise learning and strict teaching. Carrying forward the tradition of patriotism and devotion, the University makes a thorough inquiry into science, nurtures talents, inherits and passes on cultures, strengthens the nation and shapes a promising future. The goal of the University is to build a comprehensive, open, internationalized, research-oriented world class university and to contribute significantly the socio-economic development of China and the advancement of the civilization of the world. More and more overseas talents have been attracted to study and work in the University.

Jay Siegel is a renowned professor in the field of molecular design and R&D of new drugs. When hired by President Li Jaijun as the Dean of the School of Pharmaceutical Science and Technology in 2013, this American scientist expected to become the second Charles D. Tenney. The School of Pharmaceutical Science and Technology

President Li Jiajun confers a Letter of Appointment to Professor Jay Siegel appointing him as the Dean of the School of Pharmaceutical Science and Technology
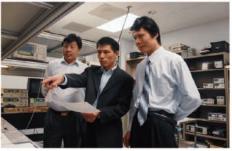
became the University's "International Talent Zone" and employed 26 prominent teachers from 7 countries, including 21 non-Chinese ethnics. Moreover, a Nobel Prize winner is planning to join the TJU pharmaceutical team by applying for the "Recruitment Program of Global Experts" (1000 Talent Plan). Prof. Siegel was approved as the chief scientist responsible for the "Research on the Construction and Basis of Corannulene New Carbon Materials", a national level key project included in "973 Plan". With his pure academic pursuit and the adventurous spirit, this "foreign dean" is making every effort to realize his Chinese dream, i.e. the establishment of a world leading Molecular Design Center in Asia.

In 2005, the micronano manufacturing was an emerging research area in the world while was a blank in China. At that time, Prof. Fang Fengzhou, an expert in this field, resolutely came back to his motherland from Singapore and established the Center of Micronano Manufacturing Technology in Tianjin. During the last decade, the Center has been built into one of the showpiece laboratories worldwide in the field. For his outstanding contributions, Prof. Fang was conferred Albert M. Sargent Progress Award by SME, becoming the first Chinese winning this award.

Professor Fang Fengzhou specializes in ultra-precision machining and measurements

Prof. Li Guifang returned from abroad to his Alma mater in 2011 and set up the Photonic Systems Lab that filled the gap in China in this field. He was selected into the "1000 Talent Plan" and also the chief scientist of the "Fundamental Research on Multidimensional Multiplexing Optical-Fiber Communications", a national level key project included in "973 Plan". The lab has been invested a fund of tens of millions RMB for construction and attracted a number of Chinese overseas young talents born in 1970s and 1980s, including Zhang Lin, Post-doctor in Materials Science and Engineering of MIT, Hu Xiaolong, Post-doctor of Columbia University and MIT, and Zhao Jian, PhD and Research Fellow of Hong Kong Polytechnic University in fiber optic communications. Prof. Li Guifang once said, "I believe that our lab would be admired by any research team in China".

Professor Li Guifang specializes in integrated optoelectronics devices and optical fiber communication systems

Among the scholars that TJU introduces from the "1000 Talent Plan", 7 have been approved as chief scientists of "973 Plan" and 2 have undertaken the "National Key S&T Special Projects" and "ITER (International Thermonuclear Experimental Reactor) Project" as researchers in charge. Regarding talents cultivation, they have offered international courses and guided students to publish in top journals. In terms of team building, two scholars' research teams have been selected as the Ministerial Innovative Teams by MoE. As regards team management, 6 of them serve as school deans, integrating advanced concepts of school running into TJU's development. On the dimension of international cooperation, 4 of them have built international cooperation and innovation centers, which strongly enhances the international influence of the University.

Centered on the urgent need of national construction, Tianjin University is making a brand-new discipline layout with the aim of building itself into a world class university with advanced systems around the world. Such first-class platforms as Tianjin Co-Innovation Center of Chemical Science and Engineering, Center for Applied Mathematics of Tianjin University, School of Marine Science and Technology, Center for Earth and Environmental Science, 3D Print Research Center, Big Data Research Center are attracting overseas talents for greener pasture, who at the same time, are contributing to the bright future of this 120-year-old University.

Founded in 1895 as Peiyang University, Tianjin University (TJU) is regarded as the pioneer of modern higher education in China. Supported by Chinese Ministry of Education, TJU is among the first group of universities to be included in the "985", "211" and "2011" Projects of national investment for developing world recognized universities. Over the years, TJU has grown into a world prestigious research university with distinctive quality and strength in education, research and social services. (www.tju.edu.cn)

Positions

Tianjin University, one of the top universities in China, invites outstanding applicants for a full-time professorship, and seeks candidates in the following areas.

In Science or Engineering:
Engineering, natural science, life science, marine science and technology, information technology, relevant emerging inter-disciplines.

In Other Academic Fields:
Architecture, economics, business, management, social sciences, relevant emerging inter-disciplines. Applicants with multidisciplinary scientific background and nontraditional research approaches are preferred.

Qualifications

Competitive applicants with outstanding academic performance are expected to be academic staff from leading universities or researchers from renowned institutions or companies. Research excellence and potential for future productivity are essential. Additional criteria include leadership and communication skills.

In Science or Engineering:
Applicants shall apply for National Recruitment Program of Global Youth Experts (the National Youth 1000-Talent Program) through Tianjin University. Successful candidates will be employed as an appointee.

In Other Academic Fields:
Applicants will be selected according to their qualifications, academic performance, innovation capability, and leadership.

Responsibilities

Responsibilities include establishing a vigorous research program, teaching undergraduate and graduate students, and providing professional/institutional services.

Salary and Support

The university offers an attractive remuneration package. Salary will be commensurate with candidates' qualifications,

Tianjin University's Binhai Industrial Research Institute

academic performance and experience. In addition, the start-up package from the university provides a research grant, lab/office space and support for the research team.

In Science or Engineering:
An annual pre-tax salary ranging from 400K to 600K RMB will be offered to appointee.
An annual pre-tax salary ranging from 350K to 400K RMB will be offered to the candidates who are shortlisted for interview but not selected in the National Youth 1000-Talent Program.

In Other Academic Fields:
Salary offered is the same as that for Science or Engineering.

Application Process

Please submit a complete application package electronically consisting of the following documents to **oplan@tju.edu.cn** .

(1) Application form
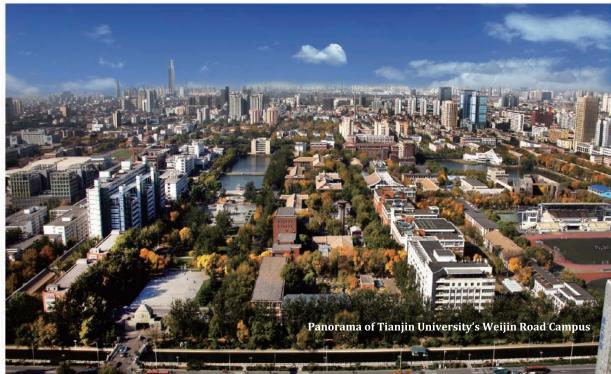(2) Detailed curriculum vitae
(3) Publications list and five full-text representative publications

A detailed application information and the application form can be downloaded from http://hr.tju.edu.cn/z-pxx/js/.

Contacts

Contact Persons : Ms. Zhang Yinlu,
Ms. Chang Xin
Human Resource Department,
Tianjin University, China
E-mail: oplan@tju.edu.cn
Telephone: (+)86-022-27403932,
(+)86-022-27402079
Fax: (+) 86-022-27404177
Address: 318/Building 9, 92 Weijin Road, Nankai District, Tianjin, 300072

FACULTY POSITIONS AT TIANJIN UNIVERSITY

Panorama of Tianjin University's Weijin Road Campus

Massachusetts Institute of Technology

Come work with us!

Tenure Track Faculty

The Department of Brain & Cognitive Sciences (BCS) (http://bcs.mit.edu) at MIT is looking to hire up to five (5) tenure-track faculty at the assistant professor level. Affiliations with the Picower Institute for Learning & Memory and the McGovern Institute for Brain Research are possible. We are most excited about candidates who work in one or more of the following four (4) areas:

i. Computational and theoretical approaches to neuroscience and cognition. Possible areas of focus include but are not limited to: statistics and data science, neural circuits, neural population representations and transformations, and cognitive processes. Candidates with the ability to build bridges across empirical domains are especially attractive. An affiliation with Electrical Engineering and Computer Science (EECS), the Computer Science and Artificial Intelligence Laboratory (CSAIL), Institute for Data, Systems, and Society (IDSS), or other allied departments is possible.

ii. Systems neuroscience in non-human animals. The ideal candidate would be driven by computational questions and ideas from human cognition, with the goal of reverse engineering the underlying neural representations and processes using tools that allow access to multiple brain regions.

iii. Cognitive neuroscience in humans, especially if the candidate's work bridges levels of analysis using a variety of methods including MRI, MEG, fMRI, theoretical modeling, genetics and reverse engineering approaches.

iv. Human cognition using behavioral methods, especially in the areas of language and/or cognitive development.

Successful applicants are expected to develop and lead independent, internationally competitive research programs and to share in our commitment to excellence in undergraduate and graduate education by teaching courses and mentoring graduate and undergraduate students. PhD must be completed by start day of employment and some postdoctoral training is preferred.

Please submit application materials – cover letter, CV, statement of research and teaching interests and representative reprints – online at https://academicjobsonline.org/ajo/jobs/5972. Please state research area in cover letter. To help direct the application, applicants should indicate which of the four areas listed above is their main research area by answering the mandatory questions included in the application. In addition, please arrange to have three letters of recommendation submitted online. Review of applications will begin on October 31, 2015.

MIT is an affirmative action employer, and we encourage applications from women and underrepresented minorities.

http://web.mit.edu

ERA Chair in Cellular and Molecular Biology of Ageing

· U C ·

UNIVERSIDADE DE COIMBRA

Faculty of Medicine of the University of Coimbra (FMUC) announces a Senior Scientist position (ERA Chair holder) for the ERA@UC 2.5 M€ project funded by Widespread 2014-ERA Chairs. The Senior Scientist position foresees an initial 4.5 years full-time appointment and the recruitment of the ERA Chair team to develop outstanding research, advanced teaching and science management in the field of Cellular and Molecular Biology of Ageing. The outstanding performance of the ERA Chair team will support a tenure position for the Senior Scientist at the University of Coimbra.

The ERA Chair team will be the first top-quality research group of the strategic project "Multidisciplinary Research Institute of Ageing-MIA" and "Vitality Campus Ageing@Coimbra", funded by the program Spreading Excellence and Widening Participation - Teaming and flagship project of "Centro" region of Portugal.

Requirements:
• Internationally leading and highly competitive scientist in ageing research, using simple model organisms such as the nematode *C. elegans*, the zebrafish *D. rerio*, or the fruit fly *D. melanogaster*
• Proven experience in science and education management
• Solid experience in securing competitive funds from international agencies (eg. ERC, H2020, 7FP, NIH and others)
• Established international network of collaborators
Find out more information online at: **http://www.uc.pt/en/fmuc/ibili/erachair/**

Application: Submit a detailed proposal according to the template provided at the website **http://www.uc.pt/en/fmuc/ibili/erachair/**, including a short CV and two-pages (max.) research plan.

The template should be submitted in pdf format to the email ggp@fmed.uc.pt **no later than November 15th, 2015**.

For additional information please send an email to **ggp@fmed.uc.pt**

DANA-FARBER CANCER INSTITUTE

CHAIR
DEPARTMENT OF PEDIATRIC ONCOLOGY
Dana-Farber Cancer Institute and Boston Children's Hospital

Dana-Farber Cancer Institute and Boston Children's Hospital are seeking an academic leader to serve as the chair of the Department of Pediatric Oncology at the Dana-Farber Cancer Institute with an appointment as Professor of Pediatrics at Harvard Medical School.

This individual will be responsible for the full scope of clinical, research and educational activities of the department as well as collaborative activities with the other departments at Harvard Medicine School and its affiliated institutions.

Candidates should have an established record as a mentor and as a teacher, national recognition for research accomplishments, and possess exceptional leadership, managerial and collaborative skills. Ideally, she/he would be a proven leader with an international reputation in pediatric oncology who can lead a complex and successful department to even higher levels of excellence.

Interested candidates are requested to submit a current Curriculum Vitae to the email address below for consideration.

Committee Chair
James D. Griffin, M.D., Professor of Medicine,
Dana-Farber Cancer Institute

Pedi_Oncology@dfci.harvard.edu

We are an Equal Opportunity Employer and all qualified applicants will receive consideration for employment without regard to race, color, religion, sex, sexual orientation, gender identity, national origin, disability status, protected veteran status, or any other characteristic protected by law.

宁波大学
NINGBO UNIVERSITY

Ningbo University invites you to apply for faculty positions

About Ningbo University

Founded in 1986 by Sir Yue-Kong Pao and autographed the name by Deng Xiaoping, Ningbo University (NBU) is a young and dynamic university located in the beautiful city of Ningbo by East China Sea, with five campuses covering 160 hectares of land. As a leading comprehensive university in Zhejiang Province, NBU offers programs in economics, law, education, liberal arts, history, science, engineering, agriculture, medicine, and management. The university now receives public funding, as well as continuous support and generous donations from many overseas Chinese and their families including Sir Yue-Kong Pao, Sir Run-Run Shaw, Chao An Chung, Hans Tang, Yue-shu Pao, Cao Guangbiao, Li Dashan, Zhu Xiushan, etc.

Academic Excellence

NBU consists of 22 faculties and offers 75 undergraduate programs, 116 master programs, and 12 Ph.D. programs. It enrolls 31,645 students including 26,527 full-time undergraduates and 5,118 graduate students. Currently NBU has around 1,400 full-time faculty members and 1,000 administrative staff members. Among them there are 5 academicians, 284 full professors, and 721 associate professors.

Research Achievements

With 77 research institutes and 14 key laboratories, NBU is the center of varieties of research and teaching activities. The research and development initiatives of the university, especially in marine science, information science and technology, engineering mechanics, and material science have contributed greatly to the economic development of the region and have been recognized by numerous national awards. The university library has a CNKI Network Administrative Service Center, and a collection of approximately 1,700,000 books and 11500GB digital resources.

International Programs

NBU maintains close links to 47 well-known institutions of higher education in Canada, Germany, France, Great Britain, USA, Sweden, Japan, South Korea and Australia. For example, the Sino-Canada joint-educational program is welcomed by international students with 100% satisfaction.

QUALIFICATIONS

Candidates should at least have (a) a Ph.D. degree in a related discipline, (b) adequate teaching ability and a strong passion for teaching, (c) an outstanding research background and influential publication record in recent three years, and (d) an ability to conducthigh-quality research and attract external funding.

REMUNERATION & CONDITIONS OF SERVICE

Salary offered will be commensurate with qualifications and experience. Remuneration package will be highly competitive. Forapplicants with titles of professor or associate professor, salary and housing compensation can be negotiated on the individual basis.For newly graduate PhD and Postdoctoral, initial appointment will be made on a fixed-term contract, with a housing compensation of 600,000 RMB upon fulfillment of the contract requirements. Re-engagement thereafter is subject to mutual agreement.

APPLICATION

Please submit completed application form, CV and cover letter via email to rsc@nbu.edu.cn. Application forms can be downloaded from http://www.nbu.edu.cn/shizi Recruitment stays open until positions are filled unless otherwise specified. Please visit http://rsc.nbu.edu.cn for more details.

INFORMATION ON POSITIONS

SCHOOL OF MARINE SCIENCE
Professor/Associate Professor
Marine Biotechnology/ Marine Sciences/Medicinal Chemistry/ Ocean Engineering/Marine planning and remote sensing /Sea port and environmental ecology/Marine Geographic Information Science

Faculty of Electrical Engineering and Computer Science
Professor/ Associate Professor Wireless Communications / New Generation Communication Networks / Underwater Acoustic Communication / Multimedia Information Processing / Embedded Systems / Integrated Circuit Design / Electronic Design Automation / Database System / Big Data Processing / Software and Theory / Information Security / Mobile Computing / Graphics and Image processing / Power system and Its Automation / Power Electronics / Pattern recognition and Intelligent system / Sensor and Intelligent detection

FACULTY OF SCIENCE
Professor/Associate Professor/Assistant Professor
Condensed Matter
Physics/Microelectronics/Optoelectronics/Solar Cell
Department of Mathematics/Computational Mathematics/Probability and Statistics / Financial Mathematics

FACULTY OF MECHANICAL ENGINEERING AND MECHANICS
Professor/Associate Professor/Assistant Professor
Mechanics/Vehicle
Engineering/ Mechanical
Engineering/Industrial Design

INTERNATIONAL COLLEGE
Professor/Assistant Professor
Accounting

SCHOOL OF MATERIALS SCIENCE AND CHEMICAL ENGINEERING
Assistant/Associate/Full Professors
Polymer Science/Chemical Engineering/Materials Science

SCHOOL OF LAW
Professor/Associate Professor/Assistant Professor
Criminal Law/Criminal Procedure Law/Civil Procedure Law/Civil Law/Electronic Commerce Law

COLLEGE OF TEACHER EDUCATION
Professor/Associate Professor/Assistant Professor
Curriculum and Teaching Methodology/Higher Education/Preschool Education/Educational Economy and Management/Cognitive Psychology/Educational Psychology/Clinical Psychology/School Psychology/Experimental Psychology/Personality Psychology/Social Psychology/Management Psychology/Computer Graphics and Digital Image Processing/Electronic Music, Game Development/3D Animation and Game Development

FACULTY OF MARITIME AND TRANSPORTATION
Professor/Associate Professor/Assistant Professor
Department of Logistics and Transportation/Department ofMaritime Technology/Department of Marine Engineering/Department of Naval Architecture and Ocean Engineering

FACULTY OF PHYSICAL EDUCATION
Assistant Professor
Sport Management/Sport Sociology/Human Movement/Sport Training/Sport Physiology

MEDICAL SCHOOL
Professor / Associate Professor
Mechanism And Prevention Of Alzheimer's Disease; Oncology; Genetics; Human Anatomy; Histology And Embryology; Cell Biology; Immunology; Microbiology; Parasitology; Analytical Chemistry; Occupational And Environmental Health; Toxicology

COLLEGE OF ARTS
Professor / Associate Professor / Assistant Professor
Performance Of All Areas, Musicology (Ethnomusicology), Music Composition
Art Design Of All Areas, Digital Arts, Fine Art, Art History,Art/Music Industry, Art/Music Therapy

SCHOOL OF ARCHITECTURE, CIVIL ENGINEERING AND ENVIRONMENT
Professor /Associate Professor /Assistant Professor
Architecture Design/Urban Design/ Urban Planning/Architecture Technology/Human Geography/ Physical Geography/Cartography and Geographic Information System/Environmental Technology/Applied Environmental Microbiology/ Civil Engineering/Engineering Management

PRESIDENT
HOWARD HUGHES MEDICAL INSTITUTE

The Trustees of the Howard Hughes Medical Institute invite nominations and applications for President of HHMI. The President serves as HHMI's chief executive officer. It is anticipated that the President will be an internationally recognized scientist with diverse leadership experiences who is passionate about advancing biomedical research and science education.

HHMI is a nonprofit medical research organization that plays a powerful role in advancing basic research and science education across the U.S. As one of the nation's largest philanthropies, HHMI has provided over $8 billion in direct support for research and science education over the past decade. In 2014, the Institute invested $706 million in U.S. research and provided $77 million in grants and other support for science education.

Unlike most science funders, HHMI invests in people, not projects. HHMI believes that scientists of exceptional talent, commitment, and imagination will make fundamental biological discoveries if given the resources, time, and freedom to pursue challenging questions. Through rigorous national competitions, HHMI selects top researchers to become HHMI investigators. Today, over 300 HHMI investigators lead laboratories at approximately 70 host institutions (universities, research institutes, and hospitals). HHMI scientists and lab staff are employees of the Institute and supported by a nationwide team of dedicated professionals.

HHMI is known for experimenting with how science is done. In addition to its Investigator program, the Institute developed its own research campus, Janelia Research Campus, in Ashburn, Virginia, to tackle some of science's most profound questions in a collaborative, interdisciplinary culture. Researchers at Janelia engage in active bench science, computational analysis, and theoretical work to probe fundamental questions and pursue groundbreaking discoveries in the field of neuroscience.

As a complement to its research programs, HHMI operates a significant grants program to enhance science education for students at all levels, with a particular focus on innovative undergraduate science education. To inspire the next generation of scientists, HHMI creates exceptional films, classroom resources, and teaching strategies for use in high schools, colleges, and universities across the country.

Founded in 1953 by Howard R. Hughes, the aviator and industrialist, HHMI is headquartered in Chevy Chase, Maryland, and employs close to 3,000 people across the U.S. It has an endowment of nearly $19 billion. More information about HHMI is available at www.hhmi.org; more information about the position of President is available at **http://www.hhmi.org/presidential-search**.

Responses should be directed to **PresidentSearch@hhmi.org** and should include a current curriculum vitae with a cover letter summarizing the candidate's scientific interests and accomplishments and administrative experience.

hhmi | Howard Hughes Medical Institute

Equal Opportunity Employer

The **Department of Systems Biology at Harvard Medical School** invites applications for tenure-track Assistant Professor positions. Two positions are available. We seek creative thinkers who take risks in defining and addressing important problems in biology and medicine, and who use quantitative experimental, computational and/or theoretical approaches in their work. The Department has a diverse faculty with backgrounds in cell biology, biochemistry, physics, mathematics, chemistry, computer science, engineering and medicine, and offers a lively, family-friendly, and supportive environment in which to perform interdisciplinary science.

The successful candidates will become members of Harvard University's Ph.D. Program in Systems Biology, a cross-campus interdisciplinary program that attracts extraordinary graduate students.

A Ph.D., M.D./Ph.D. or M.D. is required.

The deadline for applications is **15 November 2015.** Application instructions can be found at **http://academicpositions.harvard.edu/ postings/6429**.

We are an Equal Opportunity Employer and all qualified applicants will receive consideration for employment without regard to race, color, religion, sex, sexual orientation, gender identity, national origin, disability status, protected veteran status, or any other characteristic protected by law.

POSITIONS OPEN

THE DEPARTMENT OF CHEMISTRY

The Department of Chemistry at Boston University invites applications from outstanding candidates for a an Assistant Professor tenure track position in the field of Experimental Physical, beginning July 1, 2016. Candidates with research focus broadly defined in the areas of biophysical chemistry, advanced imaging, materials science, nano(bio)technology, or energy/sustainability are particularly encouraged to apply. The successful applicant should have a strong interdisciplinary focus and will benefit from the department's supportive and collegial environment which includes close affiliations with Boston University's Materials Science and Engineering Division, the Photonics Center, Neuroscience Center, and Quantitative Biology Program. Undergraduate teaching responsibilities will be in the areas of physical, analytical and general chemistry, and materials, with the opportunity to develop graduate courses in the candidate's area of expertise. Applicants should apply by submitting a letter of interest, including teaching and research objectives, and current Curriculum Vitae, and arrange to have three letters of reference sent by October 31, 2015 through website **https://academicjobsonline.org/ajo/jobs/6188**.

Boston University is an Equal Opportunity Employer and all qualified applicants will receive consideration for employment without regard to race, color, religion, sex, national origin, disability status, protected veteran status, or any other characteristic protected by law. We are a VEVRAA Federal Contractor.

DEPARTMENT OF CHEMISTRY AND BIOCHEMISTRY

The University of Windsor's Department of Chemistry and Biochemistry invites applications for two tenure-track Assistant Professor positions as part of its expanding program in Materials Science in the areas of (1) Sustainable Materials and Green Chemistry, and (2) Health Applications of Materials commencing July 1, 2016. For complete job descriptions visit our website at **www.uwindsor.ca/ 50newprofs**. For more details contact: Dr. Bulent Mutus, Head, Chemistry and Biochemistry, Faculty of Science, University of Windsor, 401 Sunset Avenue, Windsor, Ontario Canada N9B 3P4, Phone: 519-253-3000 Ext. 3526; E-mail: chembiohead@uwindsor.ca.

Post-doctoral Fellowships at the Centre for Heart and Lung Innovation and PROOF Centre of Excellence at St Paul's Hospital, University of British Columbia

PROOF Centre of Excellence and UBC Centre for Heart Lung Innovation, St. Paul's Hospital, Vancouver, BC

Salary: Commensurate with experience

Program: Computational Biology and Biomarker Research in Heart and Lung Diseases

TWO post-doctoral positions (both with one-year term and extendable for another year with satisfactory progress) are available immediately for two highly motivated recent PhD or MD/PhD graduates to join collaborative research teams at the Centre of Excellence for the Prevention of Organ Failure (PROOF Centre) and UBC Center for Heart Lung Innovation. The two positions will be focused on computational biology and the characterization of biomarkers in chronic heart or lung disease:

(1) The **Chronic Obstructive Pulmonary Disease (COPD) research fellow** will work under the supervision of James Hogg, MD. Ph.D. an emeritus professor in the Department of Pathology at the University of British Columbia, and Senior investigator at the HLI located at St Paul's Hospital and Raymond Ng, Ph.D., a professor in the Department of Computer Science, University of British Columbia and Chief Informatics Officer at the PROOF Centre. The research will involve comparing genetic, genomic and proteomic data from tissue and blood samples to enhance the biological understanding of COPD. That is currently being conducted in collaboration with Dr. Avrum Spira and his colleagues at Boston University.

(2) The **Heart Failure and Heart Transplantation research fellow** will work under the supervision of Bruce McManus, MD, PhD, a professor in the Department of Pathology at the University of British Columbia and CEO of PROOF Centre, and Raymond Ng, PhD, a professor in the Department of Computer Science at the University of British Columbia and Chief Informatics Officer at the PROOF Centre. The research will involve comparing genomic and proteomic data from tissue and blood samples to enhance the biological understanding, diagnosis, prognosis or monitoring of heart failure and heart transplant rejection.

The latest computational biology approaches will be used to identify specific biological pathways underlying heart or lung failure, thereby improving our understanding of the mechanisms and biomarkers involved in these conditions. These positions will be exceptional opportunities for highly talented and ambitious young investigators with very strong backgrounds in computational biology, plus proven experience with high-throughput data analyses. The successful applicants will be expected to make major discoveries related to cardiac or lung disease and inflammatory/immune conditions.

Eligibility: Interested individuals with a recent PhD or MD/PhD, strong publication records and excellent academic credentials are encouraged to apply. Prior expertise in computational biology approaches, including data mining and systems science, is a requirement. Prior experience in immunology, cardiac biology, or functional genomics is a bonus. UBC hires on the basis of merit and is committed to employment equity. We encourage all qualified persons to apply. However, Canadians and permanent residents of Canada will be given priority.

Duration: 1 year with possible extension for a second year.

Contact: Please submit a cover letter, curriculum vitae, transcripts from formal post-secondary school education, and the names and full contact information for three professional references. The cover letter should include a description of your previous research experience and long-term career goals. Send electronic applications by **October 9, 2015** to **kelly.ceron@hli.ubc.ca**.

Launched in 2014, the Evergrande Center for Immunologic Diseases at Harvard Medical School and Brigham and Women's Hospital comprises both basic and translational research programs focused on chronic inflammation underlying autoimmune, neurologic and metabolic diseases, and the environmental factors that trigger chronic inflammation. The Center has an ambitious ten-year growth plan, including faculty recruitment.

Evergrande Center faculty:

- Vijay Kuchroo **(Chair)**
- Arlene Sharpe **(Co-Chair)**
- Ana Anderson
- Christophe Benoist
- Diane Mathis
- Howard Weiner

HARVARD MEDICAL SCHOOL

BRIGHAM AND WOMEN'S HOSPITAL

We are an equal opportunity employer and all qualified applicants will receive consideration for employment without regard to race, color, religion, sex, national origin, disability status, protected veteran status, or any other characteristic protected by law.

EVERGRANDE Center for Immunologic Diseases

HARVARD MEDICAL SCHOOL

BRIGHAM AND WOMEN'S HOSPITAL

Assistant Professor

The Evergrande Center is inviting applications for a tenure track position at the rank of Assistant Professor commensurate with experience and accomplishments. We seek an exceptional scientist addressing fundamental or translational questions related to chronic inflammation.

Applicants should have a track record of high-quality, published research, and proposals for an exciting line of investigation related to chronic inflammation. The successful candidate will join the current six core faculty members of the Evergrande Center for Immunologic Diseases, where s/he will direct a program of independent research, taking advantage of the Center's core facilities, expertise and other resources. We are particularly interested in candidates who value a highly collaborative and interactive approach to research. The ideal candidate will have an MD and/or PhD and evidence of a creative, collegial and exceptional research track record. While a track record of grant funding is desirable, it is not required.

The appointment will be with the Department of Neurology at Brigham and Women's Hospital and the Department of Microbiology and Immunology at Harvard Medical School. The successful candidate will be provided laboratory space in a new research building due to open 2016, and a customary start-up package. Salary and benefits will be competitive with other institutions.

Interested candidates should send a cover letter, a curriculum vitae, and a brief (2-3 pages) statement of current and future research plans to the Chairs of the Committee (Vijay Kuchroo and Arlene Sharpe) at:

Admin@evergrande.hms.harvard.edu

Computational Biologist

The Computational Biologist will coordinate and perform computational analyses of the genomic and transcriptomic data generated within the Center's laboratories, including working with Center faculty to formulate strategies, assessing and applying software tools and programming languages, developing novel statistical tools and algorithms, orchestrating data integration and advising and training Center researchers. Additionally, the Computational Biologist will coordinate and lead input from other Center computational specialists and coordinate with Brigham and Women's Hospital and Harvard Medical School IT staff for access to high-performance computer resources and for the deployment and management of data analysis pipelines, databases and web servers. Special projects as assigned.

To apply for the Computational Biologist position, please visit the Brigham & Women's Hospital Career site at: **careers.brighamandwomens.org** and search for **Job ID # 3001286.**

For further details on these positions and the **Evergrande Center**, please visit our website at: **evergrande.hms.harvard.edu**

By **Rachel Yoho**

How science fairs shaped my career

O n a hot summer day nearly 10 years ago, I found myself straining pig manure to remove maggots for use in my high school science fair project. At the time, I certainly wondered if the results would be worth the effort. Although sometimes smelly, science projects were an essential part of my school experience. Now in the fourth year of my Ph.D. in an environmental microbiology lab, I wonder where I would be without those early opportunities to investigate.

I attended my first State Science Day in Ohio when I was in the seventh grade. I felt inspired while watching high school students earn scholarships for their projects. Although my path through science fairs was not smooth, I received the jury's highest category rating 6 years in a row for my environmental and microbiology projects. By the time I graduated from high school, I had also published a conference proceedings abstract in *The Ohio Journal of Science*. These early accomplishments helped me decide on a research career and earn scholarships to pay for my college and graduate education.

My senior-year project, the one that got published, investigated electrode materials for microbial fuel cells that utilized pig manure. The work later developed into an undergraduate project at Capital University, which yielded results that I presented at regional and national conferences. At the Posters on the Hill conference in Washington, D.C., my adviser and I met with congressional staff and representatives to discuss the importance of undergraduate scientific research.

Today, many schools are moving away from inquiry-based science education. A common argument against science fairs is that they take away from family time. But this needn't be the case: My parents embraced the adventure. Research rarely goes smoothly, so my parents and I have a number of now-entertaining memories from my science fair projects. The stories range from developing an efficient system to remove maggots from manure with my dad to nearly falling into a frigid reservoir with my mom while collecting water samples.

My science fair projects helped me develop many skills beyond doing research itself: I learned how to read the literature, write up results, and give presentations. I discovered that one of the most important skills for a young

"The tri-fold board of a science fair display provided an invaluable educational experience."

scientist's success is finding good mentors. Although another common complaint about science fairs is that they do not offer equal opportunities to all students, I do not feel that having two parents from nonscience backgrounds ever was a barrier. I found at home all the support and enthusiasm I needed to pursue my dreams, and I sought out research mentors and opportunities at nearby labs.

For graduate school, I received a fellowship from the National Science Foundation to expand my work on microbial fuel cell technologies using advanced electrochemical methods (and no pig poop, thankfully) at Arizona State University, Tempe. Following my Capitol Hill experience, I have added science education and communication research into my Ph.D., exploring how the educational system presents hotly debated science topics. Beyond developing my research career, I strive to become an effective communicator and advocate for science in education and public outreach.

For me, rather than something to dread, the tri-fold board of a science fair display provided an invaluable educational experience. I encourage schools and funding agencies to consider the many career benefits before removing science fairs from the curriculum. Science fairs—or maybe it was the pig poop—helped me find my path into research. ∎

Rachel Yoho is a doctoral candidate in the Biological Design Program and the Swette Center for Environmental Biotechnology at Arizona State University, Tempe. Any opinions, findings, and conclusions or recommendations are those of the author and do not necessarily reflect the views of the National Science Foundation or other entities. Send your story to SciCareerEditor@aaas.org.